

TRANSPORT PHENOMENA UNDER JETS IMPINGING  
ON A MOVING SURFACE WITH THROUGHFLOW

by

© Suna Polat

A thesis submitted to the Faculty of Graduate Studies and Research in  
partial fulfillment of the requirements for the degree of Doctor of  
Philosophy.

Department of Chemical Engineering

McGill University

Montreal

May, 1988

To

Osman, Barış and Ayşe Bikem

i

## PREFACE

This thesis on heat transfer under impinging slot jets at a moving permeable surface with and without throughflow was carried out under the supervision of Drs. W.J.M. Douglas and A.S. Mujumdar of the Department of Chemical Engineering, and was done in the Pulp and Paper Research Centre of McGill University.

The thesis results, Chapters 4-7, were written in a form close to that of the publications planned. Chapter 4 describes the most important experimental feature, the unique permeable heat flux sensor. The time and effort that went into the development of this sensor was excessive. Chapters 5 and 6 report the experimental results obtained using this sensor to measure the industrially important effects of throughflow and impingement surface motion on heat transfer under confined single and multiple slot jets. The numerical simulation of impingement heat transfer for single and multiple jets appears as Chapter 7.

Two papers listed below, which constitute an integral part of this Ph.D. thesis project, are included to only a limited extent in the thesis itself for reasons of length. The thesis contains only a 5-page condensation, Section 2.3, of the 40-page review of numerical studies on impinging jets made by the author and a fellow graduate student, Bing Huang, "Numerical Flow and Heat Transfer under Impinging Jets: A Review" (Chapter 4, Annual Review of Numerical Fluid Mechanics and Heat Transfer, Volume 2, pp. 157-197, 1988). The results contained in the paper "Evaluation of near-wall models for prediction of heat transfer under a turbulent impinging slot jet", presented at the First World Conference on Computational Mechanics, Sept. 22-26, Austin, TX, 1986,

33 pages, are given in revised and condensed form as Section 7.3 of the thesis. The results in two papers published prior to the thesis:

"Heat transfer distribution under a turbulent impinging jet- A numerical study", Drying Technology, Volume 3, No. 1, pp. 15-38, 1985.

"Numerical prediction of multiple impinging turbulent slot jets", Drying'86, Proc. of 5th Int. Drying Conf., August 13-15, Cambridge, MA, pp. 868-879, 1986.

are not included in Chapter 7 for reasons of the length of the thesis.



## ABSTRACT

A permeable highly sensitive heat flux meter has enabled the first measurements of rapidly changing local heat transfer at a moving surface with and without throughflow. This sensor was tested for turbulent confined impinging single and multiple slot jets, with throughflow and impingement surface motion both separately and in combination.

Impingement surface motion, variously claimed to increase or decrease convective transfer rate, decreases Nusselt number. At industrially used conditions this decrease for slot jets is by as much as 25%.

Convective heat transfer for both single and multiple slot jets at nondimensional nozzle-to-impingement surface spacings less than 8 is linearly enhanced by throughflow with a proportionality factor of 0.17, independently of jet Reynolds number, surface motion and extent of heat transfer surface.

In numerical prediction of impingement heat transfer with the high-Re version of the  $k-\epsilon$  turbulence model, a modified Chien-Launder near-wall model improves considerably the agreement between experiment and prediction. This model gives reasonable results for multiple and single slot jets except close to symmetry centrelines, where all such models fail, but does not eliminate the inability of numerical models to predict the effect of nozzle exit turbulence. The effect of throughflow on heat transfer under single and multiple jets is predicted for the first time, accurate to 10% for throughflow velocity up to 0.1m/s.

## RESUME

Des mesures de flux de chaleur local changeant rapidement à une surface en mouvement avec et sans airs traversant ont été effectuées pour la première fois grâce à un capteur de flux de chaleur perméable et sensible. Ce capteur a été mis à l'épreuve pour des jets rectangulaires turbulents confinés simples et multiples pour les conditions d'air traversant la surface, de surface en mouvement, et pour la combinaison de ces deux conditions.

On a trouvé que le mouvement de la surface d'impact, qui selon diverses études diminue ou augmente le transfert de chaleur par convection, diminue le nombre de Nusselt. Pour des conditions utilisées industriellement, cette diminution pour des jets rectangulaires est jusqu'à 25%.

Le transfert de chaleur par convection pour des jets rectangulaires simples et multiples avec  $H/w \leq 8$ , est augmenté par le débit à travers la surface d'impact en fonction d'un facteur,  $\Delta St/Mu_s = 0.17$ , et est indépendant de  $Re_j$ ,  $Mv_s$ , et la superficie de la surface de transfert de chaleur.

Un modèle modifié Chieng-Launder pour la région près du mur améliore considérablement l'accord entre les expériences et les prédictions numériques de transfert de chaleur par jets utilisant le modèle de turbulence  $k-\epsilon$  pour  $Re$  élevé. Le modèle donne des résultats raisonnables pour des jets simples et multiples sauf près de la ligne du centre symétrique (où aucun modèle ne donne des résultats satisfaisants), mais n'élimine pas l'incapacité des modèles numériques de prédire l'effet de la turbulence à la sortie de la buse. L'effet du débit à travers la surface de transfert de chaleur sous des jets simples et multiples a été prédit pour la première fois et est exacte jusqu'à 10% pour des vitesses d'air traversant jusqu'à 0.1m/s à la surface.

## ACKNOWLEDGEMENTS

I would like to express my gratitude to Dr. W.J.M. Douglas for his constructive advice, continuous encouragement and financial support during the long period it took to complete this work.

I would also like to thank Dr. A.S. Mujumdar for interesting discussions and suggestions on many aspects of this work, and for financial support.

My sincere thanks to the research group committee members: Dr A.R.P. van Heiningen, Dr. R.H. Crotogino, C. Ercan, B. Huang, I. Journeaux, N. Poirier for useful suggestions and discussions at various stages of this work and most important for their friendship.

I would like to thank to personnel at the machine shops of the Chemical Engineering Department and of the Pulp and Paper Research Institute of Canada, under the guidance of respectively Mr. A. Krish and Mr. D.P.W. Pounds for their help in constructing the equipment.

I am thankful to the Pulp and Paper Research Institute of Canada, McGill University and Paper Industries Management Association for their scholarship support

A special word of thanks goes to many friends especially T. Mutel, J. Giacomini, L. Pelletier, T. Samurkas and G. Lohfink for their sincere friendship.

Last, but not least, I would like to thank my parents, my husband, Osman, and my children, Barış Erinc and Ayşe Bıkm, for their love, patience, understanding and continuous moral support.

## TABLE OF CONTENTS

	<u>Page</u>
PREFACE	i
ABSTRACT	iii
RESUME	iv
ACKNOWLEDGEMENTS	v
TABLE OF CONTENTS	vi
LIST OF FIGURES	x
LIST OF TABLES	xv
NOMENCLATURE	xvii
 CHAPTER 1. INTRODUCTION	 1
1.1 Background	1
1.2 Objectives	6
 CHAPTER 2. LITERATURE SURVEY	 8
2.1 Flow Field of Impinging Slot Jets	8
2.1.1 Single Impinging Jets	8
2.1.2 Multiple Impinging Jets	13
2.2 Experimental Heat and Mass Transfer Studies	15
2.2.1 Single Impinging Jets	15
2.2.2 Multiple Impinging Jets	19
2.3 Numerical Flow and Heat Transfer Studies	25
2.4 Conclusions	30
 CHAPTER 3. EXPERIMENTAL FACILITY	 32
3.1 Overall Design Conception	32
3.2 Experimental Facility	38
3.3 Instrumentation	43
3.3.1 Position Sensor	43
3.3.2 Instrumentation for Pressure Measurements	44
3.3.3 Instrumentation for Temperature Measurements	44
3.4 Testing and Calibration of Equipment	45
3.4.1 Symmetry of Flow under Jets	45
3.4.2 Flow Distribution in Jet Nozzles	45
3.4.3 Temperature Distribution at Jet Nozzle Exits	50
3.4.4 Calibration of Orifice Meters	53

	<u>Page</u>
CHAPTER 4. SENSOR FOR TRANSIENT HEAT FLUX AT A MOVING SURFACE WITH THROUGHFLOW	56
4.1 Introduction	56
4.2 Development of a Porous Heat Flux Sensor	58
4.2.1 Selection of the Porous Sensor Material	58
4.2.2 Fabrication and Mounting of the Heat Flux Sensor	58
4.2.3 Calibration of the Heat Flux Sensor	60
4.2.4 Thermophysical Properties of Substrate	62
4.3 Instrumentation for Heat Flux Measurements	62
4.3.1 Signal Conditioning	62
4.3.2 Analog-to-Digital Converter (ADC)	65
4.4 Computation of Instantaneous Local Heat Flux	66
4.4.1 No-Throughflow Case	66
4.4.2 Throughflow Case	69
4.4.3 Uniformity of Throughflow Velocity	72
4.4.4 Display of Nusselt Number Distributions	75
4.5 Porous Sensor as a Heat Flux Measuring Instrument	75
4.6 Validation of the Heat Flux Measurements	78
4.7 Summary	88
CHAPTER 5. HEAT TRANSFER UNDER A CONFINED SLOT JET IMPINGING ON A MOVING SURFACE WITH THROUGHFLOW	89
5.1 Introduction	89
5.2 Heat Transfer without Throughflow or Impingement Surface Motion Effects	91
5.2.1 Local Heat Transfer	91
5.2.2 Average Heat Transfer	97
5.3 Impingement Heat Transfer with Throughflow	105
5.3.1 Local Heat Transfer	105
5.3.2 Average Heat Transfer	114
5.4 Heat Transfer at a Moving Impingement Surface	122
5.4.1 Heat Transfer at a Moving Impingement Surface Without Throughflow	122
5.4.1.1 Local Heat Transfer	122

	viii
	<u>Page</u>
5.4.1.2 Average Heat Transfer	128
5.4.2 Heat Transfer at a Moving Impingement Surface With Throughflow	135
5.4.2.1 Local Heat Transfer	135
5.4.2.2 Average Heat Transfer	141
5.5 Conclusions	147
CHAPTER 6 HEAT TRANSFER UNDER MULTIPLE SLOT JETS IMPINGING ON A MOVING SURFACE WITH THROUGHFLOW	151
6.1 Introduction	151
6.2 Heat Transfer without Throughflow or Impingement Surface Motion Effects	154
6.3 Heat Transfer with Throughflow	162
6.4 Heat Transfer at a Moving Impingement Surface	166
6.4.1. Without Throughflow	166
6.4.2 With Throughflow	172
6.5 Conclusions	181
CHAPTER 7 NUMERICAL STUDY OF TURBULENT SLOT JETS IMPINGING ON A SURFACE WITH THROUGHFLOW	185
7.1 Introduction	185
7.2 Mathematical Formulation of the Problem	187
7.2.1 Boundary Conditions	188
7.2.2 Grid Layout	194
7.2.3 Grid Independent Nu Profiles	195
7.2.4 Finite Difference Solution	196
7.3 Effect of Near-Wall Modelling on Predictions	196
7.4 Results and Discussion	<del>205</del>
7.4.1 Single Jet Heat Transfer without Throughflow	205
7.4.2 Single Jet Heat Transfer with Throughflow	229
7.4.3 Multiple Jet Heat Transfer with and without Throughflow	239
7.5 Summary	246

	ix
	<u>Page</u>
CHAPTER 8. CONCLUSIONS	250
8 1 Contributions to Knowledge	250
8 2 Recommendations for Future Work	25
REFERENCES	259
APPENDIX 1 DETERMINATION OF THERMAL PROPERTIES OF THE POROUS GLASS CYLINDER	265
APPENDIX 2 ERROR ANALYSIS	274
APPENDIX 3 COMPUTATIONAL ASPECTS	277
A3 1 Mathematical Formulation	277
A3 2 Near-Wall Models	278
A3 2 1 One-Layer Models	280
A3 2 2 Two-Layer Models	283
A3 2 3 Near-Wall Models for Throughflow	286
A3 3 General Form of Differential Equations	287
A3 4 General Form of Finite Difference Equations	290
A3 5 Treatment of Source Terms	292
A3 6 Numerical Treatment of Near-Wall Boundaries	295
A3 7 Solution of the Finite Difference Equations	299
A3.7 1 Line-by-Line Procedure	299
A3.7.2 Order of Updating the Variables	302
A3.8 Cell-Wise Continuity	304
A3 8.1 Finite Difference Formulation of Momentum	304
A3.8.2 Pressure Correction Equation	306
A3 8 3 Residual Sources and Convergence Criteria	306
A3.8.4 Under Relaxation	307

# LIST OF FIGURES

<u>Figure</u>	<u>Caption</u>	<u>Page</u>
2 1	Flow field of an impinging jet	9
2.2	Position of the boundaries described in Table 2.3	27
3 1	General view of experimental facility	34
3 2	Schematic diagram of experimental facility	39
3 3	Static pressure distribution under the single jet	46
3 4	Static pressure along nozzle midplane of multiple jets	48
3 5	Static pressure along nozzle midplane of the single jet	49
3 6	Temperature distribution along nozzle midplane of the cooling multiple jets	51
3 7	Temperature distribution along nozzle midplane of the heating single jet	52
3 8	Calibration of the orifice plates	54
4 1	Sensor in place	61
4 2	Sensor calibration	63
4 3	Schematic diagram of Wheatstone bridge circuit	63
4 4	Control volumes	67
4 5	Uniformity of permeability of porous impingement cylinder	73
4 6	Static pressure variation under the jets	74
4 7	Comparison of a normally determined Nu profile with that obtained using an averaged surface temperature	77
4 8	Independence of Nusselt number from $\Delta T$ : single jet test	79
4.9	Independence of Nusselt number from $\Delta T$ : multiple jet test	80
4.10	Comparison of results: profiles of local Nu for a slot jet at $Re_j = 24800$	82
4.11	Comparison of results: profiles of local Nu for a slot jet at $Re_j = 57700$	83
4.12	Comparison of results: effect of $Mv_s$ on position of off-stagnation maxima	85



4.13	Effect of throughflow on transient local Nusselt number	87
5.1	Effect of Reynolds number on profiles of local Nusselt number	93
5.2	Effect of Reynolds number on stagnation point Nusselt number	98
5.3	Profiles of average Nusselt number	100
5.4	Effect of nozzle-to-surface spacing on average Nusselt number	102
5.5	Effect of throughflow on profiles of local Nusselt number at $Re_j=24600$	107
5.6	Effect of throughflow on profiles of local Nusselt number at $Re_j=35100$	108
5.7	Effect of throughflow on profiles of local Nusselt number at $Re_j=44750$	109
5.8	Effect of throughflow on profiles of local Nusselt number at $Re_j=57300$	110
5.9	Control volumes for heat balance near impingement surface without and with throughflow	111
5.10	Profiles of enhancement of local Stanton number by throughflow	113
5.11	Effect of throughflow on profiles of average Nusselt number	115
5.12	Effect of throughflow on enhancement of average Stanton number	117
5.13	Effect of impingement surface motion on profiles of local Nusselt number at $Re_j=20800$	124
5.14	Effect of impingement surface motion on profiles of local Nusselt number at $Re_j=35400$	125
5.15	Effect of impingement surface motion on profiles of average Nusselt number	129
5.16	Comparison of results for effect of impingement surface motion on average Nusselt number	131
5.17	Effect of throughflow on profiles of local Nusselt number for an impingement surface moving at $Mv_s=0.27$	137

5.18	Profiles of enhancement of local Stanton number by throughflow for an impingement surface moving at $Mv_s=0.27$	140
5.19	Effect of small throughflow, $Mu_s=0.04$ , on profiles of local Nusselt number for a moving impingement surface	142
5.20	Effect of throughflow on profiles of average Nusselt number for an impingement surface moving at $Mv_s=0.27$	143
5.21	Effect of throughflow on enhancement of Stanton number for a moving impingement surface	145
6.1	Effect of Reynolds number on profiles of local Nusselt number	156
6.2	Effect of Reynolds number on average Nusselt number: Comparative studies	158
6.3	Effect of flow cell aspect ratio on average Nusselt number	161
6.4	Effect of throughflow on enhancement of average Stanton number without surface motion effects	165
6.5	Effect of throughflow on average Nusselt number: Correlation and experiments	167
6.6	Effect of impingement surface motion on average Nusselt number	170
6.7	Effect of throughflow on enhancement of average Stanton number at a moving impingement surface	176
6.8	Effect of throughflow on average Nusselt number at a moving impingement surface: Correlation and experiments	177
6.9	Convective drying rates by multiple impinging jets for combined impingement and throughflow drying	180
7.1	Flow configuration for a single impinging jet	190
7.2	Flow configuration for multiple impinging jets with symmetrical exhaust ports	190
7.3	Effect of near-wall model on predicted local Nusselt number	197
7.4	Effect of near-wall model on predicted wall shear stress	200
7.5	Effect of near-wall model on predicted turbulent kinetic energy	201

7.6	Effect of near-wall model on predicted generation of turbulent kinetic energy	202
7.7	Effect of near-wall model on predicted dissipation of turbulent kinetic energy	203
7.8a	Profiles of normalized static pressure at the impingement surface for H/w of 1.25 and 2.5	206
7.8b	Profiles of normalized static pressure at the impingement surface for H/w=8	207
7.9	Effect of nozzle-to-surface spacing on profiles of maximum lateral velocity	210
7.10	Effect of distance from nozzle exit on lateral profiles of axial velocity	212
7.11	Effect of nozzle-to-surface spacing on profiles of centerline axial velocity.	213
7.12	Profiles of local Nusselt number: $Re_j=10000$ , H/w of 2 and 2.6	215
7.13	Profiles of local Nusselt number: $Re_j=21800$ , H/w=2.5	216
7.14	Profiles of local Nusselt number: $Re_j=35400$ , H/w=2.5	217
7.15	Profiles of local Nusselt number: $Re_j=44300$ , H/w=2.5	218
7.16	Profiles of local Nusselt number: $Re_j=11000$ , H/w=6	220
7.17	Profiles of local Nusselt number: $Re_j=20000$ , H/w=8	221
7.18	Effect of distance from nozzle exit on lateral profiles of turbulent kinetic energy: H/w=1.25	223
7.19	Effect of distance from nozzle exit on lateral profiles of turbulent kinetic energy: H/w=2.5	224
7.20	Effect of distance from nozzle exit on lateral profiles of turbulent kinetic energy: H/w=8	225
7.21	Effect of nozzle exit turbulence intensity on profiles of local Nusselt number: $Re_j=11000$ , H/w=2	228
7.22	Effect of throughflow at the impingement surface on profiles of local Nusselt number: $Re_j=44300$ , H/w=2.5	231
7.23	Profiles of enhancement of average Stanton number	232

	<u>Page</u>
7.24 Effect of throughflow at the impingement surface on lateral profiles of axial velocity at 0.5w and 0.1 from the impingement surface: $Re_j=44300$ , $H/w=2.5$	234
7.25 Effect of throughflow at the impingement surface on profiles of lateral velocity: $Re_j=44300$ , $H/w=2.5$	235
7.26 Effect of throughflow at the impingement surface on profiles of turbulent kinetic energy near impingement surface: $Re_j=44300$ , $H/w=2.5$	236
7.27 Effect of jet-to-exhaust spacing, $S/H$ , on profiles of local Nusselt number in a multiple jet system: $Re_j=21000$ , $H/w=8$	241
7.28 Effect of throughflow at the impingement surface on profiles of local Nusselt number in a multiple jet system: $Re_j=8200$ , $H/w=2.5$ , $S/H=0.5$	243
7.29 Effect of throughflow on average Nusselt number in a multiple jet system: $Re_j=8200$ , $H/w=2.5$ , $S/H=0.5$	245
A1.1 Test assembly for thermal conductivity measurements using transient method of Ioffe and Ioffe[1958]	266
A1.2 Typical output of thermal conductivity experiment	268
A1.3 Schematic of the apparatus of Toutoungi[1983]	271
A3.1 Control volume and near-wall distributions of $\tau_w$ and $k$ for Models 1 and 2	281
A3.2 Control volume and near-wall distributions of $\tau_w$ and $k$ for Models 3 and 4	284
A3.3 Constants A and B of Eq. A3.27 as a function of throughflow	288
A3.4 Control volume for scalar variables	291
A3.5a Control volume for velocity in x-direction	293
A3.5b Control volume for velocity in y-direction	293
A3.6 Near-wall control volume for velocity component parallel to wall	296
A3.7 Near-wall control volume for scalar variables	298
A3.8 Line-by-line procedure	300
A3.9 Order of updating the variables	303

## LIST OF TABLES

<u>Table</u>	<u>Title</u>	<u>Page</u>
2.1	Experimental conditions and heat transfer correlations for single impinging slot jets	16
2.2	Experimental conditions and heat transfer correlations for multiple impinging slot jets	20
2.3	Numerical studies on turbulent impinging jets	26
5.1	Range of parameters	90
5.2	Operating conditions and results for single jet heat transfer without throughflow or impingement surface motion effects	92
5.3	Geometrical parameters of comparative studies	96
5.4	Operating conditions and results for single jet heat transfer with throughflow	106
5.5	Operating conditions and results for single jet heat transfer at a moving surface without throughflow	123
5.6	Operating conditions and results for single jet heat transfer at a moving surface with throughflow	136
6.1	Range of parameters	153
6.2	Operating conditions and results for multiple jet heat transfer without throughflow or impingement surface motion effects	155
6.3	Operating conditions and results for multiple jet heat transfer with throughflow	163
6.4	Operating conditions and results for single jet heat transfer at a moving surface without throughflow	168
6.5	Operating conditions and results for single jet heat transfer at a moving surface with throughflow	174
7.1	Summary of equations solved	189
7.2	Summary of equations of near-wall models	193
7.3	Parameter values for single jet simulations without throughflow at the impingement surface	205
7.4	Parameter values for single jet simulations with throughflow at the impingement surface, $H/w=2.5$ , $I_j=7\%$	229

7.5	Parameter values for multiple jet simulations	239
A2.1	Error analysis for Nu	275
A2.2	Error analysis for $Re_j$	276
A2.3	Error analysis for St	276
A3.1	High-Reynolds number values of empirical constants in turbulent kinetic energy and energy dissipation equations (Jones and Launder[1973])	279
A3.2	Summary of equations solved	289

## NOMENCLATURE

$a$	area of a control volume face
$A$	coefficient in Eq. A3.29
$B_1$	parameter in Eq. 5.6, $Mu_s/St_1$
$C_1$	turbulence model constant, Table A3.1
$C_2$	turbulence model constant, Table A3.1
$C_f$	skin friction coefficient
$\Delta C_f$	enhancement of average skin friction by throughflow
$C_\mu$	turbulence model constant, Table A3.1
$C_p$	specific heat, $J/kg^\circ C$
$C_{ps}$	specific heat of solid, $J/kg^\circ C$
$C_{pa}$	specific heat of air, $J/kg^\circ C$
$D_c$	diameter of impingement cylinder, m
$d_p$	particle diameter, $\mu m$
$f$	fraction open area, $w/2S$
$Fo_t$	turbulent Fourier number, Eq. 4.18
$G$	turbulence kinetic energy generation, Eq. A3.8
$h$	nondimensional enthalpy
$H$	nozzle-to-impingement surface spacing, mm
$h_i$	convective heat transfer coefficient at an impermeable surface
$h_p$	convective heat transfer coefficient at a permeable surface
$I_j$	turbulence intensity at jet nozzle exit
$J_\phi^c$	convective flux of variable $\phi$
$J_\phi^d$	diffusive flux of variable $\phi$
$k$	turbulence kinetic energy, $m^2/s^2$
$k_{eff}$	effective thermal conductivity of permeable impingement surface

$k_v$	turbulent kinetic energy at the edge of viscous sublayer, $m^2/s^2$
$L$	length of gold film, Eq. 4.3, mm
$L_p$	thickness of permeable impingement surface, mm
$Mu_s$	throughflow parameter, $\rho_s u_s / \rho_j u_j$
$Mv_s$	surface motion parameter, $\rho_s v_s / \rho_j u_j$
$Nu$	Nusselt number
$Nu_o$	stagnation Nusselt number
$\overline{Nu}_{max}$	off-stagnation maximum average Nusselt number
$\overline{Nu}_{min}$	minimum average Nusselt number
$NX$	number of gridlines in x-direction
$NY$	number of gridlines in y-direction
$P_d$	static pressure inside impingement cylinder, Pa
$P_j$	static pressure at nozzle exit, Pa
$P_s$	static pressure at impingement surface, Pa
$\Delta P$	pressure relative to ambient, Pa
$\Delta P_o$	stagnation pressure relative to ambient, Pa
$Pr$	Prandtl number
$q_i$	heat flux to an impermeable surface, $W/m^2$
$q_p$	heat flux to a permeable surface, $W/m^2$
$q_s^1$	heat flux, Eq. 4.10, W
$q_{sm}$	maximum self-heating power of sensor, Eq. 4.3, W
$Q_s$	fraction of jet flow removed through permeable impingement surface, $Mu_s/f$
$R$	resistance, ohm
$\Delta R_i$	enhancement of impingement drying rate by throughflow
$R_s$	resistance of sensor, ohm
$R_v$	variable resistance of Wheatstone bridge, ohm



$Re$	Reynolds number
$Re_c$	Reynolds number for crossflow
$Re_{c,j}$	Reynolds number for cooling jets
$Re_{h,j}$	Reynolds number for heating jet
$Re_j$	jet Reynolds number
$S$	centerline-to-centerline distance between nozzle and exhaust port, mm
$S_\phi$	source term in Eq. A3.28
$St$	Stanton number
$\Delta St$	enhancement of Stanton number by throughflow
$St_i$	Stanton number for an impermeable surface
$St^\circ$	Stanton number for the base case of no-throughflow
$t$	time, s
$\Delta t$	sampling time, s
$\Delta t_r$	time for a complete revolution of impingement cylinder, s
$T$	temperature, °C
$\Delta T$	temperature driving force, °C
$T_a$	air temperature, °C
$T_f$	temperature of near-surface fluid, °C
$T_i$	temperature of impermeable surface, °C
$T_j$	temperature at jet nozzle exit, °C
$T_p$	temperature of permeable surface, °C
$T_s$	sensor temperature, °C
$u$	velocity in x-direction, m/s
$u_j$	velocity at jet nozzle exit, m/s
$u_s$	throughflow velocity, m/s
$v$	velocity in y-direction, m/s
$\bar{v}_f$	mean velocity of near-surface fluid, m/s

$v_s$	impingement surface velocity, m/s
$v_r$	skin friction velocity, A3.27
$v^+$	nondimensional velocity, Eq. A3.12
$V$	voltage output of Wheatstone bridge, volt
$V_r$	reference voltage for Wheatstone bridge, volt
$w$	nozzle width, mm
$W$	width of gold film, Eq. 4.3, mm
$x$	coordinate, m
$x^+$	nondimensional distance from wall, Eq. A3.12
$x_v$	distance from wall to edge of viscous sublayer, m
$\Delta x$	distance between finite difference layers, Fig. 4.4, mm
$y$	coordinate, m
$y/w$	distance from nozzle centerline in terms of nozzle width
$Z$	penetration depth, Eq. 4.11, mm

#### Greek Letters

$\alpha$	thermal diffusivity, $m^2/s$
$\beta$	ratio of orifice diameter to pipe diameter
$\phi$	general variable, Eq. A3.28
$\varepsilon$	dissipation of turbulent kinetic energy, $m^2/s^3$
$\kappa$	von Karman constant, Eqs. A3.11, A3.27
$\mu$	dynamic viscosity, $kg/m\ s$
$\mu_{eff}$	effective viscosity, $\mu_L + \mu_T$
$\mu_L$	laminar viscosity, $kg/m\ s$
$\mu_T$	turbulent viscosity, $kg/m\ s$
$\nu$	kinematic viscosity, $m^2/s$
$l$	characteristic length, Eq. 4.18

$\Gamma_\phi$	transfer coefficient associated with $\phi$ , Eq. A3.28
$\rho$	density, kg/m <sup>3</sup>
$\rho_a$	density of air, kg/m <sup>3</sup>
$\rho_P$	density of permeable substrate, kg/m <sup>3</sup>
$\rho_s$	density of air at impingement surface temperature
$\sigma_k$	turbulence model constant, Table A3.1
$\sigma_L$	laminar Prandtl number, Eq. A3.9
$\sigma_T$	turbulent Prandtl number, Eq. A3.9
$\sigma_\epsilon$	turbulence model constant, Table A3.1
$\tau_w$	wall shear stress, kg/m s

# CHAPTER 1

## INTRODUCTION

### 1.1 Background

For direct heating and cooling of surfaces by a fluid, the use of jets has two intrinsic advantages: the large heat transfer coefficients obtainable under impinging jets, and the potential for local control of heat transfer rate. Some industrial applications of impingement heat transfer include the drying of paper and textiles, cooling of electronic components and of turbine hardware, tempering of glass, annealing of non-ferrous sheet metals. An industrial application of impinging jets where fine control of local heat transfer rate is crucial is the control of local temperature along paper mill calender rolls.

Heat transfer under impinging jets is characterized by an impressive number of design alternatives and parameters in addition to such basic ones as jet Reynolds number and  $\Delta T$ . Most industrial applications are with systems of multiple jets, but most laboratory investigations have been with single jets. Thus nozzle-to-nozzle spacing is as important as that for nozzle-to-impingement surface. The case of multiple jets introduces exhaust flow configuration as a design variable which, though little studied, can cause substantial changes in heat transfer rate. Likewise most industrial applications are with confined jets, most laboratory investigations with unconfined jets. Nozzle geometry is a fundamental parameter, not only as to the two principal alternatives, round and slot, but also nozzle shape, i.e. the choice between straight, tapered, or contoured nozzle walls, and selection of nozzle length.

Industrial applications such as the impingement drying of continuous webs of paper or textiles involve heat transfer at fast moving surfaces, a feature which may change the heat transfer rate substantially. If the surface to be heated or cooled is permeable, yet another variable is to draw some of the impingement flow through the surface, thereby further enhancing heat transfer. An industrial application such as drying adds the additional complication of simultaneous heat and mass transfer. Not all these major design alternatives have been studied singly, and some combinations of alternatives which have interesting industrial potential have never been investigated due to the associated experimental difficulties. A potentially important supplement to laboratory experiments is computer simulation using the techniques of numerical transport phenomena. As flow and heat transfer characteristics of simple impinging jet arrangements have been treated extensively by earlier investigators, impingement heat transfer with some of the complexities noted above are now considered briefly.

An important example of a rapidly moving impingement surface occurs in the impingement drying of paper at paper machine speed. In Yankee dryers for tissue and toweling the paper moves at speeds as high as 90km/h. under impinging jets with nozzle exit velocity and temperature of 100m/s and over 300°C. With large changes in flow field and boundary layer conditions at a surface moving at such speeds it would be expected that transfer rates would be significantly different from those measured in laboratory studies with a stationary surface. The first studies of impingement on a moving surface measured only average transfer rates for lack of a technique for obtaining local transfer rates at a speeding surface. These studies produced contradictory results, i.e.

that transfer rates either increased greatly or remained unaffected by impingement surface motion. The first measurement of profiles of local heat transfer under confined slot jets at a rapidly moving impingement surface was made by van Heiningen[1982]. This measurement was made possible by the development of a new heat flux sensor (van Heiningen, Mujumdar and Douglas[1985]), one sufficiently sensitive and fast responding for this demanding application. Contrary to earlier studies for slot jets, van Heiningen found a decrease in average impingement heat transfer with increasing surface velocity. Thus these few published studies provide all possible alternatives, i.e. that convective transport processes are increased, decreased, or unaffected by impingement surface motion.

At a permeable impingement surface, convective transport rates due to impinging jets can be further enhanced by withdrawing some of the jet flow through the surface. Baines and Keffer[1979] found that, when a uniform throughflow is applied at a permeable impingement surface moving under an unconfined slot jet, the profiles of local shear stress are increased by a uniform amount. As the assumptions associated with the analogy between momentum and heat transfer do not hold for impingement flows, heat transfer cannot be predicted with confidence from such measurements. Saad[1981] and Obot[1982] measured the increase of impingement heat transfer with throughflow at a stationary surface under single slot and single round jets. None of these studies on the effect of throughflow on convective transfer rates under single jets were sufficiently detailed to develop a correlation for the quantitative effect.

In order to consider the possibility of enhancing impingement heat

transfer at a moving permeable surface by applying throughflow, the effect on convective heat transfer of the combination of throughflow and impingement surface motion is required. For the case of simultaneous throughflow and impingement surface motion, no measurement of local transfer rates has been made, even for the simplest case of a single impinging jet, because there has been no heat flux sensor available which is applicable under such stringent conditions

In a multiple jet system such as required for industrial application the jets may be interacting, or non-interacting, depending on jet-to-jet separation. In a non-interacting jet system, single jet data may be used as a guide to design when multiple jet data are not available. Saad[1981] has provided quantitative criteria for discriminating between interacting and non-interacting multiple slot jet systems. Higher impingement heat transfer rates may be obtained in a multiple jet system with more closely spaced jets, but the limited data available does not include the conditions for which maximum average heat transfer could be expected. No reliable experimental data exist for multiple jet heat transfer on rapidly moving surfaces, and no studies exist of multiple jet heat transfer with throughflow at a moving impingement surface.

Confinement of impinging jet flows is an important design consideration for industrial heat transfer applications. A confinement hood at the nozzle exit level, parallel to the impingement surface, is normally required for reasons of thermal efficiency. Unfortunately most laboratory investigations have been with unconfined jets. In the absence of confinement, jets entrain ambient air which affects heat transfer to an indeterminate extent depending on the relative values of three tempera-

tures, i.e. nozzle exit, ambient and impingement surface. As heat transfer for unconfined jet systems inherently includes this equipment-specific effect, such data does not provide a reliable general basis for design of industrial confined jet systems.

Another design consideration for confined impinging jet systems is the exhaust flow arrangement for spent jet flow. If the removal of spent flow is not through exhaust ports located intermediate between the nozzles in the confinement surface, crossflow of spent flow under the nozzle exit flow occurs. Transfer rates can be reduced substantially by crossflow, as has been documented experimentally by Saad[1981] and numerically by Ahmad[1987].

In the paper industry pure impingement drying is used and pure through drying is used, but combined impingement and through drying is not an industrial practice. Burgess et al.[1972a,b] demonstrated with a laboratory and pilot plant facility that with combined impingement and through drying, drying rates one order of magnitude higher than those for conventional dryers could be obtained. Such a paper dryer would involve the simultaneous effects of throughflow and rapid motion of the wet web under multiple impinging jets. As noted earlier, these simultaneous effects are not known, even for a single jet, let alone under a system of confined multiple jets with some geometry of exhaust flow. The lack of such information is an obstacle to the rational design of improved dryers for permeable webs.

Complete documentation and understanding of impingement transport phenomena with all variations of the potentially interesting parameters and design alternatives outlined above would require long programs of experimentation. The amount of laboratory investigation needed would be



significantly reduced if the complex flow and temperature field of impinging jets could be calculated theoretically, i.e. by numerical solution of the complete governing equations for momentum, heat and mass transfer. When the jets are turbulent, the more difficult but more important case industrially, there are additional turbulence model equations to be solved. A diversity of methods, of varying complexity, have been tried, but with limited success. For turbulent impinging jets the predicted heat transfer agrees moderately well with that measured for the wall jet, but not for the complex flow field of the impingement region, more important because the transfer rates are higher. The discrepancies derive principally from assumptions in the turbulence models and, when required, near-wall models. As computer simulation of impingement heat transfer has great potential but is still not reliable, the methods of numerical transport phenomena remain under active development

## 1.2 Objectives

Consistent with the general background summarized above, the present study was designed with the following experimental and theoretical components:

1. The first experimental objective was to develop a heat flux sensor that would enable measurement of instantaneous local heat transfer at a rapidly moving impingement surface at which there is throughflow.
2. With such a sensor, the second experimental objective was to measure the effects, separately and in combination, of surface motion and throughflow on impingement heat transfer for confined single and multiple jets.

3. The objective of the computer simulation component of the study was to predict heat transfer numerically for confined single and multiple jets, with and without throughflow at the impingement surface.

## CHAPTER 2

## LITERATURE REVIEW

A concise review concerning turbulent single and multiple slot jets is presented which treats only those characteristics of impingement flow, heat and mass transfer most directly related to the present study. More general reviews available include those of Gauntner et al. [1970], Mujumdar and Douglas [1972], Martin [1977], Obot et al. [1979], Saad [1981] and van Heiningen [1982]. A recent extensive review of numerical impingement flow and heat transfer was published separately, Polat et al. [1988], rather than as a part of the present thesis.

## 2.1 FLOW FIELD OF IMPINGING SLOT JETS

2.1.1 Single impinging jets

The flow field of a jet, Fig. 2.1, comprises three characteristic regions, the free jet, stagnation flow and wall jet. The nature of the free jet region depends greatly on the flow at the nozzle exit which in turn is dependent on the nozzle shape and dimensions and, for the case of a sufficiently short nozzle, on flow conditions entering the nozzle. The nozzle most studied in impinging jet investigations is the ASME standard elliptically contoured entry (ECE) nozzle. This nozzle produces a nearly flat velocity profile and very low turbulence at the nozzle exit, and the free jet consists of a potential core, a developing flow and a developed flow region.

The potential core is that part of the flow region where axial velocity remains effectively equal to nozzle exit velocity. The limits of the potential core are determined by the rate of growth of the two

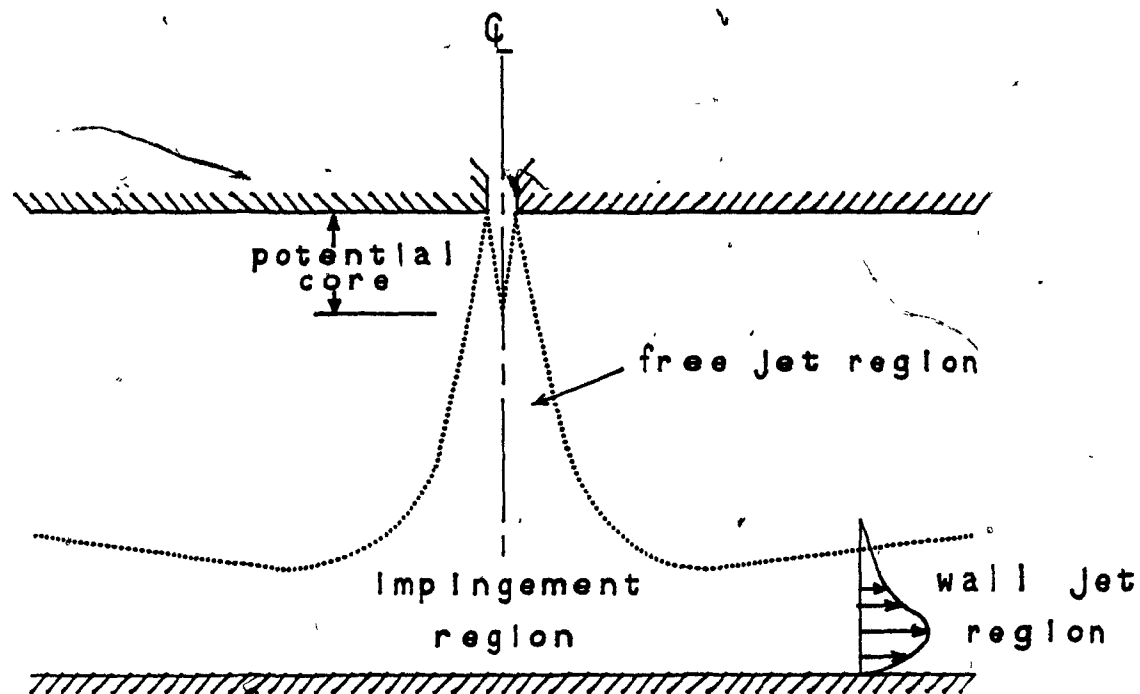


FIGURE 2.1. Flow field of an impinging jet

mixing layers originating at the nozzle edges, which in turn depends on the nozzle exit velocity and turbulence field for the particular nozzle geometry. Dosdogru[1969] found potential core length to increase from about  $2w$  for a sharp edged slot nozzle, to about  $4.5w$  for a slot formed by two plates at a small included angle, to about  $8w$  for a slot nozzle with a short elliptical entrance. For ASME standard ECE nozzles, Saad[1981] found the length of the potential core ranged from  $\approx 4w$  to  $\approx 5w$  depending on nozzle width which affects nozzle exit turbulence level.

In the developing flow region, axial velocity decays as the jet spreads. Eventually lateral profiles of axial velocity approach a bell shape. According to measurements by Saad[1981] of velocity and turbulence at the axis for a confined jet from an ECE slot nozzle, the turbulence level increases greatly even in the potential core region, i.e. before axial velocity starts to decay, and continues to increase in the developing and developed flow regions. These findings are consistent with those of Gardon and Akfirat[1965] with an unconfined impinging slot jet. Gutmark et al.[1978], on the other hand, found no increase of turbulence velocity in the free jet region of an impinging slot jet from this nozzle type at  $H/w=100$  and  $Re_j=30000$ . However the exit turbulence intensity,  $\approx 13\%$ , from their nozzle was much higher than that of Saad or Gardon and Akfirat.

Lateral profiles of axial velocity display similarity throughout the developed flow region. Characteristics of the developed flow region of impinging jets are similar to those of free jets, which are detailed in the standard references, Hinze[1959], Abramovitch[1963] and Schlichting[1979].

In the impingement or stagnation region, static pressure first increases sharply with the corresponding drop in axial velocity, then drops again as the flow accelerates along the impingement surface after impingement. From profiles of mean axial velocity at the centerline for a slot jet at  $H/w=19$ , Saad[1981] concluded that the presence of the impingement surface was not felt by the jet further than  $0.21H$  from the surface. This value agrees with that of Gutmark et al.[1978],  $0.2H$ , for a jet at  $H/w=100$ . According to Saad's measurements, axial turbulence velocity does not deviate from that of a free jet until the distance from the surface is less than  $0.05H$ , a finding in agreement with that of Gutmark et al.[1978] for an impinging slot jet and of Obot [1981] for an impinging round jet.

The end of the impingement region in the lateral direction is defined as the location where the pressure gradient at the impingement surface becomes zero. Schauer and Eustis[1963], Gardon and Akfirat [1965] and Kumada and Mabuchi[1970] measured static pressure profiles for unconfined slot jets in the ranges  $10 < H/w < 40$ ,  $2 < H/w < 32$  and  $2 < H/w < 40$  respectively. Their measurements indicate that the extent of the impingement region in the lateral direction at  $H/w > 8$  is about  $0.35H$ , which agrees with the findings of Cadek[1968] for a partially confined slot impinging jet at  $8 < H/w < 32$ . The extent of impingement region is reported by Saad to be slightly above  $0.5H$  for single confined slot jets at  $4 < H/w < 16$ .

For a confined jet, if the confinement and impingement surfaces are sufficiently long the wall jet boundary layer grows to reach the confinement surface, thereby enclosing a recirculating flow. Of the two sides of the wall jet boundary layer, the impingement surface side

shows the typical effects of a boundary layer surface, the outer region has features of a free turbulent jet. Kumada and Mabuchi[1970] reported the decay of the maximum lateral velocity in the wall jet region of an unconfined impinging slot jet at  $2 < H/w < 40$ . Such measurements for confined impinging slot jets are not available.

No publication on the effect of impingement surface motion on the flow field of a slot jet has appeared. Profiles of local heat transfer of single jets impinging on a moving surface measured by van Heiningen [1982] document quantitatively the changes which occur when impingement surface motion destroys the flow symmetry that exists for a stationary impingement surface

Studies are very limited concerning the effects on the flow field of an impinging slot jet that result from having throughflow at the impingement surface. In their study of the effect of throughflow on the impingement flow field of a two dimensional jet at  $Re_j = 5680$  ( $u_j = 13.5 \text{ m/s}$ ) for throughflow velocities in the range  $0.21 \text{ m/s} - 0.43 \text{ m/s}$ , Abdul-Wahab et al.[1975] observed a slightly faster decay of the jet centerline velocity with throughflow than that without, and a reduction of the axial fluctuating velocity component. The more comprehensive results in the same laboratory by Saad[1981] for a jet at  $H/w = 8$  and  $11400 < Re_j < 30200$  found the contrary. He observed that throughflow velocities in the range  $0.1 - 0.3 \text{ m/s}$  cause an increase in axial mean velocity at a position  $0.25H$  from the surface, i.e. roughly at the edge of the impingement region in the axial direction, with no appreciable effect on the axial fluctuating velocity component. Baines and Keffer[1979] reported a slight increase in the maximum lateral wall jet velocity with throughflow at a quite low throughflow rate,  $u_s/u_j =$

0.0029, for a jet of velocity  $u_j = 52.7 \text{ m/s}$  impinging on a rotating impingement surface. Their observation agrees with that of Obot[1982] who measured wall jet velocity profiles for an impinging round jet. Effects of surface motion and throughflow on the impingement flow field need further exploration as the available studies give limited and conflicting information.

### 2.1.2 Multiple Jets

The only intensive investigation of the flow field of a confined multiple impinging jet system was that of Saad[1981]. For a system of three slot jets with symmetrical exhaust ports alternating with jet openings, tested over the range  $4 < H/w < 16$ ,  $0.375 < S/H < 6$ ,  $5000 < Re_j < 44000$ , he showed that the middle jet is representative of a jet in an array of many such jets. For this type of multiple jet system there exists one flow region additional to those of a single impinging jet, namely, that under the exhaust ports. Saad named this the "exit flow" region.

Saad demonstrated that in the choice of the two nondimensional ratios required to characterize geometrically similar multiple confined jet systems of this type, the combination of  $H/w$  with  $S/H$  is better than  $H/w$  with either  $S/w$  or its equivalent,  $w/2S$ , the fraction of nozzle open area relative to the impingement surface. The range of aspect ratio,  $S/H$ , used by Saad extended from  $S/H = 0.375$ , where the closely spaced jets are highly interacting, to  $S/H = 6$ , where the widely spaced jets are indistinguishable from an array of non-interacting single jets. Saad showed that, for  $S/H > 0.75$ , the lateral profiles of normalized static pressure,  $\Delta P / \Delta P_0$ , could be represented by a unique curve in the important impingement region only when  $S/H$  was used as the



lateral dimension. The other parameter,  $H/w$ , had significant effect only in the wall jet region. For  $S/H < 0.75$ , centerline axial mean velocity decayed faster and axial turbulence intensity increased more, relative to a single jet, hence indicating a critical value of the aspect ratio to be  $S/H = 0.75$ .

In the exit flow region of a widely spaced confined jet array Saad[1981] observed an increase in static pressure as the wall jets from the two neighboring jets meet and turn away from the surface. When the multiple confined jets are spaced sufficiently closely that the jets interact, he found that the absolute values of static pressure in the stagnation region decrease while the values under the exhaust ports increase appreciably. Therefore the static pressure profile under a system of interacting jets is more uniform than for a non-interacting jet system. There are two earlier studies in which static pressure profiles at the impingement surface were measured, in both cases for three unconfined slot jets from nozzles with a very small included angle. The measurements of Gardon and Akfirat[1966] were made at  $Re_j = 5500$ ,  $S/w = 8$ , and two values of  $H/w$ , 4 and 16. While those of Romanenko and Davidzon[1970] were in three sets:  $Re_j = 9000$ ,  $H/w = 10$ ,  $S/w$  values of 12.5 and 20.3;  $Re_j = 9000$ ,  $H/w = 20$ ,  $S/w = 20.3$ ;  $Re_j = 6700$ ,  $H/w = 10$ ,  $S/w = 12.5$ . According to the criterion for jet interaction of Saad[1981], the conditions of Gardon and Akfirat correspond to values of the aspect ratio,  $S/H$ , of 2 and 0.5, i.e. to non-interacting and interacting jet systems, respectively, while all  $H/w$  and  $S/w$  combinations of Romanenko and Davidzon correspond to  $S/H$  values higher than 0.75. The pressure profiles measured by Gardon and Akfirat and by Romanenko and Davidzon exhibit characteristics very similar to those of Saad.

No information is available concerning flow development under multiple jets impinging on a moving surface. Neither has there been any study of the effect that throughflow at impingement surface has on flow structure in a multiple jet system. There are important industrial applications for jets impinging on a surface which may be moving or at which there may be throughflow, or both. As knowledge of the effects on the flow structure caused by surface motion and throughflow, combined or individually, are very limited for single jets and are nonexistent for multiple jet systems such investigations would be most valuable.

## 2.2 EXPERIMENTAL HEAT AND MASS TRANSFER STUDIES

### 2.2.1 Single Impinging Jets

Among the studies on heat and mass transfer from single impinging slot jets, Table 2.1, only those of Folayan[1977] and van Heiningen [1982] considered the configuration of prime significance in industrial interest, namely confined jets. Single impinging slot jets have been studied for wide ranges of the nondimensional parameters:  $1500 < Re_j < 110000$ ;  $0.25 < H/w < 80$ ;  $x/w$  to 150.

The shape of heat and mass transfer profiles at the impingement surface is very sensitive to nondimensional nozzle-to-impingement surface spacing for  $H/w$  less than 8. Gardon and Akfirat[1966] explained the off-stagnation peaks found in Nusselt number at about  $7w$  from stagnation for  $H/w < 8$  as marking the end of transition from the initial laminar stagnation flow to a wall jet with a turbulent boundary layer. The absolute values of these secondary peaks increase with increasing  $Re_j$  and decreasing  $H/w$ . At  $H/w=8$  the off-stagnation peaks

Table 2.1 Experimental conditions and heat transfer correlations for single impinging slot jets

Reference	Range of parameters			Correlations
	$Re_j$	$H/w$	$S/w$	
Metzger[1962]	1500-5000	2-20	6 25-100	$\bar{Nu} = 0.547 Re_j^{0.566} f^{0.43} Pr^{-0.63}$ $7 < H/w < 10; 3 < S/w < 50$
Schauer and Eustis[1963]	34100-45300	40	<118	analytically developed very complex correlations
Gardon and Akfirat[1966]	450-50000	0.3-80	<40	$Nu_o = 1.2 Re_j^{0.58} (H/w)^{-0.62}$ $14 < H/w < 60; 2000 < Re_j < 50000$ $\bar{Nu} = 0.66 Re_j^{0.62} f^{0.38} (H/w)^{-0.31}$ $Re_j > 2000; H/w > 8; f < 0.17$
Korger and Krizek[1966]	6000-38000	0.25-40	<20	$Nu_o = Re_j^{0.66} (H/w)^{-0.66}$
Cartwright and Russell[1967]	25000-110000	8-47	<150	$Nu_o = 0.489 Re_j^{0.672} (H/w)^{-0.604}$ $16 < H/w < 47$
Cadek[1968]	4600-102000	2-32	<36	No correlation
Schlunder et al.[1970]	1500-45000	1-40	<50	$\frac{\bar{Nu}}{Pr^{0.42}} = 3.06 (Re_j)^m / (x/w + H/w + 2.78)$ $m = 0.695 - 2 / [(x/w) + 6.12 + 0.8(H/w)^{1.33}]$ $4 < H/w < 20, 4 < S/w < 50$
Kumada and Mabuchi[1970]	10000-15000	2-40	<30	$Nu_o / Pr^{0.43} = 1.42 Re_j^{0.58} (H/w)^{-0.62}$ $10 < H/w < 40$
Folayan[1976]	3500-7100	2-12	<40	
van Heiningen [1982]	5200-20300	6	<51	$Nu_o = 0.54 (Re_j)^{1/2}$ $\bar{Nu} = \frac{0.91}{\frac{x}{w} + 22} Re_j^{0.76}$
	9700-91600	2.6		$Nu_o = 0.455 (Re_j)^{1/2}$

disappear but at about the same location from stagnation there remains an abrupt change in slope of the profile of local Nusselt number, indicating a change in boundary layer characteristics. For spacings beyond  $H/w=8$ , the heat transfer profiles assume a uniform bell shape.

Korger and Krizek[1966], Kumada and Mabuchi[1970], Schlunder et al.[1970], Cadek[1968], Saad[1981] and van Heiningen[1982] further documented the size, location, and  $Re-H/w$  dependency of the secondary peaks in local convective transfer rate at about  $5w$  to  $7w$  from stagnation. The first two studies used the naphthalene sublimation technique to study impingement mass transfer whereas Schlunder et al. computed local mass transfer rates by measuring the rate of water removal from uniformly moist, parallel strips of stoneware subjected to impinging slot jets of unsaturated air

Gardon and Akfirat[1965] and Saad[1981] observed that at  $H/w < 8$  the heat transfer profiles in the important impingement region are quite sensitive to nozzle exit turbulence level. Because of sensitivity to this boundary condition, local heat and mass transfer profiles for nozzle-to-surface spacings less than 8 from different studies differ substantially. At higher  $H/w$  spacings the profiles become insensitive to nozzle exit conditions, hence agreement between studies is much better.

These features of the heat and mass transfer profiles in the impingement region suggest that at spacings of  $H/w < 8$ , higher average transfer rates in multiple jet systems may be obtained by placing the jets sufficiently close to include the secondary peaks, and by increasing the turbulence level at the nozzle exit.

Van Heiningen[1982] measured heat transfer rate at an impingement

surface moving rapidly under confined slot jets at  $H/w$  spacings of 2.6 and 6, over the  $Re_j$  ranges 9700-89000 and 8200-13900 respectively, using a very sensitive, fast responding heat flux sensor (van Heiningen, Mujumdar and Douglas[1985]). The results of these experiments, the only study of effects of surface motion on heat transfer from confined slot impinging jets, are discussed in the Sections 2 2.2 and 5.4.

The effect that throughflow at a stationary impingement surface has on heat transfer from confined impinging slot jets was studied by Saad[1981] at  $H/w=8$  and  $Re_j$  values of 10200, 22800 and 29100 for throughflow velocities ranging from 0 to 0.3m/s. He observed that the increase in local heat transfer with throughflow was uniform across the entire impingement surface. The percentage enhancement correspondingly varies, for example about 26% and 50% at  $3w$  and  $12w$  from stagnation, respectively, for the case of a throughflow velocity of 0.1m/s ( $u_s/u_j \approx 0.0074$ ) at  $Re_j=10200$ . The maximum in enhancement of average heat transfer due to throughflow reported at  $u_s/u_j \approx 0.008$  is now attributed to experimental error.

Obot[1982] studied the effect of throughflow on average heat transfer coefficients from single confined and unconfined round jets for throughflow velocity in the range 0.3%-0.7% of that of the nozzle exit. He used two values of  $Re_j$ , about 28000 and 51000, and varied  $H/w$  between 2 and 10. Obot observed that average heat transfer rate increases linearly with throughflow and this increase was larger with than without confinement. The findings of Saad[1981] and Obot[1982] parallel those of Baines and Keffer[1979] for local and average shear stress profiles. Because of the potential industrial importance of

heat transfer using combined impingement and throughflow processes, further work on the effect of throughflow on heat transfer from impinging jets is needed to supplement the limited amount of information yet available.

### 2.2.2 Multiple Impinging Jets

There are only five studies of multiple impinging slot jets, Table 2.2, and of these, only Martin and Schlunder[1973] and Saad[1981] worked with confined jets. As industrial applications generally require recovery of the spent flow for reasons of thermal efficiency, lack of use of a confinement hood leads to laboratory results of uncertain practical significance. Unfortunately the arrangement of Martin and Schlunder provided for the exhaust flow to leave the system in the direction traverse to the impingement surface motion, i.e. in the lengthwise direction of the slot jet nozzles. Such an exhaust flow arrangement changes the flow from two to three dimensional. More important, this arrangement introduces crossflow, which reduces heat transfer, and it introduces non-uniformity in heat transfer rates from one side to the other of the moving impingement surface, a characteristic unacceptable in some industrial applications.

Saad[1981] investigated the heat transfer distribution under confined multiple impinging slot jets for a wide range of parameters,  $4 < H/w < 24$ ,  $6 < S/w < 32$  (or  $1.56\% < f < 8.313\%$ ) and  $3000 < Re_j < 30000$ . He exhausted the spent flow symmetrically between the jets, thereby maintaining two-dimensional flow, avoiding detrimental crossflow effects, and achieving uniform transfer rates in the lengthwise direction of the slot nozzles. Based on measurements of the flow field as well as of

Table 2.2 Experimental conditions and heat transfer correlations for multiple impinging slot jets

Reference	Range of parameters of the reported experiments					Correlations
	$Re_j$	$S/w$	$f, \%$	$H/w$	$S/H$	
Korger and Krizek[1966]	6500 21500	5-33 7.5	1.5-10 6.67	8 6	0.63-4.13 1.25	No correlations
Gardon and Akfirat[1966]	5500	8-16	3.13-6.25	4-40	0.2-4.0	$Nu = 0.66 Re_j^{0.62} f^{0.38} (H/w)^{-0.31}$ $6000 < Re_j < 600000; 8 < S/w < 32; H/w > 8$
Schuh and Pettersson [1966]	1260 6300 31600	2.5-50 2.5-50 2.5-10	1.0-20 1.0-20 5.0-20	2-16 2-16 2-16	0.3-25 0.3-25 0.3-5	$Nu = 0.33 Re_j^{0.598} f^{0.327}$ $1200 < Re_j < 1000000; 2.5 < S/w < 50;$ $H/w = 4$
Martin and Schlunder [1973]	750-20000	2.5-55	0.9-21.2	2-80	0.12-27.5	$\frac{Nu}{Pr^{0.42}} = 0.84 f_o^{0.75} \left( \frac{Re_j}{f/f_o + f_o/f} \right)^{0.667}$ $f_o = (60 + (H/w - 4)^2)^{-0.5}$ $750 < Re_j < 20000; 2.5 < S/w < 55; 2 < H/w < 80$
Saad[1981]	3000-30000	6-32	1.6-8.3	4-24	0.33-6	$Nu = 0.63 Re_j^{0.65} (S/H)^{-0.55} (H/w)^{-0.8}$ $3300 < Re_j < 21000; 1.5 < S/H < 4; 8 < H/w < 24$ $Nu = 0.215 Re_j^n (S/H)^{1.50} (H/w)^m$ where $m$ & $n = f(S/H)$ $300 < Re_j < 29200; 0.33 < S/H < 1.33; 8 < H/w < 24$

heat transfer Saad demonstrated that the best characterization of geometrical similarity in such multiple jet systems is provided by the two nondimensional parameters, aspect ratio  $S/H$ , and nozzle-to-surface spacing,  $H/w$ . From comparison of local heat transfer profiles of multiple jets with single jet profiles at the same  $H/w$  and  $Re_j$  over the same extent of heat transfer area,  $S/H$ , he found a critical  $S/H$  ratio, 1.5, above which profiles of a jet in a multiple jet system are indistinguishable from those of the equivalent single jet. Thus heat transfer rates in multiple jet systems of  $S/H$  greater than 1.5 may be predicted from data for single jets. Saad also showed that as the aspect ratio drops below an upper critical value,  $S/H=1.5$ , interaction between the inlet jet and exit flow begins to affect local heat transfer at the exhaust port centerline where it enhances local Nusselt number. When the aspect ratio is decreased to  $S/H=0.7$ , he found that the effect of this interaction reaches the nozzle centerline where it depresses the stagnation heat transfer rate.

From an application point of view it is of interest to know what geometric configuration of multiple confined slot jets would give the highest average heat transfer rate. Saad[1981] used the correlation of his results to predict that the highest average Nusselt number would occur at about  $H/w=5$  and  $S/H=0.5$ , a combination not used in his study. This geometrical configuration of a confined multiple slot jet system was therefore selected for the first time in the present study.

The results of Korger and Krizek[1966], Gardon and Akfirat[1966] and Schuh and Pettersson[1966] for unconfined multiple slot jets were reinterpreted by Saad[1981] using the concept of flow cell aspect ratio,  $S/H$ . For these unconfined jet systems the values of  $S/H$  ratio



are less than 1.5 for Korger and Krizek and for Schuh and Pettersson, and cover the range 0.5-2 for Gardon and Akfirat. Saad noted that the maximum value of average heat transfer rate found by Schuh and Pettersson was for  $H/w=8$  and  $S/w=7$ , i.e. at  $S/H=0.88$ , close to his predicted value  $S/H=0.5$  for maximum average Nusselt number.

The effect of surface motion on average heat transfer was studied by Fechner[1971] for unconfined multiple slot jets impinging on a 0.29m diameter rotating cylinder. Heating foils, 20mm wide, covering the outside of this cylinder caused a surface roughness of about 0.7mm. Fechner varied the number of jets impinging on this cylinder from one to four. According to Saad's criteria for interacting jets, all of Fechner's multiple jets were spaced sufficiently apart to be non-interacting. He observed that heat transfer from impinging slot jets increased with relative surface velocity,  $v_s/u_j$ , to approach the limit of convective transfer coefficients for heat transfer from a freely rotating cylinder, which he also measured. However in the range of relative surface velocity of 0.1-0.4, the increase measured in average heat transfer was rather small. Fechner also noted very high values of turbulence intensity, about 40%, near the cylinder surface, generated presumably by the extremely rough cylinder surface.

Subba Raju and Schlunder[1977] obtained average heat transfer rates at a continuous belt moving under a single unconfined impinging slot jet by measuring belt temperature with an infrared thermometer. They reported that the average heat transfer coefficient increased sharply with small increases in speed of the moving surface. At a fairly low surface speed, they found that average heat transfer passed through a high maximum which was 1.5 to 2 times greater than that for a

stationary surface.

Haslar and Krizek[1984] used the naphthalene sublimation technique to measure average mass transfer rates for unconfined multiple slot jets impinging on a rotating cylinder. They used unconfined jets from nozzles with a small included angle impinging on a cylinder of circumference 1m. The geometric arrangement of the jets was fixed at  $S/w=5$ ,  $H/w=8.5$ , thus, giving an  $S/H$  ratio of 0.6, very close to the  $S/H$  value at which Saad predicted that average heat transfer from multiple slot jets would be maximum. They reported that in the range of  $Re_j$ , 1300-3000, average heat transfer increased with increasing relative surface speed in the  $v_s/u_j$  range of 0.03-0.4. However their results include the curious finding of a substantial discontinuity between average heat transfer for surfaces moving at various low speeds and that for a stationary impingement surface, the latter being anomalously lower. Baines and Keffer[1979] found almost no effect of surface motion on the averaged shear stress at the impingement surface for an unconfined single slot jet at  $H/w=2$  for values of  $v_s/u_j$  up to 0.2. Van Heiningen[1982] showed that local and average impingement heat transfer for a single confined slot jet at a slowly moving surface is not different than at a stationary surface. The findings of Fechner, Baines and Keffer and of van Heiningen indicate that Hasler and Krizek's results are not realistic.

The only study on effect of surface motion on local and average heat transfer for confined single impinging slot jets is that of van Heiningen[1982]. Over the  $Re_j$  range 10000-90000 he varied the surface motion parameter,  $Mv_s = \rho_s v_s / \rho_j u_j$ , from near stationary,  $Mv_s=0.02$ , to relatively high values, 0.86. Instantaneous local heat flux at the

surface moving under the impinging jets was measured with a 1.15mm wide, fast responding sensor based on a resistance thermometer (van Heiningen et al.[1985]). He measured the extent to which the magnitude and location of the off-stagnation minimum and maximum in local heat transfer rate were changed by impingement surface motion. At a surface moving at sufficiently high speed these off stagnation features were found to disappear on the side where the direction of surface motion is towards the nozzle centerline. Van Heiningen found that average heat transfer decreases with increasing  $Mv_s$ . For example for  $Re_j=10000$  and  $H/w=2.6$  heat transfer averaged over  $S/w=22.5$  at  $Mv_s=0.86$  is 17% lower than at a stationary impingement surface.

Studies for unconfined slot jets have reported that with increasing impingement surface velocity, average heat transfer undergoes either a slight increase or remains unchanged, while the only study for confined slot jets, that of van Heiningen, found a decrease. Lack of a confinement surface introduces effects of unknown magnitude in impingement heat transfer because of corresponding changes in the flow structure of jets by entrainment as well as thermal changes which are equipment specific in that they depend on the temperature at the nozzle exit, the impingement surface and in the surroundings.

For the case of single slot jets, the limited amount of information concerning the effect of throughflow at the impingement surface was summarized in the previous section. For multiple confined impinging jets, the effect on heat transfer which results from throughflow at a moving impingement surface has never previously been studied.

### 2.3 NUMERICAL FLOW AND HEAT TRANSFER STUDIES

Of the investigations listed, Table 2.3, only the earliest studies, Wolfshtein[1967] and Russell and Hatton[1972], used a one-equation turbulence model combined with the required empirical specification of turbulence length scales. Wolfshtein assumed a length scale while Russell and Hatton used both the assumed length scale of Wolfshtein and their own length scale measurements, of very high uncertainty due to experimental difficulties. Flow predictions improved slightly when measured length scales were used. They did not solve the energy equation. Wolfshtein's predicted impingement heat transfer distribution agreed reasonably well with the experimental data of Gardon and Akfirat[1966] at  $H/w=8$  for  $Re_j < 11000$  but not at higher  $Re_j$ .

As empirical specification of the turbulence length scale is required, one-equation turbulence models are not adequate for the complex structure of impinging jets. Adoption of higher order models which solve transport equations for turbulence characteristics, i.e. turbulent kinetic energy, turbulent kinetic energy dissipation or individual Reynolds stresses, lead to the subsequent switch to  $k-\epsilon$  and algebraic stress models (ASM) for turbulence.

Looney and Walsh[1984] made flow and heat transfer predictions for an impinging jet for  $8 < H/w < 43$  for various  $Re_j$ . Convergence problems made results unreliable for  $H/w < 8$ . Their tests indicated that the algebraic stress models of Rodi[1972] and Ljuboja and Rodi[1979] did not predict heat transfer in the impingement region as well as the high  $Re$  version of the  $k-\epsilon$  turbulence model. Van der Meer[1987] used the low  $Re$  version of the  $k-\epsilon$  model and an anisotropic model in which the nondiagonal terms of the Reynolds stress tensor are calculated as in

Table 2.3 Numerical studies on turbulent impinging jets  
a) Two dimensional plane jet studies

Reference	Boundary conditions	Turbulence Model	Equations solved in
Wolfshtein[1967]	C2, D1, D2, D3, D4, E1, F1	one-equation model	$\Psi - \omega$
Russell and Hatton[1972]*	C2, D1, D2, D3, D4, E1, F1	one-equation model	$\Psi - \omega$
Folayan[1976]	no information	k- $\epsilon$ , high Re model	primary variables
Agarwal and Bower[1982]*	A2, B2, C2, D1, D2, D3, D4, E1, F1	k- $\epsilon$ , low Re model	$\Psi - \omega$
Huang et al.[1984]	A2, B2, C2, D1, D2, D3, D4, D6, E1, G1, G2	k- $\epsilon$ , high Re model	primary variables
van Heiningen[1982]	A1, B2, C2, D1, D2, D3, D4, E1	k- $\epsilon$ , high Re model	primary variables
Guo and Maxwell[1984]*	C2, D1, D2, D3, D4, E1, F1	k- $\epsilon$ , high Re model	$\Psi - \omega$
Looney and Walsh[1984]	C2, D1, D2, D3, D4, E1, F1, F2	k- $\epsilon$ , high Re model and two ASM's	primary variables
Polat et al.[1985]	A1, B2, C2, D1, D2, D3, D4, E1	k- $\epsilon$ , high Re model	primary variables

b) Two-dimensional axisymmetric jet studies

Reference	Boundary Conditions	Turbulence Model	Equations solved in
Amano[1980]*	A1, A2, B1, C1, C2, D1, D2, D3, D4, E1	k- $\epsilon$ , high Re model	primary variables
Amano[1983]*	A1, A2, B1, C1, D1, D2, D3, D4, E1	k- $\epsilon$ , high Re model	primary variables
Amano and Brandt[1984]*	A1, A2, B1, C1, D1, D2, D3, D4, E1	k- $\epsilon$ , high Re model	primary variables
Amano and Sugiyama[1985]	A1, A2, B1, C1, C2, D1, D2, D3, D4, E1	k- $\epsilon$ , high Re model	primary variables
van der Meer[1987]	A1, B1, C2, D1, D2, D3, D4, E1	k- $\epsilon$ , low Re model the anisotropy model	primary variables

\* Impingement heat transfer was not predicted

Boundary Conditions (Refer to Fig. 2.2)

Boundary A	D3. Smooth
A1. Flat jet inlet velocity profile	D4. Stationary
A2. Developed jet inlet velocity profile	Boundary E
Boundary B	E1. Symmetry
B1. Without confinement	Boundary F
B2. With confinement	F1. Well-developed, unbounded submerged turbulent jet profile
Boundary C	F2. Partially developed unbounded turbulent jet profile
C1. No flow (discharge is at the nozzle level)	Boundary G
C2. Free discharge (no crossflow)	G1. Crossflow
Boundary D	G2. No-crossflow
D1. Plane	
D2. Impermeable	

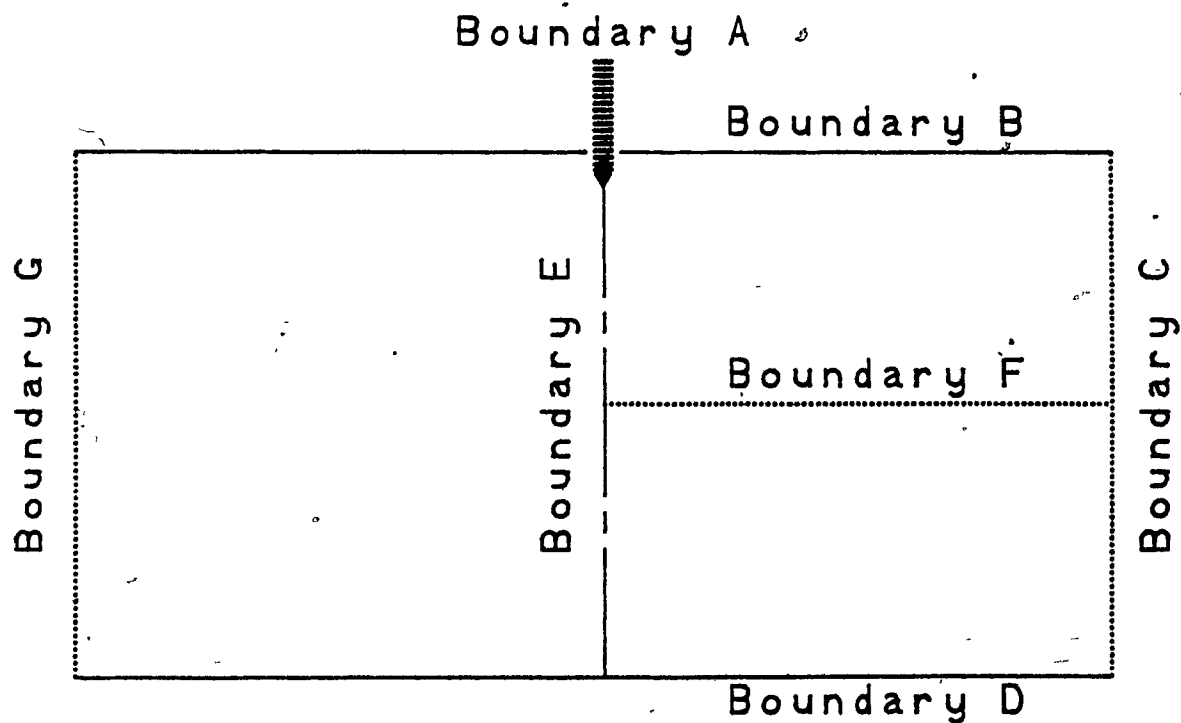


FIGURE 2.2. Position of the boundaries described in Table 2.3

the case of the low-Re version of the  $k-\epsilon$  model, and the anisotropy term,  $g = \overline{u'^2} - \overline{v'^2}$ , is calculated by solving an additional equation. He found that, when used to predict local heat transfer from impinging axisymmetric jets for  $Re_j = 6400$  at  $H/w$  of 2, 4 and 6, the conventional  $k-\epsilon$  model was superior to the anisotropy model. Looney and Walsh's ASM results and van der Meer's experience with the anisotropic model indicates that use of more complex turbulence models does not always improve the heat transfer predictions. Further modification and testing of these models appears required.

As the high-Re version of the  $k-\epsilon$  model of Jones and Launder[1973] is valid only where viscous effects are negligible, a separate model must be used to treat the distribution of turbulent shear stress and turbulent kinetic energy in the near-wall boundary. Overall success of the numerical simulation then depends on both the  $k-\epsilon$  model and the choice of near-wall model. The majority of the studies in Table 2.3 have used the high-Re version of the  $k-\epsilon$  model of Jones and Launder and therefore used near-wall models for turbulent shear stress and kinetic energy. Amano and Sugiyama[1985] claimed a better prediction of stagnation point heat transfer coefficient with one of the three models they tested for treating the near-wall boundary of an axisymmetric impinging jet. However, when a separate near-wall model is used, stagnation heat transfer is calculated at the grid node next to the actual stagnation point. Therefore comparisons of results must take into account the fact that the value of predicted stagnation heat transfer varies with the location of the gridlines near the jet centerline and impingement surface.

Van Heiningen[1982] and Polat et al.[1985] predicted heat transfer

for an impingement surface located within the potential core of a plane jet, i.e. for  $H/w$  of 2.6 and 6 for  $Re_j$  in the range 5000 to 20000. The minimum within the stagnation point Nusselt number peak found by van Heiningen may be attributed to the grid distribution near the symmetry line. He reported that a few grid points next to the wall near the symmetry line were in the viscous sublayer region (i.e.  $x^+ < 11.5$ ). Because the high-Re version of the  $k-\epsilon$  model was used together with near-wall functions, all values of  $x^+$  or local turbulent  $Re$  should be at least 100, according to Guo[1982] and Guo and Maxwell[1984]. Polat et al. predicted the off-stagnation heat transfer maximum to occur at about  $y/w \approx 7$ , which agrees well with experiment. The inflection point that marks the end of the stagnation region was predicted at about  $0.5w$  to  $1.5w$ , which is about  $\approx 2.5w$  smaller than the experimental observations. Both van Heiningen and Polat et al. obtained good agreement with experiments in the wall jet region.

Huang et al.[1984] predicted impingement heat transfer distribution for  $Re_j$  of 11000 and 22000, at  $8 < H/w < 16$ , with and without imposed crossflow. Their predicted results without crossflow or surface motion effects agreed with the experimental data of Gardon and Akfirat[1966] within 25% at  $Re_j = 11000$  and  $H/w = 8$ . With an induced crossflow in the channel between the impingement and confinement surfaces, they documented the extent of decrease in maximum  $Nu$  number and the amount by which it was shifted downstream from the jet centerline as a function of the crossflow parameter,  $Re_c/Re_j$ , at a particular  $Re_j$ . They also found that impingement surface motion in the presence of crossflow caused the heat transfer rate to increase on the upstream side, and to decrease downstream. The effect of surface motion on average heat



transfer was found to be quite small due to these compensating effects on either side of the nozzle centerline. The effect of surface motion without crossflow could not be studied because of the difficulty in defining the upstream boundary conditions

Polat et al.[1986] tested the high-Re version of the  $k-\epsilon$  model for the case of heat transfer by multiple slot jets with exhaust ports located symmetrically between the jets. For small  $S/H$  values, the stagnation region and exit flow region under the exhaust port are sufficiently close to affect the intermediate flow region, a circumstance which renders inappropriate the near-wall model, which is based on Couette flow assumptions

Simulation of the effect of throughflow on impingement heat transfer from turbulent jets, not previously attempted, constitutes one of the major objectives of this study.

## 2.4 CONCLUSIONS

Review of studies on impingement heat transfer due to single and multiple jets without and with the industrially important effects of confinement, surface motion and throughflow, led to the following conclusions:

1. Despite the much greater industrial relevance of confined jet systems, laboratories elsewhere have focussed mostly on unconfined impinging jets.
2. Experimental studies of the effect on flow and heat transfer of throughflow at the impingement surface are very limited for single impinging jets and none exists for multiple impinging jets.
3. Five studies of the effect of surface motion on convective

transport processes under impinging jets provide contradictory indications. Four of the studies involve the additional uncertainty of unconfined jet systems. The five reports on effect of impingement surface speed on convective transfer rate range from indications of a large increase, to no effect, to a significant decrease. There is no study for the case of confined multiple impinging slot jets.

4. The combined effects of surface motion and throughflow on impingement heat transfer have never been studied due to the lack of an experimental technique applicable for this combination of conditions of industrial relevance.

5. No generally applicable model for the numerical prediction of impingement heat transfer due to turbulent jets is available.

## CHAPTER 3

### EXPERIMENTAL FACILITY

#### 3.1 OVERALL DESIGN CONCEPT

An experimental facility was built for study of local heat transfer under single and multiple confined turbulent slot jets of air impinging on a moving surface with or without throughflow at the surface. The impingement surface was the external wall of a rotating porous cylinder, 0.48m diameter. Steady-state operation of the overall system was obtained by locating a heated single impinging slot jet at a position  $180^\circ$  from the unheated multiple jets. Thus the cylindrical impingement surface assumes a steady average temperature intermediate between the heating and cooling jets. The length of each slot jet was the same as the length of the cylindrical impingement surface, 0.2m. A unique sensor, developed in the present study, enabled obtaining instantaneous local values of Nusselt number at a rapidly moving impingement surface with throughflow.

The impingement flows were confined by a 0.58m diameter cylindrical hood, concentric with and of length equal to the impingement cylinder, providing a spacing of 50mm between the confinement and the impingement surfaces. The flows from the heating and cooling jets in this annular section were kept separate and were removed through exhaust ports. Thus the entire system consisted of two isolated subsystems, one for the heating single jet, one for the cooling multiple jet array. This overall design concept was developed and used in the SIMTEST I Apparatus by van Heiningen[1982] to obtain local heat transfer profiles at a moving impingement surface under single impinging jets. The present

equipment, the first to incorporate multiple jets, is termed the SIMTEST III Apparatus for the objective of testing present and future computer simulations of single or multiple jet impingement heat transfer on moving surfaces with or without throughflow. A photograph of the experimental equipment is shown as Fig. 3.1. The multiple jets and the single jet appear at the top and bottom, respectively, of the rotating cylinder assembly.

The combination of three key features of this design, i.e., use of a rapidly moving impingement surface, of jets which are confined by a hood parallel to the impingement surface, and removal of some of the impingement flow through the impingement surface reflects the orientation of this study to the possibility of drying of paper by combined impingement and through flow from hot jets, proposed by Burgess et al.[1972a, b]

The experimental facility was closed with circular plates at the ends of the impingement cylinder-confinement hood. The single jet and the multiple jet system were provided with separate exit ports. The two exit ducts for the single jet were positioned  $90^\circ$  from that nozzle. The multiple jet assembly comprised three slot jets, with slot exhaust ports located symmetrically between the jet nozzles. This arrangement avoids exhaust crossflow under the impinging jets. To provide symmetry of flow two exterior exhaust ports, each half the width of the two interior exhaust ports, were located at the two sides of the three jet assembly. All jet nozzle exits and exhaust port inlets were positioned flush with the confinement surface. As proven by Saad[1981] for a stationary impingement surface with this symmetrical exhaust flow configuration, the middle jet of such an array of three identical jets



FIGURE 3.1. General view of experimental facility

is representative of a slot jet in a multi-jet array. The symmetrical arrangement of an exhaust port between each jet nozzle was selected to avoid the strong disadvantage of crossflow of spent flow under an adjacent jet nozzle. The degradation of impingement heat transfer by exhaust crossflow has been demonstrated experimentally by Saad[1981] and numerically by Ahmad[1987].

The single jet and the multiple jet systems were isolated by two pairs of skimmer plates, one pair located at either end of the multiple jet assembly, the other pair at the mid-points of the exit ports for the single jet. Mixing of spent air from the heated and unheated jets was thereby minimal in the annular channel between the impingement and confinement surfaces. Thus the two sub-systems, the heating single jet and the cooling multiple jets, occupy respectively  $180^\circ$  or 0.75m, and  $36^\circ$  or 0.15m, of the 0.2m wide impingement surface. The remaining two sections, each  $72^\circ$  of the heat transfer cylinder circumference, form buffer zones between the single and the multiple jet sub-systems.

At steady state, when the rotating cylindrical impingement surface has assumed a steady average temperature intermediate between that of the heating and cooling jets, the maximum variation in local temperature over this entire surface is small, about  $\pm 2^\circ\text{C}$ . Thus the convective heat transfer coefficients obtained with this equipment design correspond to the boundary condition of an isothermal surface.

The rotating impingement surface was made of porous glass (3M, brand name "porous glass", Grade 55). Throughflow at the impingement surface was provided by applying suction. The range of throughflow velocity,  $u_s$ , and peripheral velocity of the impingement surface,  $v_s$ , were chosen with reference to the proposed "Papridryer" process which

would use a combination of impingement and throughflow drying mechanisms to enhance drying rates of paper (Burgess et al. [1972a,b]). Thus the maximum speed of rotation,  $\sim 6$  rps, corresponds to  $v_s \sim 9$  m/s which is in the range of paper machine speeds. The range of throughflow rates at the impingement surface, expressed as the non-dimensional ratio,  $\rho_s u_s / \rho_j u_j$ , is from 0 to 0.023. The maximum percent of jet nozzle exit flow drawn through the impingement surface is therefore 11.5% and 86% on the multiple and single jet sides respectively. The Reynolds number of the jets was varied from 8000 to 26000 for the multiple jets, from 17000 to 58000 for the single jet.

For a multiple jet array configuration similar to that of the present study, operated over the range  $3000 < Re_j < 30000$ , Saad [1981] showed experimentally that the combination of non-dimensional spacings which produce a maximum value of average Nusselt number for a stationary impingement surface with no throughflow is  $H/w=5$  and  $S/H=0.5$ . Because of the importance of average Nu in industrial application, these non-dimensional spacings, i.e.,  $H/w=5$ ,  $S/H=0.5$ , were chosen for the present study of multiple slot jets impinging on a moving surface with throughflow. The width of the multiple jet nozzles,  $w=10$  mm, was selected such that the desired range of other geometrical and flow variables were within the constraints of the equipment design and fabrication. With this selection of  $w$ , a 50 mm nozzle-to-impingement surface spacing and a 25 mm nozzle centerline-to-exit port centerline spacing gave the desired  $H/w$  and  $S/H$  spacings indicated above.

For the single jet side, a nozzle width of 20 mm was selected to obtain a nondimensional nozzle-to-surface spacing,  $H/w$ , of 2.5, thus facilitating comparison of results with those of the SIMTEST I

apparatus for which one of the single jets had an H/w spacing of 2.6.

Development of a porous sensor for determination of instantaneous local heat transfer rate at an impingement surface moving at speeds up to 9m/s, with or without throughflow at the impingement surface, was the most critical part of the SIMTEST III apparatus. Van Heiningen, Douglas and Mujumdar[1985] developed an impermeable sensor made of a very thin gold film with this capability for the case of no throughflow at the impingement surface of the SIMTEST I apparatus. However they confirmed that, with throughflow, even a narrow impermeable sensor can not be used in an otherwise uniformly permeable moving impingement surface because the turbulent boundary layer adapts so rapidly to the momentary change of boundary condition. For the case of throughflow at the impingement surface, therefore, it was essential to develop for the present study a permeable sensor of the same porosity and thermal characteristics as the impingement surface. The ideal choice is the same porous material for the sensor substrate as for the cylindrical impingement surface. After an extensive search for a porous material which would have the desired properties as an impingement surface and as well as a sensor substrate, a porous glass material (3M Company, brand name "porous glass", grade 55) was selected.

The sensor, a thin film resistance thermometer, was a 70mm long x 1mm wide gold filament, about  $0.15\mu\text{m}$  thick, deposited on the porous glass substrate. By mounting the sensor flush with the impingement surface the instantaneous local surface temperature could be monitored. Instantaneous heat flux, and thereby local Nusselt number, was obtained from surface temperature through solution of the one-dimensional unsteady state heat conduction equation for experiments without



throughflow. For throughflow experiments the solution scheme was modified to account for convection heat transfer between throughflow and the porous substrate. Use of a micro computer for on-line data acquisition and data reduction permits determination of about 500 values of local Nusselt number per rotation of the heat transfer cylinder. Thus the Nusselt number profile is defined at about 250 points for the single jet, at 50 points for the multiple jets. A detailed description of the heat flux sensor, a critical and original part of the present study, appears as Chapter 4.

### 3.2 EXPERIMENTAL FACILITY

The schematic diagram, Fig. 3.2 illustrates the experimental facility. The discharge of a 22.4kW blower (1)(Industrial Combustion and Equipment Ltd., 3600rpm ODP motor,  $1\text{m}^3/\text{s}$  at 13.8kPa) located in an acoustic shelter adjacent to the laboratory, is split into one stream for the single jet, one for the multiple jet side. The two flowrates, measured by orifice meters (3,4), are controlled by gate valves, one at the blower exit, the other in the line (2) to the multiple jets.

Air at about  $40^\circ\text{C}$  (due to heating by the blower) enters the multiple jet section via the 0.25m diameter pipe. After the 4.75m long flow measuring section (11 pipe diameters before and 8 diameters after the orifice meter), a 1.45m long diverging section adapts (5) this pipe to a box (6) 0.205m x 0.4m in cross-section, 0.3m deep. Two 0.19m high movable flow dividers (7) in this box serve to control the flow to each jet in the three-jet system. These flow dividers, hinged at their lower ends, are positioned from outside the box with control rods. A 100-mesh screen placed at the entrance of this box reduces the

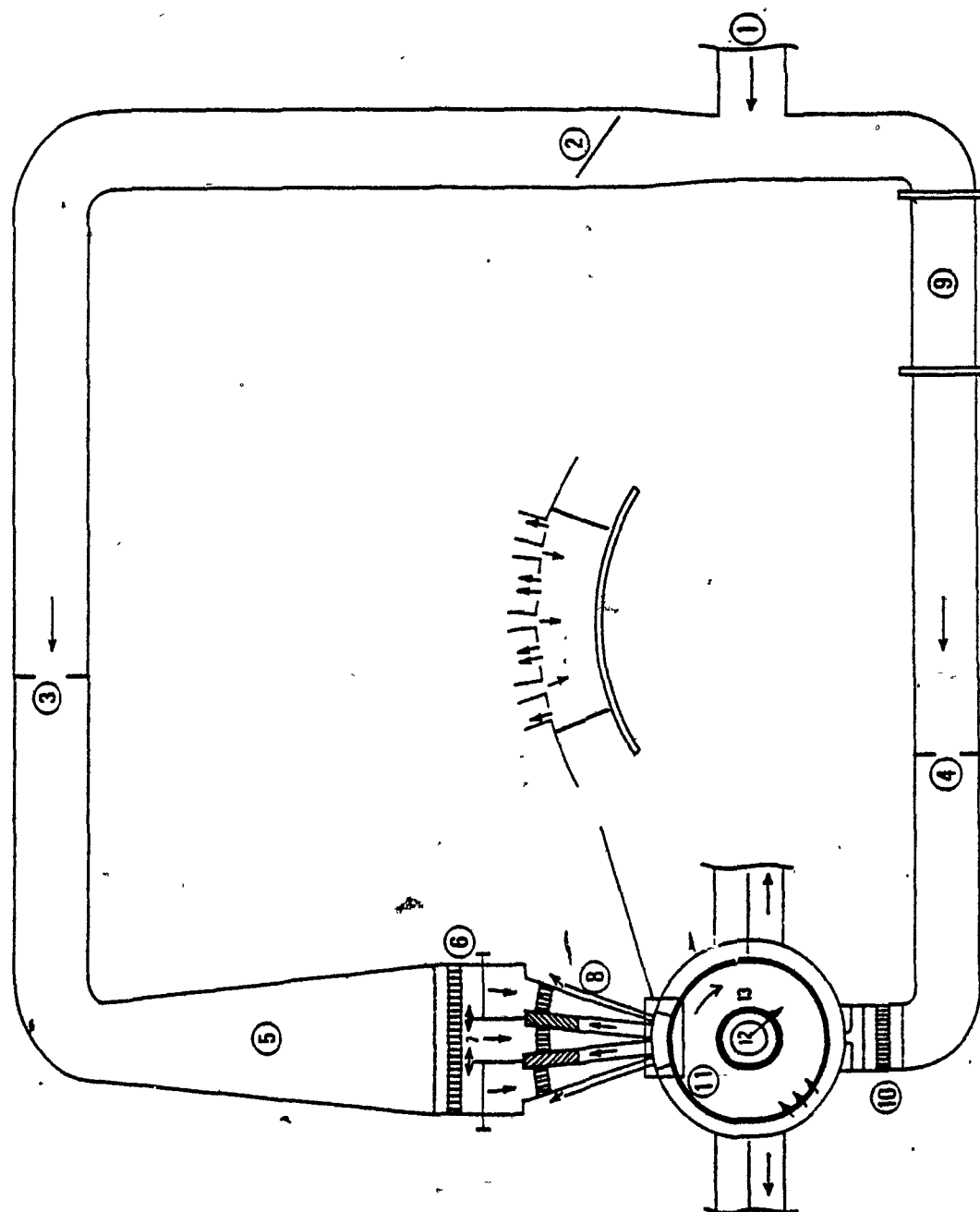


FIGURE 3.2. Schematic diagram of experimental facility

turbulence level, and a .50mm thick aluminum honeycomb, (hexagonal, size 4.7mm), located 50mm from the box entrance, straightens the flow.

Three nearly parallel channels (8), about 0.4m long x 0.2m in the axial dimension, adapt the flow from about 90mm wide at their inlet to the 10mm wide multiple jet nozzles at the outlet. The enclosed angle is  $5.7^\circ$ . At the nozzle exit end the nozzle channels terminate flush with the confinement surface. The 10mm x 0.2m slot jets impinge on the porous surface spaced at 50mm ( $H/w=5$ ) from the nozzle exit. This type of nozzle geometry was selected for its simplicity, low pressure loss and ease of adapting to the overall system design.

The fraction of nozzle exit flow which is not withdrawn as through-flow is exhausted at the confinement surface through the exit ports. The area of the exhaust ports is twice the nozzle exit area. For the symmetrical multiple exhaust arrangement, each of the two interior ports is therefore 20mm wide, while the two side exhaust ports are each 10mm wide. The length of all nozzle and exit ports is identical, 0.2m, i.e. the full length of the impingement surface. As the centerline-to-centerline distance,  $S$ , between nozzles and adjacent exhaust ports is 25mm in order to achieve the nondimensional spacing  $S/H=0.5$ , there is 10mm of confinement surface on both sides of each nozzle. The two interior 40mm wide exhaust channels contain flow vanes to redirect the spent flow by  $60^\circ$  towards the exhaust ducts located at the two ends of the equipment. Slide gates at the exit of these interior exhaust channels are adjustable with extension bars to achieve symmetry of flow under the multiple jets.

For the single jet, air from a 0.2m diameter line is heated by a 6kW, 12-stage duct heater (9) located in a 0.2m square box, 0.8m long.

Ten of the heater stages are operated at 220V, connected in pairs to 5 on-off switches, while the remaining two stages are connected in series as a pair to a 120/140V variac (Staco Energy Products Co., type 3PN1010) for fine tuning purposes. This arrangement gives a very uniform nozzle exit temperature, within  $\pm 0.3^{\circ}\text{C}$  over the important central region of the single jet. The heater exit is located 9 pipe diameters upstream from the orifice inlet, which is 10 pipe diameters upstream from the elbow to the plenum chamber. The line from the heater to the single jet nozzle is well insulated for safety and heat loss prevention. The 0.27m long, 0.2m square plenum chamber (10) for the single jet, located beneath the equipment, contains two 100-mesh screens at 0 and 150mm from the plenum entrance to reduce the turbulence level. A 50mm thick aluminum honeycomb (hexagonal, size 4.7mm) at 50mm from the plenum entrance straightens the flow. In order to obtain comparable results, the 20mm wide single jet nozzle has the same geometry (ASME standard elliptical contoured entrance) as the 14mm and 6.2mm wide nozzles that were used in the SIMTEST I Apparatus.

The unheated multiple jets and the heated single jet impinge on a porous glass cylinder (11) of 13mm wall thickness, 0.48m outside diameter, 0.185m long. This porous impingement cylinder is supported by aluminum rings, 0.48m outside diameter x 13mm thick, glued with epoxy to each end. A 7mm portion of each aluminum ring rests on a shoulder of the same length provided on 0.48m diameter, x 13mm thick end plates. At the outer ends of the aluminum rings, 5.4mm diameter Neopherene O-rings provide air-tight contact with the end plates. The excess length between the 0.2m length of the nozzle slots and the combined length, 0.223m, of the porous cylinder, aluminum rings and end plates remains

outside the equipment. The two protruding ends are sealed with 13mm thick Teflon rings from outside.

As suction is applied for experiments with throughflow at the heat transfer surface, the impingement cylinder is mounted on a hollow shaft (12), a 0.114m O.D., 0.37m long steel pipe. Over the length corresponding to the impingement surface this hollow pipe is perforated with 28 holes of 25.4mm diameter from which throughflow air is withdrawn. To obtain radially uniform throughflow a 0.165m diameter cylinder (13), of the same porous glass material but of a more open area (grade 155) than the impingement surface, is located between the perforated steel shaft and the impingement surface. One end of the 0.114m O.D. hollow shaft terminates in a bearing sealed with Rulon which provides the suction line connection. The other end of the hollow shaft is attached to the main drive shaft, 102mm O.D., 16mm I.D., 0.85m long, supported by two pillow block bearings spaced 0.457m apart. A pulley between these bearings is driven through a no-slip belt from the drive pulley of a 3.7kW variable speed motor. Leads from the heat flux sensor, pressure transducer and thermocouples pass through the 16mm I.D. of the drive shaft to a low-noise, 14-channel slip ring assembly (IEC Corp., Austin, Texas, Model IEC-TX-14) mounted at the end of the shaft.

The suction system consists of a 7.46kW rotary type blower ( $0.11\text{m}^3/\text{s}$  at  $-40.7\text{kPa}$ ), an orifice meter, and a gate valve at the entrance to the blower. The suction line, seen in the Fig. 3.1 photograph, is connected to the interior of the porous cylinder by a 102mm I.D. flexible SS line via the bearing sealed with Rulon. The throughflow rate is measured by an orifice meter in the straight PVC (108mm I.D.) portion of the suction line (13 pipe diameters before, 7

pipe diameters after the orifice meter).

The average of fifty profiles of surface temperature is used as the boundary condition to the equation for one dimensional unsteady-state conduction (including convection when there is throughflow). This equation is solved iteratively to obtain the profile of local Nusselt number under the jets, as detailed in Section 4.4. The pressure distribution under the jets can be measured with a calibrated pressure transducer (Kulite Semiconductor, XT-190-5) mounted flush with the impingement surface at  $180^\circ$  from the heat flux sensor. Manometers are used to measure pressure drop across the orifices and gage pressure at locations one pipe diameter above the orifices and at the jet nozzle inlets. Air temperatures were measured by E type (chromel/constantan) thermocouples (0.25mm wire diameter) at the jet nozzle inlets and at one pipe diameter from the orifice meters (Omega, CXSS-116C-L2). Chromel/constantan thermocouples (0.25mm wire diameter) were glued flush with the impingement surface, 5mm from each end of the heat flux sensor, through 1 mm holes, to measure the substrate temperature during in-place calibration of the sensor.

### 3.3 INSTRUMENTATION

#### 3.3.1 Position Sensor

Heat flux sensor position is determined with an optical slotted switch (Spectronics, SPX-1878-14) mounted at a fixed position next to the impingement cylinder. An aluminum tab fixed to its end plate passes once every rotation through the slot of the switch. The relative position of the switch and the tab is such that, as the cylinder rotates clock-wise, when the tab enters the switch slot the

heat flux sensor is at the skimmer plate  $90^{\circ}\text{C}$  upstream of the single jet nozzle centerline. Before sampling of the heat flux sensor signal starts the switch signal is sampled via the trigger of the A/D board. The intervals between each trigger is measured with the A/D board timer and converted to rpm. Based on this rpm and the desired number of samples per rotation the interval between successive samples of the sensor output is determined.

### 3.3.2 Instrumentation for Pressure Measurement

Local pressure difference across the permeable impingement surface is measured with a differential pressure transducer (Kulite XT-190-5) with the interior pressure as the reference pressure. The transducer is mounted flush with the impingement surface, equidistant from its ends, at  $180^{\circ}$  from the heat flux sensor. Sensitivity of the transducer given by the manufacturer is  $0.0025\text{mV/Pa}$  at 10 volts excitation. The compensated temperature range of this transducer,  $25^{\circ}\text{--}90^{\circ}\text{C}$ , exceeds that used.

### 3.3.3 Instrumentation for Temperature Measurement

The fixed positions at which temperature is monitored with chromel/constantan thermocouples are one pipe-diameter before each of three orifice plates (heating jet, cooling jet and suction line), one at each end of the heat flux sensor, one at the interior surface of the impingement cylinder located at the axial mid-point. Axial temperature profiles at the jet nozzle exits are measured with movable thermocouples. Reference junctions of all thermocouples are kept at  $0^{\circ}\text{C}$  with an ice point reference (Kaye Instrument K140-4). Thermocouple

output is measured with a digital nanovolt meter (Keithley Instruments, Model 180) via a multi-position rotating switch (Omega).

### 3.4 TESTING AND CALIBRATION OF EQUIPMENT

#### 3.4.1 Symmetry of Flow under Jets

Profiles of local static pressure at the impingement surface at various jet Reynolds numbers at very slow cylinder rotational speeds are measured with the impingement surface pressure transducer via the IBM-PC data acquisition system. Before each flow experiment, this transducer is sampled when there is no jet flow to determine the zero pressure output, base line from the transducer. This base line is subtracted from the actual profile.

Fig. 3.3 displays the distribution of surface pressure relative to nozzle exit static pressure under the single jet at two values of jet Reynolds number. As is apparent from this figure, flow is quite symmetrical under the single jet. The interesting phenomena of pressure recovery in a confined impingement flow, discussed extensively by van Heiningen[1982], is displayed in Fig 3.3.

For multiple jets as closely spaced ( $S/H=0.5$ ) as in the present study the pressure distribution is practically flat, as can be seen in Fig. 4.6. Thus for the multiple jet side, profiles of local impingement surface pressure do not provide much information about symmetry of flow.

#### 3.4.2 Flow Distribution in Jet Nozzles

Each multiple slot jet issues from a 0.4m long, slightly converging ( $5.7^\circ$ ) nozzle, of width 90mm and 10mm at the nozzle entrance and exit. In addition to the fine screen and honeycomb to reduce turbulence and



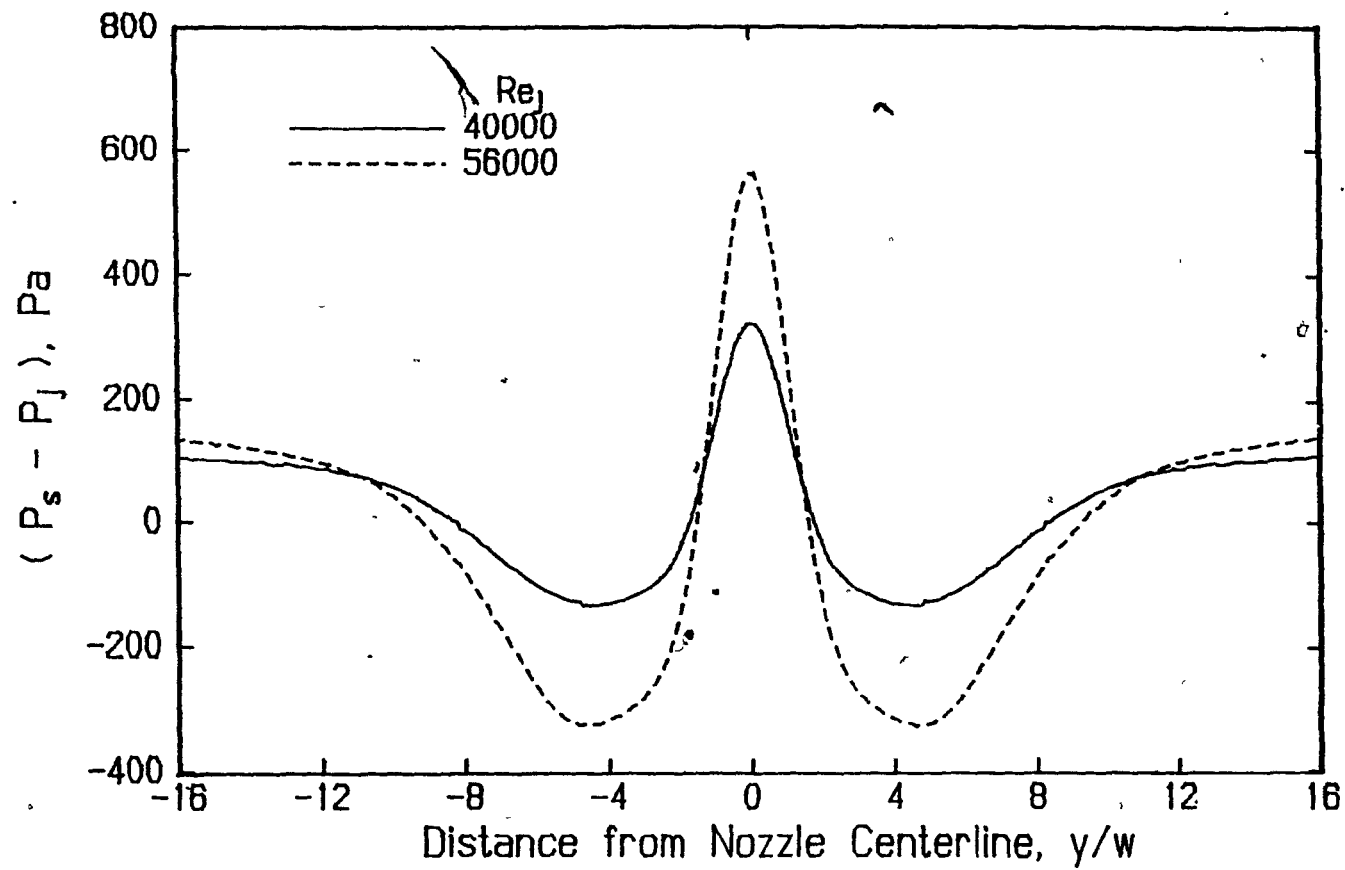


FIGURE 3.3. Static pressure distribution under the single jet

straighten the flow in the box above the nozzle entrance, honeycomb sections set parallel to the flow at the inlet of each channel ensure that the jets issue normally to the impingement surface. The flow rate to the three jets is equalized by adjusting the flow dividers (item 7 of Fig. 3.2) to achieve uniform static pressure at the nozzle exits. Then the sliding gates at the exits of the two interior exhaust channels are adjusted to obtain uniformity of jet flow along the length of the nozzle exits. Fig. 3.4 displays pressure profiles for each jet in the multiple jet assembly, as measured with a pitot tube along the axial length of the nozzles in the mid-plane of the converging channel, at about 50mm above the nozzle exit. Uniformity of these profiles over 90% of the length and close agreement between the profiles of the three jets confirms the two dimensionality and the symmetry of these multiple jet flows.

The single jet nozzle, of the same ASME standard elliptical entry geometry as those of the SIMTEST I apparatus, provides a standardized low turbulence and a flat velocity profile across the width of the nozzle. A flat velocity profile is easier to incorporate into computer simulation programs for impinging jets, thus facilitating comparison of experimental and predicted results for a standard nozzle exit velocity profile. Nozzle design details are given by van Heiningen[1982]. Lengthwise profiles for the single jet at the entrance to the contoured portion of the nozzle are displayed in Fig. 3.5. Again the uniformity of the pressure profile confirms that the jet flow is two-dimensional.

#### 3.4.3 Temperature Distribution at Jet Nozzle Exits

Accurate calculation of Nu profiles depends sensitively on accurate

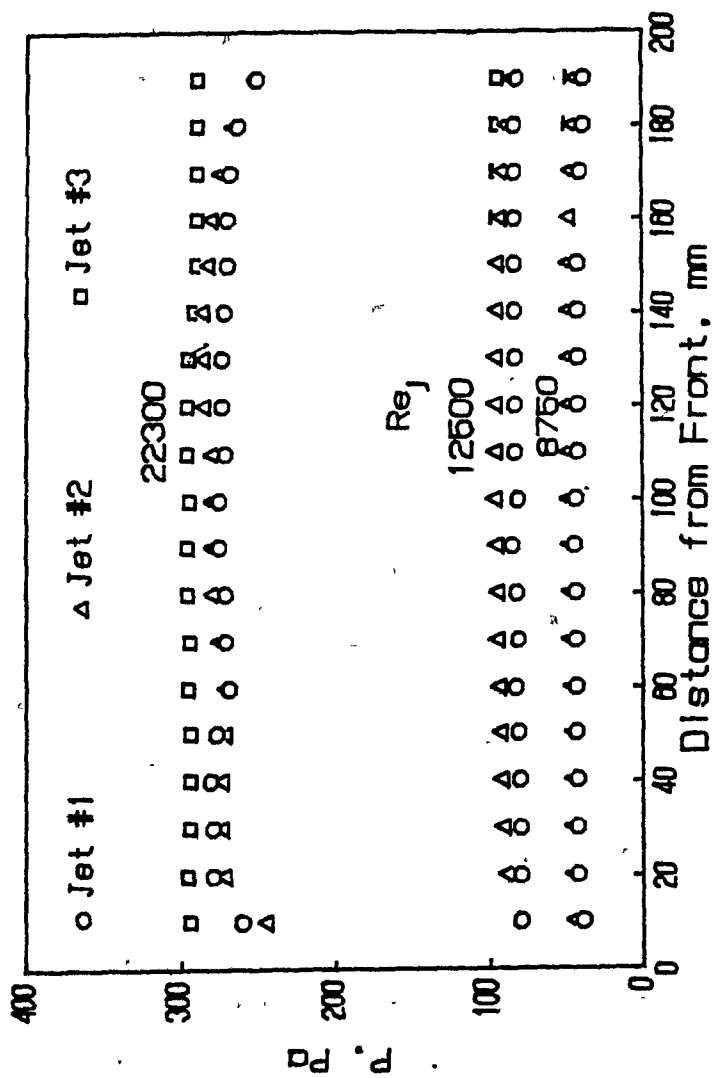


FIGURE 3.4. Static pressure along nozzle midplane of multiple jets

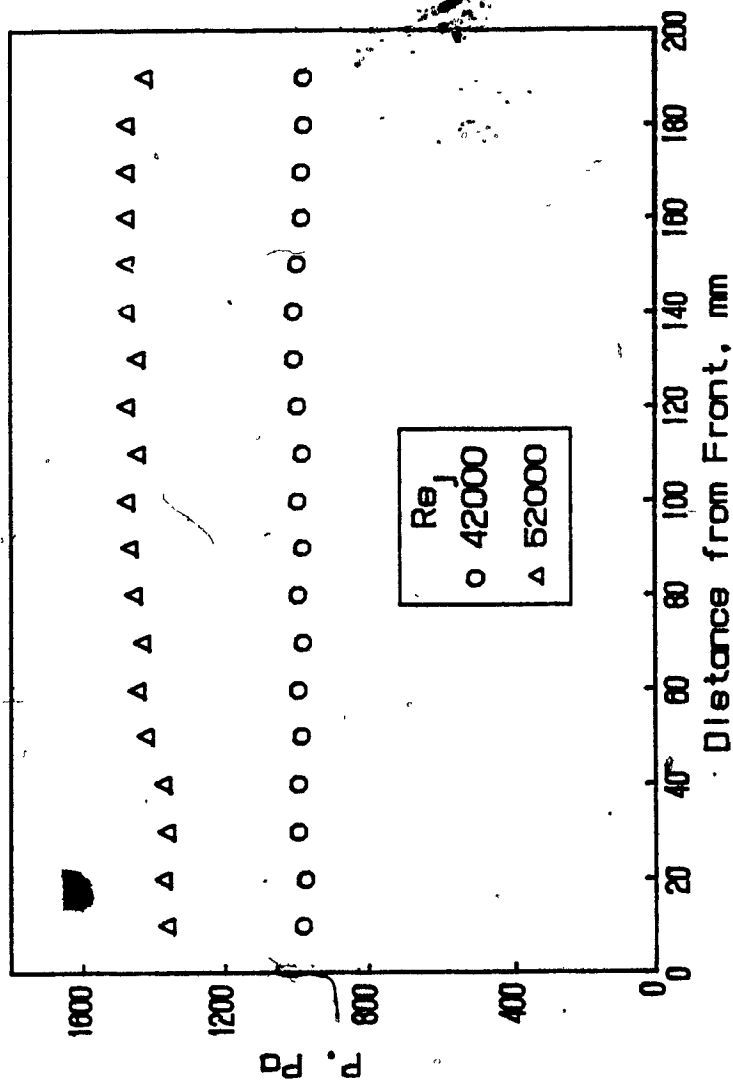


FIGURE 3.5. Static pressure along nozzle midplane of the single jet

measurement of temperature at the nozzle exit since heat transfer coefficients are based on the temperature difference between the impingement surface and the nozzle exit. As this temperature difference is typically  $10^{\circ}$ - $25^{\circ}\text{C}$ , an error of  $\pm 0.5^{\circ}\text{C}$  in temperature measurement would correspond to 2-5% error in Nusselt number.

Another important constraint is that the nozzle exit temperature of each jet in the multiple jet assembly should be the same in order that the middle jet be representative of a jet in an infinite array of such jets. In the original design the single jet was unheated and the multiple jet assembly was heated by a duct heater located on top of the flow adjustment box. After finding that the nozzle exit temperatures of the three jets could differ by as much as  $5^{\circ}$ - $10^{\circ}\text{C}$  and that the profiles of nozzle exit temperature along the nozzle length were not flat, apparently due to insufficient mixing length after the heater, the choice of heating and cooling jets was reversed. In this major equipment design change the original heater on the multiple jet side was eliminated and a new heater installed on the single jet side, located sufficiently far from the jet nozzle that very uniform jet temperatures at the nozzle exit were obtained. Evidence of satisfactory performance by the final arrangement is provided by in Figs. 3.6 and 3.7 which display the nozzle exit temperature profiles of the multiple jets and the single jet. As the nozzle exit temperature profiles of the three jets in the multiple jet assembly were almost identical, the middle jet temperature was used to calculate Nusselt number.

For each run, axial profiles of centerline nozzle exit temperature of the middle jet of the multiple jet assembly and of the single jet

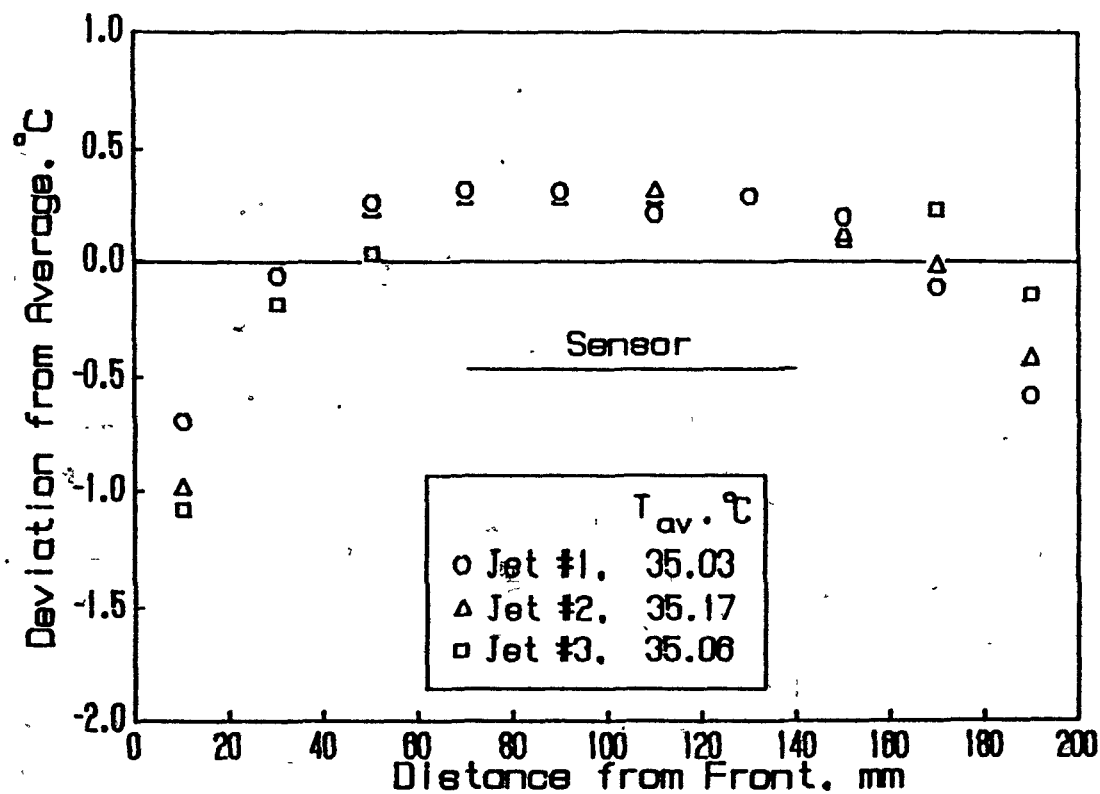


FIGURE 3.6. Temperature distribution along nozzle midplane of the cooling multiple jets

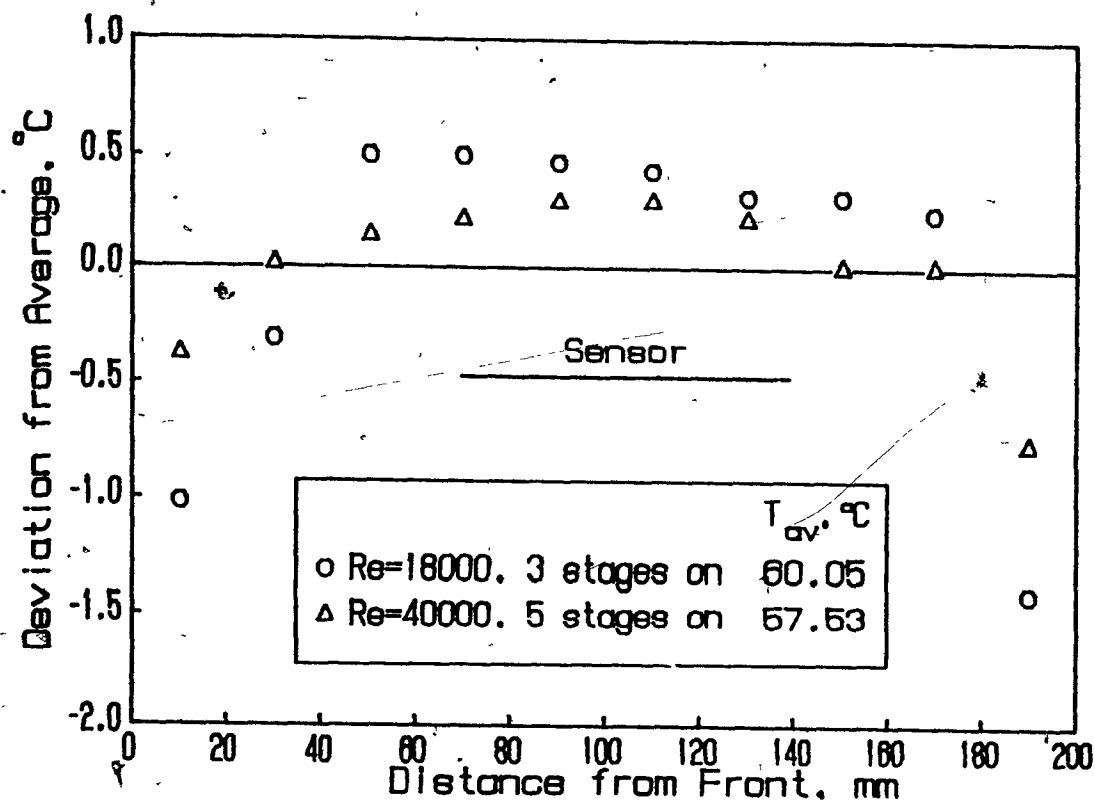


FIGURE 3.7. Temperature distribution along nozzle midplane of the heating single jet

were measured with a movable thermocouple. These profiles are uniform to within  $\pm 0.5^\circ\text{C}$  over the central 90% of nozzle length. The temperature used for Nu calculations is the average value over the axial length corresponding to the sensor. The maximum variation of the nozzle exit temperature over the sensor length is small,  $\pm 0.3^\circ\text{C}$ .

Temperature across the nozzle width is very uniform for both multiple and single jets. The nozzles of the multiple jets are sandwiched between the exhaust ducts through which spent flow leaves at somewhat above nozzle exit temperature. For the single jet side, the pipeline downstream of the heater and the plenum chamber are well insulated, and very uniform nozzle exit temperatures are obtained.

#### 3.4.4 Calibration of Orifice Meters

Flow to multiple jets, single jet and of throughflow were measured with orifice meters. An orifice to pipe diameter ratio of 0.5 was used. To measure pressure drop across the orifice plates, radius pressure taps (1 ID before and 1/2 ID after the plate) were used. The mass flow rate is related to pressure drop by

$$\dot{m} = C A_o (2 \rho_1 \Delta P)^{1/2} \quad (3.1)$$

where C is the discharge coefficient of orifice plate, determined by calibration against pitot tube measurements. Pitot tube pressure drop was measured with a calibrated inclined monometer (Wilh. Lambrecht KG Gottingen, type: 655). As shown in Fig. 3.8, there is excellent agreement with the following empirical equation, derived by Bentley and Riley[1983] from the extensive experimental data

$$C = 0.5959 + 0.0312 \beta^{2.1} - 0.0184 \beta^8 + 0.0029 \beta^{2.5} \left( \frac{10^6}{Re_d} \right) + 0.090 L_1 \beta^4 (1 - \beta^4)^{-1} - 0.0337 L_2 \beta^3 \quad (3.2)$$



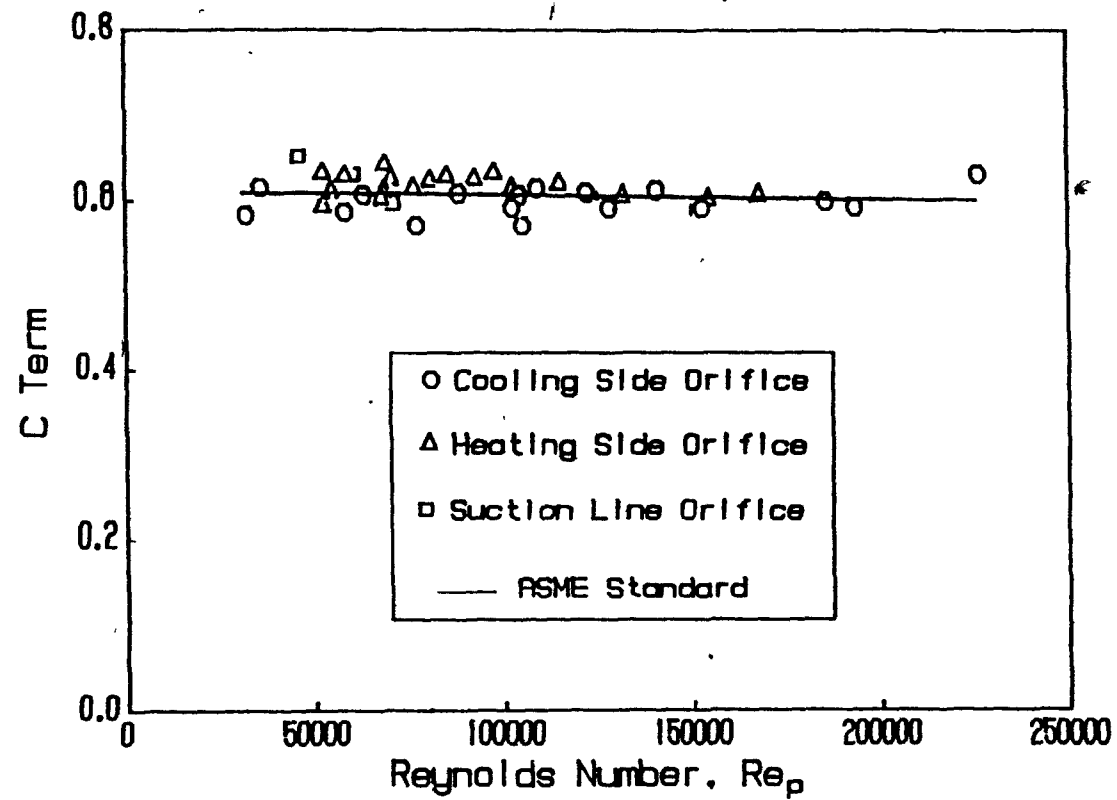


FIGURE 3.8. Calibration of the orifice plates

where  $L_1$  and  $L_2$  are 1 and 0.47, respectively, for radius pressure taps. Hence the above equation is used to predict the orifice coefficient for all three orifice plates at all flow rates.

## CHAPTER 4

## SENSOR FOR TRANSIENT HEAT FLUX AT A MOVING SURFACE WITH THROUGHFLOW

## 4.1. INTRODUCTION

The objective was to develop a sensor capable of measuring instantaneous local heat flux at a permeable surface at which there is throughflow and which is subject to a rapidly varying cyclical transient heat transfer. No heat flux sensor for these constraints has been reported. The closest approach to a heat flux sensor satisfying these requirements is that developed by van Heiningen, Douglas and Mujumdar[1985]. Their analysis of the features and limitations of various fast response heat flux gauges such as thin-film surface thermometry, thick-film calorimetry and hot-film probes (Rose[1958], Scheuter and Dosdogru[1970], D.J. Baines[1970], W.D. Baines and Keffer[1976] and van Heiningen, Mujumdar and Douglas[1976]) showed that an appropriate thin-film sensor based on a resistance thermometer is the preferred choice for measurement of a rapidly and widely fluctuating transient heat flux. With this type of a sensor van Heiningen, Douglas and Mujumdar[1985] could measure such varying local values of transient heat flux, but only at an impermeable surface.

Their sensor was a thin-film resistance thermometer, flush mounted on the heat transfer surface, made by deposition of a gold filament, about  $0.27\mu\text{m}$  thick, on an electrically insulating substrate of appropriate thermal and mechanical properties. With a heat transfer surface and sensor substrate that is thermally "semi-infinite", they demonstrated the validity of local transient heat flux measurements obtained with such a sensor.

In the present case the sensor for local transient heat transfer with throughflow was validated for the cyclical heat flux at a rotating cylindrical heat transfer surface, with throughflow, subjected on one side to cooling by multiple slot jets and, at a position about  $180^\circ$  away, to heating by a single slot jet. However the sensor is not restricted to the study of impingement heat transfer but is generally applicable for throughflow heat transfer surfaces subject to cyclical heat transfer..

The present work is devoted to developing a thin-film heat flux sensor which satisfies similar basic constraints, i.e. for cyclical local heat flux, but with the additional requirement that the sensor be applicable for a permeable surface at which there is throughflow. Development of a sensor with such capability would enable experimental investigation of an important class of problems in transport phenomena, those in which there is simultaneous but independent heat transfer and mass transfer at a surface, i.e. where the heat and mass transfer is not coupled. One industrial problem with large economic consequences for which the development of such a sensor is also particularly relevant concerns the possibility of developing new processes for paper drying, processes which could combine through drying with impingement drying. In such a process, impingement heat transfer at the surface of a wet sheet of paper moving rapidly through a dryer is affected strongly by the variable of throughflow rate at the surface. Thus the objective set for the present study relates to significant problems in theoretical transport phenomena and in industrial process development.

## 4.2. DEVELOPMENT OF A POROUS HEAT FLUX SENSOR

### 4.2.1. Selection of the Porous Sensor Material

There are numerous constraints on the choice of material of the porous substrate for the sensor. Its throughflow characteristics and transient temperature response must match those of the throughflow surface in which the sensor is mounted, the porous media used should be homogeneous, machinable, durable to  $100^{\circ}\text{C}$  and, as the substrate for a thin-film resistance thermometer, it must have negligible electrical conductivity. The ideal solution was found possible in this case, i.e. use of the identical material, porous glass, for the sensor substrate and for the permeable heat transfer surface in which the sensor is mounted. Experiments established that a continuous thin-film of gold could be vacuum deposited on porous glass obtained from the 3M Company. As it is necessary in the present case that the permeable heat transfer surface be a rotating cylinder, a 0.48m diameter, 13mm wall thickness porous glass cylinder obtained from the 3M Company was found to satisfy all constraints as the material for both the heat transfer surface and the sensor substrate. To achieve the desired range of throughflow rates across the permeable heat transfer surface, porous glass of a uniform particle size,  $d_p$ , of  $50\mu\text{m}$  (3M Grade 55), of porosity 30%, was selected. Thus the thickness of the heat transfer surface and the sensor is about  $260d_p$ .

### 4.2.2. Fabrication and Mounting of the Heat Flux Sensor

From the analysis of sensitivity of the thin-film resistance thermometer based heat flux sensor made by van Heiningen et al. [1985] it was estimated that a gold film of resistance in the range 100 to 350

ohms and of thickness in the same order as their sensor (about  $0.25\mu\text{m}$ ) was required for the desired accuracy of the transient heat flux measurement. Extensive development of techniques for depositing very thin, electrically continuous filaments of gold on a porous glass substrate was required. The following procedure evolved for fabricating a porous sensor consisting of a gold film of dimensions  $1\text{mm} \times 70\text{mm}$ , i.e.  $20d_p$  wide and  $1400d_p$  long.

1) Sections,  $10\text{mm} \times 100\text{mm}$ , cut from the excess length of the  $13\text{mm}$  wall thickness porous glass cylinder were checked visually, then microscopically for irregularities.

2) A  $1\text{mm} \times 70\text{mm}$  Scotch tape mask was glued to the substrate surface. The photofabrication technique of van Heiningen et al. [1985] for preparation of the thin gold filament was inapplicable because the chemicals ~~damage~~ the porous glass binder. The Scotch tape mask adhered well during deposition, then was easily removed.

3) About  $0.115\text{g}$  of  $0.9999\%$  purity gold was vacuum deposited (Edwards Vacuum Coater, Model 306) to produce films in the desired range of resistance before aging,  $500$  to  $1000$  ohms. Many times a seemingly continuous gold film had infinite resistance. Non-conducting and conducting sensors were indistinguishable under a microscope.

4) Good sensors were "aged" at  $100^\circ\text{C}$  for 6 hours, during which the resistance dropped by half.

5) The gold film was connected with a high conductivity silver paint (Conductive Silver 200 from Degussa A.G.) to  $1.3\text{mm}$  diameter silver lead wires fixed with Easypoxy in holes drilled through the substrate.

6) For measurement of substrate surface temperature during in-situ calibration, two thermocouples were glued (high thermal conductivity adhesive, Trabond 2151, Tra-Con Inc., Medford, Mass.) flush with the substrate surface, 5mm from the gold film ends.

As the gold film thickness was about  $\sim 0.15\mu\text{m}$ , i.e. about  $1/300\text{th}$  of the average particle diameter in a substrate about  $260d_p$  thick, these are truly thin-film sensors.

The 100mm long sensor was flush mounted in the center of the 200mm long porous wall of the 0.48m diameter heat transfer cylinder, Fig. 4.1. Before insertion of a sensor, Teflon tape covered on both sides by a very thin layer of a silicon based adhesive is applied around the sensor circumference for ease of sensor replacement and to prevent by-passing of the throughflow between the sensor and the surrounding heat transfer surface.

#### 4.2.3. Calibration of the Heat Flux Sensor

The sensor and associated thermocouples were calibrated in a thermostated bath before installation. However, as the calibration was not sufficiently stable, possibly due to the complex substrate micro structure, in situ calibration was made before each run. During calibration, the sensor resistance was measured with a four decade Wheatstone bridge. The unbalanced bridge output voltage was monitored on a storage oscilloscope. The surface temperature was measured with the two calibrated thermocouples at either end of the thin gold film. After  $1/2$  to 1h to reach equilibrium under a heated air jet, the thin film temperature was taken as the average from the calibrated thermocouples, which never differed by more than  $0.25^\circ\text{C}$ . Stability of



FIGURE 4.1. Sensor in place



calibration under throughflow conditions was also checked by measuring the thin film resistance and temperature with throughflow. The maximum in-situ calibration temperature, about  $60^{\circ}\text{C}$ , which exceeds the maximum attained in the runs, was always measured at the end of the experiments to confirm calibration stability.

The following is typical of the always linear calibrations (Fig. 4.2).

$$R_s = 170.27 + 0.3178 T_s$$

#### 4.2.4. Thermophysical Properties of Substrate

The specific heat of the porous glass was determined from DSC measurements (Perkin Elmer DSC7), as described in Appendix 1.

$$C_p = 875.51 - 6.48 T_s + 7.23 \times 10^{-2} T_s^2$$

Its thermal conductivity,  $0.414\text{W/m}^{\circ}\text{C}$ , was measured using two techniques detailed in Appendix 1.

The measured bulk density,  $1447\text{kg/m}^3$ , compared with  $1600\text{kg/m}^3$  reported by the manufacturer.

### 4.3. INSTRUMENTATION FOR HEAT FLUX MEASUREMENTS

#### 4.3.1. Signal Conditioning

Sensor resistance was converted to voltage by a Wheatstone bridge with a 4-decade variable rheostat and a 7-decade multiplier ratio (J.C. Biddle Co., Cat. No. 601022). A schematic of the bridge circuit is shown in Fig. 4.3.

The stable and noise-free voltage source required by the Wheatstone bridge, designed and built by Huang[1988], has a typical reverse breakdown voltage of 1.2 volts and a maximum temperature coefficient of

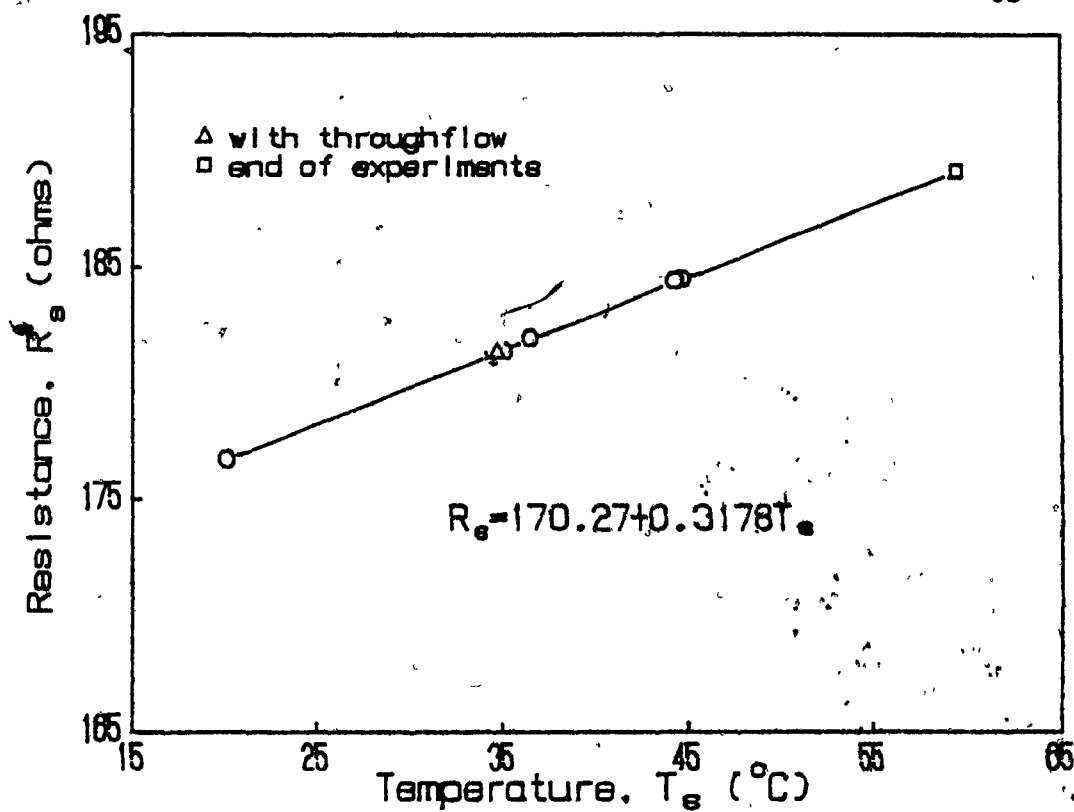


FIGURE 4.2. Sensor calibration

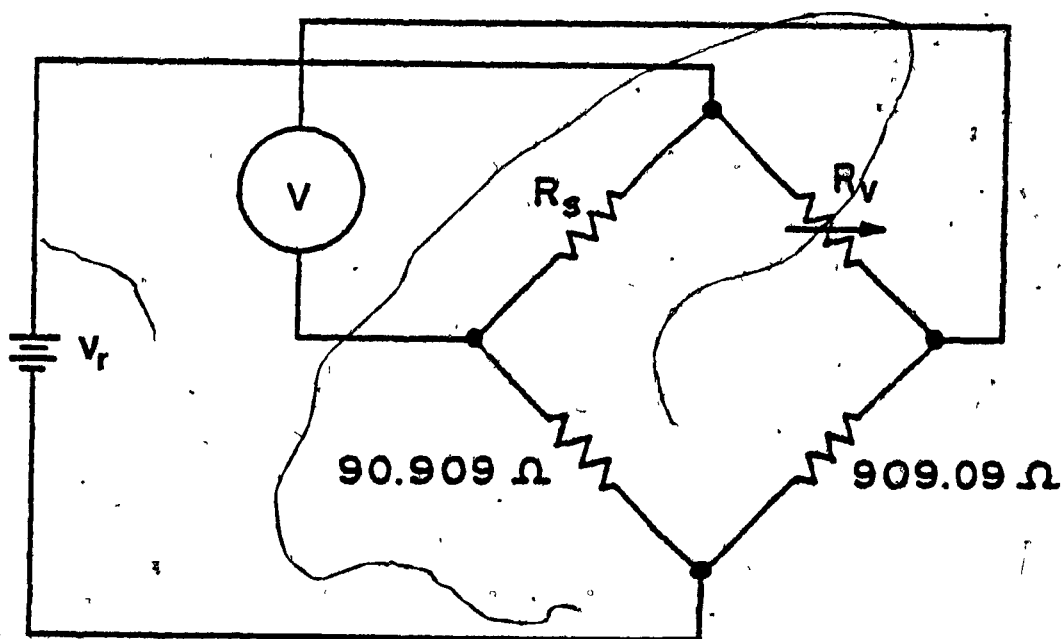


FIGURE 4.3. Schematic diagram of Wheatstone bridge circuit

0.001%/°C.

With a multiplier ratio of 1:10 and  $R_v$  set slightly higher than  $10R_s$ , the fluctuating voltage remains always positive. The sensor resistance,  $R_s$ , is related to the unbalanced bridge voltage,  $V$ , as

$$R_s = \frac{\frac{R_v}{10} (V_r + V) + 90.909 V}{V \left( \frac{R_v}{909.09} + 1 \right) + V_r} \quad (4.1)$$

with  $V_r$  the bridge voltage source, and  $R_v$  the variable bridge resistance.

Rearrangement and differentiation of Eq. 4.1 gives

$$\frac{\Delta V}{\Delta T_s} = \frac{V_r b (90.909 + R_v/10)}{\left( 1 + \frac{R_v}{909.09} \right) (R_s + 90.909)^2} \quad (4.2)$$

where  $b$  is the slope,  $dR_s/dT_s$ , of the calibration curve.

For a typical sensor temperature of 50°C,  $R_s$  is 186.2 ohms,  $R_v = 10R_s$  and from Eq. 4.2,  $\Delta V/\Delta T_s = 459 \mu V/^\circ C$ . This value is one order of magnitude larger than typical thermocouple sensitivities. Such high sensitivity, combined with a sensor response time of order of  $10^{-10}$ s, justifies the selection of a thin-film sensor to measure local values of rapidly varying, cyclical transient heat transfer.

The sensor self-heating heat flux, an undesirable characteristic, is  $52 W/m^2$  obtained from

$$q_{sm} = \frac{R_s V_r^2}{(R_s + 90.909)^2 L W} \quad (4.3)$$

where  $L$  and  $W$  are sensor length and width, 70mm and 1mm. As this value is about 5% of the lowest heat flux of the present study, that is the maximum error contributed. The self-heating flux makes the measured heat transfer slightly too high when the surface is being heated, and vice versa.

The bridge output  $V$  is amplified 2500-fold with a low noise (over the full bandwidth  $2\mu\text{V}$  RTI and  $2\text{mV}$  RT0) differential amplifier (DANA Model 2820). High frequency noise in the amplifier output is removed by a tuneable low-pass filter (Frequency Devices, Inc., Model 901F1). The low-pass frequency is selected by 3 decade switches, as well as the multiplier switch. The lower cut-off frequency was set to one half of the data acquisition sampling frequency (Nyquist criterion). The data acquisition software automatically calculates and displays this value from the desired number of points to be sampled per rotation and from the rpm of the heat transfer cylinder.

#### 4.3.2. Analog-to-Digital (A/D) Converter

The 27.5 kHz throughput A/D board (Data Translation, DT2801-A) includes a high level, 12-bit analog to digital (ADC) converter system for 16 single-ended or 8 differential analog input channels. Software selectable gains of 1, 2, 4 and 8 allow a range of input signal levels. An on-board programmable clock is included as a pacer clock. During data acquisition, signals from the sensor and the optical switch for heat transfer cylinder position are sampled by the ADC in differential mode. Depending on sensor voltage output, A/D board gains 1 or 2 are selected via the data acquisition software in addition to a gain of 2500 from the amplifier.

The minimum voltage change that can be differentiated by the ADC is 0.0012 volt ( $2^{12}=4096$ , variation from 0 to 5 volts for gain 2). A variation of 0.0012 volt corresponds to a change of sensor temperature  $0.0005^{\circ}\text{C}$ , the resolution of the heat flux sensor developed here.

#### 4.4. COMPUTATION OF INSTANTANEOUS LOCAL HEAT FLUX

##### 4.4.1. No-Throughflow Case

The transient heat conduction equation

$$\frac{1}{\alpha} \frac{\partial T}{\partial t} = \frac{\partial^2 T}{\partial x^2}, \quad (4.4)$$

where  $\alpha$  ( $=k_{eff}/\rho_s C_{P,s}$ ) and  $T$  are the thermal diffusivity and porous substrate temperature, is integrated in  $t$  and  $x$  for the control volume shown in Fig. 4.4:

$$\int_n^s \int_0^1 \frac{1}{\alpha} \frac{\partial T}{\partial t} dt dx = \int_0^1 \int_n^s \frac{\partial^2 T}{\partial x^2} dx dt \quad (4.5)$$

where '0' and '1' indicate old and new time values. By assuming an explicit behavior in time and a linear temperature variation between grids in the  $x$ -direction, the integrated equation becomes

$$(T_1^1 - T_1^0) \Delta x = \alpha \left( \frac{T_{i+1}^0 - T_1^0}{\Delta x} - \frac{T_1^0 - T_{i-1}^0}{\Delta x} \right) \Delta t. \quad (4.6)$$

The discretization equation for  $T$  is obtained by rearranging Eq. 4.6.

$$T_1^1 = \frac{\alpha \Delta t}{\Delta x^2} (T_{i+1}^0 + T_{i-1}^0) + (1 - 2 \frac{\alpha \Delta t}{\Delta x^2}) T_1^0. \quad (4.7)$$

For the numerical stability requirement that all Eq. 4.7 coefficients be positive,

$$\Delta x = (2 \alpha \Delta t)^{1/2}. \quad (4.8)$$

With this limiting condition, Eq. 4.7 becomes

$$T_1^1 = \frac{1}{2} (T_{i+1}^0 + T_{i-1}^0). \quad (4.9)$$

The instantaneous surface heat flux,  $q_s$ , calculated from Patankar's [1980] half-control volume concept, Fig. 4.4, is.

$$q_s^1 = \frac{k_{eff}}{\Delta x} (T_1^1 - T_2^0). \quad (4.10)$$

Since Eqs. 4.9 and 4.10 are explicit, a simple marching technique is used to calculate the temperature distribution in the substrate at time '1' from the previous values at time '0'. The initial and boundary conditions required for Eqs. 4.9 and 4.10 are the measured

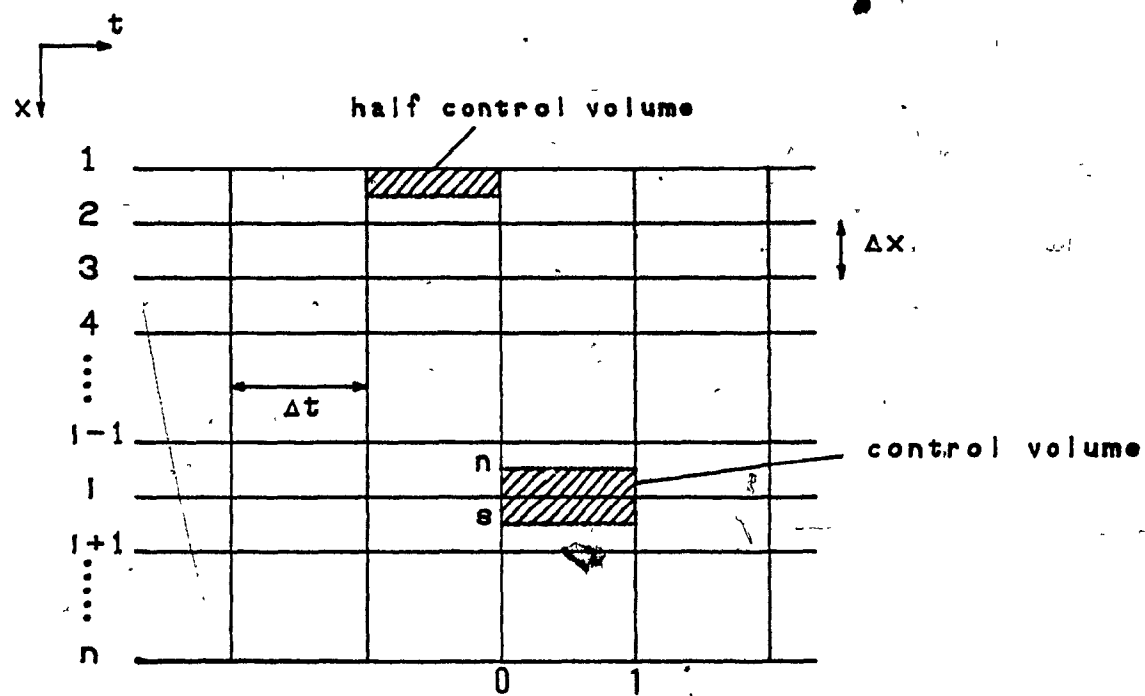


FIGURE 4.4. Control volumes

surface temperature  $T_1$  and the equality  $T_{n-1} = T_n$  because, under the condition of cyclic transient heat transfer at the sensor surface, the sensor substrate can be considered thermally semi-infinite. The latter assumption was verified by temperature measurements at that surface.

For the semi-infinite analysis, the cyclical variation of conditions at the heat transfer surface may be approximated as sinusoidal. For a sinusoidal surface temperature variation of frequency  $1/\Delta t \text{ s}^{-1}$ , the thermal penetration length, Chapman[1967], is

$$Z = -\ln(0.001)/(\pi/\Delta t \alpha)^{1/2} \quad (4.11)$$

where  $Z$  is the depth where the amplitude of the temperature fluctuation is 0.1% of that at the heat transfer surface. For even the slowest rpm used,  $Z$  from the above equation is 3mm (i.e.  $60d_p$ ), much less than the sensor substrate thickness, 13mm (i.e.  $260d_p$ ). Thus, the semi-infinite substrate assumption is justified. The number of finite difference layers ' $n$ ' is calculated as the integer value of the ratio  $Z/\Delta x$ . For about 500 samples per rotation  $n$  is 44.

The initial condition chosen for solution of Eq. 4.9 is the average cylinder temperature. The effect of this 'initial temperature disappears completely after 2 revolutions of the heat transfer cylinder. After the correct temperature distribution in the substrate is obtained, Eqs. 4.9 and 4.10 are solved consecutively to obtain local flux distribution at the heat transfer surface.

The surface temperature boundary condition for Eqs. 4.9 and 4.10 is that corresponding to the sensor resistance averaged over 50 rotations of the heat transfer cylinder.

The errors in computation of heat flux amplitude and phase shift when Eqs. 4.9 and 4.10 are used instead of the exact solution to the

unsteady heat conduction equation were estimated by D.J. Baines[1970] as

$$\text{Error in amplitude: } 1 - \left( \frac{\sin\left(\frac{2\pi \Delta t}{\Delta \tau_m}\right)}{\frac{2\pi \Delta t}{\Delta \tau_m}} \right)^{1/2} \quad (4.12a)$$

$$\text{Error in phase shift: } \frac{\pi \Delta t}{3 \Delta \tau_m} \quad (4.12b)$$

where  $\Delta \tau_m$  is the time for a complete cycle of the fastest heat flux frequency. In the present application the fastest complete cycle occurs in about 50mm of heat transfer surface as it passes under the multiple jets. As 500 measurements per rotation provides about 16 measurements over this 50mm length, the corresponding errors are very small, 1.3% in heat flux amplitude and  $3.6^\circ$  in phase shift.

#### 4.4.2. Throughflow Case

The energy equations including heat transfer between throughflow air and the substrate become:

Substrate:

$$\rho_P C_{P_s} \frac{\partial T_P}{\partial t} = k_{eff} \frac{\partial^2 T_P}{\partial x^2} - h'_p (T_P - T_a) \quad (4.13)$$

Air:

$$\rho_a C_{P_a} \frac{\partial T_a}{\partial t} = - \rho_a C_{P_a} u_a \frac{\partial T_a}{\partial x} + h'_p (T_P - T_a) \quad (4.14)$$

where

$$h'_p = h_p a$$

$h'_p$  = heat transfer coefficient for throughflow air within the substrate, per unit volume of the substrate,

$h_p$  = heat transfer coefficient for throughflow air within the substrate, per unit internal surface area of the substrate,



$a$  = internal surface area per unit volume of the substrate,  
and where subscripts 'p' and 'a' denote the 'substrate' and 'air'.

If within the substrate the local average substrate temperature equals the local air temperature, i.e.,  $T_p = T_a = T$  - by omitting energy accumulation term for air, negligible compared to that of the substrate- Eqs. 4.13 and 4.14 reduce to the single energy equation

$$\rho_p C_{ps} \frac{\partial T}{\partial t} = k_{eff} \frac{\partial^2 T}{\partial x^2} - \rho_a C_{pa} u_s \frac{\partial T}{\partial x} \quad (4.15)$$

To test whether this simplification applies,  $h_p$  was estimated from the Eq. 4.16 correlation for packed beds and porous media (Yoshida et al. [1962]).

$$J_h = 0.84 Re_p^{-0.51}, \quad 0.01 < Re_p < 50 \quad (4.16)$$

where

$$Re_p = \frac{\rho_a u_s}{a \mu} \quad \text{and} \quad J_h = \frac{h_p}{C_{pa} \rho_a u_s} Pr^{2/3}$$

For the minimum (0.09m/s) and maximum (0.5m/s) throughflow air velocities the predicted values of  $h_p$  are 215 and 500 W/m<sup>2</sup>.K.

Interfacial area,  $a$ , for the porous material used can be estimated from experiments made to check the uniformity of permeability (Section 4.4.3). Assuming laminar throughflow, the value predicted from the Kozeny-Carman relation (Carman [1956])

$$a = \left\{ \frac{\Delta P}{L_p} \frac{\epsilon^3}{5 u_s \mu (1-\epsilon)^2} \right\}^{1/2} \quad (4.17)$$

is  $a = 20000 \text{ m}^2/\text{m}^3$ . Thus the predicted values of  $h_p$  ( $= h_p a$ ) are  $4.4 \times 10^6$  and  $10.2 \times 10^6 \text{ W/m}^3 \cdot \text{K}$  for the minimum and maximum throughflow rates.

Nu distributions were calculated twice, once from Eq. 4.15, once from Eqs. 4.13 and 4.14 using the estimated  $h_p$  values with the assumption that air enters the substrate at the substrate surface temperature. These Nu distributions are completely indistinguishable, use of the simplification  $T_p = T_a = T$  in the present case is justified.

The assumption that air enters the substrate at the exterior surface temperature of the substrate is verified as follows. Considering air flow in the pores of the sensor and heat transfer cylinder to be laminar, an "adaptation time" of the fluid to the thermal boundary condition imposed by the solid may be expressed in terms of the Fourier number

$$Fo_t = 4 \frac{\alpha t}{\ell^2} \quad (4.18)$$

According to the manufacturer of the porous glass, supported by our microphotographs, mean pore size is about the same as the mean particle size,  $d_p = 50 \mu\text{m}$ . Therefore  $d_p$  is used as the characteristic length,  $\ell$ , in Eq. 4.18. For a porous cylinder mean temperature about  $50^\circ\text{C}$ ,  $\alpha$  is  $2.8 \times 10^{-5} \text{m}^2/\text{s}$ . At the maximum superficial throughflow velocity, 0.5 m/s, pore air velocity for  $\epsilon = 0.3$  is 1.7 m/s. Therefore, air travels  $ld_p$  in  $3 \times 10^{-5} \text{s}$ . The corresponding Fourier number is 1.3. At Fourier number  $> 1$ , adaptation to the new thermal boundary condition is complete. Actually adaptation may be even faster since the flow at the pore entrance may be transitional or turbulent, not laminar.

The discretized form of Eq. 4.15 is

$$T_1^1 = \left( \frac{\alpha \Delta t}{\Delta x^2} + \frac{\rho_a u_s C_{Pa}}{\rho_P C_{Ps}} \frac{\Delta t}{\Delta x} \right) T_{1-1}^0 + \left( \frac{\alpha \Delta t}{\Delta x^2} \right) T_{1+1}^0 + \left( 1 - 2 \frac{\alpha \Delta t}{\Delta x^2} - \frac{\rho_a u_s C_{Pa}}{\rho_P C_{Ps}} \frac{\Delta t}{\Delta x} \right) T_1^0 \quad (4.19)$$

For numerical stability, the coefficient of  $T_1^0$  was set equal to zero, which specifies the relation between  $\Delta x$  and  $\Delta t$  as

$$\Delta x_{1,2} = \frac{C \Delta t \pm ((C \Delta t)^2 + 8 \alpha \Delta t)^{1/2}}{2}$$

where

$$C = \frac{\rho_a u_s C_{Pa}}{\rho_P C_{Ps}}$$

Thus the finite difference equation with throughflow is

$$T_i^1 = \left( \frac{\alpha \Delta t}{\Delta x^2} + \frac{\rho_s u_s C_{Pa}}{\rho_P C_{Ps}} \frac{\Delta t}{\Delta x} \right) T_{i-1} + \left( \frac{\alpha \Delta t}{\Delta x^2} \right) T_{i+1} \quad (4.20)$$

which, for  $u_s=0$ , reduces to the no-throughflow equation.

After obtaining  $q_s^1$  from Eq. 4.10, the local heat transfer coefficient at the impingement surface

$$h = \frac{q_s^0}{T_j - T_s} \quad (4.21)$$

for the nozzle exit temperature,  $T_j$ , of the heating or cooling jet leads finally to the corresponding Nusselt number

#### 4.4.3 Uniformity of Throughflow Velocity

Eq 4.20 assumes uniformity of throughflow velocity. This assumption depends on the degree of uniformity of permeability and of local pressure over the heat transfer surface. Uniformity of permeability was checked by measuring throughflow rate and pressure drop across the cylindrical surface with various fractions of the surface blocked to throughflow by plastic sheets. The linear relation for the results, Fig 4.5, indicates that the permeability of the porous cylinder is reasonably uniform. These results, for which the maximum throughflow velocity is almost twice the maximum in heat transfer experiments, serve additionally to indicate no leaks into the throughflow exhaust (suction) line.

The variation of throughflow velocity due to local static pressure variation under impinging jets would be maximum for the combination: highest jet Reynolds number - minimum throughflow rate, the case shown in Fig 4.6.  $\Delta P_{max}$  for the multiple jets with  $Re_{c,j}=28500$ ,  $Mu_s=0.0022$  is twice the average value, while for the single jet with  $Re_{h,j}=69000$ ,  $Mu_s=0.0018$ , there is about 70% variation of local static pressure from the average. At the same minimum suction pressure, but with more

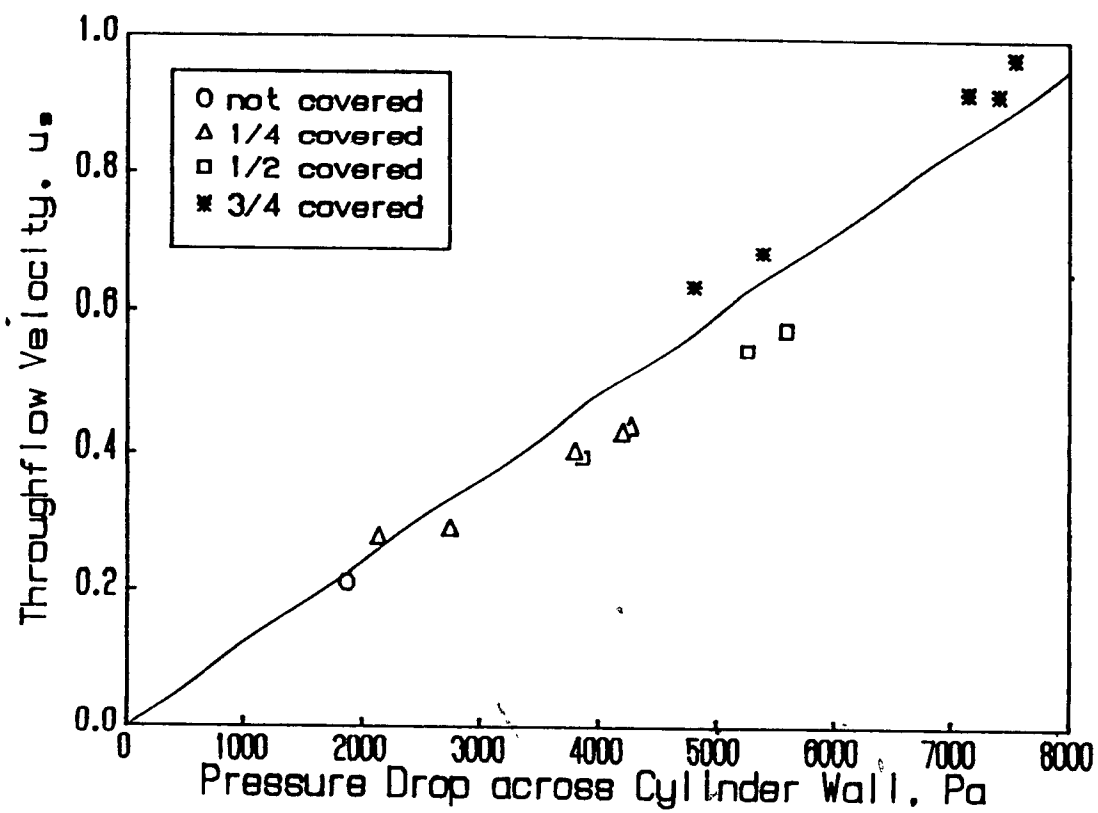


FIGURE 4.5. Uniformity of permeability of porous impingement cylinder

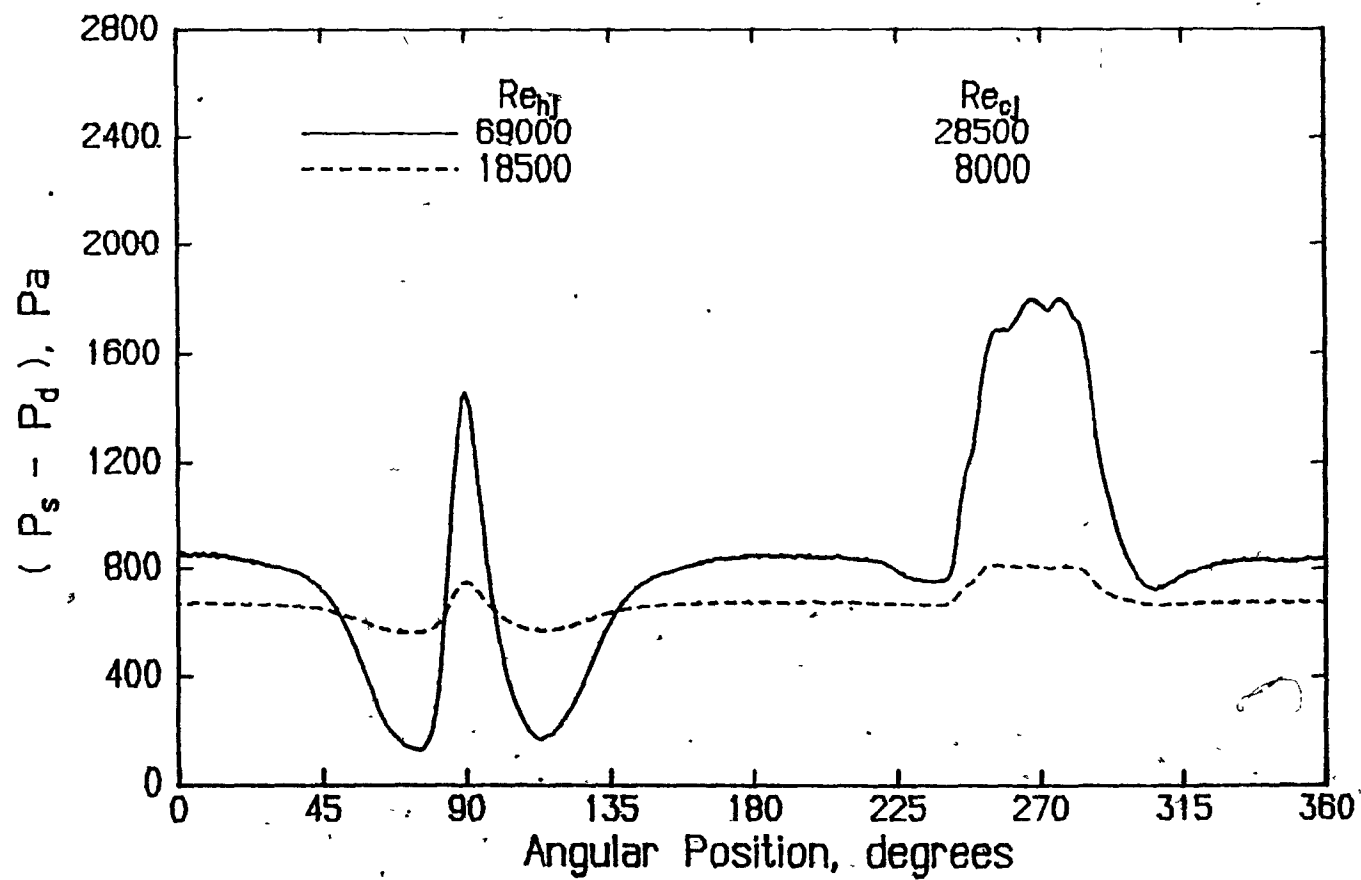


FIGURE 4.6. Static pressure variation under the jets

typical values of jet Reynolds number, Fig. 4.6 indicates that the maximum variation in local throughflow is about  $\pm 13\%$ . Therefore, except for the worst case combinations of  $Re_j$  and  $Mu_s$ , local throughflow rate variation would be less than a few percent.

#### 4.4.4 Display of Nusselt Number Distributions

The data acquisition/data reduction program is equipped with plotting routines which allow on line screen display of profiles of local values of surface temperature, heat transfer rate and Nusselt number as a function of position on the heat transfer cylinder and, as well, the history of average surface temperature over 50 rotations. The last option is useful for detecting any dramatic changes in surface temperature during data acquisition which could affect accuracy of results. For the single jet side, the first and last  $12.5^\circ$  ( $2.7w$ ) of each  $180^\circ$  ( $75w$ ) half cylinder impingement surface are omitted from local Nusselt number plots as conditions in those sections are affected by proximity to the skimmer plates. The abscissa scale is given as  $y/w$ , the nondimensional distance from the stagnation point for the single jet, the nondimensional distance from the stagnation point of the middle jet for the multiple jets.

#### 4.5. POROUS SENSOR AS A HEAT FLUX MEASURING INSTRUMENT

With a heat flux sensor for a throughflow heat transfer surface, fabrication of a thin-film surface thermometry sensor by deposition of a gold film on the surface of a porous substrate is accompanied unavoidably by some gold deposition on substrate particles below the exterior surface layer. Examination under a microscope revealed areas

of gold film at as much as three particle diameters below the surface. However the great difficulty, noted earlier, in obtaining an electrically continuous gold film should be recalled. Thus even at the exterior surface of the substrate, where the surface of the particles is completely accessible during gold deposition, achieving a thin film without a discontinuity over the 70mm ( $1400d_p$ ) length of the sensor filament is extremely difficult. It is therefore highly improbable that a continuous gold film could form in the interior of the substrate where particles are shielded from gold deposition by the layer of particles at the exterior surface. Such regions of gold film below the surface, electrically isolated in the lateral direction, would have negligible effect on the resistance of the filament at the sensor surface and hence on the value of heat flux at the surface obtained with this thin-film sensor.

It is, moreover, possible to determine the sensitivity of Nu profiles to any such averaging effect of gold film over more than the surface layer of substrate particles. Thus a Nu profile may be recalculated taking the sensor temperature as the average of the surface temperature as normally determined and the temperature at one grid node ( $\sim 1d_p$ ) below the surface. A Nusselt number profile as normally determined and for the hypothesis of "averaged" surface temperatures are compared in Fig. 4.7. This hypothesis represents an extreme case as it assumes that the gold film is distributed uniformly on the first and second layers of particles. As the effect of averaging seen in Fig. 4.7 is not large for even this extreme case, this test confirms that the effect of having some areas of gold film below the surface layer of substrate particles is indeed insignificant.

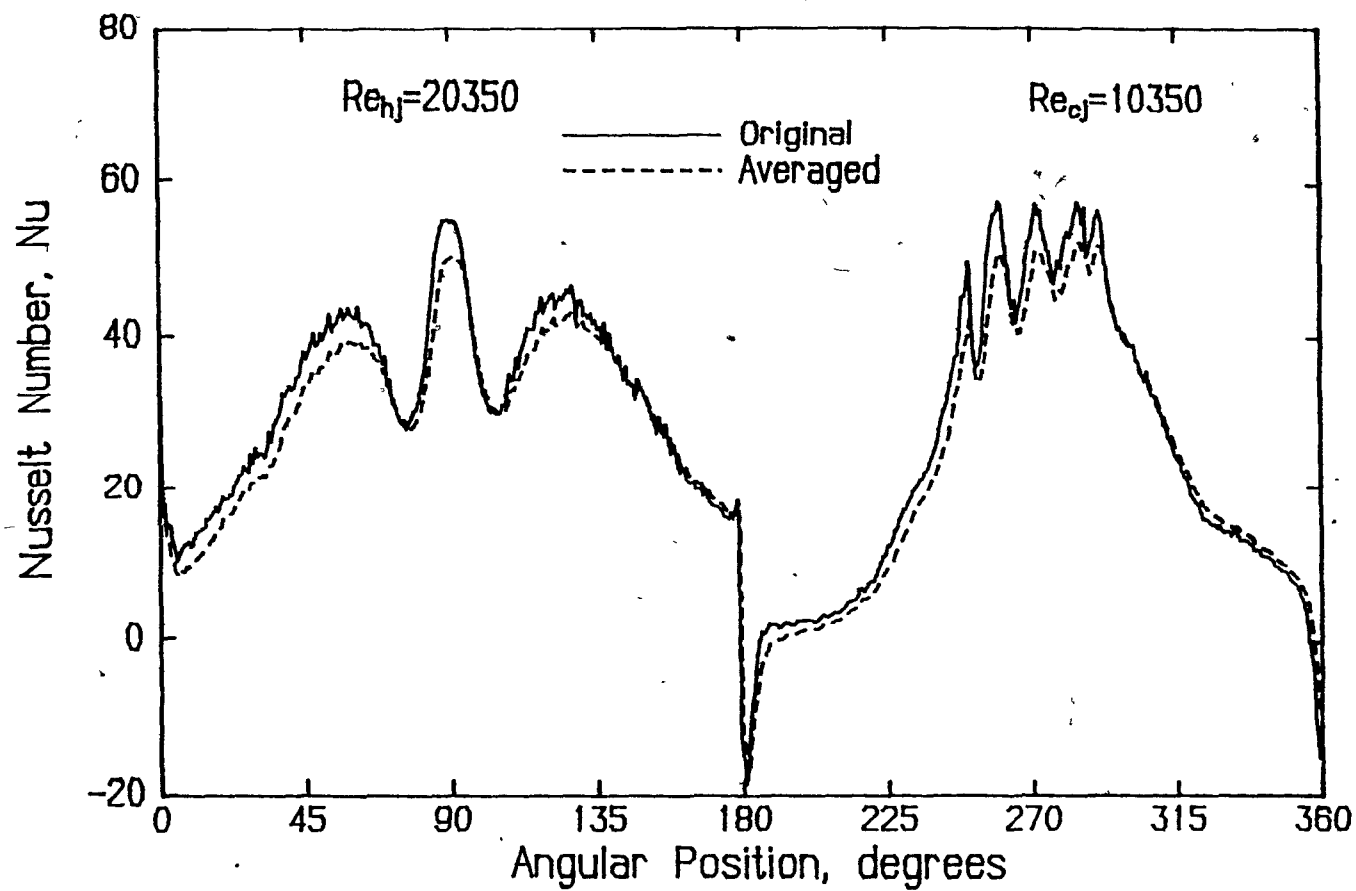


FIGURE 4.7. Comparison of a normally determined  $Nu$  profile with that obtained using an averaged surface temperature



#### 4.6 VALIDATION OF THE HEAT FLUX SENSOR

Any heat flux sensor of a new type and with novel capabilities requires validation. One feature sought for the sensor developed in the present study was that it should have fast response characteristics in order to be capable of measuring rapidly changing transient heat flux. This capability could be tested by subjecting the sensor to validation tests under slot jets of air impinging on a moving surface, using an experimental facility described in Chapter 3. The results of such a sensor test program are now presented.

A basic test is to establish that a new sensor produces heat transfer coefficients which are independent of temperature difference. This test was made by varying the temperature difference for impingement heat transfer,  $T_j - T_s$ , by a factor of 2.7:1 for a single slot jet, and by a factor of 2:1 for multiple slot jets. The results of these tests, expressed as Nusselt number averaged over 16 slot widths for the single jet, Fig. 4.8, and as average Nusselt number for the multiple jets, Fig. 4.9, confirm that this heat flux sensor provides Nusselt number data which are independent of the temperature driving force.

A second validation test was to compare published results with local profiles of impinging jet transient heat transfer obtained with the new sensor. Two reference studies were used. Cadek[1968] used a thin-disk heat flux sensor, known as a Gardon foil. His sensor, of diameter 0.9mm, gave a resolution of 0.28 of the slot jet nozzle width for the profiles of local Nusselt number at a stationary impingement surface. Due to the difficulty of accurate calibration of the Gardon

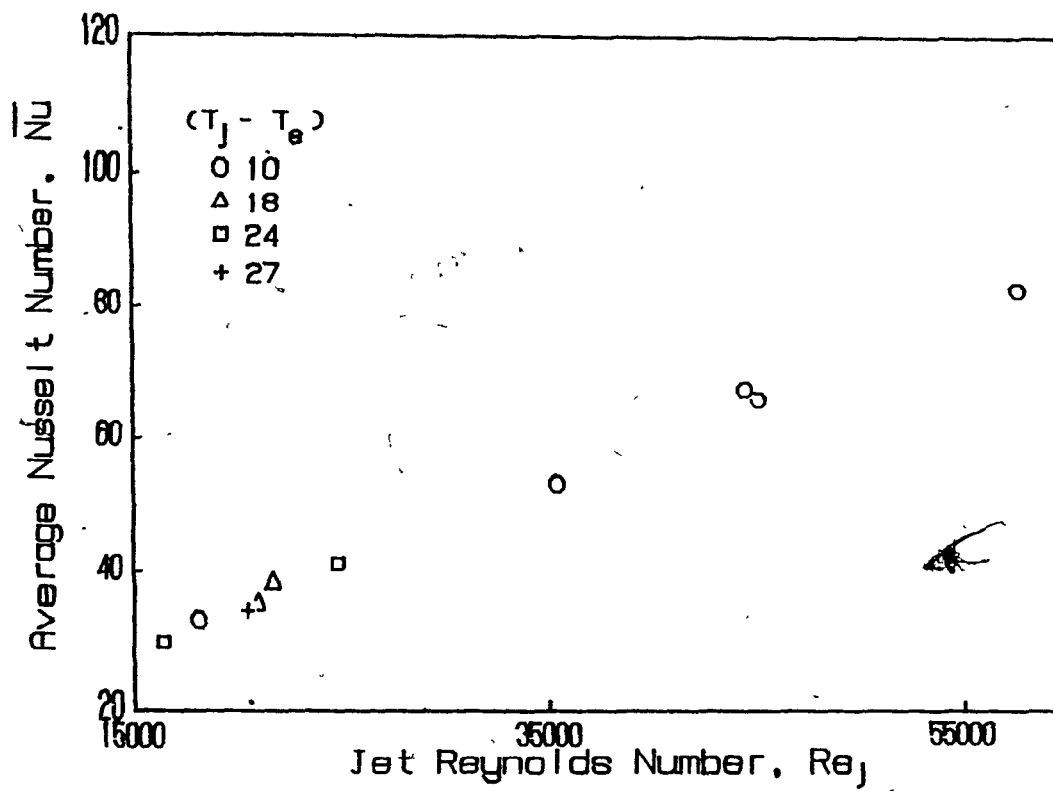


FIGURE 4.8. Independence of Nusselt number from  $\Delta T$ : single jet test

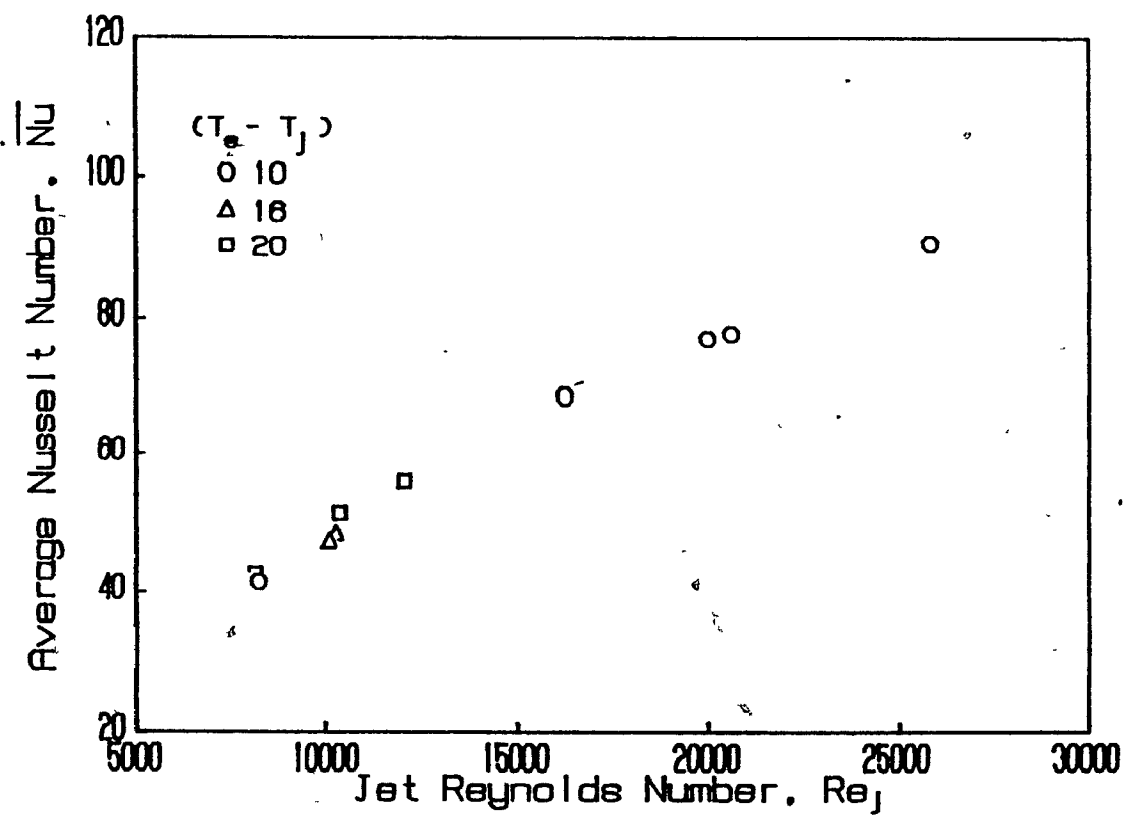


FIGURE 4.9. Independence of Nusselt number from  $\Delta T$ : multiple jet test

foil, Cadek used it to measure heat transfer profiles relative to the stagnation heat transfer. The impermeable thin-film heat flux sensor of van Heiningen, Douglas and Mujumdar[1985], described earlier, differs basically from the new sensor of the present study, which is porous. Their sensor, proven to be very sensitive and fast responding, could be calibrated to give profiles of heat transfer of higher resolution and accuracy with a moving impingement surface than those of Cadek with a stationary surface.

The profiles of local Nusselt number under a single impinging slot jet obtained with the new type of sensor, shown in Figs. 4.10 and 4.11 are for conditions of jet Reynolds number,  $Re_j$ , and nozzle-to-impingement surface spacing,  $H/w$ , matching as closely as possible those of the two best reference studies available. In order to bring all results to a common Reynolds number, Cadek's results were adjusted for this effect using standard procedures, as detailed in Chapter 5. For these test conditions the Nusselt number under highly turbulent jets reflect complex flow phenomena at the impingement surface. The central peak corresponds to a thin but a laminar boundary layer, while the secondary maxima correspond to completion of transition to turbulent boundary layer.

In the region of the central peak the heat transfer measured by the new sensor agrees with the reference studies at the lower  $Re_j$ , Fig. 4.10, but is somewhat higher at the higher  $Re_j$ , Fig. 4.11. In the latter case, stagnation region heat transfer for a high stagnation pressure is enhanced with a porous sensor due to transient local throughflow. This small difference is of no practical significance because a porous sensor is not needed for studies at an impermeable

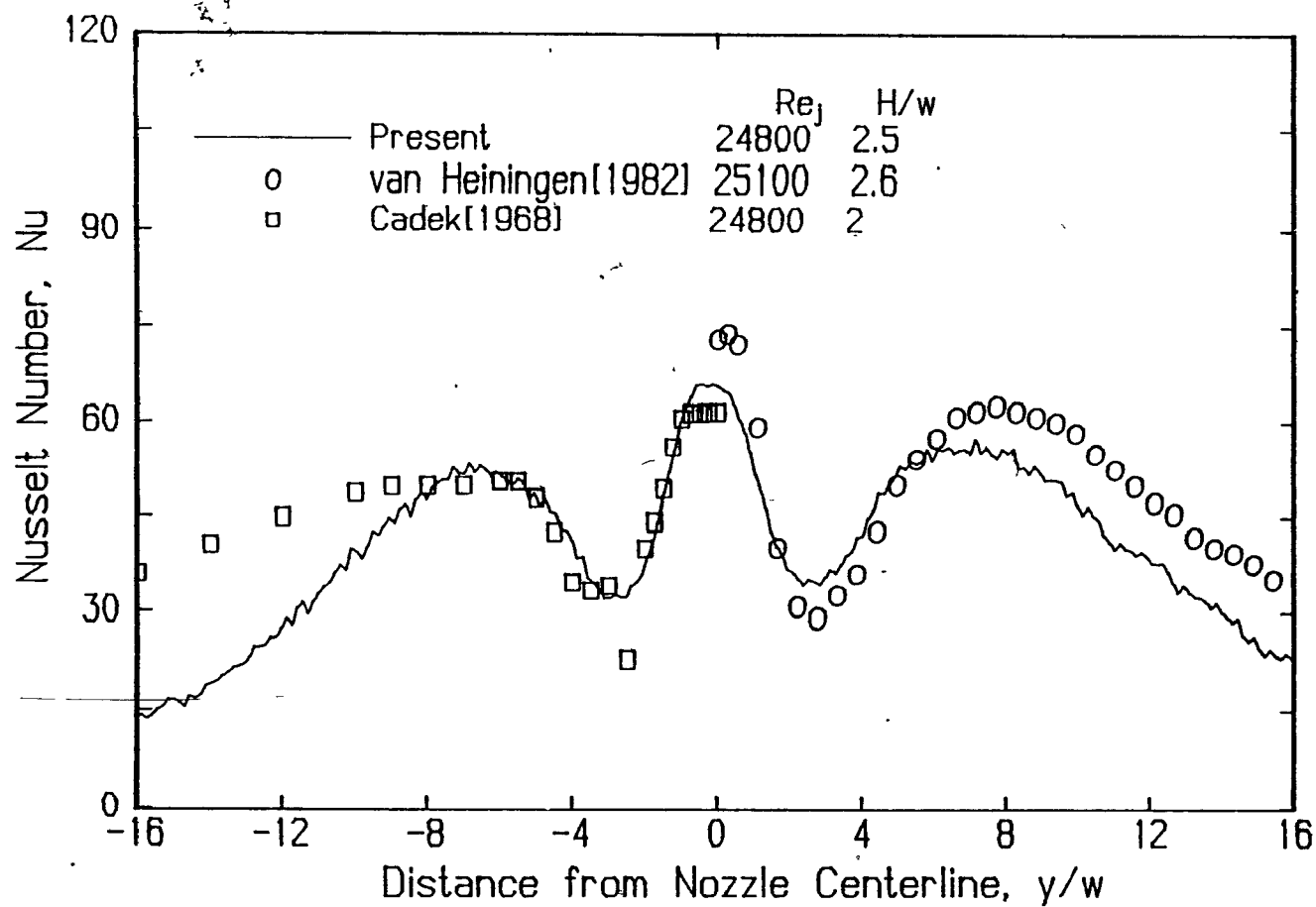


FIGURE 4.10. Comparison of results: profiles of local Nu for a slot jet at  $Re_j = 24800$

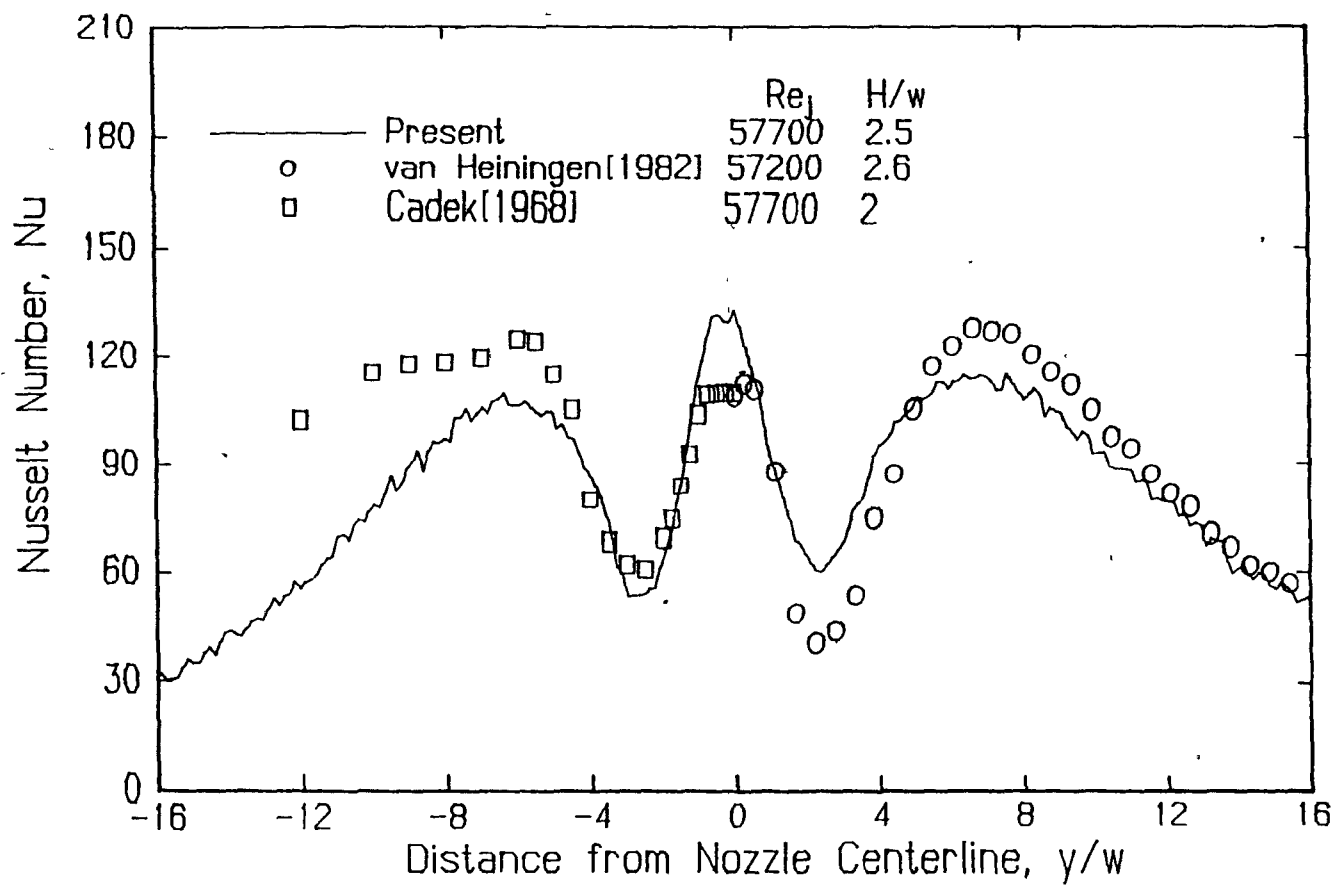


FIGURE 4.11 Comparison of results: profiles of local Nu for a slot jet at  $Re_j=57700$

heat transfer surface.

The design features necessary to obtain a porous sensor applicable for throughflow at a heat transfer surface result in a sensor with slightly less resolution than the previous impermeable sensors, that of Cadek[1968] for a stationary surface, and that of van Heiningen et al.[1985] for a moving surface. Thus the new sensor slightly overestimates the Nusselt number at the off-stagnation minimum and correspondingly underestimates the off-stagnation maximum. As these specific Nu values are not much interest, and as these effects tend to cancel, the new sensor provides sufficiently precise resolution of this heat transfer profile.

The third type of validation was to test the aspects of high sensitivity and fast response of the new sensor by monitoring heat transfer at an impingement surface moving rapidly under an impinging jet. The only heat flux sensor with this capability for impermeable heat transfer surface is that of van Heiningen et al.[1985]. Their single jet results with this sensor showed that Nu profiles are depressed on the side where surface motion is towards the jet nozzle but are enhanced on the leaving side. The Nu profiles at a rapidly moving impingement surface obtained with the porous sensor developed in the present study are essentially identical with their profiles for comparable conditions. A particularly sensitive characteristic of such Nu profiles is the extent of shift in position of the off-stagnation maxima in the direction of the heat transfer surface motion. Thus Fig. 4.12 compares the shift in position of the off-stagnation maxima on the approaching and leaving side of the slot jet nozzle as determined with the new sensor with the shifts established by van Heiningen[1982] with

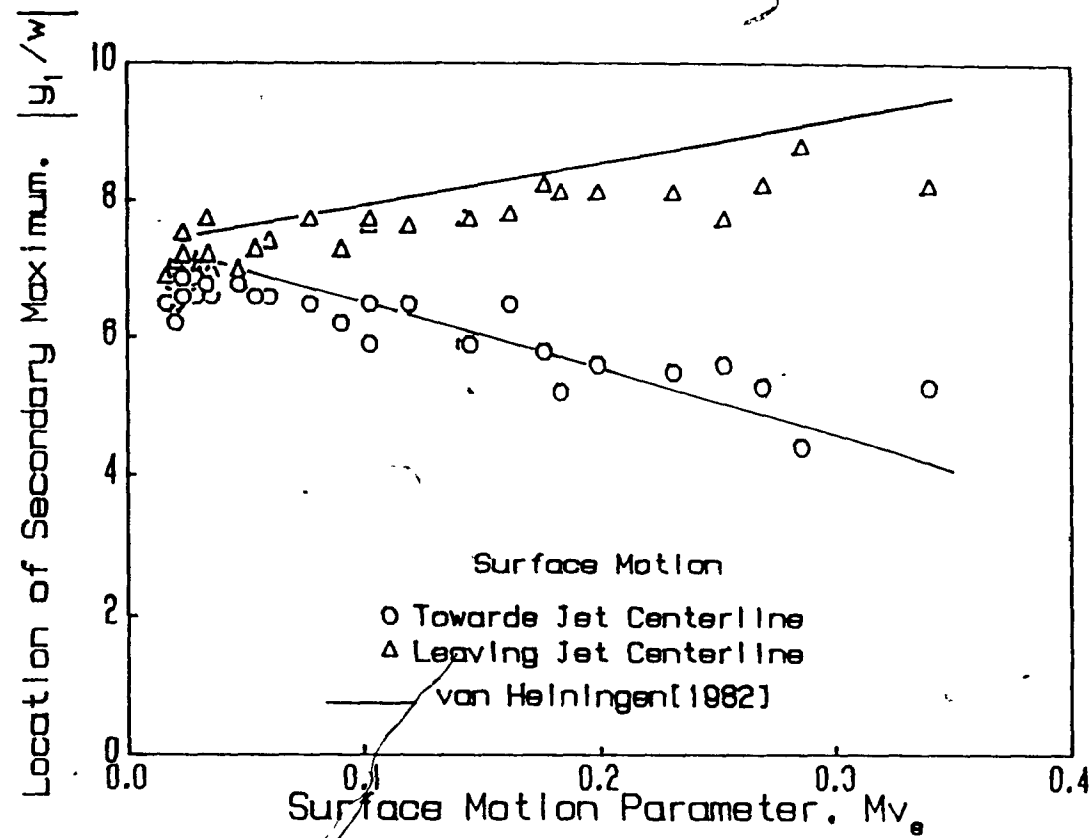


FIGURE 4 12. Comparison of results. effect of  $Mv_s$  on position of off-stagnation maxima



an impermeable sensor. Heat transfer surface motion is characterized by the nondimensional parameter,  $Mv_s$ , described by van Heiningen et al [1985], with  $Mv_s=0$  for a stationary surface. The good agreement for this sensitive feature of Nusselt number profiles for a jet impinging on rapidly moving surface provides further validation that the permeable heat flux sensor developed in the present study has excellent sensitivity and fast response characteristics for measuring rapidly changing transient heat transfer.

The three types of tests described above complete the validation of the new type of sensor. It is not possible to validate directly the unique feature of this permeable sensor, its ability to measure rapidly changing heat flux when there is throughflow at the heat transfer surface, because no previous sensor had this capability. On Fig. 4.13 is displayed a sample set of profiles of transient local Nusselt number under an impinging slot jet for a range of rates of throughflow at the heat transfer surface. Throughflow rate is characterized by the nondimensional parameter,  $Mu_s$ , discussed in Chapter 5. The maximum value of the throughflow parameter,  $Mu_s=0.0163$ , for the results of Fig. 4.13 corresponds to 52% of the nozzle exit flow leaving the system as throughflow for a heat transfer surface extent of  $\pm 16$  nozzle widths from the nozzle centerline. A detailed discussion of these results, which is beyond the scope of this chapter, appears in Chapter 5. The enhancement of local heat flux by throughflow for jets impinging on a moving heat transfer surface is thus documented for the first time with the porous, thin-film heat flux sensor developed in the present study.

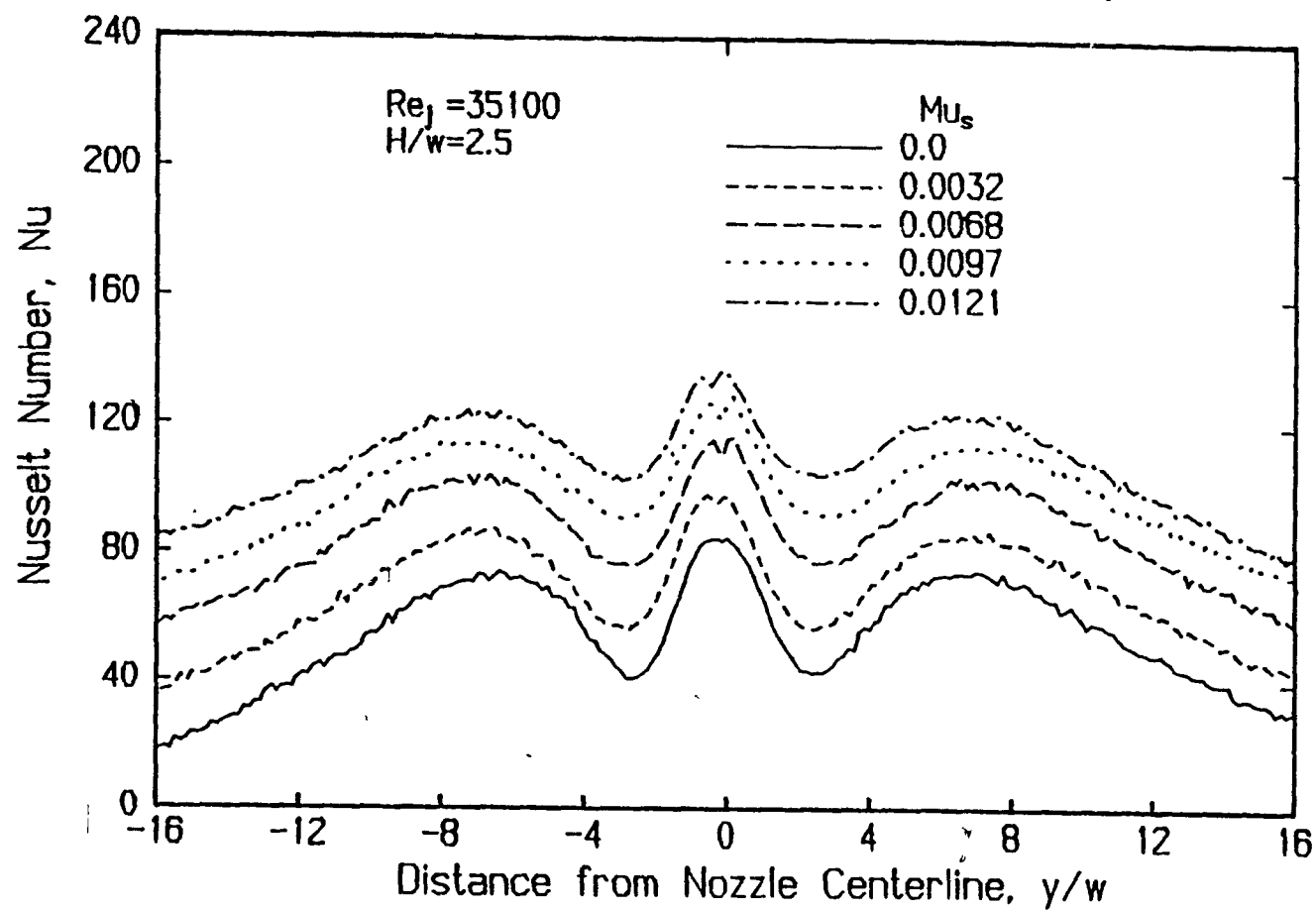


FIGURE 4.13. Effect of throughflow on transient local Nusselt number

## 4.7 SUMMARY

A permeable, high sensitivity, fast responding thin-film heat flux sensor was developed which has made it possible to measure rapidly changing heat flux at a surface with or without throughflow at the heat transfer surface. This sensor and the associated measurement system was shown to produce accurate and reliable results for a specific case, one where rapidly changing heat flux is due to jets impinging on a moving surface with throughflow. However, this new type of heat flux sensor is not restricted to this particular case but is of general applicability for the measurement of rapidly changing heat flux at permeable surfaces at which there may be throughflow.

The present study is unique in the sense that this is the first and only study today whereby local impingement heat transfer profiles have been measured at a moving surface with throughflow, a problem with great industrial relevance.

## CHAPTER 5

HEAT TRANSFER UNDER A CONFINED SLOT JET IMPINGING ON A MOVING  
SURFACE WITH THROUGHFLOW

## 5.1 INTRODUCTION

Local and average heat transfer were measured for a confined turbulent slot jet impinging on a permeable moving surface, with and without throughflow at the impingement surface. Local Nusselt number was obtained using the unique porous sensor, Chapter 4, designed for measurement of instantaneous local heat flux at a permeable surface at which there may be throughflow and which is subject to rapidly and widely varying heat transfer. The sensor was mounted in the wall of a rotating heat transfer cylinder of material identical to the sensor porous substrate. Because of the industrial importance of impinging jet flows which are confined, the impingement flows on the external surface were confined by a concentric cylindrical hood. A detailed description of this experimental facility, the SIMTEST III apparatus, is given in Chapter 3. The ranges of parameters are given in Table 5.1.

This study, a continuation of a series in the same laboratory, relates particularly to two previous investigations. Saad[1981] provided the first measurement of slot jets impinging on a permeable, stationary heat transfer surface with throughflow at the impingement surface. Van Heiningen, Douglas and Mujumdar[1985] developed the first sensor with which local heat transfer can be measured at an impermeable impingement surface moving rapidly under a single slot jet. However, a case of industrial importance is confined impinging jet heat transfer at a moving permeable surface with throughflow at the

Table 5.1. Range of parameters

$w$ (mm)	20
$H/w$	2.5
$T_j - T_s$ ( $^{\circ}C$ )	9.3-27.3
$Re_j$	16400-57700
$u_j$ (m/s)	17.5-50.4
$u_s$ (m/s)	0-0.4
$v_s$ (m/s)	0.45-9

surface. Measurement of heat transfer for this case was then the objective of the present study. Relative to the investigation of Saad, the present study adds the major complication of the impingement heat transfer surface being in rapid motion. Relative to that of van Heiningen et al., the new aspect is measurement of transient heat transfer for an impingement surface at which there is throughflow.

While the unique feature of the new technique is its applicability with throughflow, key dimensions of the experimental facility were chosen to facilitate validation of this technique with data previously published for the limiting case without throughflow. For this reason the dimensions  $w=20\text{mm}$ ,  $H=50\text{mm}$ , were selected to provide a nondimensional nozzle-to-surface spacing,  $H/w$ , of 2.5. This spacing closely matches one value used by van Heiningen[1982] in the SIMTEST I apparatus in the only other study of transient local heat transfer under an impinging slot jet.

Experiments are presented in Section 5.2 for the base case of heat transfer without either throughflow or impingement surface motion effects. In Section 5.3 measurements are given for heat transfer at an impingement surface with throughflow, but without surface motion effects. Section 5.4 provides the unique results, i.e. local instantaneous heat transfer for an impingement surface, with throughflow, moving rapidly under a slot jet.

## 5.2. HEAT TRANSFER WITHOUT THROUGHFLOW OR IMPINGEMENT SURFACE

### MOTION EFFECTS

These local and average heat transfer results, summarized in Table 5.2, were obtained without throughflow and at a speed of rotation of the impingement cylinder sufficiently low as to make the effect of surface motion negligible. Thus the mass velocity ratio,  $Mv_s = v_s \rho_s / u_j \rho_j$ , which characterizes the effect of surface motion, was kept less than 0.05, a value below which heat transfer does not differ significantly from that for a stationary impingement surface. Comparison of these results with equivalent data for impermeable stationary or nearly stationary impingement surfaces provides one validation of the present experimental procedures.

#### 5.2.1 Local Heat Transfer

Lateral profiles of local heat transfer at five values of  $Re_j$  are superimposed on Fig. 5.1. The slight asymmetry of the profiles shows that, though negligible, surface motion effect is not entirely eliminated even at these low surface velocities ( $<0.6\text{m/s}$ ). This slight profile asymmetry derives from the fact that on the approach side, i.e.

Table 5.2. Operating conditions and results for single jet heat transfer without throughflow or impingement surface motion effects.

$Re_j$	$Mv_s$	$T_j$	$T_j - T_s$	$Nu_o$	$\overline{Nu}_{min}$	$\overline{Nu}_{max}^*$	$\frac{S}{W}$ for $Nu$				
							8	10	12	14	16
16400	0.034	82.4	23.9	52.4	34.9	36.1	36.1	35.8	34.4	32.4	30.3
18100	0.033	59.3	12.0	57.7	38.0	39.6	39.5	39.4	38.0	35.8	33.5
20400	0.035	86.2	27.3	55.2	38.1	40.1	40.0	40.0	38.7	37.0	34.8
20900	0.047	70.2	19.9	58.4	39.9	42.1	42.0	41.9	40.4	38.3	35.6
21600	0.029	64.4	18.4	62.0	42.4	45.0	44.8	44.8	43.3	40.9	38.4
24800	0.023	79.1	22.2	65.6	44.9	48.3	48.1	48.0	46.2	43.8	41.0
35400	0.029	57.8	12.3	82.3	55.8	62.1	61.7	61.8	59.8	56.8	53.3
35400	0.020	57.8	12.4	84.9	57.9	64.3	63.8	63.8	61.6	58.5	54.8
44400	0.023	54.8	10.1	106.6	69.4	78.0	77.4	77.8	75.3	71.5	67.3
45100	0.020	52.2	12.6	103.0	68.1	76.3	75.9	75.9	73.4	69.8	65.7
57700	0.016	43.9	9.3	132.1	83.7	95.2	94.6	94.7	91.6	87.2	82.0

\*  $\overline{Nu}_{max}$  indicates off-stagnation maximum

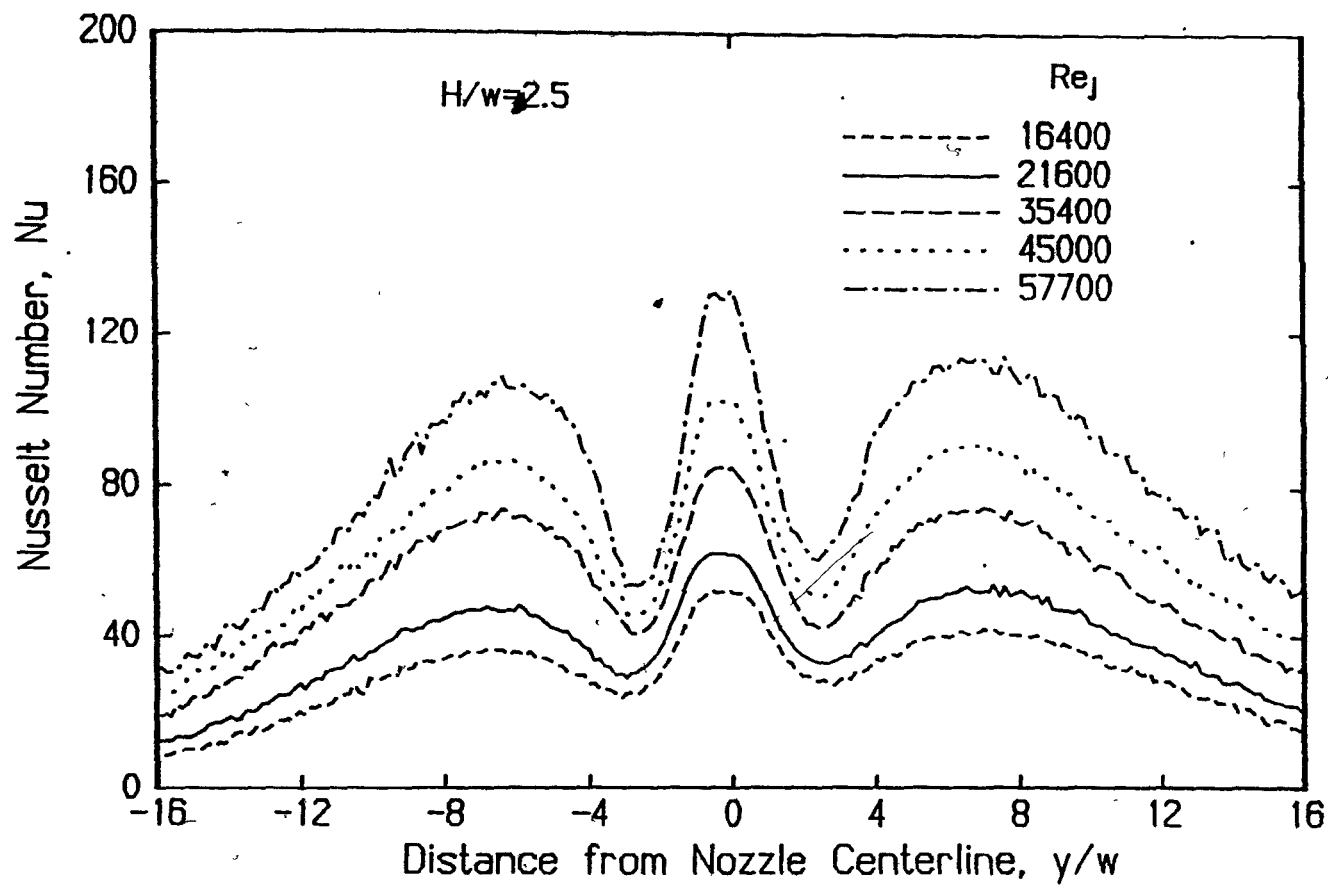


FIGURE 5.1. Effect of Reynolds number on profiles of local Nusselt number



where surface motion is towards the nozzle centerline (always the left-hand side of the profiles), a layer of cooler air is dragged by the moving surface towards the heating jet zone. This surface layer of lower temperature air reduces the local heat transfer rate by decreasing the effective local  $\Delta T$  in the wall jet region on the approach side. This effect is enhanced near the pair of skimmer plates, located at  $18.7w$  on either side of the nozzle centerline, because of the small gap which must be left between these skimmer plates and the impingement surface. Within the central region of prime importance for heat transfer, up to  $8w$  from the nozzle centerline, the profiles are satisfactorily symmetrical, within 10%. Van Heiningen[1982] observed about the same degree of profile asymmetry with the SIMTEST I Apparatus.

Principal features of the five curves in Fig. 5.1 are the occurrence of off-stagnation minima and maxima at the lateral locations of about  $\pm 2.6w$  and  $\pm 7w$  from the stagnation line. Previous investigators have identified the off-stagnation minima and maxima as reflecting, respectively, the onset and the completion of transition from a laminar to turbulent boundary layer. The minima in  $Nu$  profiles reflect the end of the growth of a purely laminar boundary layer from its minimum thickness at the stagnation point. The increase in heat transfer in the region  $2.6 < y/w < 7$  is due to the enhanced transport characteristics of a boundary layer in transition to turbulence. Beyond the off-stagnation maxima,  $Nu$  profiles decline again with growth of the turbulent boundary layer..

Key parameters of several comparable studies are given in Table 5.3. For about the same  $H/w$  spacing, van Heiningen[1982] reported that

the transition point minimum moved slightly inward, from about  $2.9w$  at  $Re_j \approx 10000$  to  $2.3w$  at  $Re_j \approx 91500$ . He also observed a similar slight movement in location of the secondary maximum over the  $Re_j$  range 30000-91500. Present minima and maxima locations,  $\sim 2.6w$  and  $\sim 7w$  agree closely with the values reported by both van Heiningen[1982] and, for  $H/w=2$ , by Cadek[1968] (see Figs. 4.10 and 4.11).

In the comparisons of local heat transfer profiles at  $Re_j=24800$  and 57700, Figs. 4.10 and 4.11, the measurements of van Heiningen[1982] are for  $H=2.6w$  and  $Re_j$  of 25100 and 57200, i.e. for conditions sufficiently close to those of the present study to permit direct comparison. Cadek[1968] made measurements for nozzle-to-surface spacings,  $H/w$ , of 2 and 4, for Reynolds numbers of 20750 and 52300. As the small difference in spacing between  $2w$  and  $2.5w$  corresponds to very little effect on  $Nu$ , Cadek's profiles at  $2w$  are used for comparison. Because the Reynolds number differences correspond to appreciable differences in  $Nu$ , Cadek's profiles were therefore corrected to the same  $Re_j$  using his relations for dependence of local Nusselt number, i.e. proportional to  $Re_j^{0.5}$  and  $Re_j^{0.86}$  in the stagnation ( $y/w < 2.5$ ) and wall jet regions ( $y/w > 2.5$ ) respectively. In spite of some differences in geometry, Table 5.3, generally good agreement exists between the profiles of local  $Nu$ , Figs. 4.10 and 4.11, for these three studies. Some gold penetration into the permeable sensor of the present study, discussed in Chapter 4, produces an averaging effect resulting in the minima and off-stagnation maxima being not quite as pronounced as those obtained with the impermeable sensor of van Heiningen et al.[1985]. Comparison with Cadek's data in the far wall jet region is inappropriate as his jets were not fully confined and impinged on a flat surface. Both

Table 5.3. Geometrical parameters of comparative studies

	Present	Cadek[1968]	van Heiningen[1982]		Saad[1981]		
w (mm)	20 .	8.2	14.2	6.2	3.3	10	13.3
H/w	2.5	2 0	2.6	6.0	4	4	4
Surface	cylindrical	flat	cylindrical		flat		
D <sub>e</sub> /w	24	-	34	77	-		
Nozzle type	ECE*	ECE*	ECE*		ECE*		
Confinement	yes	partially	yes		yes		

\* Elliptically Contoured Entry

confinement and surface curvature affect wall jet spreading and thereby the heat transfer. In any case, the far wall jet region is of negligible practical importance.

Based on laminar boundary layer theory, stagnation region heat transfer is

$$Nu_o = C (Re_j)^{1/2} \quad (5.1)$$

where  $C$  is expected to be a function of  $H/w$  and nozzle exit flow conditions but not  $Re_j$ . The moderate increase of  $Nu_o/(Re_j)^{1/2}$  with  $Re_j$  in the present study, Fig. 5.2, is attributed to enhancement of heat transfer by a small transient throughflow of impingement air into the porous sensor, proportional to the stagnation pressure of the jet. However the average value,  $C=0.445$ , compares well with the values 0.455 by van Heiningen[1982] and 0.428 obtained by interpolation of Cadek's results at  $H/w$  of 2 and 4 in the appropriate  $Re_j$  range. The slight increase in  $C$  with  $Re_j$  recorded by Cadek was probably due to some Reynolds number dependence of his upstream flow conditions.

The difference between these experimental values of  $C$  and the theoretical value of 0.31 computed by Miyazaki and Silberman[1972] for a two-dimensional laminar impinging jet is attributed to the jets being turbulent, not laminar, at the nozzle exit. As Gardon and Akfirat [1965] and Saad[1981] demonstrated, nozzle exit turbulence enhances stagnation point heat transfer appreciably for  $H/w$  less than 8.

### 5.2.2 Average Heat Transfer

Local heat transfer rates provide a sensitive indication of the basic mechanisms of boundary layer phenomena, but for industrial application it is heat transfer averaged over the impingement surface

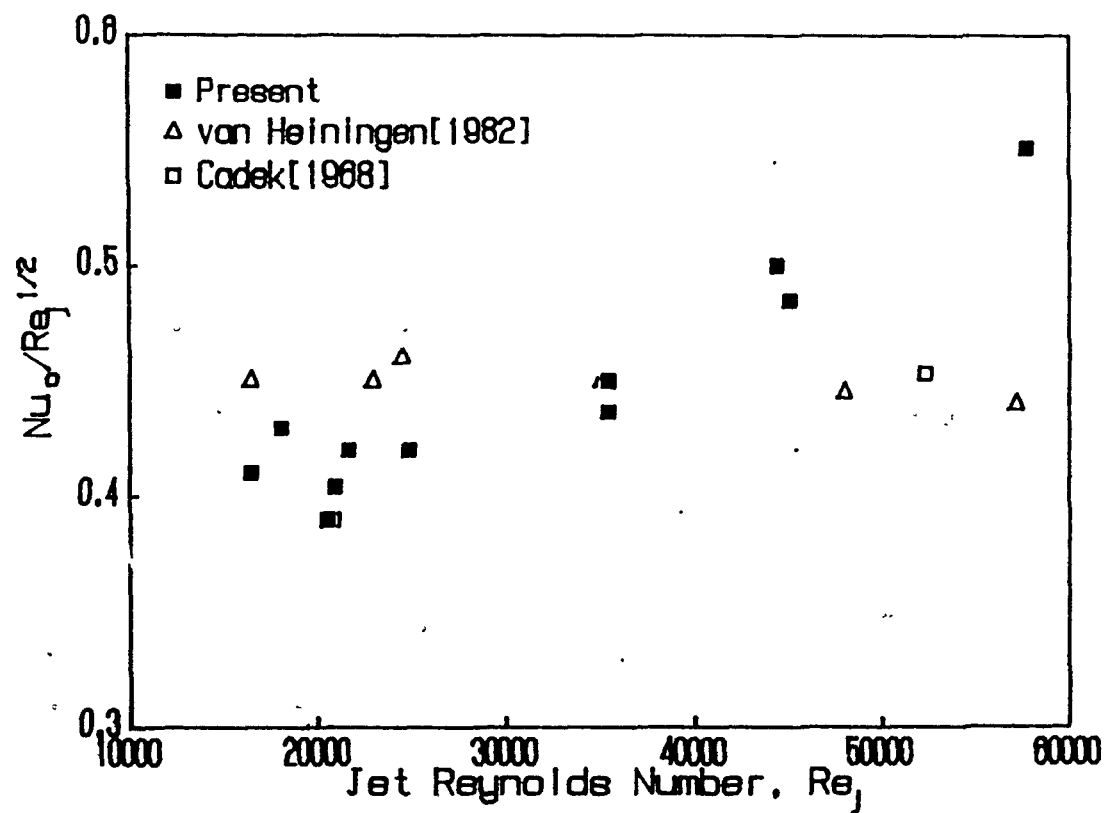


FIGURE 5.2. Effect of Reynolds number on stagnation point Nusselt number

which is important. The extent of transfer surface over which heat transfer is averaged is defined as the width  $2S$ , where  $S$  is the distance on either side of the nozzle centerline, a definition which enables direct comparison with published multiple jet results. Thus Nusselt number was averaged for heat transfer surfaces of half-width,  $S$ , by integrating the profiles of local heat transfer from  $-S/w$  to  $+S/w$ . For a confined multiple jet system in which slot jet nozzle openings alternate with symmetrically located exhaust ports at the confinement surface,  $S$  is the distance between a jet nozzle centerline and the neighboring exhaust port centerline. This alternation of exhaust ports with jet nozzles eliminates the detrimental effect of crossflow on impingement heat transfer, documented experimentally by Saad[1981] and numerically by Ahmad[1987]. At internozzle spacings,  $S/H$ , sufficiently wide as defined by Saad, the average heat transfer of such a multiple jet system converges to that for an array of single jets.

Fig. 5.3 shows the average heat transfer profiles obtained from the local profiles of Fig. 5.1, together with results of van Heiningen [1982] for a single jet at  $H/w=2.6$  and those of Saad[1981] at  $H/w=4$  for a jet in a widely spaced array of jets with symmetrical exhaust ports between the jets. The off-stagnation minima and maxima in  $\overline{Nu}$ , Fig. 5.3, correspond to the same features as for local  $Nu$ , Fig. 5.1, but less pronounced. Extent of the heat transfer surface,  $S$ , in Fig. 5.3 is expressed nondimensionally as  $S/H$  rather than  $S/w$  in order to facilitate application of the present single jet results to multiple jet systems. Thus on Fig. 5.3, the  $S/H$  scale applies for all data, the  $S/w$  scale only for data at a particular  $H/w$ , 2.5. Saad[1981] showed

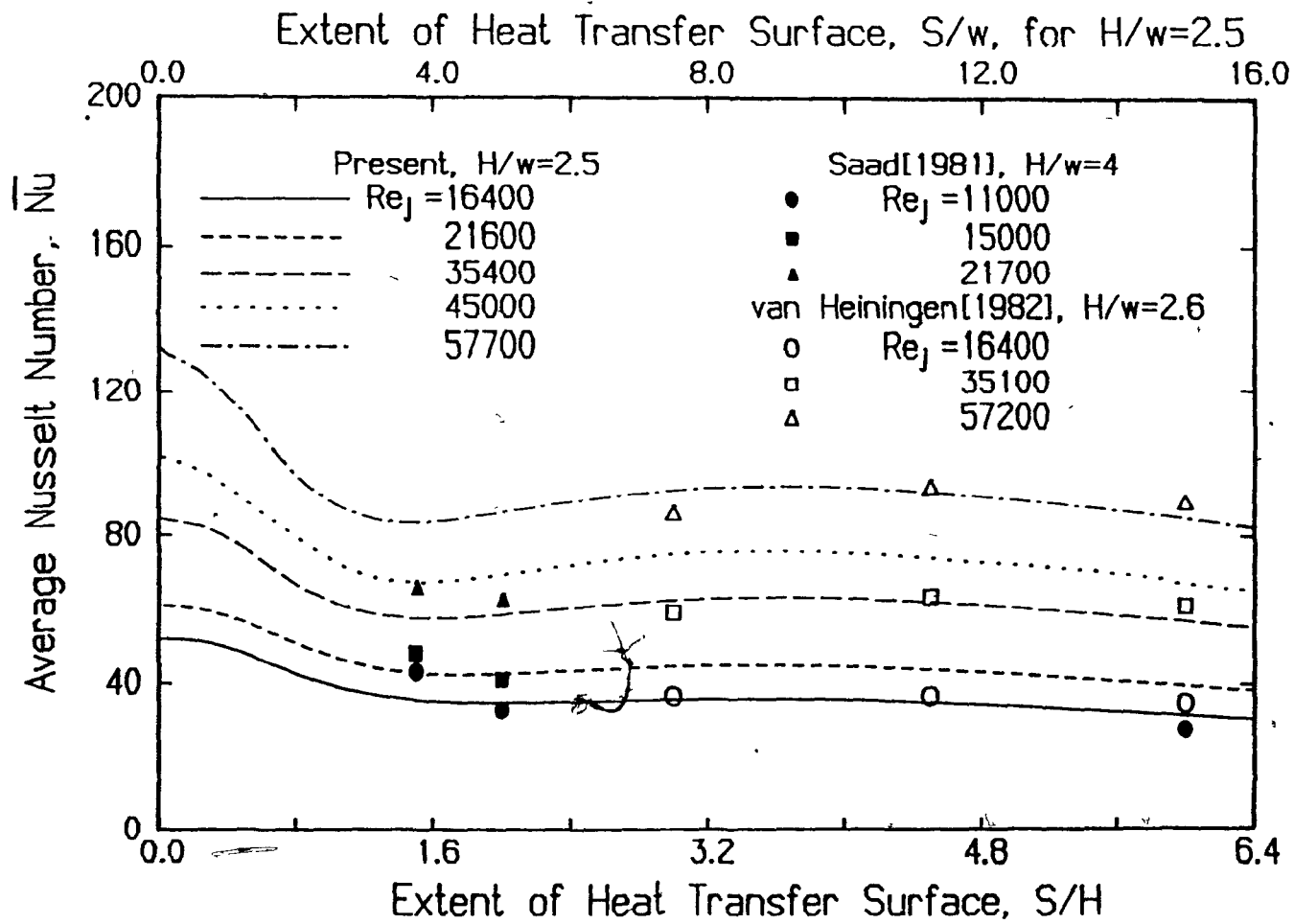


FIGURE 5.3. Profiles of average Nusselt number.

that the combination of nondimensional parameters  $H/w$  and  $S/H$  characterizes multiple jet system geometry better than the alternate choice of  $H/w$  with either  $S/w$  or its equivalent,  $w/2S$ , commonly referred to as fraction open area of nozzles. For the  $Re_j$  and  $H/w$  ranges of 3000-30000 and 4-24, Saad demonstrated that there exists a critical aspect ratio,  $S/H=1.5$ , beyond which such a multiple jet system is effectively a series of single jets. Only his data for  $S/H > 1.5$  is shown on Fig 5.3.

Fig. 5.3 indicates good agreement, within 10%, between the present data for  $Nu$  and those of van Heiningen at effectively the same  $H/w$ . For nozzles of elliptically contoured entry it is well established that in  $Nu=f(H/w)$ ,  $Nu$  passes through a maximum which, in the case of  $Nu_0$ , occurs at about  $H/w=8$ . Thus the fact that at the same  $Re_j$  the  $Nu$  data of Saad at  $H/w=4$  are higher on Fig 5.3 than those of the present study is as expected.

This effect of  $H/w$  spacing on average heat transfer at  $Re_j \sim 21000$  for a surface of half-width  $S=8w$  (i.e. nozzle open area,  $f=6.25\%$ ) is shown in Fig. 5.4 with corresponding  $S/H$  values also indicated. All studies are for single jets except for Saad, and all used jets which were confined over the entire heat transfer surface except Cadek, where confinement was out to from  $6w$  to  $18w$  from the nozzle centerline, i.e. over the most important region.

For an extent of heat transfer surface fixed relative to nozzle width at  $S=8w$ , average heat transfer for single jets from elliptically contoured nozzles, Fig. 5.4, increases by 50% with impingement surface spacing from  $H/w=2$  to 6. This behaviour derives from the development of turbulence downstream from the low level at the exit of such



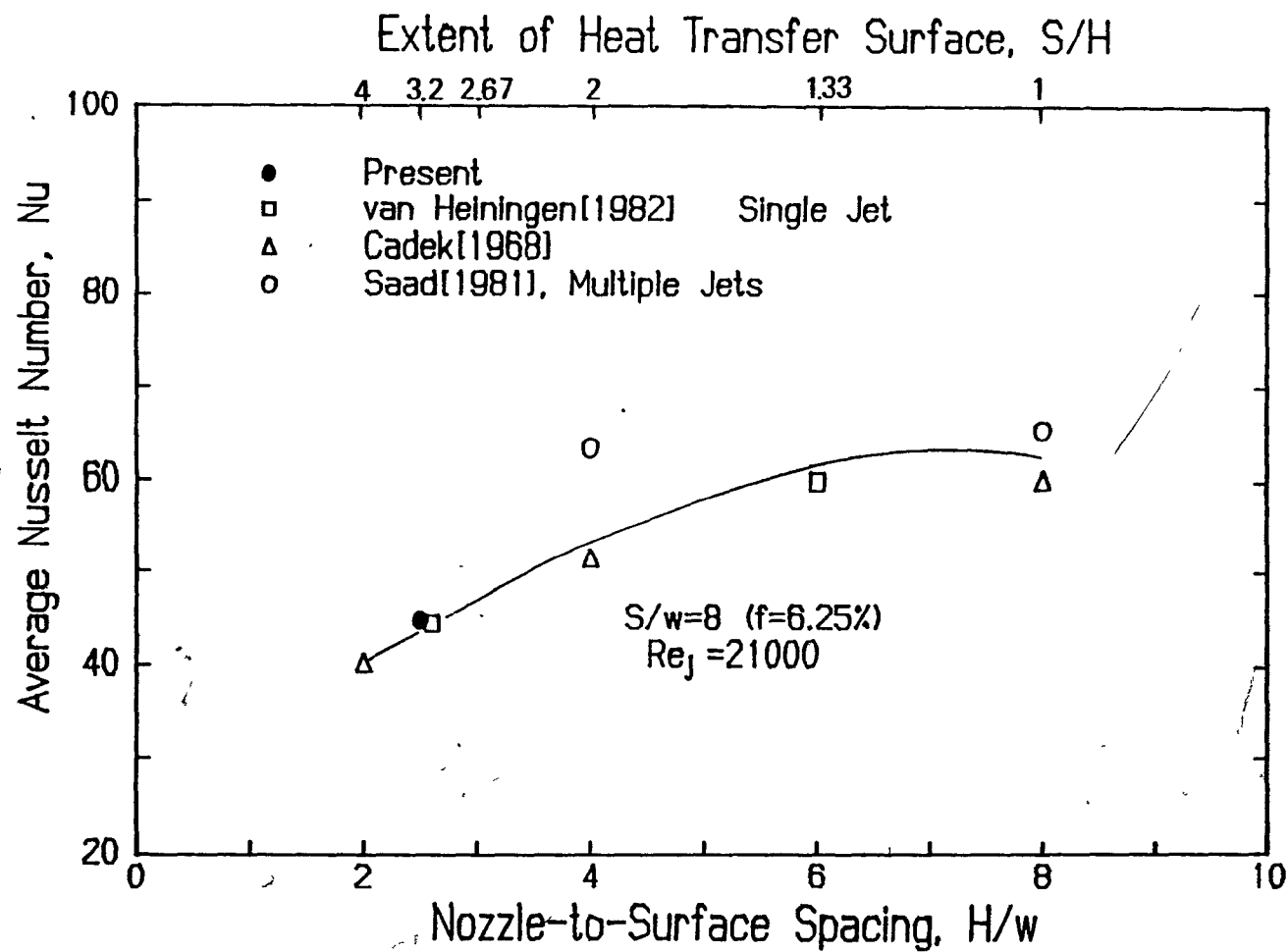


FIGURE 5.4. Effect of nozzle-to-surface spacing on average Nusselt number

nozzles. After passing through a flat maximum value,  $\overline{Nu}=60$ , for spacings,  $H/w$ , in the range 6 to 8, it is well established that  $\overline{Nu}$  decreases with further increases in nozzle spacing. If Saad's critical aspect ratio of  $S/H=1.5$  applied, then at spacings less than  $H/w=8/1.5=5.3$  the average Nusselt number at  $S/w=8$  for multiple jets on Fig. 5.4 would converge to that for a single jet. However  $\overline{Nu}$  remains substantially higher for a jet in an array of jets spaced even as widely as with  $S/H=2$ . As Saad determined the  $S/H=1.5$  limit with data for  $4 < H/w < 24$ , this  $S/H$  limit is in fact unknown for a spacing as close as the  $H/w=2.5$  value of the present study. As spacings are decreased below  $H/w=8$ , impingement heat transfer becomes increasingly sensitive to jet turbulence at the nozzle exit. For  $H/w=4$ , Saad[1981] observed about 17% increase in stagnation heat transfer when nozzle exit turbulence was increased marginally, from 0.65% to 0.8%. For  $H/w=2$  and  $Re_j=11000$ , Gardon and Akfirat[1965] reported that when turbulence at the nozzle exit was increased from 2.5% to 18%, heat transfer increased, by 90% at stagnation, and substantially even out to 10w from stagnation. Differences in results between investigators probably derive from such great sensitivity of impingement heat transfer to nozzle exit turbulence. As it offers a great potential for heat transfer enhancement, this feature of impingement heat transfer at small  $H/w$  spacing should be investigated fully in future studies.

The correlation of the present results for average heat transfer with elliptically contoured entry nozzles at  $H/w=2.5$ ,

$$\overline{Nu} = 0.0314 Re_j^{0.756} \left(\frac{S}{H}\right)^{-0.22} \quad (5.2)$$

, valid for the range  $16400 < Re_j < 57700$ , applies for heat transfer surfaces of half-width,  $S$ , between  $3.2H$  and  $6.4H$ , thereby including

both off-stagnation minima and maxima. For the  $H/w=2.5$  data this extent of averaging surface  $3.2 < S/H < 6.4$ , may be stated alternately as  $8 < S/w < 16$  or  $6.25\% < f < 3.125\%$ . Considerations of energy economy normally preclude practical interest in impingement heat transfer areas smaller than the lower limit of this correlation. The error limits on the empirical constants, 0.0314, 0.756 and 0.22 are, respectively, 0.003, 0.008 and 0.01. Eq. 5.2 is a limiting form of subsequent correlations, Eqs. 5.7 and 5.11, which incorporate additional effects.

The value of the  $Re_j$  exponent, 0.756, is close to the 0.8 value for fully developed turbulent flow, as would be anticipated for a heat transfer surface of this size. This exponent is also close to the range, 0.7 to 0.744, obtained for  $S/w > 7.5$ ,  $S/H > 2.9$ , by van Heiningen [1982] for a single slot jet with  $H/w$  spacing of 2.6.

It is apparent from Fig. 5.3 and Table 5.2 that, except for small distances from stagnation,  $\bar{Nu}$  is not very sensitive to extent of heat transfer area and passes through a flat maximum around  $S/w=9$ ,  $S/H=3.6$ . Thus the  $S/H$  exponent, -0.22 in the present case, could be either slightly positive or negative depending entirely on the  $S/H$  interval used. The correlation for  $\bar{Nu}$  of van Heiningen [1982] for  $H/w=2.6$  over the range  $1.4 < S/H < 8.7$  in fact predicts a maximum for  $\bar{Nu}$  at about  $S/H=4$ , which is consistent with Fig. 5.3.

The objective of this preliminary work, validation of the new technique for the base case of no throughflow, is achieved by the good agreement obtained with earlier studies. Beyond that objective these results also add significantly to the knowledge of impingement heat transfer without throughflow.

### 5.3. IMPINGEMENT HEAT TRANSFER WITH THROUGHFLOW

The principal operating conditions and results of experiments conducted with throughflow and without significant impingement surface motion effect are summarized in Table 5.4. Throughflow velocity is expressed nondimensionally as  $Mu_s = \rho_s u_s / \rho_j u_j$ , the ratio of throughflow mass velocity to jet mass velocity.

#### 5.3.1 Local Heat Transfer

The enhancement of heat transfer due to throughflow considered here refers only to the increase in convective heat transfer at the impingement surface. Thus all heat transfer occurring between the throughflow air and the permeable material below the impingement surface is irrelevant to and is entirely separate from the convective heat transfer at the impingement surface.

Figs. 5.5 to 5.8 display the effect of impingement surface throughflow on lateral Nu profiles at  $H/w=2.5$  for the  $Re_j$  range 24600-57300. The observation that over the entire profile the local heat transfer coefficient increases approximately linearly with  $Mu_s$  is in agreement with the results of Baines and Keffer[1979] and Saad[1981] for slot nozzles, and Obot[1982] for a round nozzle.

A heat balance near the impingement surface, Fig. 5.9, indicates that enhancement in convective heat transfer due to throughflow is best expressed in terms of Stanton number. Here  $q_p$  and  $q_i$  denote the heat transfer flux at, respectively, a permeable surface with throughflow, and at an impermeable surface. Assuming only fluid in the immediate neighbourhood of the surface is removed by throughflow and that fluid lateral velocity is not appreciably affected, the difference,  $q_p - q_i$ , is

Table 5.4 Operating conditions and results for single jet heat transfer with throughflow

$Re_j$	$Mv_s$	$Mu_s$	$T_j$	$T_j - T_s$	$Nu_o$	$Nu_{max}^*$	$\frac{S}{W}$ for $Nu$				
							8	10	12	14	16
16400	0.034	0.0	82.4	23.9	52.4	36.1	36.1	35.8	34.4	32.4	30.3
16400	0.034	0.0064	83.2	23.0	68.0	49.7	49.7	49.4	48.1	46.2	44.0
18100	0.033	0.0	59.3	12.0	57.7	39.6	39.5	39.4	38.0	35.8	33.5
17800	0.033	0.0055	59.8	11.3	73.5	54.3	54.2	54.0	52.6	50.5	48.1
17700	0.033	0.0139	61.1	11.2	98.0	77.2	77.2	76.5	74.8	72.4	69.7
17700	0.033	0.0139	62.2	11.5	96.0	75.2	75.1	74.4	72.6	70.4	67.9
17100	0.033	0.0205	63.9	11.5	102.0	**	85.2	84.1	82.1	79.7	77.2
20400	0.035	0.0	86.2	27.3	55.2	40.1	40.0	40.0	38.7	37.0	34.8
20350	0.035	0.0055	86.3	26.7	66.0	52.4	52.1	52.3	51.3	49.5	47.4
20300	0.034	0.0114	86.6	26.2	82.0	68.5	68.4	68.2	67.0	65.2	62.9
20900	0.047	0.0	70.2	19.9	58.4	42.1	42.0	41.9	40.4	38.3	35.6
20750	0.047	0.0044	69.9	19.3	67.0	50.9	50.6	50.8	49.7	47.8	45.5
20640	0.046	0.0121	71.2	19.4	83.0	69.6	69.5	69.3	67.9	65.7	63.2
20000	0.045	0.0202	73.3	18.9	103.0	91.8	91.8	91.0	89.3	87.0	84.6
24800	0.023	0.0	79.1	22.2	65.6	48.3	48.1	48.0	46.2	43.8	41.0
24800	0.023	0.0055	79.2	21.5	79.0	61.8	61.5	61.7	60.5	58.3	55.8
24600	0.022	0.0094	80.0	21.4	90.0	73.3	73.1	73.0	71.6	69.3	66.7
24450	0.021	0.0163	81.4	21.5	106.0	89.9	89.4	87.6	85.5	83.1	80.7
35400	0.020	0.0	57.8	12.4	84.9	64.2	63.8	63.9	61.6	58.5	54.8
35300	0.020	0.0032	58.5	12.1	97.5	76.6	76.0	76.5	74.6	71.7	68.3
35150	0.020	0.0068	59.7	12.1	116.0	94.2	93.4	94.0	92.4	89.6	86.2
34900	0.020	0.0097	60.7	12.1	129.0	106.4	105.9	106.3	104.5	101.6	98.5
34800	0.020	0.0121	61.3	12.1	137.0	117.0	116.7	116.5	114.5	111.7	108.5
45100	0.020	0.0	52.2	12.6	103.0	76.3	75.9	75.9	73.4	69.4	65.7
44900	0.020	0.0019	53.3	12.6	112.0	84.2	83.4	84.0	81.8	78.4	74.5
44250	0.020	0.0053	55.4	12.5	128.0	101.0	100.1	101.0	99.1	95.9	92.2
57700	0.016	0.0	43.9	9.3	132.1	95.2	94.6	94.7	91.6	87.2	82.0
57500	0.016	0.0043	45.5	9.3	161.0	121.9	120.7	121.8	119.6	115.8	111.1
57300	0.016	0.0043	46.8	9.3	161.0	121.0	119.7	120.9	118.8	114.9	110.4
56250	0.016	0.0074	48.9	9.4	170.0	141.0	139.3	141.0	139.5	136.2	132.0
55700	0.015	0.0081	50.0	9.1	177.0	147.5	146.2	147.3	145.1	141.4	137.2
55200	0.015	0.0086	51.0	9.2	180.0	146.4	145.0	146.3	144.4	140.9	136.8

\*  $Nu_{max}$  indicates off-stagnation maximum

\*\* does not display an off-stagnation maximum

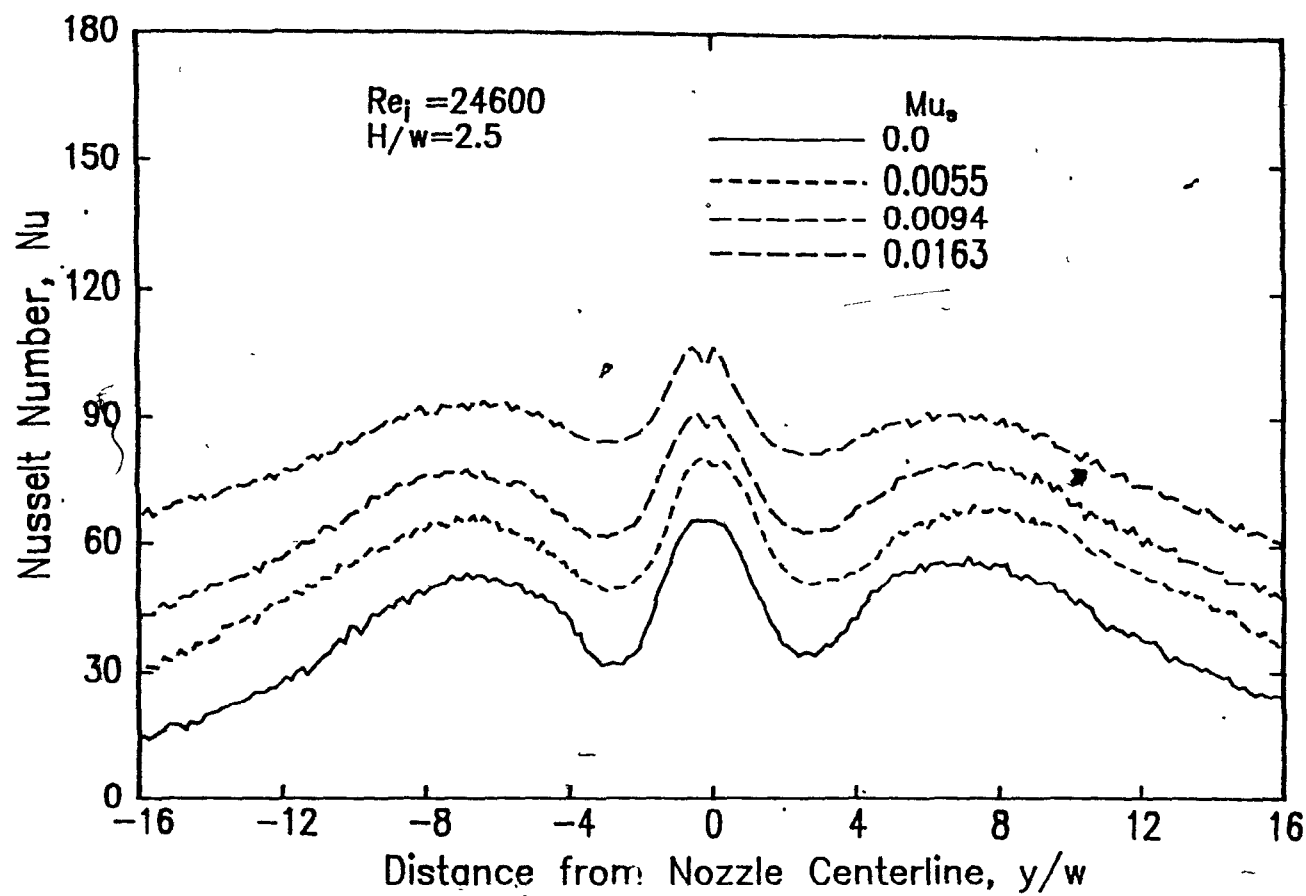


FIGURE 5.5. Effect of throughflow on profiles of local Nusselt number at  $Re_j = 24600$

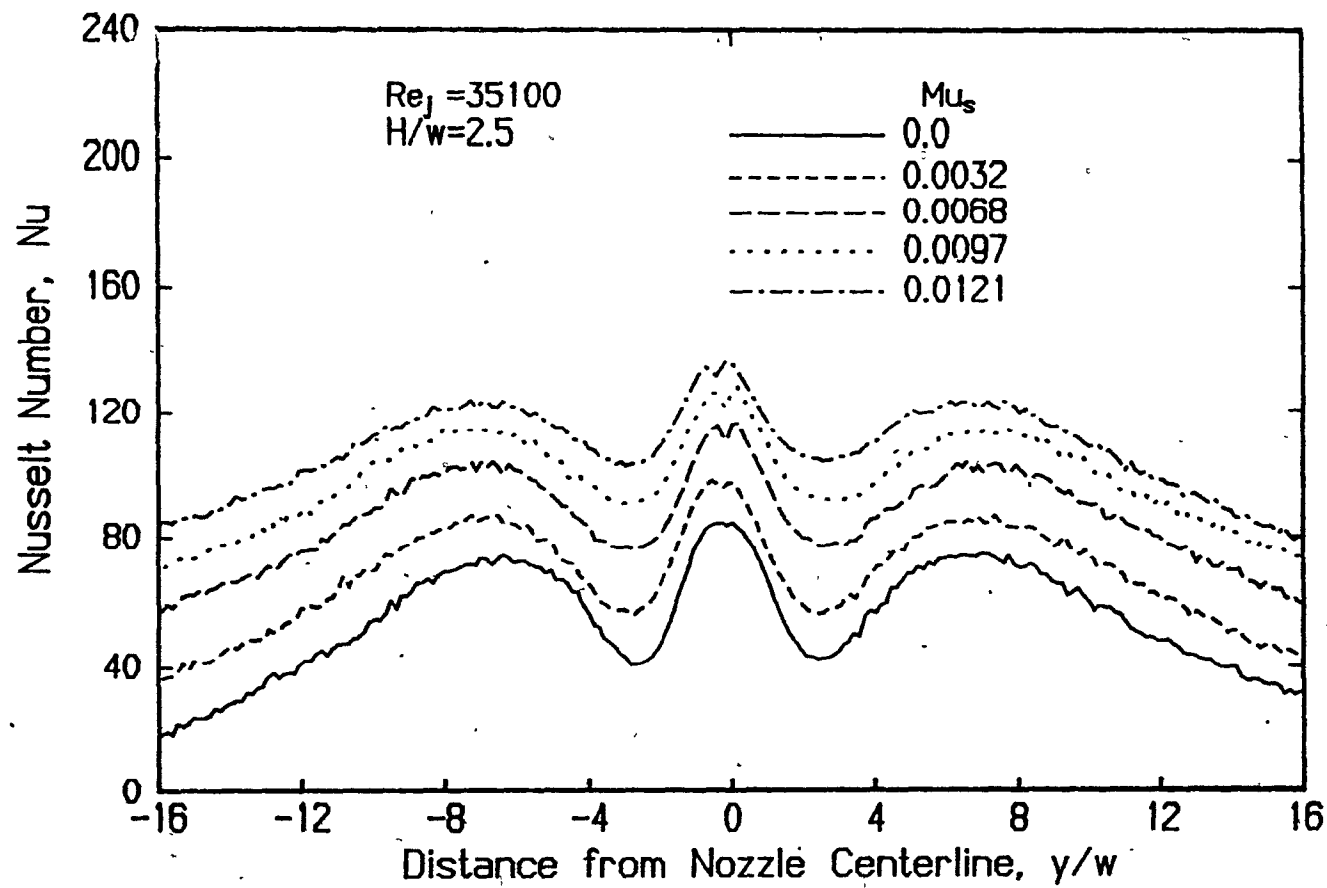


FIGURE 5.6. Effect of throughflow on profiles of local Nusselt number at  $Re_j = 35100$

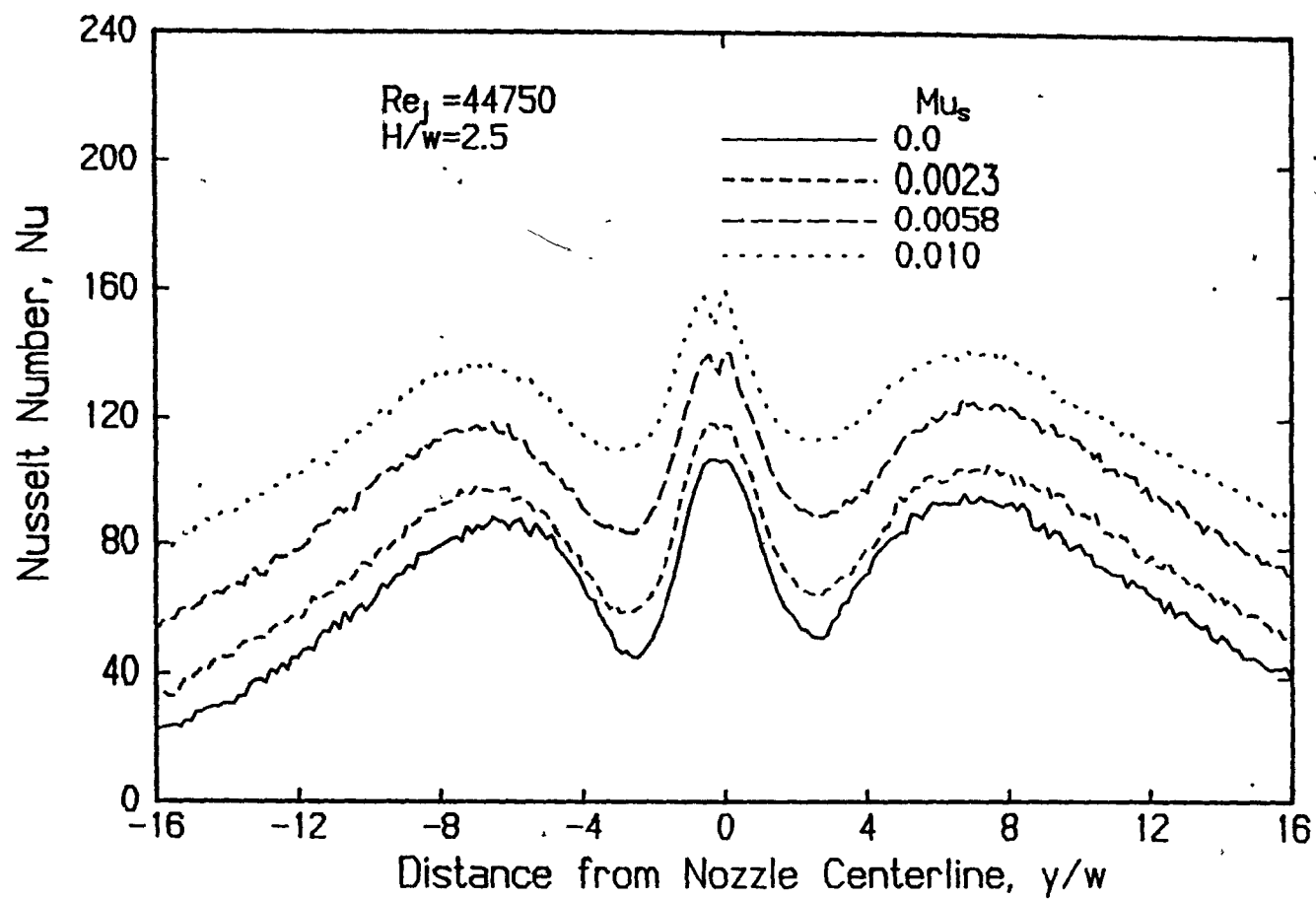


FIGURE 5.7. Effect of throughflow on profiles of local Nusselt number at Re<sub>j</sub> = 44750



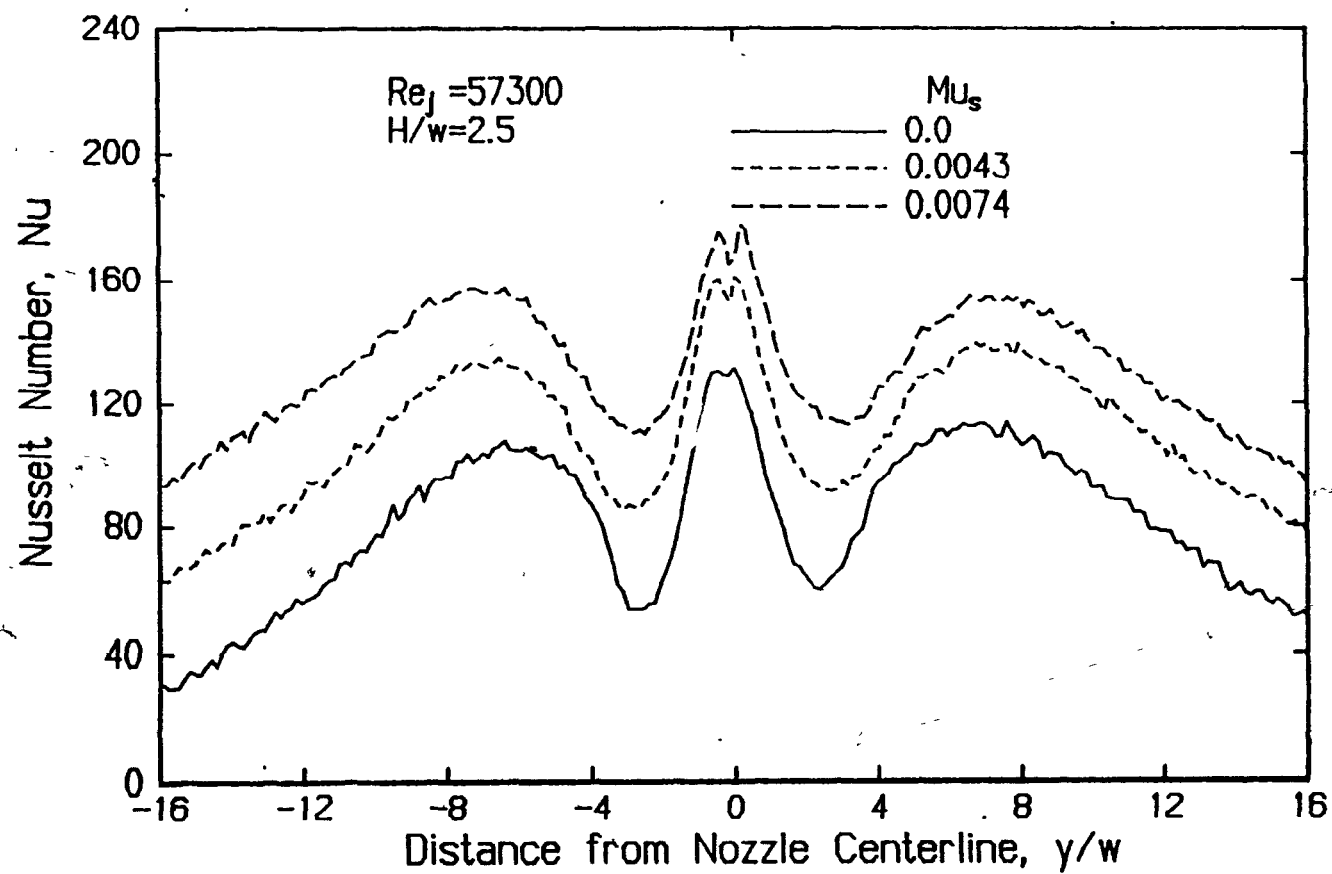


FIGURE 5.8. Effect of throughflow on profiles of local Nusselt number at Re<sub>j</sub> = 57300

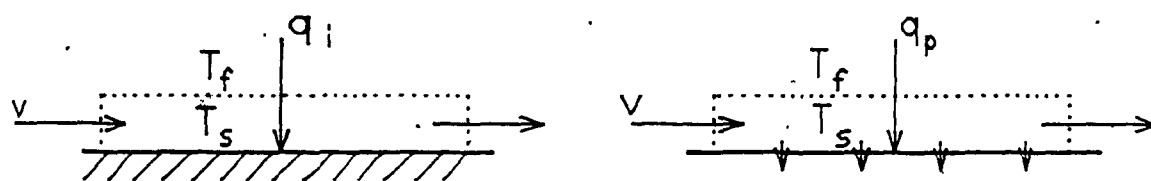


FIGURE 5.9. Control volumes for heat balance near impingement surface without and with throughflow

proportional to throughflow velocity and to the temperature difference,  $T_f - T_s$ ,

$$q_p - q_i = \rho_s u_s C_{Pa} (T_f - T_s) \quad (5.3)$$

Dividing both sides by  $\rho_j u_j C_{Pa} (T_s - T_j)$  gives

$$\frac{(h_p - h_i)}{\rho_j u_j C_{Pa}} \propto \frac{\rho_s u_s}{\rho_j u_j} \frac{(T_s - T_f)}{(T_s - T_j)}$$

or

$$St_p - St_i = C Mu_s = \Delta St \quad (5.4)$$

where the proportionality constant  $C$  includes the ratio  $(T_s - T_f)/(T_s - T_j)$  which is determined by near surface flow and heat transfer conditions.

Consistent with the above analysis, the increase in convective heat transfer due to throughflow appears in Fig. 5.10 as the enhancement of local Stanton number,  $\Delta St$ . For clarity Fig. 5.10 displays only the two limiting cases from Figs. 5.5-5.8, i.e. highest  $Mu_s$  at the lowest and the highest  $Re_j$  ( $Mu_s = 0.0163$  at  $Re_j = 24600$ ,  $Mu_s = 0.0074$  at  $Re_j = 57300$ ). It is shown in Appendix 2 that Stanton number is subject to slightly higher experimental uncertainty,  $\pm 7.5\%$ , than Nusselt number,  $\pm 5\%$ , as it includes uncertainty in  $Re_j$ . A constant value of  $Pr$ , 0.7, is used. Moreover, as the data is differenced to obtain the enhancement, the error bound for  $\Delta St$  is thereby increased to the order of  $\pm 15\%$ .

In Fig. 5.10, the terminology "approaching" and "leaving" defines the direction of surface motion relative to the nozzle centerline. Profiles of local  $Nu$  and  $\Delta St$  are represented consistently with the "approaching" side shown on the left. As throughflow removes the air near the surface, throughflow eliminates the cause for the slight asymmetry of local Nusselt number profiles, i.e. the boundary layer of cooler air dragged by surface motion into the heating jet test section.

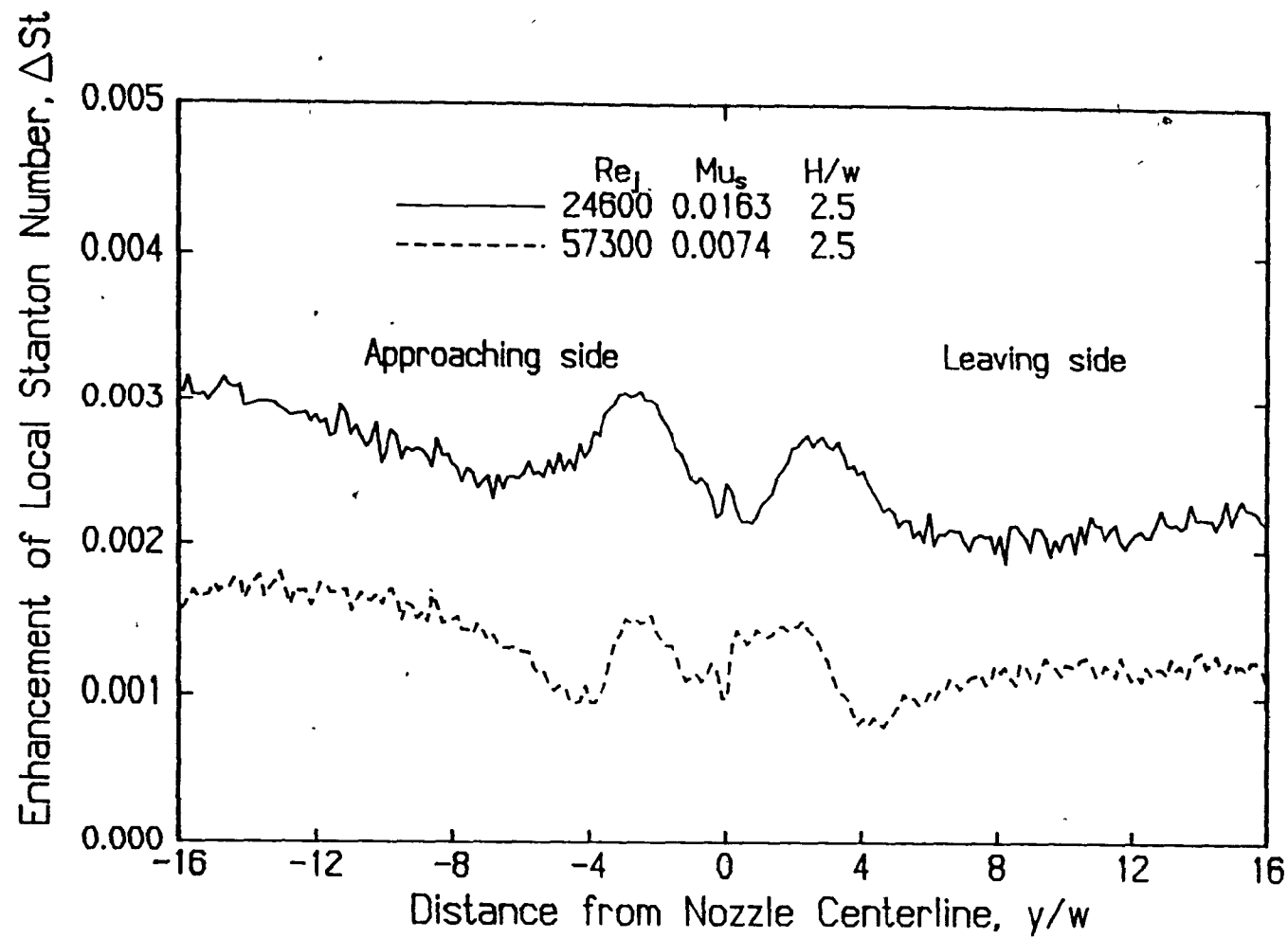


FIGURE 5.10. Profiles of enhancement of local Stanton number by throughflow

As local Nusselt number profiles thereby become more symmetrical with throughflow, the enhancement of heat transfer due to throughflow,  $\Delta St$ , is consistently slightly larger on the approaching than the leaving side.

The trend in these particular profiles for a slight maximum around  $2.5w$  and a minimum in the region  $4w-6w$  from stagnation is typical of all  $\Delta St$  profiles. As noted earlier the boundary layer transition, from laminar to turbulent, begins at about  $2.6w$  and is complete at about  $7w$  from stagnation. Throughflow increases velocity and temperature gradients normal to the impingement surface. In a laminar boundary layer region, enhancement of heat transfer by throughflow is solely due to the associated increase in temperature gradient at the surface, analogous to the increase in coefficient of friction due to increase in velocity gradient. However where the boundary layer is turbulent, throughflow both increases the temperature gradient and decreases turbulence intensity near the surface, as documented for round and slot impinging jets by Obot[1981] and Saad[1981]. Thus in a region of laminar boundary layer, the enhancement by throughflow is a maximum where the boundary layer is thickest, but where the boundary layer is turbulent these opposing effects of throughflow lead to an increase of heat transfer, Fig. 5.10, generally less than where there is a thick laminar boundary layer.

### 5.3.2 Average Heat Transfer

The effect of throughflow on average heat transfer profiles for  $Re_j \approx 35100$  is expressed in terms of  $\overline{Nu}$  and  $\overline{St}$  in Fig. 5.11. The relative extent of off-stagnation minima and maxima, always less

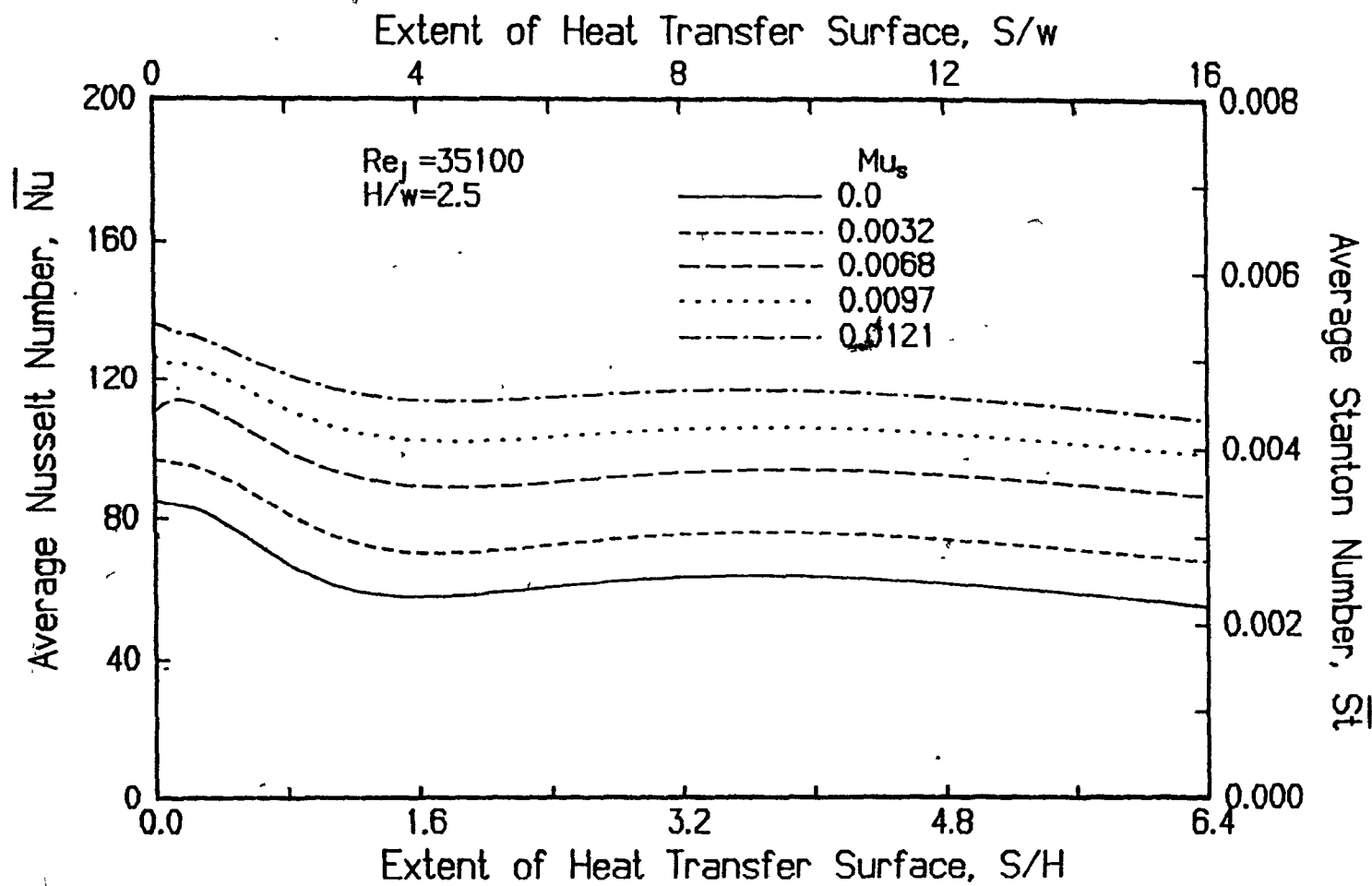


FIGURE 5.11. Effect of throughflow on profiles of average Nusselt number.

pronounced for average than for local heat transfer profiles, decreases further yet with increasing throughflow, Fig. 5.11, for reasons discussed above. In the absence of throughflow Fig. 5.3 indicated that outside the stagnation region  $\bar{Nu}$  passes through a flat maximum at about  $S/w=9$ ,  $S/H=3.6$ , at all Reynolds numbers. Fig. 5.10 and Table 5.4 show that at all values of throughflow this flat maximum in  $\bar{Nu}$  occurs for an impingement surface of about the same half-width,  $S$ , of  $9w$  or  $3.6H$ . Thus the highest average heat transfer is obtained for a surface which extends about  $2w$  beyond the  $7w$  width needed in order to include the secondary maximum in local  $Nu$ .

As the enhancement of local heat transfer by throughflow,  $\Delta St$ , varies only to a limited extent with distance from stagnation, Fig. 5.10, the enhancement of average heat transfer,  $\Delta \bar{St}$ , is almost independent of distance from stagnation, Fig. 5.11.  $\Delta \bar{St}$  varies linearly with the throughflow parameter,  $Mu_s$ , independently of  $Re_j$  and of extent of heat transfer surface, as expressed by

$$\Delta \bar{St} = 0.18 Mu_s \quad (5.5)$$

for  $H/w=2.5$ , in the range  $16400 < Re_j < 57700$ ,  $0 < Mu_s < 0.023$  for heat transfer surfaces of half-width,  $S$ , up to at least  $6.4H$ ,  $16w$ . Eq. 5.5 expresses the important concept that the throughflow effect on average convective heat transfer is linearly additive. The complete experimental results of the present study shown on Fig. 5.12 indicates that Eq. 5.5 adequately represents the measurements for this wide range of throughflow and Reynolds number.

For a single unconfined slot jet with  $u_j=53\text{m/s}$  and  $H/w=2$  at a constant  $u_s/u_j$  ratio of 0.0029, Baines and Keffer[1979] measured the local and average shear stress profiles up to  $\Delta y/w=32$  and similarly

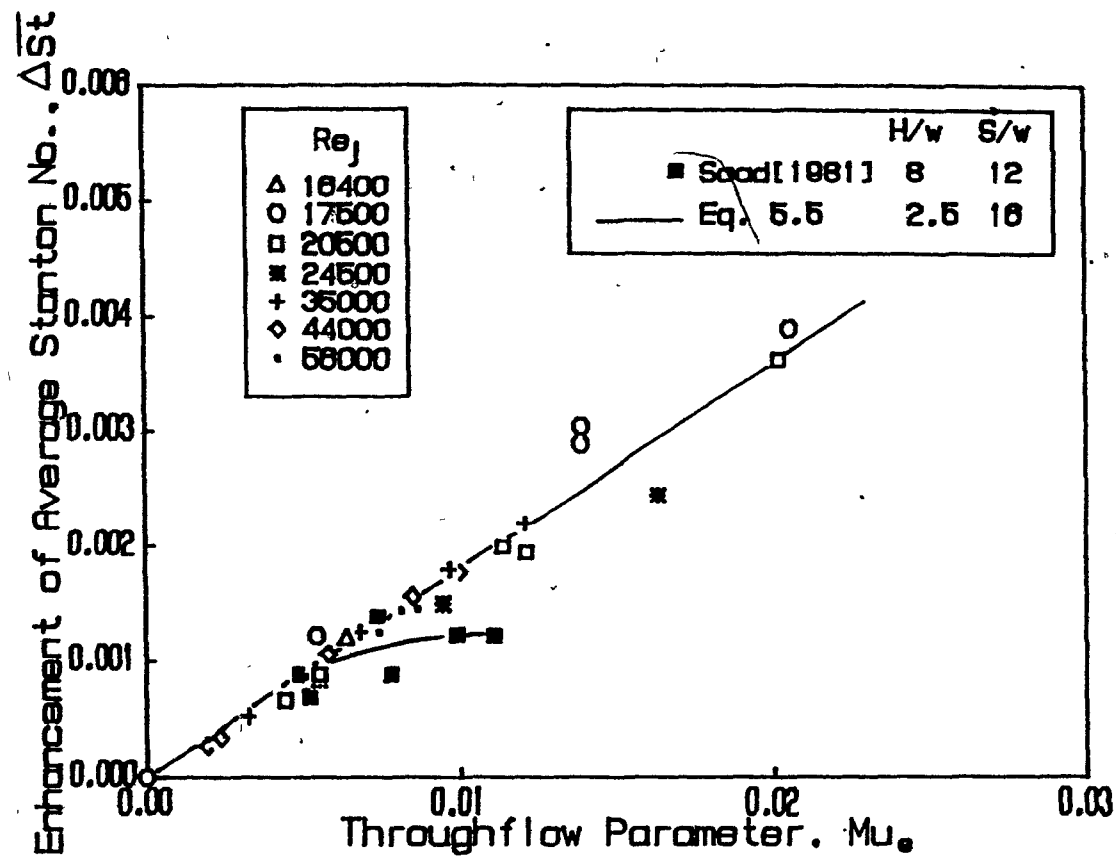


FIGURE 5.12. Effect of throughflow on enhancement of average Stanton number



found that shear stress increased throughout the entire profile by roughly a constant amount due to throughflow. For a moving surface they expressed the increase in average wall shear stress due to throughflow as

$$\bar{\tau}_p - \bar{\tau}_i = -\kappa \rho u_s (v_s + \bar{v}_f)$$

where  $\bar{v}_f$  is the mean free stream velocity.

It is possible, with some assumptions, to predict approximately the effect of throughflow on heat transfer using Baines and Keffer's measurements of the effect of throughflow on shear stress. In the present analysis relatively low surface velocities, i.e.  $v_s \ll \bar{v}_f$ , are considered because throughflow on a rapidly moving surface has additional effects on the boundary layer, Section 5.4.2.2. For  $v_s \ll \bar{v}_f$  the enhancement of skin friction due to throughflow,  $\Delta \bar{C}_f / 2$ , can be expressed as

$$\frac{\Delta \bar{C}_f}{2} = \kappa \frac{\rho u_s}{\rho u_j} \frac{\bar{v}_f}{u_j} = \Delta \bar{S} \bar{E}.$$

Baines and Keffer calculated  $\kappa = 0.3$  ( $\pm 0.11$ ) from their hot wire anemometry measurements of velocity profiles near the surface. Their measurements show that, in the range  $2 < H/w < 10$ ,  $\bar{v}_f$  is equal to at least half the nozzle exit jet velocity. Hence one can obtain  $\Delta \bar{C}_f / 2 = \Delta \bar{S} \bar{E} = 0.15 \text{ Mu}_s$ . Although subject to the high uncertainty of the  $\kappa$  value, this predicted value for the proportionality constant for enhancement of heat transfer by throughflow, 0.15, is remarkably close to that found in the present study, 0.18.

For  $H/w = 8$ ,  $10200 < Re_j < 29100$  and with values of  $\text{Mu}_s$  up to 0.011, Saad[1981] measured the enhancement of heat transfer by throughflow at a stationary surface under a single confined slot jet impinging on a heat transfer surface of half-width,  $S$ , of  $2.25H$ ,  $18w$ . The values of

Saad's average heat transfer represented on Fig. 5.12 were determined by integrating local heat transfer out to  $S=1.5H-12w$ . However his Nu profiles, like those of the present study, show that enhancement of average heat transfer is not a function of width of the heat transfer surface. It is highly significant that in spite of substantial differences between the two studies in terms of experimental techniques as well as H/w spacing, 8 vs 2.5, the agreement evident on Fig. 5.12 at low  $Mu_s$  values between the present data and that of Saad is remarkably good. As Saad's technique to measure heat transfer with throughflow was susceptible to systematic errors which increased with throughflow rate, only his data at low throughflow are considered reliable. Close agreement at low throughflow with Saad's results indicates that over the H/w range from 2.5 to 8 the proportionality constant 0.18 of Eq. 5.5 is also independent of H/w. Thus enhancement of average impingement heat transfer due to throughflow may be estimated from Eq. 5.5 for  $2.5 < H/w < 8$ ,  $16000 < Re_j < 58000$ ,  $0 < Mu_s < 0.023$ , for surfaces of any half-width up to at least  $S/H=6.4$ ,  $S/w=16$ .

For the ideal case of flow of a frictionless fluid of uniform velocity and temperature over a permeable surface of uniform temperature, enhancement of convective heat transfer due to a uniform throughflow is  $\Delta St = Mu_s$ . In a boundary layer flow, however, the enhancement of heat transfer,  $\Delta St$ , is proportional to rather than equal to  $Mu_s$ . For a flat plate turbulent boundary layer, Mickley et al. [1954] and Spalding [1960] independently derived the following relationship for the ratio of local convective heat transfer at a permeable surface with throughflow, relative to that at an impermeable surface.

$$\frac{St_p}{St_i} = \frac{-B_1}{e^{-B_1} - 1} \quad \text{where} \quad B_1 = \frac{Mu_s}{St_i} \quad (5.6)$$

At very low throughflow rates,  $Mu_s < 0.004$ , Moffat and Kays[1968] found agreement between Eq. 5.6 and their experimental data for effect of throughflow on convective heat transfer for turbulent flow over a flat porous surface. At higher throughflow, however, their measured Stanton number was always lower than the theory. For turbulent impinging jets, Eq. 5.6 also predicts much greater effect of throughflow on heat transfer than that measured by Baines and Keffer [1979], Saad[1981], van Heiningen[1982] and the present work. For example, according to the present study, Eq. 5.5, a  $St$  enhancement of 32.5% is expected for  $Mu_s = 0.0044$  at  $H/w = 2.5$  and  $Re_j = 20800$ . The Mickley and Spalding theory, Eq. 5.6, predicts a value of almost four times higher than this, 116%. As boundary layer development under an impinging jet differs substantially from simple boundary layers it is not surprising that the simplifying assumptions of the Mickley-Spalding theory lead to poor prediction of heat transfer enhancement by throughflow.

Because the throughflow effect on average convective heat transfer is linearly additive, average Nusselt number with throughflow at the impingement surface for non-interacting multiple impinging jet systems as well as single impinging jets from elliptically contoured entry nozzles at  $H/w = 2.5$  can be estimated by combining Eqs. 5.2 and 5.5 with the relation  $St = \frac{Nu}{Re Pr}$ , to give

$$\bar{Nu}|_{v_s=0} = 0.0314 Re_j^{0.756} \left(\frac{S}{H}\right)^{-0.22} + 0.18 Mu_s Re_j Pr \quad (5.7)$$

valid over the range  $16000 < Re_j < 58000$ ,  $0 < Mu_s < 0.023$  and  $S/H$  from 3.2 to at least 6.4. For  $H/w = 6$ , an analytic expression for  $\bar{Nu}$  as a function of throughflow may likewise be obtained by combination of Eq. 5.5 with

the correlation of van Heiningen[1982] for  $\bar{Nu}$  without throughflow at  $H/w=6$ . For values of  $H/w$  intermediate between 2.5 and 6, Fig. 5.4 indicates that linear interpolation for  $H/w$  in this range is within the accuracy of experimental data available. For values of  $H/w$  between 6 and 8, Fig. 5.4 indicates that  $\bar{Nu}$  is essentially independent of  $H/w$ .

The importance of these results for industrial application is apparent from the finding that by using  $Mu_s=0.0121$ , the maximum value tested at  $Re_j=35000$ , the average convective transfer rate may be approximately doubled for heat transfer surfaces of any half-width,  $S$ , over the broad range  $0.8H-6.4H$ , i.e.  $2w-16w$ . These  $S/w$  values correspond to nozzle areas in the range 3%-25% of the impingement surface. In this context it is more informative to convert the throughflow parameter,  $Mu_s$ , to the equivalent values of the ratio, throughflow rate to jet flow rate,  $Q_s=Mus/f-Mus(2S/w)$ . Thus for heat transfer surfaces of half-width,  $S$ , in the range of  $2w$  to  $16w$ , the use of  $Mus=0.0121$  corresponds to removal by throughflow,  $Q_s$ , of from 4.8% to 38.7% of the jet flow. The ability to double the convective heat transfer rate by removal as throughflow of from 5% to 40% of the jet flow has considerable practical significance. In order to obtain the same enhancement of  $\bar{Nu}$  without application of throughflow, jet inlet flow would have to be increased ~250%. Additional to this impressive enhancement of convective heat transfer there is of course the further large enhancement of total heat transfer by the mechanism of heat transfer in the interior of such a permeable media, an aspect outside the scope of the present study.

The present investigation extends substantially the only previous experimental results available concerning convective heat transfer

under slot jets impinging on surfaces with throughflow, Saad[1981].

Moreover, the good agreement between the present results and those of Saad at low rates of throughflow adds confidence to the present results which apply for throughflow rates up to twice those of Saad and for a closer nozzle spacing,  $H/w$ , than any he used.

#### 5.4 HEAT TRANSFER AT A MOVING IMPINGEMENT SURFACE

##### 5.4.1 Heat Transfer at a Moving Impingement Surface Without Throughflow

Operating conditions and results given in Table 5.5 apply for impingement surface velocities corresponding to quite high values of the characteristic nondimensional mass velocity ratio,  $Mv_s = v_s \rho_s / u_j \rho_j$ , up to 0.34.

##### 5.4.1.1 Local Heat Transfer

For jet Reynolds numbers in the range 18100-35400 the surface motion parameter,  $Mv_s$ , was varied from 0.029 to 0.34 by varying the heat transfer surface velocity from 0.5 to 9m/s, i.e. from 20 to 362rpm for the heat transfer cylinder. The effects of surface motion on local heat transfer profiles for  $H/w=2.5$ , displayed for two Reynolds numbers on Figs. 5.13 and 5.14, are:

1. Even the highest heat transfer surface velocities,  $v_s=9\text{m/s}$ ,  $Mv_s=0.34$ , cause no significant variation in either the magnitude or location of the stagnation heat transfer.

2. The location of the off-stagnation minima and maxima are displaced by a small but measurable extent in the direction of surface motion. Fig. 4.12 of the previous chapter shows that the displacement in position of the off-stagnation maxima compares well

Table 5.5. Operating conditions and results for single jet heat transfer at a moving surface without throughflow

$Re_j$	$Mv_s$	$T_j$	$T_j - T_s$	$Nu_o$	$\overline{Nu}_{min}$	$\overline{Nu}_{max}^*$	$\frac{S}{W}$ for $\overline{Nu}$				
							8	10	12	14	16
18100	0.054	58.4	11.6	57.6	37.8	39.5	39.4	39.2	37.8	35.6	33.3
18100	0.119	58.8	11.9	53.8	35.2	36.5	36.5	36.2	34.9	32.8	30.6
18100	0.162	58.8	11.8	54.0	35.1	36.4	36.4	36.0	34.6	32.6	30.6
20400	0.035	86.2	27.3	55.2	38.1	40.1	40.0	40.0	38.7	37.0	34.8
20400	0.09	85.3	27.0	55.0	37.2	39.4	39.4	38.9	37.4	35.2	32.9
20400	0.176	83.7	26.2	55.8	35.4	37.4	37.4	37.0	35.5	33.5	31.5
20900	0.269	83.4	27.0	54.5	35.2	36.3	36.3	35.5	34.1	32.1	30.3
21200	0.34	79.5	26.9	56.0	34.7	35.5	34.8	33.5	32.1	30.5	28.7
21600	0.029	64.4	18.4	62.0	42.4	45.0	44.8	44.8	43.3	40.9	38.4
21600	0.102	64.9	18.8	56.0	37.9	40.2	40.1	40.0	38.5	36.3	34.1
21600	0.143	65.0	18.8	57.0	37.2	39.5	39.5	39.1	37.5	35.4	33.2
21600	0.199	65.1	19.0	58.0	36.8	38.8	38.8	38.2	36.4	34.3	32.1
21100	0.252	68.8	19.5	55.0	35.9	37.4	37.4	36.4	35.0	33.0	31.0
35400	0.029	57.8	12.3	82.3	55.8	62.1	61.7	61.8	59.8	56.8	53.3
35400	0.06	57.7	12.4	81.3	54.0	60.0	59.7	59.7	57.5	54.6	51.1
35400	0.077	57.7	12.5	78.0	52.4	58.2	57.8	57.8	55.8	52.9	49.5
35400	0.102	57.7	12.5	81.0	52.6	58.5	58.3	58.1	55.8	52.7	49.4
35400	0.145	57.7	12.4	78.3	53.0	58.1	57.8	57.6	55.4	52.1	48.8
35400	0.183	57.6	12.5	79.9	51.2	56.0	55.8	55.5	53.2	50.1	46.9
35400	0.231	57.5	12.4	83.4	51.6	56.0	56.0	54.8	52.3	49.4	46.4
35400	0.285	57.6	12.5	84.9	51.6	55.0	54.9	53.6	51.3	48.3	45.6

\*  $Nu_{max}$  indicates off-stagnation maximum

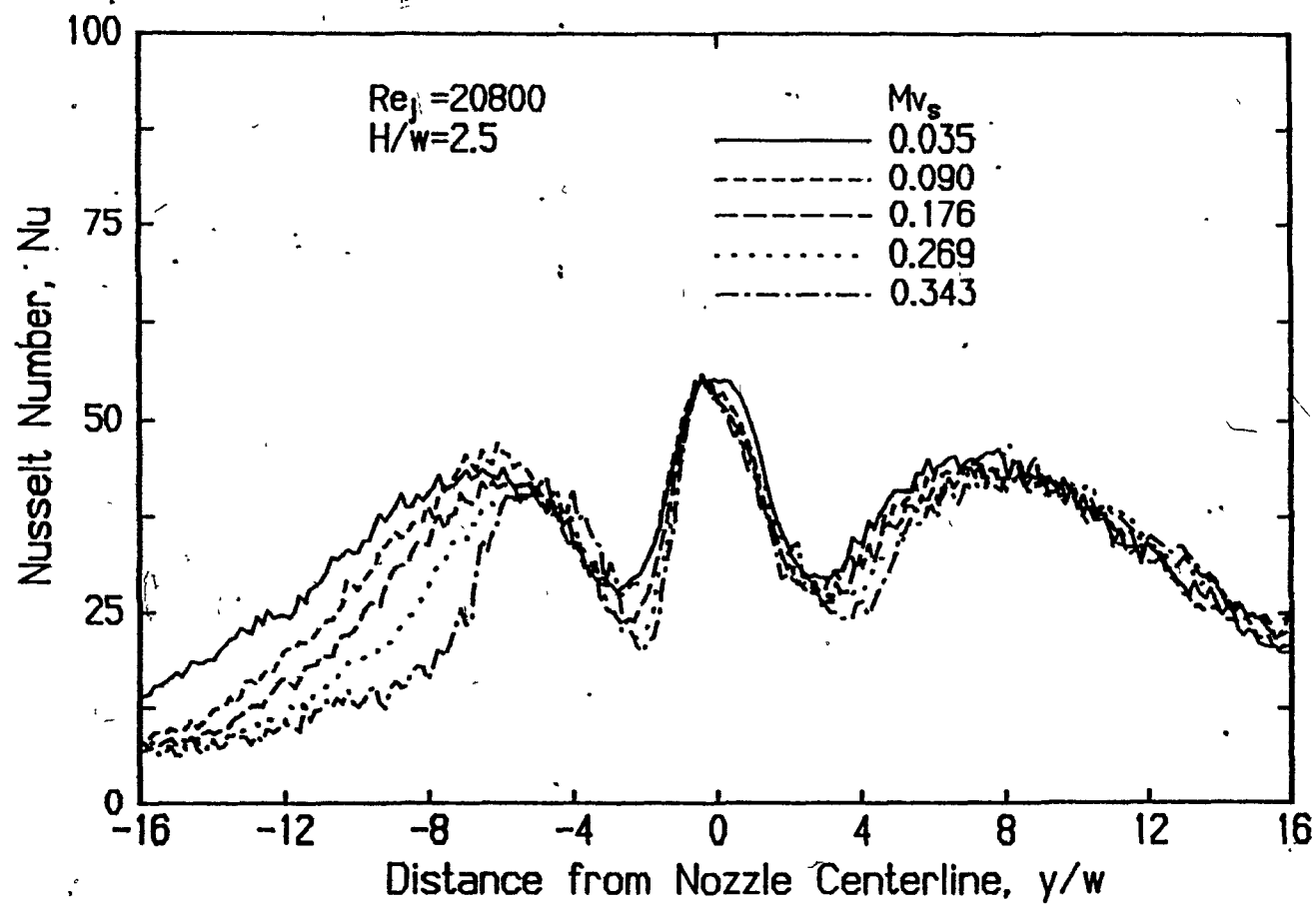


FIGURE 5.13. Effect of impingement surface motion on profiles of local Nusselt number at Re<sub>j</sub> = 20800

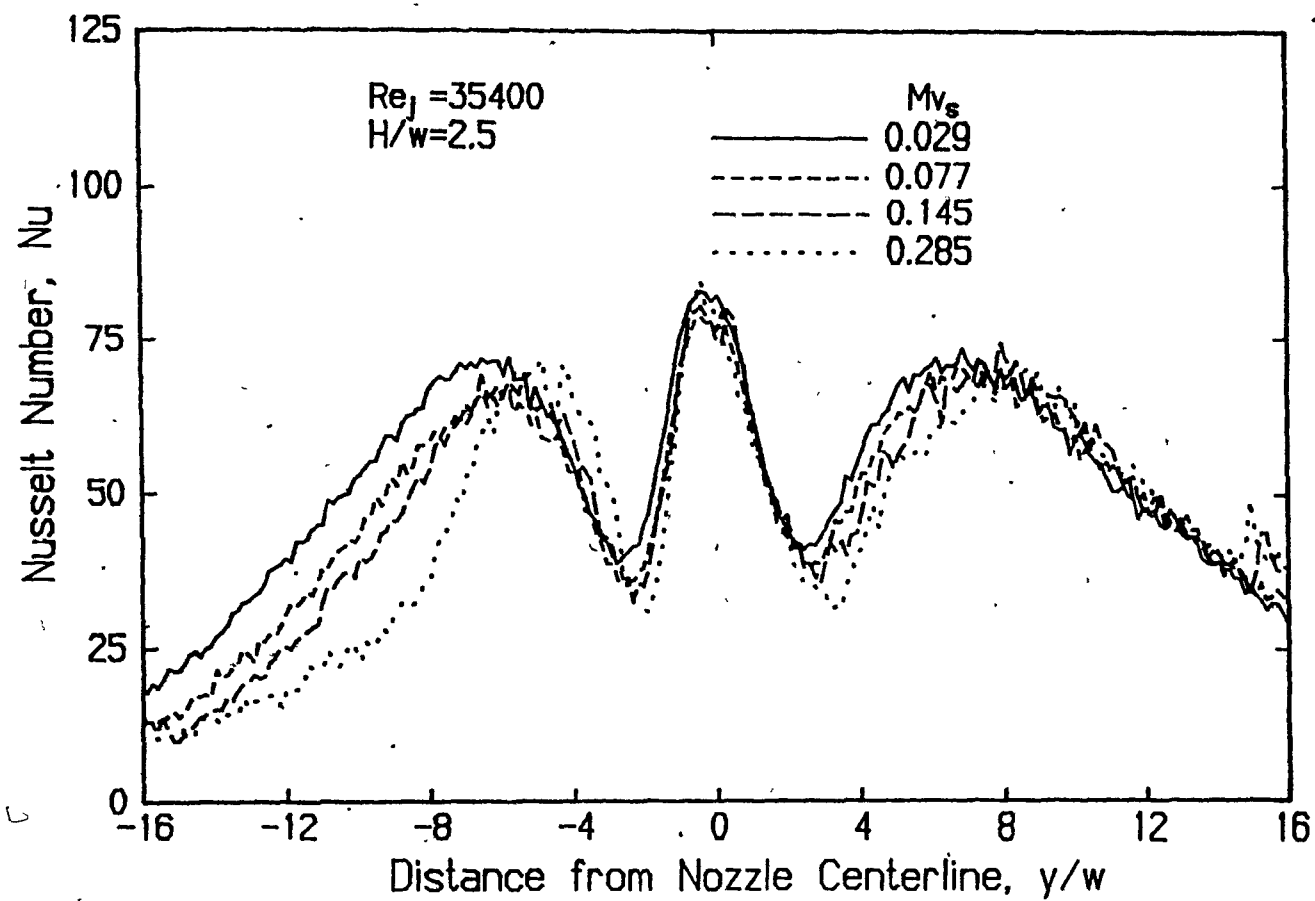


FIGURE 5.14. Effect of impingement surface motion on profiles of local Nusselt number at  $Re_j = 35400$



with the results of van Heiningen[1982] obtained with an impermeable sensor.

3. With increasing  $M_v$ , the Nusselt number at both off-stagnation minima decreases, but at the off-stagnation maxima  $Nu$  is not significantly affected.

4 The largest effect of surface motion on local heat transfer is a substantial change in the profile in the wall jet region beyond the off-stagnation maximum on the side where surface motion is towards the nozzle centerline, shown on the left in all graphs. By contrast, there is little effect in the comparable region on the side where surface motion is away from the nozzle centerline.

These observations on the effect of  $M_v$  in the absence of through-flow reproduce those of van Heiningen[1982]. Impingement surface motion affects boundary layer behaviour, including destruction of the symmetry which otherwise applies to all flow and heat transfer phenomena around the nozzle centerline. As pressure forces dominate the flow in the stagnation region there is less effect of surface motion here. Transition to a turbulent boundary layer starts at the off-stagnation minimum, i.e. at the end of the region of strong pressure gradient in the stagnation region, and finishes at the secondary maximum. An increase in  $M_v$  from nearly zero to its maximum value causes this transition to occur at a distance from the nozzle centerline about  $2w$  shorter and  $2w$  longer for the approaching and leaving sides, respectively. These shifts result from the corresponding increase and decrease in velocity gradient at the surface due to surface motion on, respectively, the approach side where surface motion opposes the fluid motion, and the leaving side where aiding

surface motion prevails.

Nusselt number for impinging jet heat transfer is defined on the basis of the temperature difference  $(T_j - T_s)$ . While  $(T_j - T_s)$  characterizes the  $\Delta T$  for the system as a whole, local heat transfer is a function of local  $\Delta T$ , a variable impractical to use. The standard definition of local Nu thereby takes no account of the local temperature driving force. Thus profiles of local Nu over an impingement surface are in fact profiles of local heat flux divided by a constant, the system  $\Delta T$ , not the local  $\Delta T$ . This interpretation of local Nu profiles as being in reality profiles of local heat flux provides an understanding of the largest effect of heat transfer surface motion, i.e. the large reduction in Nu (i.e. in heat flux) on the approach side, between the off-stagnation maximum and the far wall jet region. The increase in shear rates due to opposing surface motion at the heat transfer surface on the approach side in fact acts to increase local heat flux. But local  $\Delta T$ , which is maximum at the nozzle centerline, decreases with distance from the centerline. Thus on the approach side, surface motion drags fluid from regions of lower local  $\Delta T$ , thus decreasing the local  $\Delta T$  relative to that in the absence of surface motion. On the leaving side, the same mechanism causes the opposite effect. On the approach side, the effect of this reduction of local  $\Delta T$  is augmented by the equipment end effect noted in Sections 5.2.1 and 5.3.1, i.e. by the boundary layer of cool air which is dragged by the moving impingement surface into the heating jet region through the small gap between this surface and the skimmer plate. In the approach side wall jet area, these two effects tending to reduce local heat flux evidently predominate over the opposing effect of shear rate increase

at the surface. On the leaving side, where there is no mechanism analogous to the approach side end effect, the two opposing tendencies, i.e. enhancement of heat flux by the local  $\Delta T$  effect and decrease by the aiding flow effect on shear rate, evidently approximately cancel.

According to this view of near-surface heat transfer mechanisms, the reductions in off-stagnation  $Nu$  minima at the approach and leaving sides with increasing surface motion occur for different reasons. On the approach side, the decrease of minimum Nusselt number with increasing surface velocity indicates that the effect on heat transfer coefficient caused by the decrease in local  $\Delta T$  by near-wall fluid dragged from the region farther out is more important than the opposite effect of increase in shear rate associated with surface motion opposing the wall jet flow. On the leaving side the same two opposing effects apply. However the boundary layer at and near the stagnation point is so thin that there is little scope for increase in  $Nu$  by fluid dragged with the surface from the region of higher to lower local  $\Delta T$ . Thus on the leaving side the dominant effect at the off-stagnation minimum is a reduction in heat transfer associated with the reduction in shear stress at the surface for the aiding surface motion.

#### 5.4.1.2. Average Heat Transfer

At  $Re_j = 20800$  the decrease in  $\bar{Nu}$  in going from negligible to high surface motion, Fig. 5.15, increases with extent of the heat transfer surface for which the average applies, a trend predictable from the corresponding trends in local  $Nu$ , Figs. 5.13 and 5.14. The positions of off-stagnation minimum and maximum for local  $Nu$  on the approach and leaving sides are both displaced by about the same amount in the

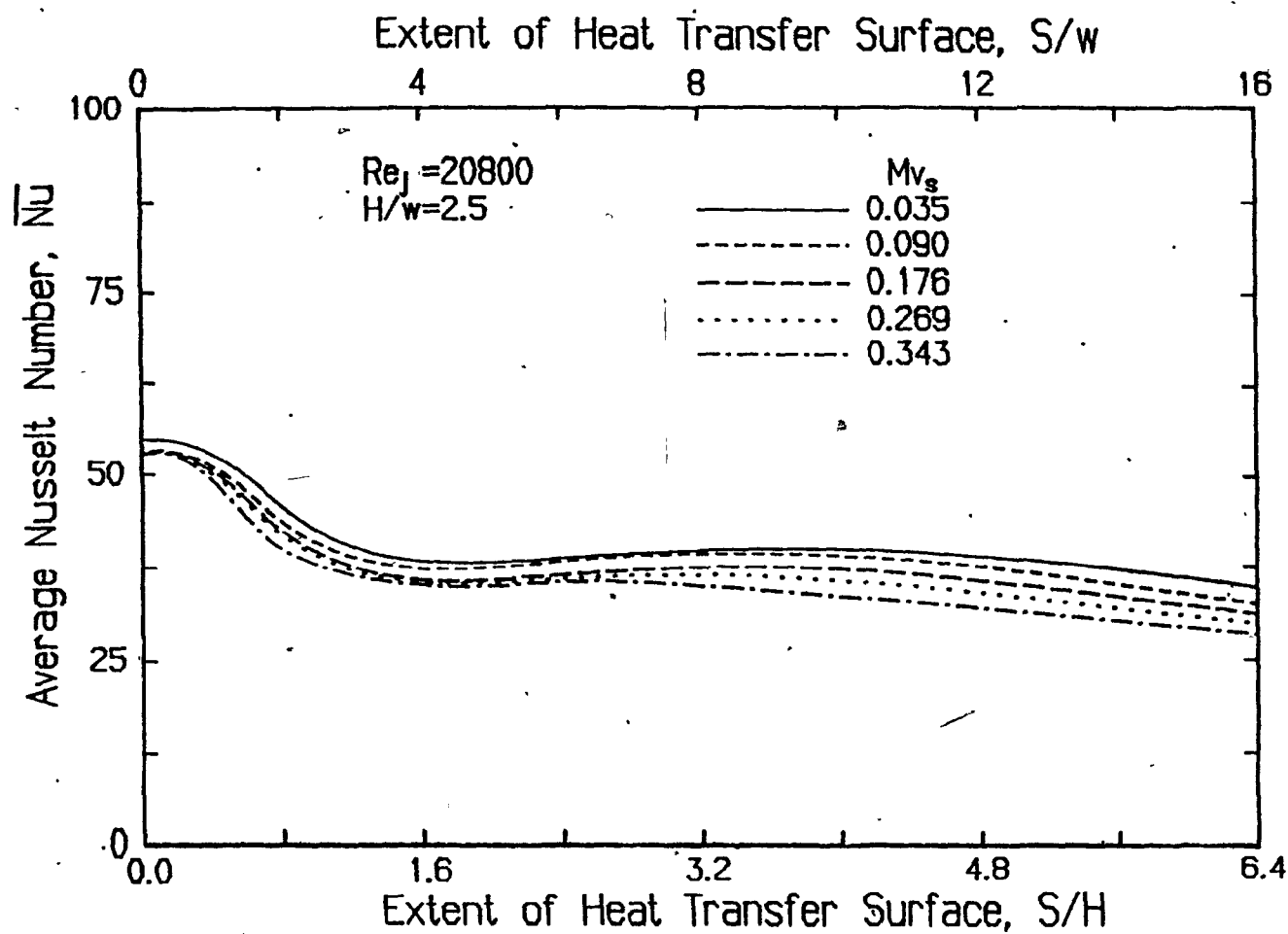


FIGURE 5.15. Effect of impingement surface motion on profiles of average Nusselt number

direction of heat transfer surface motion. Consequently the locations,  $4w$  and  $9w$ , of off-stagnation minimum and maximum of average profiles,  $\overline{Nu}_{min}$  and  $\overline{Nu}_{max}$ , Table 5.5 and Fig. 5.15, are essentially unaffected by surface velocity just as Fig. 5.3 established that these locations are unaffected by Reynolds number.

Average Nusselt number for  $H/w=2.5$  was correlated for heat transfer surfaces of half-width,  $S$ , in the range  $3.2H-6.4H$ , i.e.  $8w-16w$ , in the form:

$$\overline{Nu} = 0.0314 Re_j^{0.756} (1 + Mv_s)^{-0.89} \left(\frac{S}{H}\right)^{-0.22} \quad (5.8a)$$

over the range  $16400 < Re_j < 57700$  and for  $Mv_s$  values up to the high value of 0.34. Eq. 5.8a converges to Eq. 5.2 for the limiting case of a stationary impingement surface. For heat transfer surfaces smaller than covered by Eq. 5.8a, in the range  $1.2 < S/H < 3.2$ , i.e.  $3 < S/w < 8$ ; Fig. 5.15 indicates that  $\overline{Nu}$  is effectively independent of  $S$ , i.e. a modified equation, 5.8b, applies for which there is no  $S/H$  term.

$$\overline{Nu} = 0.0314 Re_j^{0.756} (1 + Mv_s)^{-0.89} \quad (5.8b)$$

For heat transfer surfaces narrower yet, i.e. for  $S$  less than  $1.2H$ ,  $3w$ , the nonlinear dependence of  $\overline{Nu}$  on  $S/H$  or  $S/w$  is provided by Fig. 5.15. In practice there is typically less interest in this range because at the limit  $S=1.2H=3w$ , the nozzle area is 16.7% of the impingement surface, a value uneconomically high for most industrial application.

The Fig. 5.16 comparison with the results at the two  $H/w$  spacings, 2.6 and 6, used by van Heiningen[1982], who did not present a correlation of his results, is made by expressing Nusselt number in a normalized form,  $\overline{Nu}/\overline{Nu}|_{v_s=0}$ , thereby isolating the surface motion effect. The comparison of Fig. 5.16 is for a heat transfer surface of

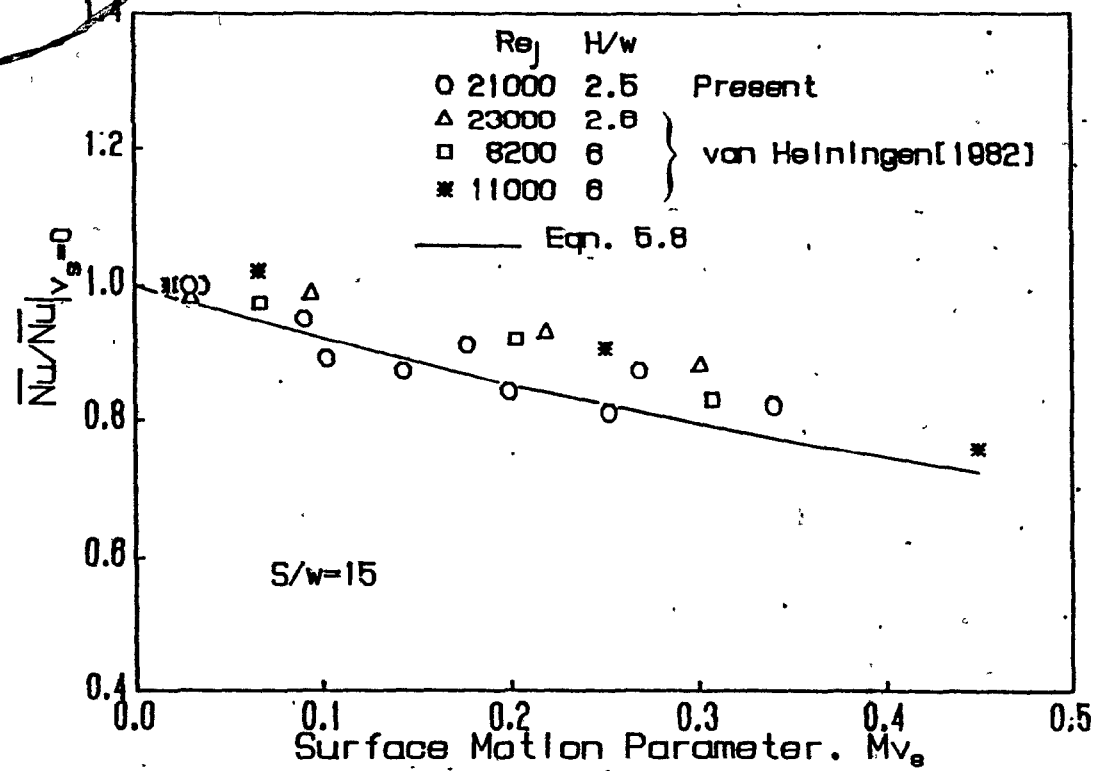


FIGURE 5.16. Comparison of results for effect of impingement surface motion on average Nusselt number

half-width,  $S$ , of  $15w$ , i.e. for nozzle area equal to 3.3% of the heat transfer area. Relative to the line representing the Eq. 5.7 factor,  $(1+Mv_s)^{-0.89}$ , the extent of scatter of the experimental data of the present study is quite good. The somewhat smaller decreases in  $\bar{Nu}$  of van Heiningen derive from his finding some enhancement of  $Nu$  on the leaving side at higher  $Mv_s$  values, an effect not found in the present study. More important, when calculated in this form the van Heiningen data indicate nearly the same effect of  $Mv_s$  on  $\bar{Nu}$  for both his values of  $H/w$ , 2 and 6. Thus it appears that the Eq. 5.7 and 5.8 factor,  $(1+Mv_s)^{-0.89}$ , can be used for spacings over the range  $2.5 < H/w < 6$ , and in the absence of data, may be used as the only guide available for values of  $H/w$  beyond those limits.

For the study of heat transfer without significant effect of surface motion, Section 5.2.1, the surface motion parameter,  $Mv_s$ , was kept less than 0.05, mostly in the range 0.02-0.035. From the above correlation it is now apparent that at  $Mv_s=0.05$ , average Nusselt number differs from that of a stationary impingement surface by indeed a small amount, <4%.

The decrease in  $\bar{Nu}$  with increasing  $Mv_s$  observed here and by van Heiningen[1982] is mainly due to the reduction of heat transfer on the side where surface motion is towards the nozzle centerline. By contrast to the results of these two studies using confined slot jets, for unconfined multiple jets impinging on a cylinder Fechner[1971] found that average heat transfer increased slightly with increasing  $Mv_s$  in the  $Mv_s$  range of the present study. As pointed out earlier by van Heiningen, this may be related to the effect of entrainment of ambient air in the absence of a confinement hood and to interaction of the

opposing wall jets from adjacent impinging jets which occurred in his equipment. As most industrial applications concern confined jet systems, the effect in Fechner's study attributable to the lack of confinement limits the significance of these results. Yet another factor which may have significantly enhanced his heat transfer rates, especially at higher  $Mv_s$  values, is high surface roughness of his cylinder,  $\sim 0.73\text{mm}$ .

In another study with a single unconfined slot jet impinging on a rotating cylinder Baines and Keffer[1979] found no appreciable effect of surface velocity on average wall shear stress for an averaging distance of  $\Delta y/w=32$  in the range  $0.01 < Mv_s < 0.2$ . The maximum limit of their investigation,  $Mv_s=0.2$ , is however much lower than those of the studies of van Heiningen, Fechner and the present study.

Subba Raju and Schlunder[1977] measured 1.5 to 2 times higher average heat transfer rates when a slot jet impinged on a slowly moving surface instead of a stationary one. In view of the heat transfer results of van Heiningen[1982] and the present study, which extend to much higher heat transfer surface velocities, it seems that the findings of Subba Raju and Schlunder at relatively slow surface velocities,  $Mv_s < 0.1$ , are not credible.

Thus for the four preceding studies of jets impinging on a moving surface, the findings as to the effect of impingement surface motion were highly contradictory. Subba Raju and Schlunder reported a large increase in heat transfer with increasing surface velocity. Fechner reported some increase. Baines and Keffer found no effect of surface motion on wall shear stress, which implies no effect on heat transfer. Van Heiningen found a significant reduction in impingement heat



transfer with increasing speed of the impingement surface. The good agreement between the results of the present study and that of van Heiningen, carried out with totally different experimental equipment and heat flux sensors, provides a definite answer at last to this contentious question. It is now clear that heat transfer from jets decreases substantially from that for stationary surfaces when impingement surface speed is increased to the range of some important industrial applications. For example, at the highest  $Mv_s$  value of 0.34, the appropriate term from Eq. 5.8 is  $(1+Mv_s)^{-0.89} = 0.77$ . This indicates a 23% reduction in  $\overline{Nu}$  relative to that for a stationary impingement surface. Thus if the amount of heat transfer surface required for an impingement surface moving under a typical industrial confinement hood at a velocity corresponding to  $Mv_s = 0.34$  were to be calculated using  $Nu$  data for a stationary surface, the result would be an area too small by about 23%, a design error of substantial magnitude.

The present study has also contributed an analytic correlation, Eq. 5.8, for the effect of impingement surface motion on average heat transfer, a correlation of a form applicable beyond the specific  $H/w$  spacing used. Finally, the agreement between the present results and those of van Heiningen for effect of surface motion provides another validation of the new heat flux sensor of the present study which, in the subsequent section, is applied to a case for which no previous experimental results exist.

#### 5.4.2 Heat Transfer with Throughflow at a Moving Impingement Surface

Measurement of local and average heat transfer for a jet impinging

on a rapidly moving surface at which there is throughflow has not previously been reported because no experimental technique existed for this difficult case. Development in the present study of a unique porous heat flux sensor, Chapter 4, enabled investigation of this industrially important problem.

In order to cover a wide range of nondimensional parameters of surface motion and throughflow for a jet with  $H/w=2.5$ , the local and average heat transfer results were determined for a fixed value of  $Re_j$ , 21000, a parameter thoroughly studied in the preceding sections. The ranges of the surface velocity and throughflow parameters,  $Mv_s$  and  $Mu_s$ , are 0.035-0.348, and 0.0-0.02, respectively. At the nozzle exit velocity of 22m/s for this jet of  $Re_j=21000$ , these ranges of  $Mv_s$  and  $Mu_s$  correspond roughly to a variation of surface velocity from 0.75m/s to 8m/s, and throughflow velocity from 0 to 0.4m/s. A summary of operating conditions and results is given in Table 5.6.

#### 5.4.2.1 Local Heat Transfer

The effect of throughflow on local heat transfer profiles for quite a high value of the surface motion parameter,  $Mv_s=0.27$ , displayed on Fig. 5.17 is analogous to the effect of  $Mu_s$  at very low  $Mv_s$  shown on Figs. 5.5 to 5.8. The base case of  $Mu_s=0$  for a very low  $Mv_s$  value, 0.035, is also displayed on Fig. 5.17. Thus in the absence of throughflow, Fig. 5.17 shows the shift from the symmetrical profile for the  $Mu_s=0$ ,  $Mv_s=0.035$  case, to the highly nonsymmetrical profile for  $Mu_s=0$ ,  $Mv_s=0.27$ . For this high speed of impingement surface, the remaining profiles of Fig. 5.17 show the effect of increasing throughflow at constant, high  $Mv_s$ .

Table 5.6. Operating conditions and results for single jet heat transfer at a moving surface with throughflow

$Re_j$	$Mv_s$	$Mu_s$	$T_j$	$T_j - T_s$	$Nu_o$	$\overline{Nu}_{max}^*$	$\frac{S}{W}$ for $\overline{Nu}$				
							8	10	12	14	16
20900	0.047	0.0	70.2	19.9	58	42.1	42.0	41.8	40.4	38.3	36.0
20750	0.047	0.0044	69.9	19.3	67.0	50.9	50.6	50.8	49.7	47.8	45.5
20650	0.046	0.0121	71.2	19.4	83.0	69.6	69.5	69.3	67.9	65.7	63.2
20000	0.045	0.0202	73.3	18.9	103.0	91.8	91.8	91.0	89.2	87.0	84.6
21600	0.2	0.0	65.1	19	56	38.8	38.8	38.2	36.4	34.3	32.2
21350	0.2	0.0043	65.3	19	67	49.2	48.9	48.9	47.5	45.4	43.1
21250	0.2	0.0102	66.3	17.8	83	64.9	64.8	64.5	63.1	61.1	58.7
21150	0.2	0.0171	67.7	17.4	98	83.6	83.6	82.8	81.0	78.7	76.4
21100	0.252	0.0	68.8	19.5	55	37.4	37.4	36.4	34.9	33.0	31.0
21050	0.251	0.0040	69.1	19.1	61.5	46.5	46.4	46.3	44.8	42.8	40.6
21000	0.250	0.0092	69.6	18.9	81.0	59.5	59.4	59.1	57.7	55.7	53.3
20400	0.035	0.0	86.2	27.3	55.2	40.1	40.0	40.0	38.7	37.0	34.8
20350	0.035	0.0055	86.3	26.7	66.0	52.4	52.1	52.3	51.3	49.5	47.4
20300	0.034	0.0114	86.6	26.2	82.0	68.5	68.4	68.2	67.0	65.2	62.9
20400	0.090	0.0	85.3	27.0	53.0	39.4	39.4	39.0	37.4	35.2	32.8
20400	0.090	0.0051	85.1	26.1	63.0	49.0	48.8	48.9	47.8	46.1	43.9
20400	0.090	0.0111	86.0	26.2	75.0	62.1	62.0	61.9	60.7	59.0	57.0
20200	0.086	0.0188	88.2	25.9	86.0	- **	75.4	74.4	72.5	70.1	67.3
20400	0.176	0.0	83.7	26.2	53.0	37.4	37.4	37.0	35.5	33.6	31.5
20650	0.175	0.0046	83.4	25.6	65.0	48.7	48.6	48.4	46.9	44.7	42.4
20650	0.174	0.0108	84.1	25.5	80.0	63.4	63.3	63.1	61.7	59.6	57.2
20200	0.172	0.0198	86.5	25.0	94.0	-	81.5	80.6	78.8	76.7	74.5
20850	0.270	0.0	83.4	27.0	54.0	36.3	36.3	35.5	34.0	32.2	30.3
20600	0.270	0.0066	83.8	25.6	67.0	51.7	51.5	51.4	50.2	48.1	45.8
20600	0.270	0.0104	84.3	25.5	73.0	58.4	58.3	58.2	57.1	55.2	53.1
20500	0.270	0.0186	85.8	25.0	90.0	79.3	79.3	78.5	76.7	74.5	72.3
21250	0.343	0.0	79.5	26.9	55.0	-	34.8	33.5	32.1	30.5	28.7
21100	0.342	0.0057	81.4	24.9	67.0	50.7	50.3	50.2	48.7	46.5	44.3
20900	0.344	0.0106	82.8	24.8	80.0	62.2	62.2	61.8	60.3	58.1	56.0
20500	0.348	0.0161	84.1	24.8	90.0	76.3	76.2	75.5	73.7	71.4	69.2

\*  $\overline{Nu}_{max}$  indicates off-stagnation maximum

\*\* Does not display an off-stagnation maximum

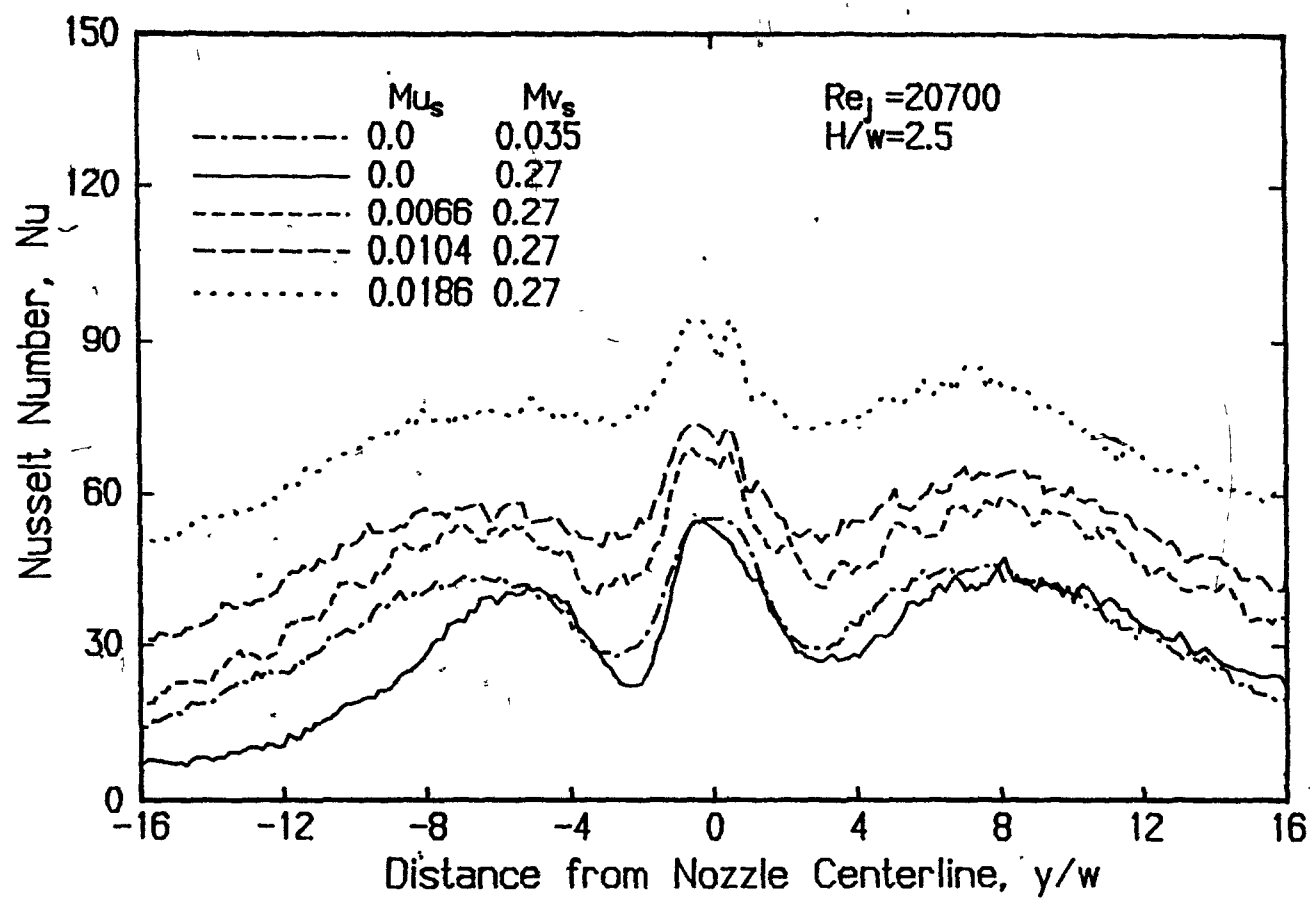


FIGURE 5.17. Effect of throughflow on profiles of local Nusselt number for an impingement surface moving at  $Mv_s = 0.27$

At high  $Mv_s$ , throughflow increases the distance out to the off-stagnation minimum and maximum on the approach side, by as much as  $1w$  in each case, while leaving the location of these features unchanged on the leaving side. With high surface velocity,  $Mv_s=0.27$ , the application of throughflow shifts the locations of the off-stagnation minima and maxima of the profiles back towards the symmetrical positions corresponding to the base case of no throughflow and negligible surface motion,  $Mv_s=0.035$ . Thus throughflow at a speeding surface acts to neutralize the effects of surface motion. Local heat transfer may be affected by the boundary layer carried by a moving heat transfer surface. Application of throughflow removes boundary layer fluid, hence counteracts this effect of a moving surface. Thus throughflow acts through two mechanisms to delay the boundary layer transition to turbulence that is signalled by the observed changes in position of these off-stagnation features. Throughflow is known to suppress near-surface turbulence, and as well, throughflow removes fluid from the boundary layer, thus delaying the onset of the instabilities in the thickening laminar boundary layer which lead to transition. These shifts in location of the off-stagnation features have the effect of making more-symmetrical these profiles which, at high  $Mv_s$  and without throughflow, are quite asymmetric. The shifts are substantial on the approach side, where surface motion transports the boundary layer in the direction from wall jet to impingement region. On the leaving side the direction of transport starts from the stagnation point, where the boundary layer is thinnest, hence the surface motion effect on the leaving side is minimal.

Comparison of the enhancement of local heat transfer by throughflow

at high  $Mv_s$ , Fig. 5.18, and at negligible  $Mv_s$ , Fig. 5.10, shows that high surface motion causes a more pronounced minimum and maximum in  $\Delta St$  profiles on the approach side while reducing these features on the leaving side. It was noted earlier that surface motion, without throughflow acts to decrease  $Nu$  at the off-stagnation minima and, for the approach side, over the region from the secondary maximum out to the far wall jet area. From Fig. 5.18 it is seen that the enhancement of heat transfer by throughflow is generally greatest in these regions. At the condition of high  $Mv_s$ -no throughflow, a mechanism for the large reduction in local heat flux for the approach side is the fluid dragged with the moving surface. Removal of such fluid by throughflow eliminates this source of decrease in heat flux. However the higher turbulence levels produced by the higher shear rates with opposing motion of the surface and the fluid flow on the approach side, is suppressed by throughflow. Thus as  $Mv_s$  increases, the turbulence damping effect would diminish to some extent the heat transfer enhancement associated with boundary layer removal on the approach side.

For the high  $Mv_s$ -no throughflow case, the leaving side minima of the  $Nu$  profiles, Figs. 5.13 and 5.14, reflect the reduction in heat transfer caused by the increase in the maximum thickness of the laminar boundary layer at this position. The withdrawal of boundary layer fluid by throughflow thus provides a large potential for increase in heat transfer in this region. Enhancement of heat transfer rate resulting from this effect produces a broad maximum centered at  $-4w$  from the nozzle centerline, Fig. 5.18, as compared to the sharper maximum at  $-2.5w$  on the  $\Delta St$  profiles for negligible  $Mv_s$ , Fig. 5.10.

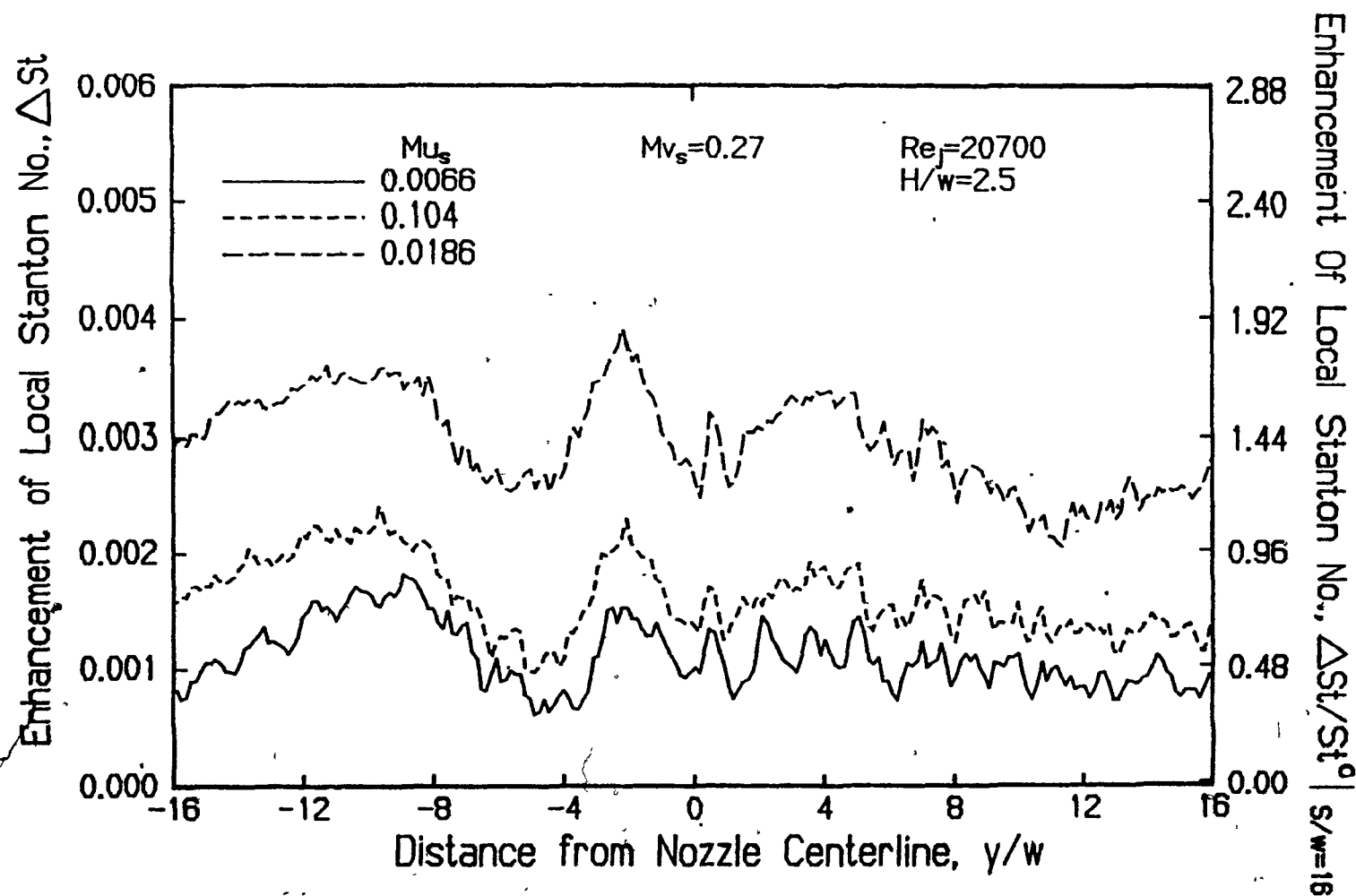


FIGURE 5.18. Profiles of enhancement of local Stanton number by throughflow for an impingement surface moving at  $Mv_s = 0.27$ .

In view of the interpretation given above it is of interest to compare the effect of surface motion on the heat transfer profile for two cases, with just a very small throughflow, Fig. 5.19, and at no throughflow, Figs. 5.13 and 5.14. The Fig. 5.19 conditions of  $Mu_s = 0.004$  and  $Re_j = 21000$ , correspond to throughflow and jet velocities of about 0.08m/s and 22m/s. As the present study used values up to  $Mu_s = 0.02$ , the throughflow of Fig. 5.19 is very low. It is impressive that the presence of a throughflow velocity even as small as  $Mu_s = 0.004$  stabilizes heat transfer over the entire impingement surface, making heat transfer with even a very small throughflow remarkably independent of surface motion. This behaviour is in sharp contrast to the high sensitivity to surface motion, Figs. 5.13 and 5.14, in the absence of throughflow. As boundary layer phenomena are central to determining impingement heat transfer rates, it is not surprising that throughflow, which so directly affects the boundary layer, plays this dominant role.

#### 5.4.2.2 Average Heat Transfer

Fig. 5.20 displays the effect of throughflow on profiles of average  $Nu$  for the  $Re_j (\approx 20700)$  and  $Mv_s (\approx 0.27)$  of Fig. 5.17. These profiles for an impingement surface moving at high speed show trends similar to those for throughflow effect without surface motion, Fig. 5.11. Thus as enhancement of local heat transfer by throughflow is greatest at the off-stagnation minimum, this minimum disappears with increasing throughflow. The values of the off-stagnation  $Nu_{max}^*$  listed in Table 5.6 are seen to correspond to the very flat maxima displayed by the profiles over the region near  $9w$ , Fig. 5.20.

On Fig. 5.20 it is seen that the enhancement by throughflow of



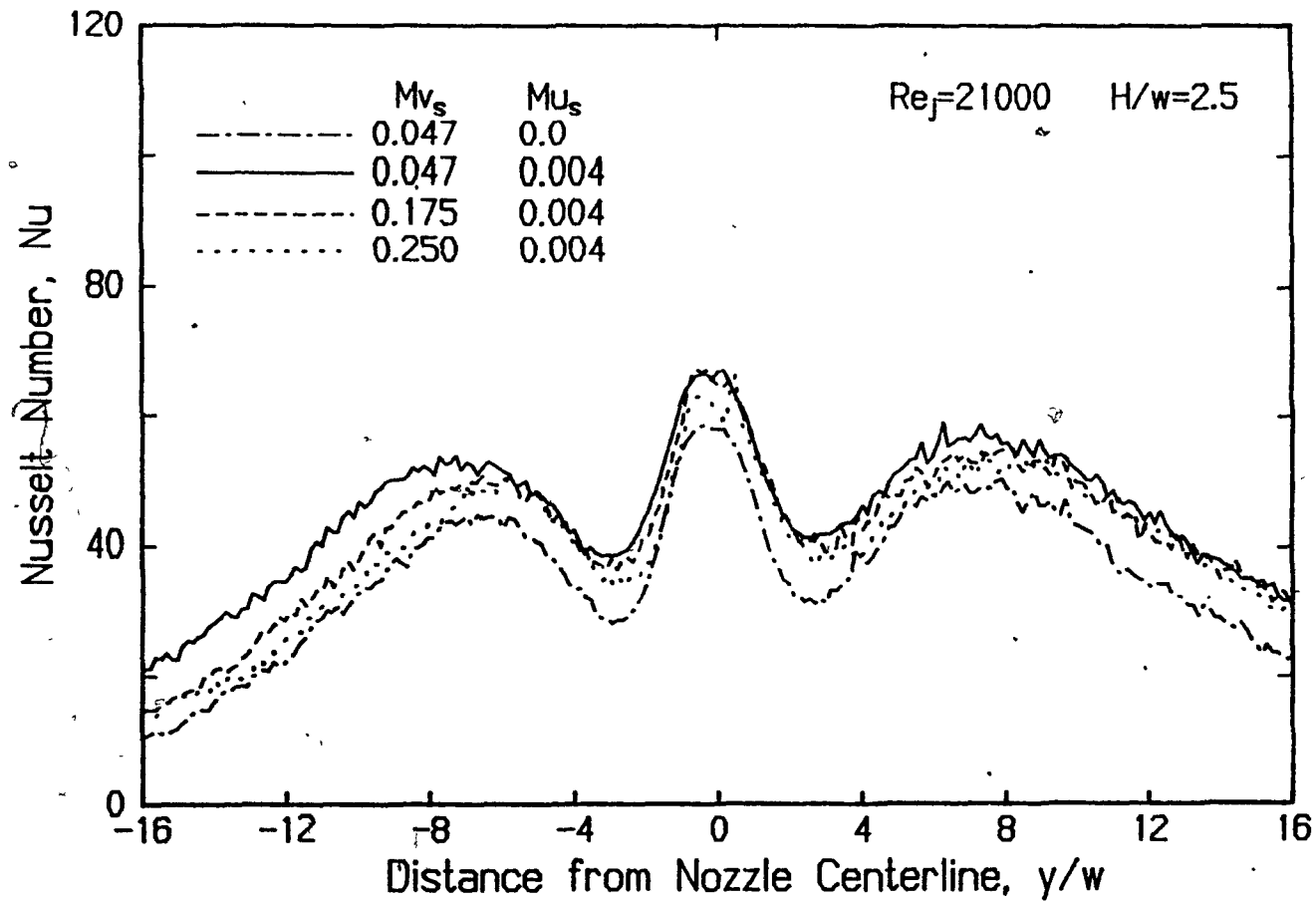


FIGURE 5.19. Effect of small throughflow,  $Mu_s = 0.04$ , on profiles of local Nusselt number for a moving impingement surface

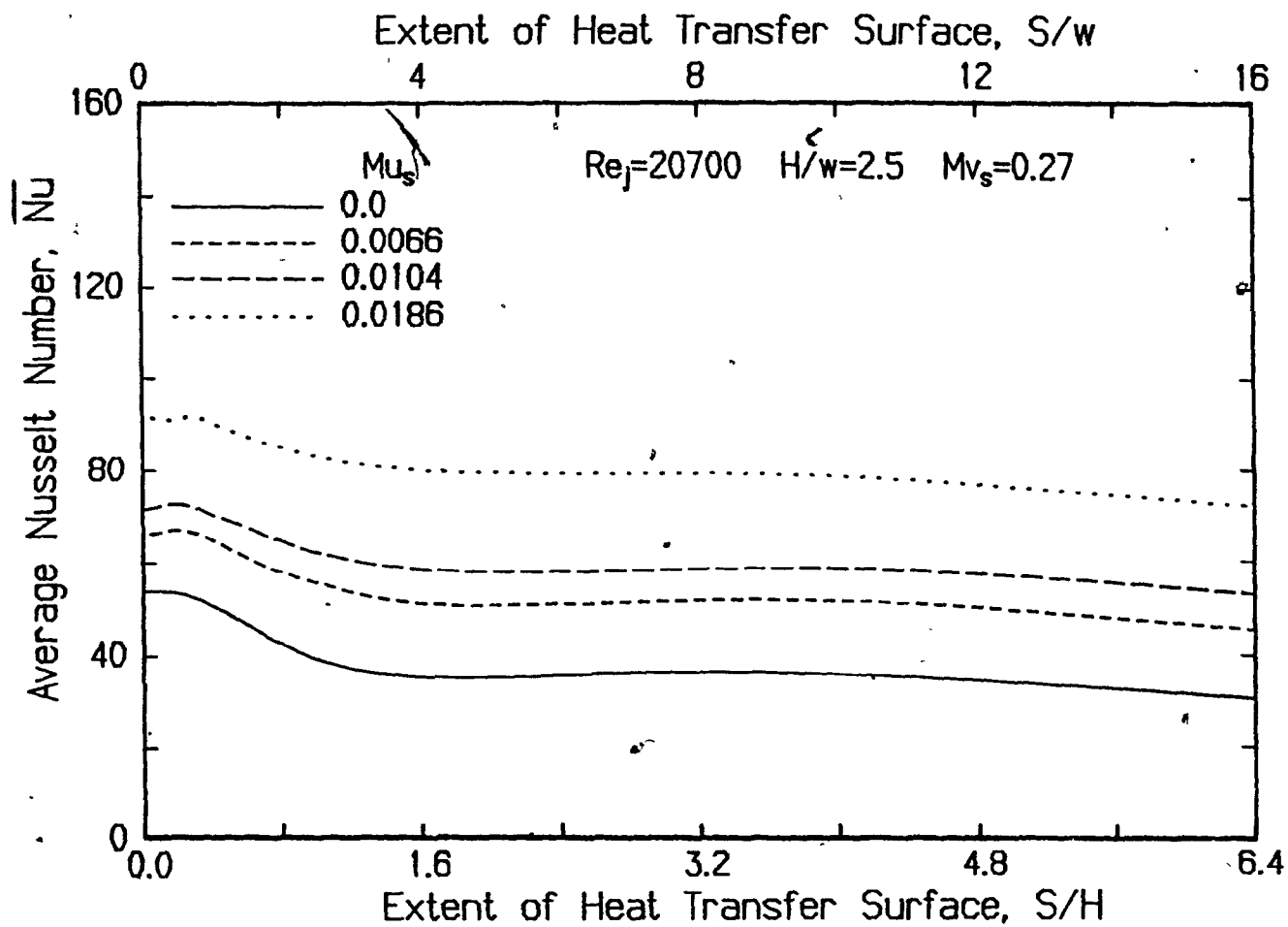


FIGURE 5.20. Effect of throughflow on profiles of average Nusselt number for an impingement surface moving at  $Mv_s=0.27$

integrated mean heat transfer rate at an impingement surface moving at high speed is nearly independent of the extent of transfer surface,  $S$ . This finding parallels exactly the throughflow enhancement behaviour in the absence of surface motion effects, as illustrated by Fig. 5.11. Thus the conclusion from Fig. 5.11, i.e. that the throughflow effect on  $\bar{Nu}$  for a stationary surface is linearly additive to that without throughflow, is seen by Fig. 5.20 to apply equally for an impingement surface moving at high speed.

This heat transfer enhancement, expressed as  $\Delta\bar{St}$ , appears on Fig. 5.21 as a function of  $Mu_s$  for the entire range of surface motion parameter  $Mv_s$ . Fig. 5.12 established that, in the absence of surface motion effects, the linear proportionality of  $\Delta\bar{St}$  with  $Mu_s$  is the same at all Reynolds number. Fig. 5.21 establishes that for impingement surfaces moving at up to quite high speeds, the linear proportionality of  $\Delta\bar{St}$  with  $Mu_s$  is the same at all values of  $Mv_s$ . The linear relation, Fig. 5.21, for the effect of throughflow on average heat transfer for any surface velocity up to maximum value used,  $Mv_s=0.35$ , is

$$\Delta\bar{St} = 0.17 Mu_s \quad (5.9)$$

for  $H/w=2.5$  and  $Re_j=21000$ , over the range  $0 < Mu_s < 0.02$ , and independent of extent of the impingement heat transfer area over the experimental range of  $S$  up to  $6.4H$ ,  $16w$ .

Fig. 5.12 establishes that  $\Delta\bar{St}$  is independent of  $Re_j$  over the range 16000-58000, and is represented by Eq. 5.5. Fig. 5.21 establishes that  $\Delta\bar{St}$  is independent of  $Mv_s$  up to the maximum value tested,  $Mv_s=0.35$ , and is represented by Eq. 5.9. As there is no significant difference between the slopes of Eqs. 5.5 and 5.9, the enhancement of heat transfer by throughflow applicable over the entire range of  $Re_j$ ,  $Mv_s$ ,

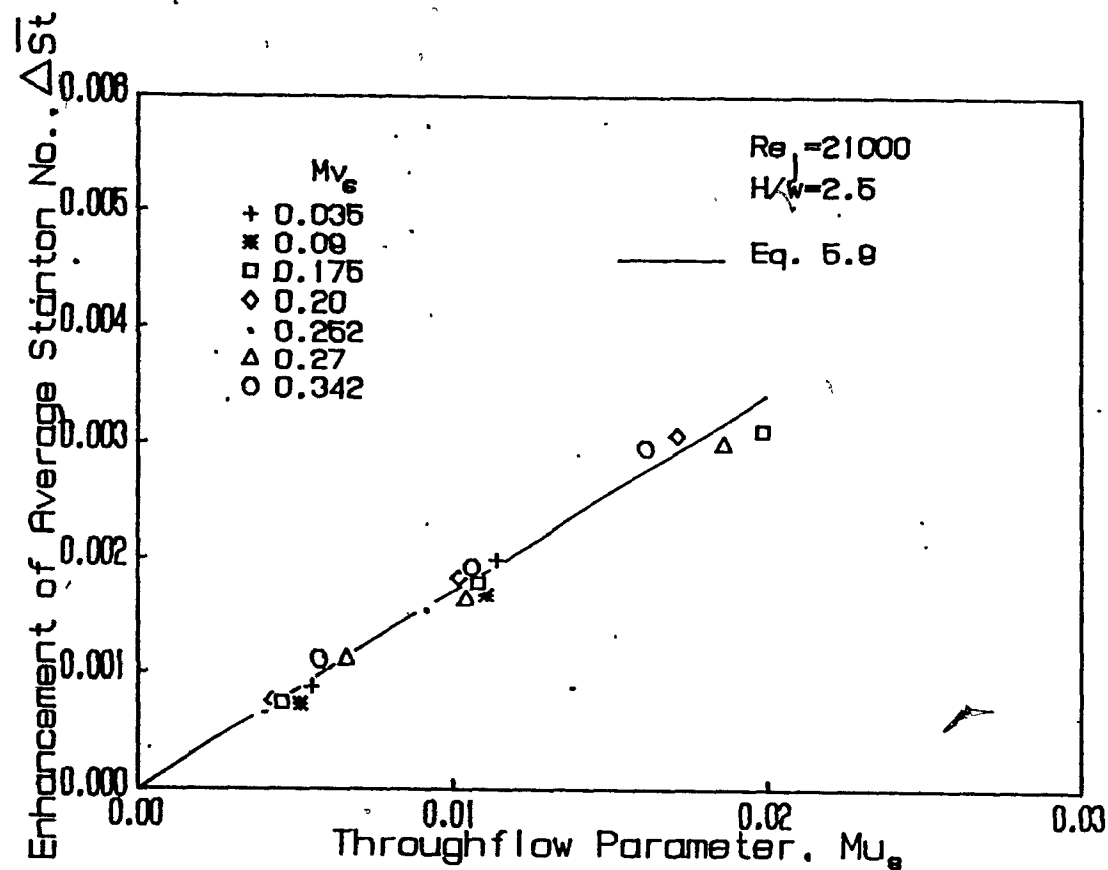


FIGURE 5.21. Effect of throughflow on enhancement of Stanton number for a moving impingement surface

and  $S/H$  tested may therefore be expressed by the single relation.

$$\Delta \bar{T} = 0.175 \text{ } \mu_{s} \quad (5.10)$$

Average Nusselt number under a confined slot jet at a spacing of  $H/w=2.5$  and subject to the combined effects of surface motion for  $Mv_s$  up to 0.35 and throughflow for  $\mu_s$  up to 0.02, for  $16000 < Re_j < 58000$  and with an extent of heat transfer surface in the range  $3.2 < S/H < 6.4$  (or  $8 < S/w < 16$ ) can therefore be predicted by combining Eqs. 5.8 and 5.10,

$$\bar{Nu} = 0.0314 \text{ } Re_j^{0.756} (1 + Mv_s)^{-0.89} \left( \frac{S}{H} \right)^{-0.22} + 0.175 \text{ } \mu_s Re_j Pr \quad (5.11)$$

The significance of this correlation incorporating all effects on average heat transfer for confined slot jets can be illustrated by a sample case, for the limiting values of  $\mu_s$  and  $Mv_s$ , 0-0.02 and 0-0.35 respectively, for which Eq. 5.11 is valid. For a jet with  $Re_j=20000$  impinging on a surface  $18w$  wide, i.e. which extends  $9w$  to each side of the jet nozzle centerline, thereby giving a nozzle open of 5.6%, the values of  $\bar{Nu}$  predicted by Eq. 5.10 are,

$\mu_s$	$Mv_s$	$\bar{Nu}$ for $S=9w$
0	0	42.2
0	0.35	32.5
0.02	0.35	80.2
0.02	0	89.8

Thus when throughflow is applied at the stationary heat transfer surface to achieve  $\mu_s=0.02$ , which corresponds to removal through the impingement surface of 36% of jet inflow, heat transfer is enhanced by about 110% relative to the no throughflow case. When the impingement surface without throughflow moves at a high velocity such that  $Mv_s=0.35$ , the average heat transfer is 23% less than for a stationary surface. However if the same throughflow,  $\mu_s=0.02$ , i.e. 36% of the

jet flow, is applied for the case of the high speed ( $Mv_s=0.35$ ) heat transfer surface, then the heat transfer enhancement due to throughflow is 150%. The higher relative enhancement of average heat transfer by throughflow when surface motion is present, established by the results of this study, is particularly promising for industrial applications which combine impingement heat transfer with throughflow at a heat transfer surface moving at relatively high speed.

### 5.5 CONCLUSIONS

Both local and average heat transfer under a confined slot jet impinging on a moving surface with or without throughflow at the surface was determined for a jet spacing of  $H/w=2.5$  and over the ranges of  $16000 < Re_j < 58000$ ,  $0.0 < \mu_s < 0.02$  and  $0.02 < Mv_s < 0.35$ .

The reliability of the present experimental methods was tested through use of operating conditions which have been studied previously to some extent. As the experimental facility provided the capability of operating with or without either throughflow or impingement surface motion effects, three combinations were used in the verification experiments, i.e. operation with neither of these effects, and with each effect in the absence of the other. In all cases good agreement with previous results was obtained, thus confirming the reliability of the experimental techniques. Moreover these new results extend substantially the published information concerning these cases.

In addition to local heat transfer profiles, complete profiles of average heat transfer were obtained with and without surface motion effects, and with and without throughflow. Correlations of analytical form for average heat transfer were determined for heat transfer

surfaces of half-width,  $S$ , in the range represented by  $1.2 < S/H < 6.4$  (i.e.  $3 < S/w < 16$ ). The corresponding range of nozzle open area is 16.7% down to 3.1%. Although in practice heat transfer surfaces smaller than this would probably be avoided as uneconomical, average heat transfer over smaller surfaces may be determined from the graphical relations provided. The confined single jet correlation obtained in this study may be used also for a confined multiple jet system with individual jets spaced sufficiently apart that their interaction does not significantly affect heat transfer. According to Saad[1981], that requirement is satisfied for  $S/H=1.5$ .

For impingement heat transfer without surface motion effects, the effect of throughflow on convective heat transfer is linearly additive to the heat transfer without throughflow. This proportionality for average heat transfer is independent of both Reynolds number and size of the heat transfer surface. The proportionality of convective heat transfer to the nondimensional throughflow parameter is much less than the Minkley-Spalding prediction. The reasons for this discrepancy are identified.

The present study contributes a method of using measurement of the effect of throughflow on shear stress at an impingement surface in order to predict the effect of throughflow on impingement heat transfer. Rather surprisingly, this prediction is within 20% of that measured experimentally.

The present experimental results for effect of throughflow without surface motion effects extend to throughflow rates about two times as high the information available from the only previous such investigation, Saad[1981].

For a confined slot jet impinging on a surface without throughflow, the addition of surface velocity was found to decrease average heat transfer, a result which corroborates the finding of van Heiningen [1982]. Thus the present results substantiate that the heat transfer measurements of Fechner[1971] and Subba Raju and Schlunder[1977] and the wall shear stress measurements of Baines and Keffer[1979] provide misleading guides as to the effect of speed of a moving impingement surface on heat transfer rate. The correlation for effect of surface motion on average heat transfer, Eq. 5.8, shows that designing the heat transfer area for a rapidly moving impingement surface ( $Mv_s = 0.34$ ) using data available previously for stationary impingement surfaces would lead to underestimating the required area by 23%. One major industrial process with a moving impingement surface, the Yankee dryer for drying paper, is operated in this range of  $Mv_s$ .

The most important contribution of this study is the measurement of convective heat transfer enhancement due to throughflow at a fast moving impingement surface. The measurement of profiles of local heat transfer with very high spatial resolution serve to identify flow and heat transfer effects in the boundary layer that are associated with throughflow, surface velocity and the combination of these conditions. As the main interest from an application point of view is in average heat transfer, this was determined in the form of an analytic correlation, Eq. 5.11. The results establish that the enhancement of average heat transfer, expressed as  $\Delta \overline{ST}$ , is linearly additive to the heat transfer without throughflow, and that this proportionality is a function only of throughflow ratio,  $Mu_s$  and, over substantial limits, is independent of  $Mv_s$ ,  $Re_j$  and extent of the heat transfer area. Close



agreement with results at low  $Mu$  values of Saad[1981] for a stationary impingement surface at  $H/w=8$  indicates that this correlation for throughflow effect should apply also for  $H/w$  spacings over the range 2.5 to 8, which covers the extent of major industrial interest.

## CHAPTER 6

HEAT TRANSFER UNDER MULTIPLE SLOT JETS IMPINGING ON A MOVING SURFACE  
WITH THROUGHFLOW

## 6.1 INTRODUCTION

This experimental investigation relates to the industrial importance of systems of impinging multiple jets for achieving high rates of heat transfer at rapidly moving surfaces. In practice, moving impingement heat transfer surfaces may also be permeable, as in the drying of paper. The case of a permeable impingement surface provides the possibility of inducing throughflow at the surface in order to further enhance heat transfer rates. Industrial impingement heat transfer systems involve multiple jets, and these generally cannot be unconfined. Thermal efficiency requirements normally dictate the use of a confinement hood which retains the impingement flow and which permits heat recovery or reuse of the spent flow. The present study is the first to provide heat transfer rates for a confined system of multiple slot jets impinging on a permeable moving surface at which there can be throughflow.

In the use of multiple jets, one basic design feature is the location of the ducting to exhaust the spent flow from the impingement system. In the arrangement chosen here, the spent flow exhausts at the confinement hood through slot ports which are located symmetrically between the slot jets and at a jet centerline-to-exhaust centerline spacing,  $S$ . This location of exhaust ports eliminates the detrimental effect of crossflow on impingement heat transfer, Saad[1981], Ahmad[1987]. Such a multiple slot jet system consists of repeating

flow cell units, each of width  $S$  and depth  $H$ , the confinement surface-to-impingement surface spacing. As three variables  $S$ ,  $H$  and the jet nozzle width,  $w$ , define the geometry of this confined multiple jet system, two independent nondimensional ratios define geometrically similar jet systems. One universally used ratio is the nozzle-to-impingement surface spacing,  $H/w$ . In his investigation of confined impingement system with a stationary heat transfer surface and with slot jets alternating with slot exhausts, Saad[1981] demonstrated that the appropriate choice for the second nondimensional ratio is  $S/H$ , the aspect ratio of the repeating flow cell units in such systems. He found that for  $S/H > 1.5$ , multiple slot jets become equivalent to an assembly of non-interacting single jets while for aspect ratios below a critical value of  $S/H = 0.7$ , the adjacent impinging jet and exhaust flows are sufficiently close that the flow and heat transfer characteristics are affected over the entire impingement surface.

Based on data for a wide range of jet Reynolds number,  $Re_j$ , (3000-30000) and geometrical parameters Saad obtained a general correlation for average Nusselt number,  $\bar{Nu}$ , which indicated that jet maximum value would be obtained for a multiple jet system with geometrical parameters  $H/w = 5$ ,  $S/H = 0.5$ . However these are only predicted conditions for maximum  $\bar{Nu}$  because this  $H/w$ - $S/H$  combination was not included in the experimental study of Saad for a stationary impingement surface, nor indeed of any other investigator. In view of the above noted aspect ratio critical value,  $S/H = 0.7$ , the predicted condition for maximum  $\bar{Nu}$ , i.e.  $S/H = 0.5$ , evidently corresponds to a multiple jet system in which the entering jets and leaving spent flows interact significantly.

The present study was thus undertaken to examine the effect of

throughflow at a surface moving at high speed under confined multiple impinging jets. The particular system used was chosen to provide the first experimental measurements of heat transfer at values of the geometrical parameters  $H/w$  and  $S/H$  for maximum impingement heat transfer rate. The range of operating variables was selected so that the results would be relevant for an important industrial application, the drying of paper. Local heat transfer rates under the multiple jets were measured with the unique heat flux sensor, Chapter 4, for a moving surface at which there may be throughflow. The principal fixed dimensions were  $H=50\text{mm}$ ,  $S=25\text{mm}$ ,  $w=10\text{mm}$ , and the range of various parameters is given in Table 6.1.

Table 6.1 Range of parameters

$w$ (mm)	10
$H/w$	5
$S/H$	0.5
$T_s - T_j$ ( $^{\circ}\text{C}$ )	9 to 23
$Re_j$	8100 to 25800
$u_j$ (m/s)	13.8 to 40
$u_s$ (m/s)	0 to 0.4
$v_s$ (m/s)	0.45 to 8

Heat transfer under multiple jets but without either throughflow or effects of surface motion is discussed in Section 6.2; the effect of throughflow without surface motion effects in Section 6.3; and the

effect of surface motion with and without throughflow in Section 6.4.

## 6.2 HEAT TRANSFER WITHOUT THROUGHFLOW OR IMPINGEMENT

### SURFACE MOTION EFFECTS

These experiments without throughflow were carried out at sufficiently low values of the surface motion parameter,  $M_v$ , ( $<0.05$ ), to make the effect of surface motion on heat transfer negligible. Table 6.2 summarizes operating conditions and heat transfer results.

The profiles of local heat transfer, Fig. 6.1, correspond to three jets located at positions,  $y$ , of  $-5w$ ,  $0$  and  $5w$ , or  $-1H$ ,  $0$  and  $1H$ , relative to the centerline of the middle jet, with the exhaust ports located symmetrically at  $-7.5w$ ,  $-2.5w$ ,  $2.5w$  and  $7.5w$ , or  $-1.5H$ ,  $0.5H$ ,  $0.5H$  and  $1.5H$ . The off-stagnation minima and maxima seen in local profiles of single impinging jets over this range of  $Re_j$  with  $H/w=5$  do not occur for jets as closely spaced as in the present case with  $S=2.5w=0.5H$ . For a stationary impingement surface, Saad[1981] showed that in flow cells of aspect ratio as narrow as  $S/H=0.5$ , interaction between jets and adjacent exhaust flows acts to depress jet centerline  $Nu$  by  $\sim 10\%$  and to enhance exhaust centerline  $Nu$  by  $\sim 25\%$  relative to profiles of  $Nu$  for a single jet. Fig. 6.1 demonstrates these two effects by reference to the  $Nu$  profile of Saad[1981] at  $H/w=4$ , i.e. at a nozzle-to-surface spacing which closely corresponds to  $H/w=5$ . Because of these two effects the Fig. 6.1 profiles are more uniform than for the equivalent single jet. Thus a system of multiple jets as closely spaced as that of the present study yields values of average and stagnation  $Nu$  number within  $10\%$ , Table 6.2.

Average  $Nu$  number, the main interest of the design engineer, is

Table 6.2. Operating conditions and results for multiple jet heat transfer without throughflow or impingement surface motion effects

$Re_j$	$M_{vs}$	$T_j$	$T_s - T_j$	$Nu_o$	$\overline{Nu}$
8100	0.038	39.7	18.8	48	42.8
8200	0.039	37.1	10.2	45	41.4
10350	0.038	36.9	22.3	57	51.5
12000	0.026	38.3	18.5	60	55.8
16200	0.024	34.6	10.8	75	68.7
20000	0.027	35.3	9.4	83	76.9
20600	0.023	27.8	14.8	84	77.7
25800	0.019	25.3	9.3	97	90.4

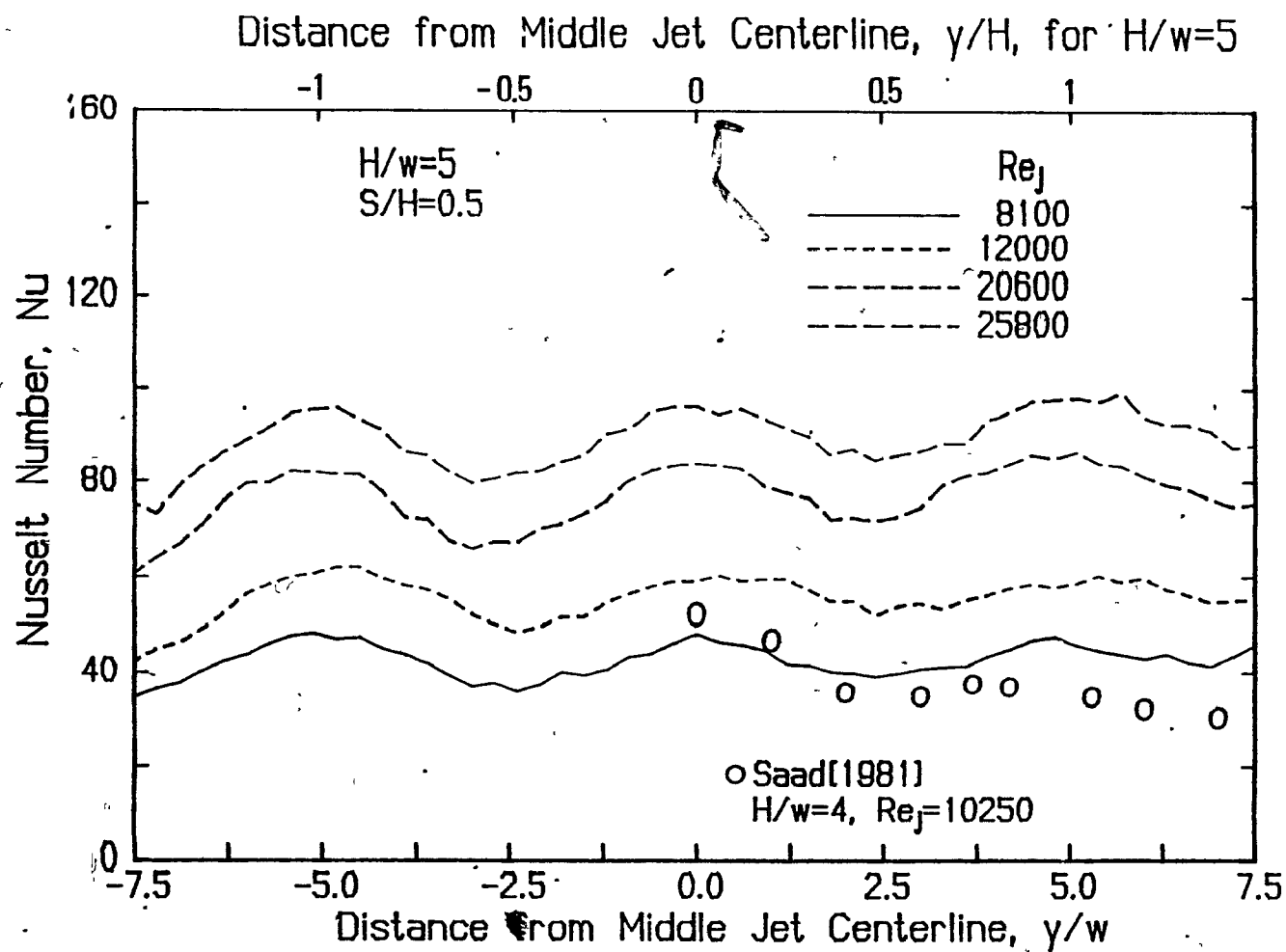


FIGURE 6.1. Effect of Reynolds number on profiles of local Nusselt number

obtained by integrating the local heat transfer distribution for the middle jet over the heat transfer surface of width  $2S$ , i.e. from  $-2.5w$  to  $2.5w$ , from  $-0.5H$  to  $0.5H$ . Thus each experimental profile of local heat transfer yields one value of average Nusselt number. Saad[1981] demonstrated that the center slot jet of a three-jet system is representative of a jet in multiple jet array.

In Fig. 6.2, the results for average heat transfer at  $H/w=5$ ,  $S/H=0.5$  as a function of  $Re_j$  are displayed with the results of correlations proposed by Saad[1981], Martin and Schlunder[1973], Schuh and Pettersson[1966] and Gardon and Akfirat[1966]. The range of validity of the geometrical and flow parameters of these correlations is shown in Table 2.2. Saad's correlation is for  $H/w \geq 8$  but by reference to his data for  $H/w=4$  he concluded that a 5% increase in  $\overline{Nu}$  above that for  $H/w=8$  would constitute a satisfactory estimate of  $\overline{Nu}$  at  $H/w=5$ . The Fig. 6.2 line for Saad corresponds to this recommendation. Gardon and Akfirat's correlation is limited to a percent open area of nozzles,  $f \leq 6.25\%$  and to  $H/w \geq 8$ . The values of the present study,  $H/w=5$ ,  $S/H=0.5$  or  $f=20\%$  are outside these limits. Since  $\overline{Nu}$  is not much affected by  $H/w$  over the range  $4 < H/w < 8$ ,  $\overline{Nu}$  at  $H/w=5$ ,  $S/H=0.5$  should be approximated by  $\overline{Nu}$  at  $H/w=8$ ,  $S/H=0.5$ , for which  $f=12.5\%$ . Thus the line for Gardon and Akfirat[1966] on Fig. 6.2 corresponds to their correlation evaluated at  $H/w=8$ ,  $f=12.5\%$ . As the correlations of Schuh and Pettersson[1966] and Martin and Schlunder[1973] apply for the conditions of the present study, i.e. for  $H/w=5$ ,  $S/H=0.5$ ,  $f=20\%$ , these correlations can be applied directly.

Schuh and Pettersson[1966] and Gardon and Akfirat[1966] studied unconfined multiple jets while Saad[1981], Martin and Schlunder[1973]



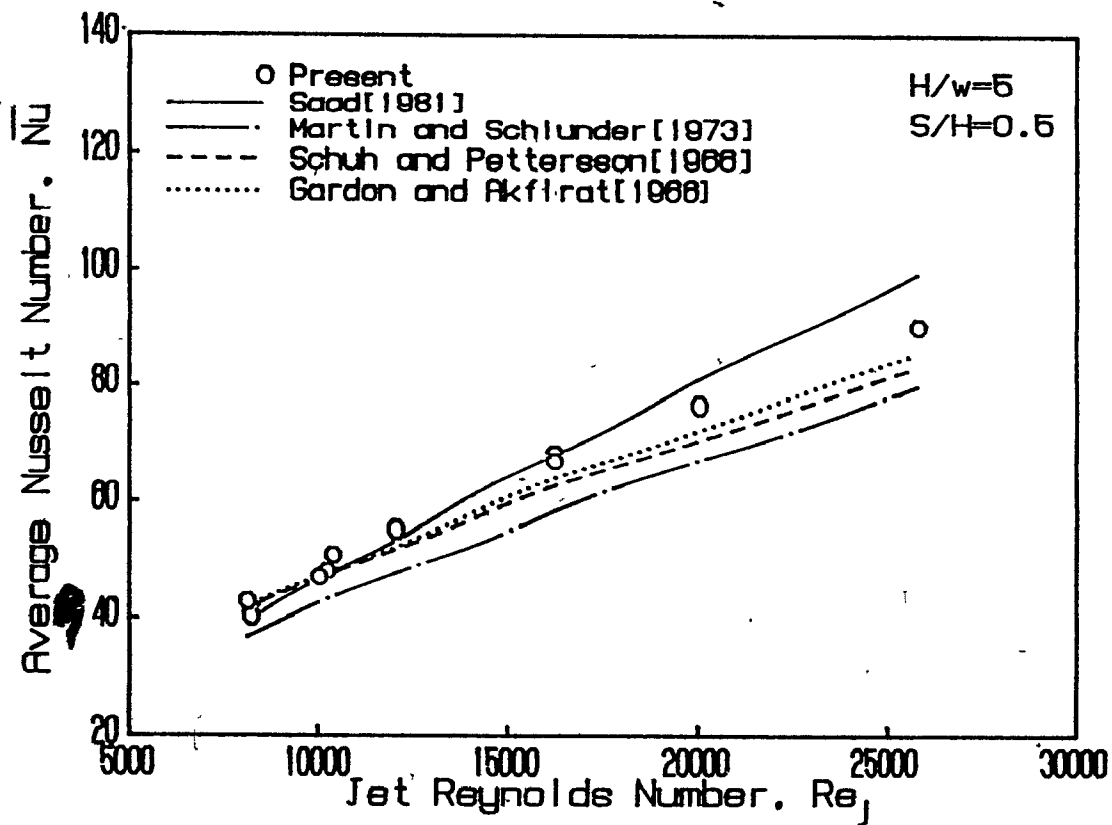


FIGURE 6.2. Effect of Reynolds number on average Nusselt number: Comparative studies.

and the present study used confined jets. The experimental system of Martin and Schlunder introduced a deleterious crossflow effect from their design of exhausting the spent air in the transverse direction at two ends of the slot jets. Thus it is as expected that, as indicated by Fig. 6.2, their correlation gives the lowest heat transfer rates. As this type of crossflow exhaust also causes a second disadvantage, i.e. nonuniformity of heat transfer in the cross machine direction, this arrangement is unacceptable for those industrial applications where uniformity of the dried product is essential, for example paper drying. The other studies exhausted the spent air between the jets, without crossflow, in the direction normal to the impingement surface. Heat transfer data from unconfined jets generally provide an unreliable basis for designing confined impingement systems because unconfined jet heat transfer is subject to several effects specific to the equipment used, i.e. the relationship between three temperatures- nozzle exit, impingement surface, ambient- as well as equipment dimensions near the nozzle exit that influence the amount of ambient air entrained by the jets. However the closer the internozzle spacing,  $S$ , in a multiple jet system, the less is the deviation of unconfined jet results from the performance characteristics of a confined jet system. With a flow cell aspect ratio,  $S/H$ , as small as in the present case, impingement heat transfer without confinement should differ less than usual from that for confined jets. Thus for the case of very closely spaced jets, Fig. 6.2, the unconfined jet results are never more than 10% lower than results with a confinement hood. In most industrial applications, including paper drying with impingement systems, use of confined jets is essential for containment and recovery of spent air to achieve good

thermal efficiency.

The following correlation applies for the results of the present study at  $H/w=5$ ,  $S/H=0.5$  in the absence of surface motion effects

$$\overline{Nu} = 0.0938 Re_j^{0.679} \quad (6.1)$$

for  $8100 < Re_j < 25800$ . This equation is the limiting form for  $Mv_s=0$  of the subsequent correlation, Eq. 6.4, which includes the surface motion effect. The  $Re_j$  exponent, 0.679, is in the middle of the range of all other studies, i.e. from 0.598 (Schuh and Pettersson[1966]) to 0.8 (Saad[1981]), Table 2.2.

From his correlations, Saad[1981] predicted that average heat transfer rate would be a maximum at  $H/w=5$  and  $S/H=0.5$ , but it is important to note that he made no measurement of heat transfer with this combination of  $H/w$  and  $S/H$ . For narrow flow cells, of aspect ratio,  $S/H$ , in the range 0.375-0.75 Saad's experiments were all for much larger spacings, in the range  $8 \leq H/w \leq 24$ . At  $H/w=4$ , the narrowest aspect ratio used by Saad was  $S/H=1.5$ , and multiple jets spaced this far apart act effectively as single jets. For  $Re_j=10500$ , Fig. 6.3 compares the  $\overline{Nu}$  value from the present study with Saad's results. The observation of Saad that the maximum in  $\overline{Nu}$  occurs between spacings,  $H/w$ , of 4 and 8 is substantiated by the measurement of present study at  $H/w=5$ . The line for  $\overline{Nu}$  at  $H/w=5$  presumably parallels the lines on Fig. 6.3 for other values of the  $H/w$  spacing. In conclusion, for a system of multiple confined slot jets interspaced symmetrically with slot exhaust ports the present study provides the first experimental measurement of  $\overline{Nu}$  for  $H/w=5$ ,  $S/H=0.5$ , and this measurement, made over a range of  $Re_j$ , is consistent with the prediction by Saad that the highest  $\overline{Nu}$  would be obtained for a system with the spacings  $H/w=5$ ,  $S/H=0.5$ .

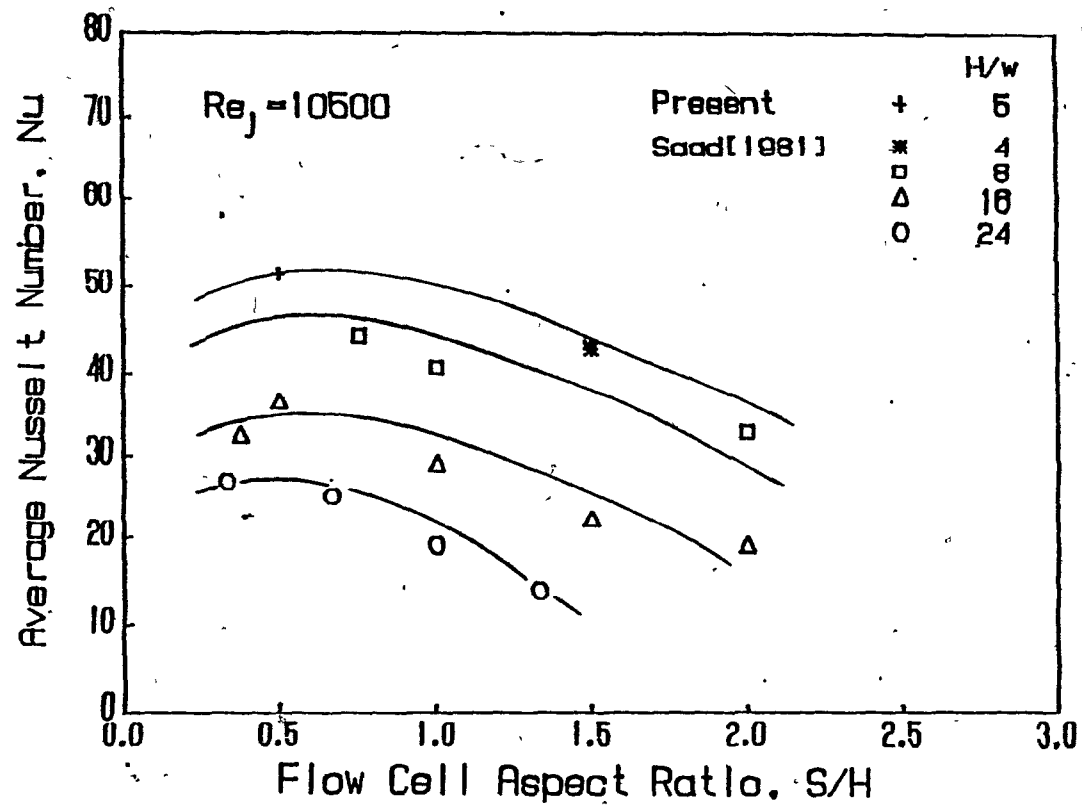


FIGURE 6.3. Effect of flow cell aspect ratio on average Nusselt number

### 6.3 HEAT TRANSFER WITH THROUGHFLOW

The effect of throughflow on local and average heat transfer under single slot jets has been studied by Saad[1981] for the case of a stationary heat transfer surface, and with and without the effects of impingement surface motion in Chapter 5 of the present study. Saad varied throughflow velocity from 0 to 0.3m/s in the  $Re_j$  range of 10200-29100 for a heat transfer surface of half width,  $S$ , of  $2.25H$ ,  $18w$ .

In the present case, the effect of throughflow on heat transfer under multiple jets was studied by varying the throughflow parameter,  $Mu_s$ , over the range 0 to 0.0235 for values of  $Re_j$  of from 8100 to 25800. These limits of the nondimensional parameters correspond to throughflow velocities from 0 to 0.35m/s and nozzle exit velocities from 15.6m/s to 47.7m/s. At the maximum value of the throughflow parameter,  $Mu_s=0.0235$ , only about 12% of the jet flow is removed through the heat transfer surface. Operating conditions and results are summarized in Table 6.3.

For each value of the throughflow parameter,  $Mu_s$ , every profile of local Nusselt number under multiple jets, when compared to profiles determined with no throughflow, were found to increase by a uniform amount over the entire impingement surface. Sets of profiles of local Nusselt number at various values of  $Mu_s$  are not shown because visually they are indistinguishable from sets of local  $Nu$  profiles at various  $Re_j$ . Fig. 6.1. This effect of throughflow on local profiles of multiple jets is consistent with the throughflow effect for single jets as reported by Saad and by the present study, Section 5.3.1.

The enhancement of heat transfer by throughflow is most appropriately expressed in terms of Stanton number for reasons documented for

Table 6.3 Operating conditions and results for multiple jet heat transfer with throughflow

$Re_j$	$M_{v_s}$	$Mu_s$	$T_j$	$T_s - T_j$	$Nu_o$	$\bar{Nu}$
8100	0.038	0.0	39.7	18.8	48	42.8
8100	0.038	0.0071	39.7	20.5	54	49.0
8200	0.039	0.0	37.1	10.2	45	41.4
8180	0.039	0.0063	37.6	11.0	50	46.9
8130	0.038	0.0159	38.5	11.4	60	57.2
8120	0.038	0.0159	39.1	11.6	57	55.3
7900	0.037	0.0235	40.6	11.9	65	63.1
10350	0.038	0.0	36.9	22.3	57	51.5
10350	0.039	0.0060	36.8	22.8	66	59.4
10320	0.037	0.0125	36.8	22.8	73	68.1
12000	0.026	0.0	38.3	18.5	60	55.8
12000	0.026	0.0063	38.4	19.3	67	63.1
11700	0.026	0.0109	38.7	19.9	69	65.9
11900	0.024	0.0184	39.8	20.1	78	73.8
16200	0.024	0.0	34.6	10.8	75	68.7
16050	0.024	0.0038	35.0	11.4	80	74.8
16000	0.023	0.0079	35.9	11.8	89	82.0
15750	0.025	0.0114	36.6	12.0	95	87.7
15950	0.024	0.014	37.0	12.1	96	91.0
20000	0.027	0.0	35.3	9.4	83	76.9
19930	0.027	0.0027	35.8	10.0	91	81.9
19700	0.027	0.0068	37.4	10.3	97	90.4
19600	0.026	0.0099	39.0	10.5	105	98.0
19500	0.026	0.0116	39.9	10.6	106	99.5
20600	0.023	0.0	27.8	11.8	84	77.7
20550	0.023	0.0022	28.5	12.2	89	81.6
20380	0.023	0.0062	30.1	12.8	94	87.5
25820	0.019	0.0	25.3	9.3	97	90.4
25700	0.019	0.0051	26.3	9.9	110	105.1
25550	0.019	0.0051	27.5	10.0	108	102.2
25400	0.018	0.0086	29.1	10.4	110	108.3
25000	0.018	0.0095	30.7	10.2	114	110.0
24860	0.018	0.0101	31.7	10.1	115	112.3

single jets in Section 5.3.1. Fig 6.4 shows that for multiple jets, the enhancement of average Stanton number due to throughflow is a linear function of the throughflow parameter,  $Mu_s$ ,

$$\Delta \overline{St} = 0.16 Mu_s \quad (6.2)$$

Moreover, the linear relationship between  $\Delta \overline{St}$  and  $Mu_s$  is independent of  $Re_j$  for a multiple confined slot jet system at  $H/w=5$ ,  $S/H=0.5$ , just as was found in Section 5.3.1 to be the case for a single slot jet. Comparison of Fig. 6.4 and Eq. 6.2 for this multiple confined jet system with Fig. 5.12 and Eq. 5.10 for a single confined jet at  $H/w=2.5$  and with heat transfer surfaces of half-width,  $S$ , up to  $6.4H$ ,  $16w$ , shows that essentially the same proportionality factor,  $\Delta \overline{St}/Mu_s$ , applies for the single and multiple jet cases. The line on Fig. 6.4 representing the single jet results of Saad for  $Mu_s < 0.012$  agrees at lower values of  $Mu_s$  and diverges at higher  $Mu_s$  for reasons given in Section 5.3.2. It is striking that the proportionality between average convective heat transfer enhancement and the throughflow parameter,  $Mu_s$ , is essentially the same for a single jet and for very closely spaced multiple jets, over a wide range of  $Re_j$  and width of heat transfer surface, and for nozzle spacings,  $H/w$ , over the range 2.5 to 8.

As enhancement of heat transfer due to throughflow is a linear function of throughflow velocity,  $u_s$ , the fraction of the jet flow rate which must be removed through the surface,  $Q_s = Mu_s/f$ , to produce a particular amount of heat transfer enhancement,  $\Delta \overline{St}$ , is inversely proportional to the fraction open nozzle area,  $f$ . Hence the present arrangement of closely spaced multiple jets,  $S/H=0.5$ ,  $S/w=2.5$ ,  $f=0.2$ , chosen for the objective of achieving the highest average heat transfer rate, has also the advantage of producing a high ratio of heat transfer

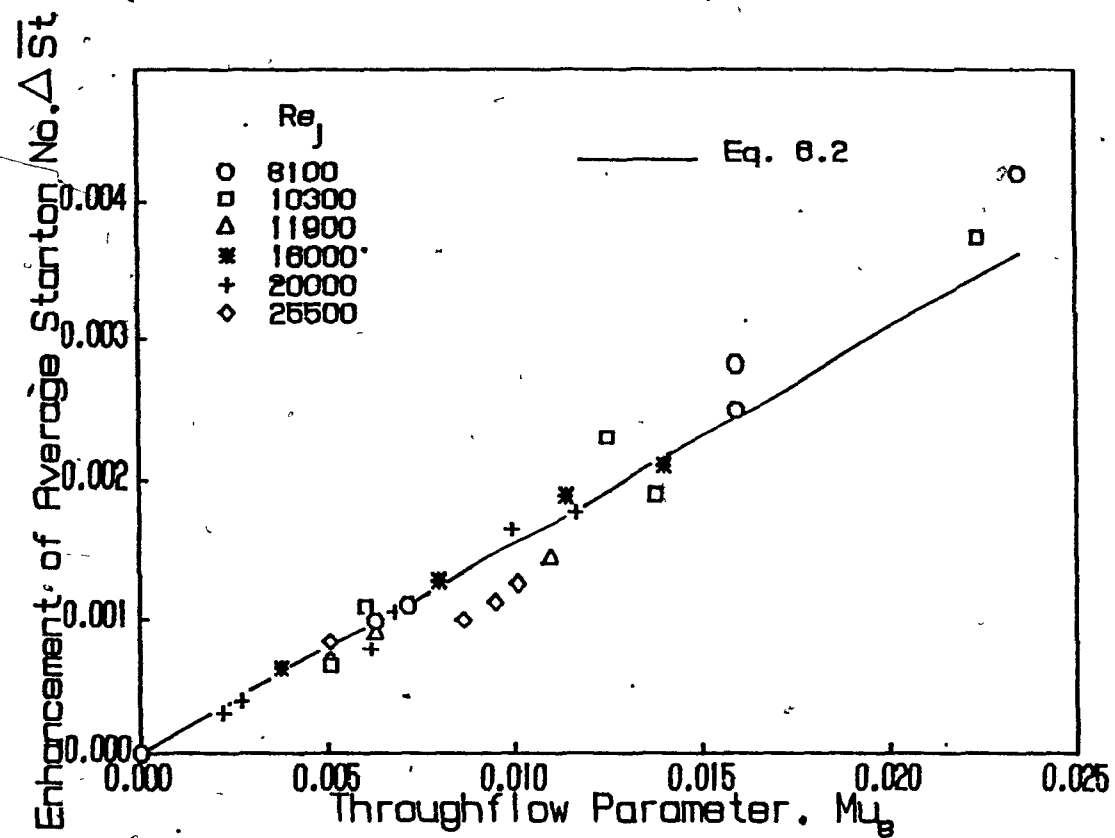


FIGURE 6.4. Effect of throughflow on enhancement of average Stanton number without surface motion effects



enhancement to the fraction of jet flow removed as throughflow,  $Q_s$ . For example, for  $Re_j = 25800$  with as little as 12% of  $Q_s$  average heat transfer enhances 75% as compared to a 16% enhancement in a widely spaced jet system with  $S = 6.4H$ , calculated using Eq. 5.11 for a single jet at  $H/w = 2.5$ .

As the throughflow effect on convective heat transfer is linearly additive, average Nusselt number in the presence of throughflow for a multiple confined slot jet system at  $H/w = 5$ ,  $S/H = 0.5$ , obtained by combining Eq. 6.1 and 6.2 with the relation  $St = \frac{Nu}{Re Pr}$ , is

$$\bar{Nu} = 0.0938 Re_j^{0.679} + 0.16 Mu_s Re_j Pr \quad (6.3)$$

for  $8100 < Re_j < 25800$  and  $0.0 < Mu_s < 0.0235$ . Excellent agreement between this correlation and the experimental measurements over the entire experimental range of  $Re_j$  is demonstrated with Fig. 6.5. Further discussion of the effect of throughflow is deferred to the following section where the combined effects of throughflow and surface motion are treated.

#### 6.4 HEAT TRANSFER AT A MOVING IMPINGEMENT SURFACE

##### 6.4.1. Without Throughflow

Operating conditions and heat transfer results for the effect of impingement surface velocity on multiple jet heat transfer are given in Table 6.4. Surface velocity was varied to achieve values of the nondimensional surface motion parameter,  $Mv_s$ , in the range 0.019-0.38, which corresponds to surface velocities from 0 to 8m/s for  $8200 < Re_j < 16200$ .

With the close internozzle spacing  $S/H = 0.5$ , chosen for the present study, profiles of local  $Nu$  reveal no important information concerning

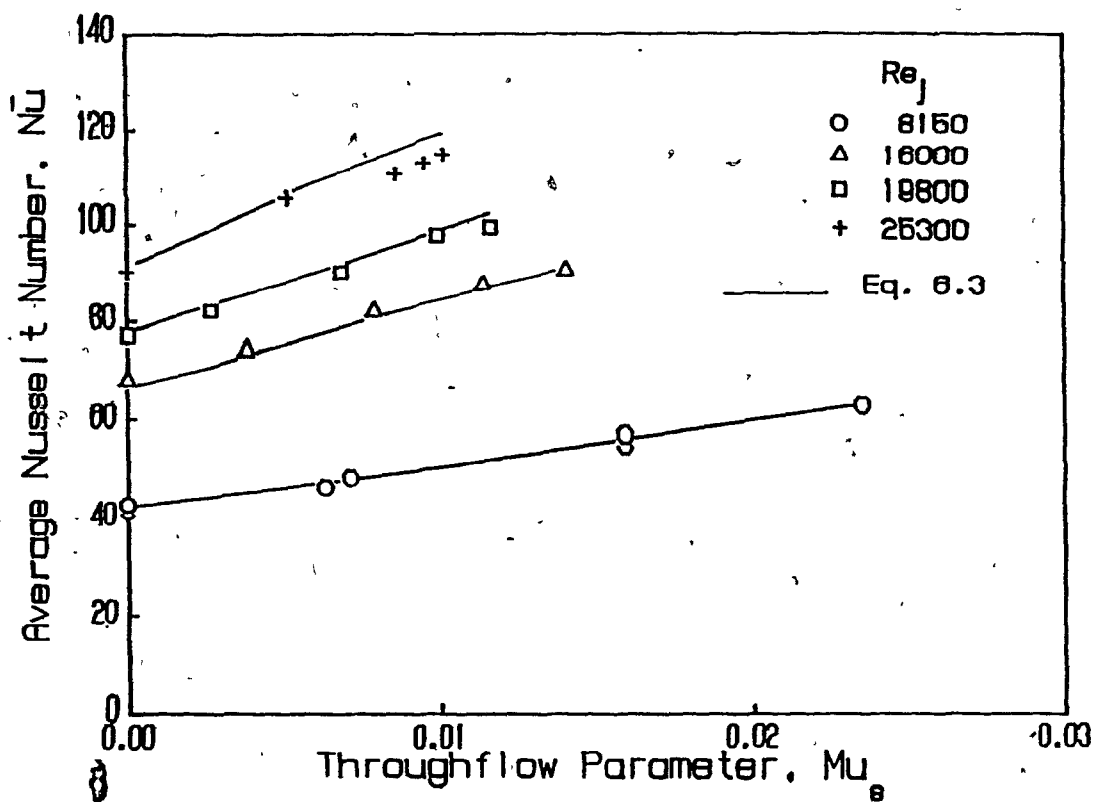


FIGURE 6.5. Effect of throughflow on average Nusselt number: Correlation and experiments

Table 6.4 Operating conditions and results for multiple jet heat transfer at a moving surface without throughflow

$Re_j$	$M_{vs}$	$T_j$	$T_s - T_j$	$Nu_o$	$\overline{Nu}$
8200	0.039	37.1	10.2	45	41.4
8100	0.038	39.7	18.8	48	42.8
8200	0.063	36.7	10.1	44	40.3
8200	0.139	36.9	10.0	40	38.1
8200	0.189	36.9	10.2	40	37.1
10200	0.033	29.5	16.5	53	48.4
10350	0.038	36.9	22.0	57	51.5
10050	0.053	33.2	17.1	52	47.2
10360	0.099	36.4	21.9	53	47.3
10200	0.117	29.7	16.3	47	43.8
10200	0.164	29.8	16.3	46	42.6
10500	0.192	35.6	21.9	48	43.1
10200	0.229	29.9	16.2	46	41.8
10100	0.286	32.6	16.8	43	41.0
10600	0.295	34.9	21.5	48	43.2
10700	0.380	32.8	19.8	52	43.0
16200	0.024	34.6	10.8	75	68.7
16200	0.033	34.7	10.7	75	67.2
16200	0.069	34.6	10.7	69	63.2
16200	0.089	34.6	10.6	67	63.2
16200	0.118	34.6	10.7	68	60.9
16200	0.168	34.6	10.7	66	60.2
16200	0.211	34.6	10.6	65	58.2
16200	0.267	34.6	10.5	65	58.2
16200	0.329	34.6	10.8	65	57.0

heat transfer mechanisms at the impingement surface, hence simply provide the basis of determining the measurement of prime interest, average heat transfer

Average Nusselt number, determined for  $H/w=5$ ,  $S/H=0.5$  by integration of the experimentally determined profiles of local Nusselt number, was correlated in the form.

$$Nu = 0.0938 Re_j^{0.679} (1 + Mv_s)^{-0.69} \quad (6.4)$$

over the range of  $8200 < Re_j < 25800$  and  $Mv_s$  values up to 0.38. Eq. 6.4 converges to Eq. 6.1 for the limiting case of a stationary impingement surface. Fig. 6.6 displays the excellent agreement between the above correlation and the experiments

Surface motion affects local Nu profiles through two mechanisms, its effect on wall shear stress and on local  $\Delta T$ . Wall shear stress is increased on the side where the surface motion is towards the nozzle centerline and thereby opposes the jet flow. The opposite effect exists on the other side where surface motion and the jet flow are in the same direction. Correspondingly, the local Nusselt number on a moving impingement surface is expected to increase at the approach side, decrease at the leaving side.

The moving impingement surface alters local  $\Delta T$  by dragging a fluid layer of different temperature in the direction of surface motion. The change in local  $\Delta T$  by surface motion reduces heat transfer rate on the approach side and enhances it on the leaving side. Thus on the approach side of the nozzle centerline, local Nusselt number tends to increase because of the wall shear stress effect and decrease because of the change in local  $\Delta T$ , while these opposing effects each act in the opposite way on the leaving side. The experimentally

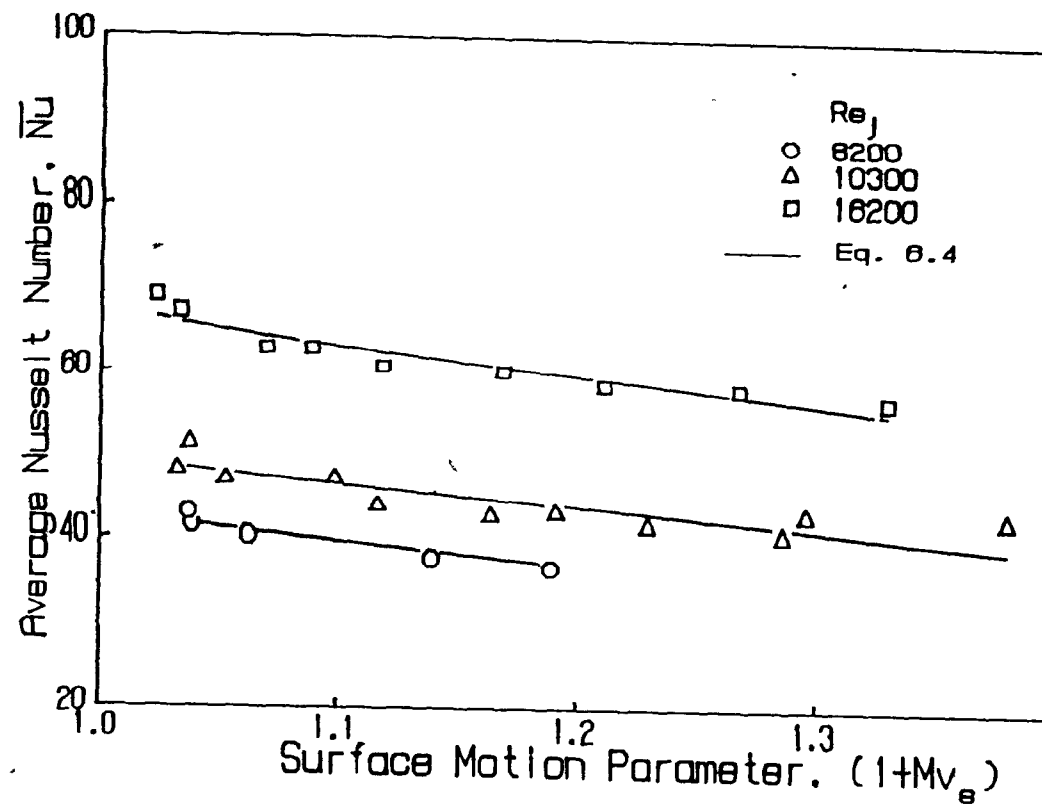


FIGURE 6 6. Effect of impingement surface motion on average Nusselt number

determined overall effect of surface motion on average Nusselt number, Eq. 6.4, is, as for the case of the single jet, to decrease  $NU$ . Thus the mechanisms noted are not linear and, although opposite on the two sides of the nozzle centerline, the effects do not cancel.

The average Nusselt number data for the single jet, Chapter 5, was correlated for a heat transfer surface half width of from  $3.2H$  to  $6.4H$ , i.e. in the wall jet region including the off-stagnation minima and maxima of the local profiles. For the present multiple jet system the half width of the heat transfer surface is only  $0.5H$ ,  $2.5w$ , i.e. within the stagnation region of a corresponding single jet. As pressure forces dominate the flow in the stagnation region of a single jet at small  $H/w$  spacings, the effect of surface motion on Nusselt number is less in this region than its effect on  $Nu$  in the wall jet region, Fig. 5.15. Thus the exponent of the  $1/(1+Mv_s)$  term, Eq. 6.4, for the present multiple jet system,  $0.69$ , is as expected smaller than that,  $0.89$ , for the single jet, Eqs. 5.8a and 5.8b.

Haslar and Krizek[1984] measured average mass transfer rates from an impermeable rotating cylinder under multiple unconfined slot jets at  $H/w=8.5$ ,  $S/H=0.6$  for  $Re_j$  values in the range  $1300-3300$  and  $Mv_s$  values up to  $0.4$ . For these low values of  $Re_j$  they reported that the average mass transfer rate at a slowly moving surface was substantially higher than that at a stationary surface. After this sudden enhancement in average mass transfer for a very low  $Mv_s$ , they observed a much smaller increase in mass transfer with further increase in surface velocity. In light of the extensive results of the present study on the effect of surface motion on impingement heat transfer Haslar and Krizek's findings in the narrow  $Re_j$  range of their study are not realistic and

may be presumed to derive from some equipment specific aspect of their mass transfer experiment.

For the study of heat transfer without appreciable effect of surface motion, Section 6.1, the surface motion parameter,  $Mv_s$ , was kept less than 0.05. Indeed at  $Mv_s = 0.05$ , Eq 6.4 gives a  $Nu$  value which is only marginally less, 3%, than that for a stationary heat transfer surface. On the other hand, one important industrial application of multiple jet impingement systems, the Yankee dryer, operates with quite high values of  $Mv_s$ , about 0.3. Eq 6.4 indicates that in the design of a multiple jet system for the case of  $Mv_s = 0.3$ , use of heat transfer data obtained with a stationary impingement surface would lead underestimating the heat transfer area required by about 17%, not a negligible amount in the design of expensive equipment.

#### 6.4.2. With Throughflow

Results are now presented for the most exacting aspect of the present study, the measurement of local and average heat transfer at a permeable surface at which throughflow is varied over a wide range and which is moving at up to quite high speed under multiple impinging jets. The effect of throughflow on impingement heat transfer for a broad range of surface velocities was studied for a constant  $Re_j$ , about 10000, by determining profiles of local heat transfer for 27 combinations of the throughflow parameter,  $Mu_s$ , from 0 to 0.022 and the surface motion parameter,  $Mv_s$ , from 0.038 to 0.38. If the permeable impingement surface were a sheet of moist paper, then these conditions would describe a combined impingement and through dryer for paper.

Although that is not a process used in the paper industry, results have been reported by Burgess et al. [1972a, b] for experiments with a prototype of a combined impingement and through dryer, called the "Papridryer", operated at conditions which are listed below for comparison with those of the present study.

	Present investigation	Papridryer
$u_s$ , m/s	0-0.35	0.046-0.269
$u_j$ , m/s	18	12.7-97
$v_s$ , m/s	0.7-8	2-3.6
$Re_j$	8200-25800	1000-3000
$Mu_s$	0-0.0235	0.0005-0.0054
$Mv_s$	0.038-0.38	0.035-0.48
$Q_s$ , %	0-12	2.7-34

Operating conditions and heat transfer results are summarized in Table 6.5.

With multiple jets as closely spaced as in the present study, i.e. of flow cell aspect ratio  $S/H=0.5$ , the profiles of local heat transfer provide no indication of flow and heat transfer conditions along the impingement surface. In the presence of surface motion these profiles become simply the nonsymmetrical equivalents of the profiles shown on Fig. 6.1. Thus in this part of the study the local heat transfer profiles simply provide the basis of determining the aspect of prime interest, average heat transfer, by means of the integration procedure described earlier.

The average heat transfer results with throughflow, again expressed as



Table 6.5. Operating conditions and results for multiple jet heat transfer at a moving surface with throughflow

$Re_j$	$M_{v_s}$	$Mu_s$	$T_j$	$T_s - T_j$	$Nu_o$	$\overline{Nu}$
10350	0.038	0.0	36.9	22.3	57	51.5
10350	0.038	0.0060	36.8	22.8	66	59.4
10320	0.038	0.0125	36.8	22.8	73	68.1
10050	0.053	0.0	33.2	17.1	52	47.2
9940	0.054	0.0050	33.0	17.6	55	51.1
9920	0.052	0.0138	33.4	18.5	68	60.0
9860	0.050	0.0224	34.7	19.7	75	72.3
10360	0.099	0.0	36.4	21.9	53	47.3
10360	0.100	0.0056	36.3	22.7	55	52.4
10350	0.099	0.0122	36.8	23.0	65	60.7
10480	0.192	0.0	35.6	21.9	48	43.1
10480	0.192	0.0050	35.5	22.3	57	51.6
10380	0.193	0.0120	36.0	22.5	62	59.0
10320	0.188	0.0217	36.4	24.1	71	66.4
10200	0.229	0.0	29.9	16.2	46	41.8
10180	0.229	0.0049	30.2	17.1	51	46.7
10140	0.228	0.0116	31.0	17.5	60	54.3
10075	0.227	0.0195	32.4	17.9	64	62.5
10075	0.286	0.0	32.6	16.8	43	41.0
10080	0.286	0.0046	32.4	17.5	48	45.6
10070	0.285	0.0104	32.7	18.0	55	51.6
10570	0.296	0.0	34.9	21.5	48	43.2
10400	0.299	0.0073	35.2	23.0	54	50.4
10380	0.299	0.0115	35.6	23.1	56	53.0
10350	0.294	0.0206	36.8	23.9	70	64.9
10660	0.380	0.0	32.8	19.8	52	43.0
10380	0.383	0.0178	35.8	23.6	66	62.1

Stanton number, are differenced at each of the 8 levels of  $Mv_s$  used in order to obtain the average Stanton number enhancement,  $\Delta St$ , due to throughflow at the moving impingement surface. These results, displayed on Fig. 6.7, show that for multiple jets the linear relation between  $\Delta St$  and  $Mu_s$  found for operation without surface motion effects applies also for impingement surfaces moving at speeds up to that corresponding to  $Mv_s=0.38$ . Thus the proportionality factor,  $\Delta St/Mu_s$ , is shown to be independent of  $Mv_s$  (Fig. 6.7) as well as of  $Re_j$  (Fig. 6.4). Hence a single equation, Eq. 6.2, correlates all the experimental data for enhancement of convective heat transfer by throughflow independent of  $Re_j$  and  $Mv_s$ , in the range of variables  $8200 < Re_j < 25800$ ,  $0.038 < Mv_s < 0.38$  and  $0 < Mu_s < 0.022$ . Although the data on which Eq. 6.2 is based were determined for multiple jets at  $H/w=5$ , it was noted in Section 6.3 that Eq. 6.2 also applies for the single jet of Chapter 5 at  $H/w=2.5$  and for Saad's single jet data at  $H/w=8$ .

As throughflow provides a linearly additive effect on convective heat transfer, the comprehensive relation

$$\bar{Nu} = f(Re_j, Mv_s, Mu_s, Pr)$$

for average Nusselt number due to multiple jets at  $H/w=5$ ,  $S/H=0.5$  impinging on a moving heat transfer surface where there is throughflow may be given as

$$\bar{Nu} = 0.0938 Re_j^{0.679} (1+Mv_s)^{-0.69} + 0.16 Re_j Pr Mu_s \quad (6.5)$$

valid for  $8200 < Re_j < 25800$ ,  $0 < Mv_s < 0.38$  and  $0 < Mu_s < 0.0235$ . The excellent agreement between the experiments with throughflow at a high speed impingement surface and Nusselt number calculated from Eq. 6.5 at  $Mv_s=0.3$  is displayed in Fig. 6.8.

The effect of throughflow on convective heat transfer, has now been

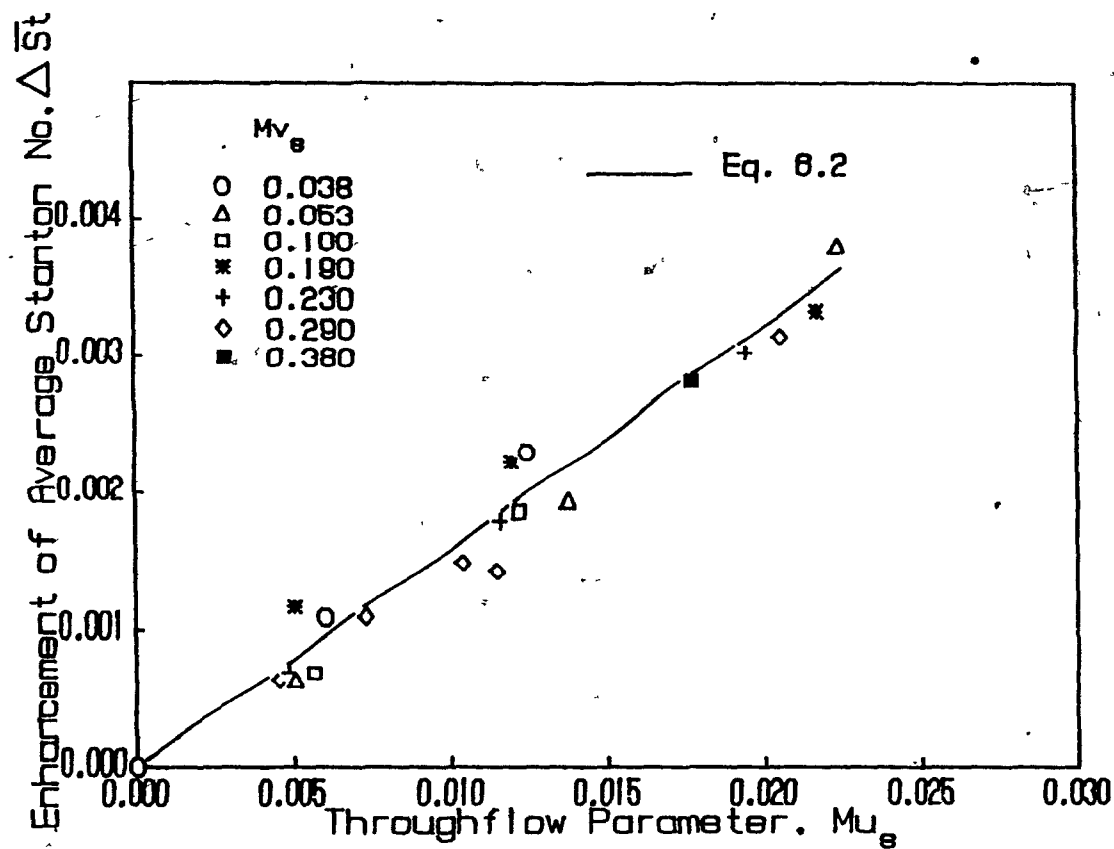


FIGURE 6.7. Effect of throughflow on enhancement of average Stanton number at a moving impingement surface

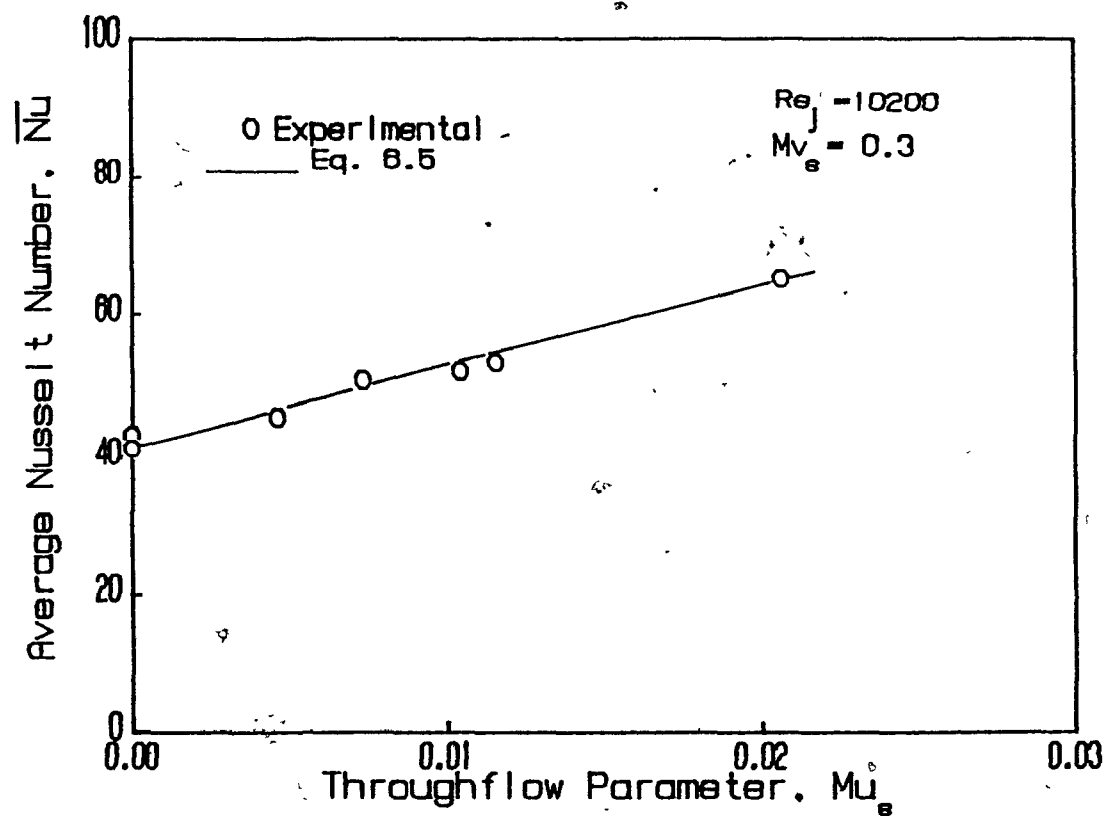


FIGURE 6.8. Effect of throughflow on average Nusselt number at a moving impingement surface: Correlation and experiments

documented for single and for multiple confined jets impinging on heat transfer surfaces moving at speeds from near stationary up to quite high velocities. In all cases throughflow is found to provide a linearly additive enhancement of convective heat transfer, with the amount of enhancement being uniform over the entire impingement surface from the stagnation point out. The amount of the throughflow enhancement, expressed most appropriately in terms of Stanton number, is found to vary directly with the throughflow parameter  $Mu_s$ . The proportionality,  $\Delta\bar{St}/Mu_s$ , is found to be independent not only of jet Reynolds number,  $Re_j$ , but also of  $Mv_s$ , the parameter which describes impingement surface speed. Moreover the proportionality factor,  $\Delta\bar{St}/Mu_s$ , is found to be 0.16 for closely spaced multiple jets at  $H/w=5$ ,  $S/H=0.5$ , while for single jets the proportionality of 0.175 found in the present study at  $H/w=2.5$  applies also for the low throughflow rate results of Saad[1981] at  $H/w=8$ . These findings indicate that the enhancement of average convective heat transfer by throughflow for all confined impinging jets, from single jets to closely spaced multiple jets, can be adequately expressed by

$$\Delta\bar{St} = 0.17 Mu_s \quad (6.6)$$

at  $H/w$  spacings from 2.5 to 8 in the  $Re_j$  range of 8000-58000 and with impingement surfaces that can be either stationary or moving under the jets at high speed, up to  $Mv_s=0.38$ .

In the absence of such information previously the projection of convective heat transfer rates for combined impingement and throughflow drying of paper had to be based on unsubstantiated assumptions. The effect of high speed impingement surface on impingement heat transfer was neglected entirely by the earlier studies (Crotagino and Allenger

[1979] and Randall[1984]). As shown in this study, when  $Mv_s$  values are in the range attained in paper machines this is not a negligible effect. For example a reduction of 17% in impingement heat transfer is found at  $Mv_s=0.3$ , a value applicable to Yankee dryer.

Moreover, the Crotogino and Allenger[1979] model of combined impingement and through drying assumes that, with part of the jet flow withdrawn as throughflow, the rate of convective heat transfer by the multiple confined impinging jets would decrease linearly with the fraction of jet flow which becomes throughflow, Fig. 6.9. A comparison of this assumption with the experimental data now available may be made for the present multiple jet system with  $Mu_s=0.0235$ , for which the fraction of jet flow removed as throughflow,  $Q_s$ , is 12%. The linear proportionality assumption of Crotogino and Allenger, which implies the temperature of the exhaust is independent of  $Q_s$ , indicates that the average convective heat transfer rate by impingement would be reduced by 12% relative to the case of no throughflow. The present study establishes that in fact the trend is just the opposite, and that withdrawal of 12% of the jet flow as throughflow would actually enhance average convective impingement heat transfer by from 53% to 76% in the  $Re_j$  range tested. Thus relative to the present finding on the effect of throughflow on convective impingement heat transfer, Crotogino and Allenger's model underestimates the impingement heat transfer contribution to drying by 65% to 88% for this range of jet Reynolds number.

In another model of combined impingement and throughflow drying of paper, Randall[1984] assumes that impingement and throughflow transport phenomena take place in sequence, i.e. first impinging air is giving up its heat to paper then throughflow air. This model predicts neither

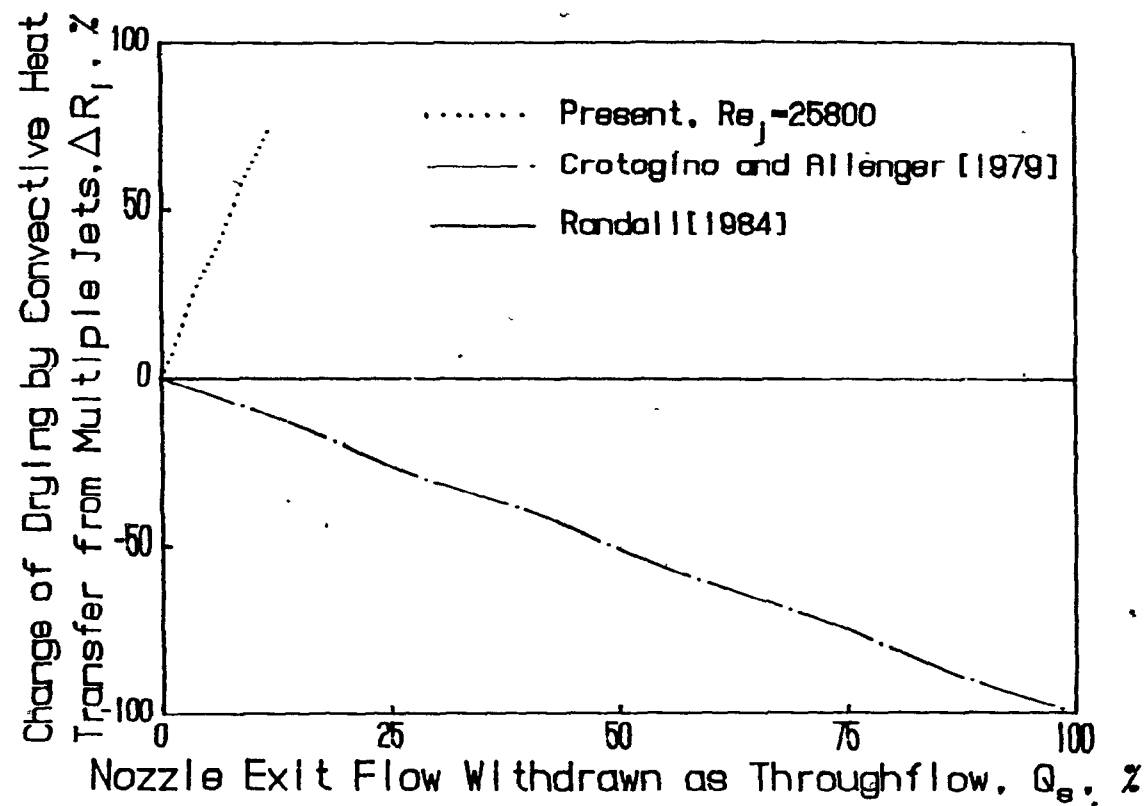


FIGURE 6.9. Convective drying rates by multiple impinging jets for combined impingement and throughflow drying

reduction nor enhancement of impingement heat transfer rate by throughflow, i.e. it is constant for fixed nozzle exit conditions. Thus relative to the present finding on the effect of throughflow on convective impingement heat transfer Randall's model underestimates the impingement heat transfer contribution to drying by 53% to 76% in the  $Re_j$  range tested, Fig. 6.9.

### 6.5 CONCLUSIONS

Industrial heat transfer applications of impinging jets typically involve systems of multiple jets, and these are usually housed under a confinement hood for containment of the spent flow to obtain good thermal efficiency. Moreover, in important commercial processes the impingement surface moves at relatively high speeds under the array of multiple jets. Only a few investigations of multiple jet heat transfer to stationary impingement surfaces have been reported. The significance of several of these studies is limited either by the use of unconfined jets, for which entrainment effects on the heat transfer are not easily identifiable, or by the use of an exhaust flow arrangement producing crossflow of the spent air under the jets, which is strongly deleterious to heat transfer. The present study was carried out to avoid these shortcomings which make the results of several earlier investigations of limited industrial significance.

In the most extensive previous study of confined multiple slot jet heat transfer on stationary impingement surfaces, Saad[1981] obtained a correlation with which he predicted that with such a system, designed to avoid crossflow of the spent flow, the value of average Nusselt number would pass through a maximum for a nozzle-to-impingement



surface spacing,  $H/w$ , of 5, and for a nozzle centerline-to-exhaust centerline spacing,  $S/H$ , of 0.5. Saad's experimental measurements did not however include this combination of geometrical parameters. The present study, the first to provide a direct experimental measurement for the  $H/w=5$ ,  $S/H=0.5$  condition, documents  $Nu$  over a wide range of jet Reynolds number,  $8200 < Re_j < 25800$ , for this condition of maximum heat transfer rate.

The second conclusion from this study is that the disagreement concerning the effect of impingement surface motion on convective heat transfer from impinging jets has been resolved. Subba Raju and Schlunder[1977] reported that convective heat transfer rates for single slot jets increased by a factor of 1.5 to 2 with increasing speed of an impingement surface. Fechner[1971] and Haslar and Krizek [1984] reported some increase in convective mass transfer rates with increasing speed of an impingement surface under multiple slot jets. Baines and Keffer[1979] found no effect of surface motion on average wall shear stress under a single slot jet. Van Heiningen[1982] found that Nusselt number decreases with increasing speed of the heat transfer surface moving under a single confined slot jet. The present study, carried out in such a way as to avoid factors which contribute uncertainty to some of the earlier studies, has confirmed and extended van Heiningen's finding that convective transport coefficients decrease significantly as impingement surface motion increases.

The present study provides the first documentation of the decrease of Nusselt number with impingement surface velocity for the industrially important case of confined multiple impinging slot jets. This effect is not negligible for the range of surface motion

parameter,  $Mv_s$ , used in industry. For example, for the conditions of one important industrial application, the Yankee dryer for drying paper, an impingement surface moving at the velocity found in a modern high speed paper machine would reduce convective heat transfer coefficients of a multiple impinging jet system by a substantial amount, 17%.

The effect of throughflow on convective heat transfer for jet systems impinging on moving surfaces has previously not been open to experimental study for lack of a heat flux sensor applicable to this difficult combination of conditions. With the unique heat flux sensor developed as part of the present study, such measurements are reported here for the first time. The effect of surface throughflow on impingement heat transfer is shown to be linearly additive for the confined multiple jet system of closely spaced jets,  $S/H=0.5$ ,  $H/w=5$ , as was established in the earlier part of this study for a single jet at  $H/w=2.5$  for heat transfer widths up to  $S/H=6.4$ . The fact that  $\Delta \bar{St}$  relates to  $Mu_s$  with nearly the same proportionality constant for multiple jets and a single jet indicates a conclusion of considerable scope, namely, that this constant, 0.17, appears to be applicable over a much broader range of parameters than was tested in the present investigation.

With the present findings on the effects of surface motion and throughflow on impingement heat transfer the assumptions of the two earlier models, Crotagino and Allenger[1979] and Randall[1984], of a combined impingement and throughflow dryer were reexamined. Both models neglect the effect of surface motion which is shown to decrease impingement heat transfer by 17% at  $Mv_s=0.3$ , a value comparable to that

of Yankee dryer.

Crotogino and Allenger[1979] assumes that impingement heat transfer decreases linearly with increasing  $Q_s$ , fraction of jet flow removed as throughflow, whereas Randall[1984] assumes no effect of throughflow on impingement heat transfer. Comparison with the present results indicates that the first model underestimates impingement heat transfer rate by 65% to 88% and the second model by 53% to 76%, indeed very substantial amounts, in the  $Re_j$  range tested

A comprehensive analytical correlation, Eq 6.5, has been obtained with which average convective heat transfer rate may be predicted for the range of parameters  $8200 < Re_j < 25800$ ,  $0 < Mu_s < 0.0235$  and  $0.019 < Mv_s < 0.38$  for a multiple jet system with  $H/w=5$  and  $S/H=0.5$ . In this expression the proportionality constant for the effect of throughflow, 0.17, and the  $(1+Mv_s)^{-0.7}$  factor for the effect of surface motion are applicable in a much wider  $Re_j$ ,  $H/w$  and  $S/H$  range i.e., 8200-58000, 2.5-8 and 0.5-6.4 respectively.

## CHAPTER 7

NUMERICAL STUDY OF TURBULENT SLOT JETS IMPINGING ON A SURFACE  
WITH THROUGHFLOW

## 7.1 INTRODUCTION

Design of an impinging jet system for a given thermal application requires specification of a rather large number of geometric and flow parameters e.g. jet type (round/slot), jet configuration, nozzle-to-impingement surface spacing, nozzle-to-nozzle spacing, jet Reynolds number. Depending on the application there may be additional important effects such as surface motion, nozzle design, mass transfer at the impingement surface, induced or imposed cross flow, large temperature differences between the jet and the impingement surface. With this impressive number of design parameters an advantageous strategy is the use of complementary numerical and experimental studies of transport processes under impinging jets.

For laminar impinging jets, the good consistency between various numerical predictions, and between predictions and available data was recorded in a recent review of numerical studies, Polat et al.[1988]. This is not so with predictions for the more difficult case of turbulent impinging jets. Iterative solution of the exact transport equations for turbulent flows is currently limited by computer capacity since the small scale of turbulence requires an unrealistically large number of grids in the flow domain. This introduces the necessary alternative of using a turbulence model to predict the turbulence quantities that appear in the time averaged transport equations for turbulent flows. As for turbulence models, all have shortcomings.

For the complex flow structure under impinging jets, the earlier use of one-equation models of turbulence has been replaced by higher order turbulence models which solve transport equations for various turbulence quantities, i.e. turbulent kinetic energy, turbulent kinetic energy dissipation or individual Reynolds stresses. Table 2.3 summarizes numerical studies on plane and axisymmetric impinging jets. All recent work uses the high Reynolds number version of the  $k-\epsilon$  turbulence model except for Agarwal and Bower[1982], who used the corresponding low-Re version to predict flow characteristics of a compressible impinging jet. As flow in the impingement region is pressure driven, mean flow characteristics are generally predicted well regardless of the turbulence model. By contrast, for heat and mass transfer rates under impinging jets, an aspect of great engineering interest, there is great variation between results of various studies as well as between predictions and experimental measurements. A contributing factor is that a separate model must be used to treat the near-wall boundary when a high-Re turbulence model is employed. Discrepancies may derive from either the turbulence model or the near-wall model. Comparison of results is hindered by the variety of specifications of conditions at the several boundaries. Finally, there remain the sources of error related to the particular numerical solution technique used.

Van de Meer[1987] now suggests that the assumptions to model the turbulence generation term in the  $k$  equation are not valid in an impingement region, hence  $k-\epsilon$  type models should not be used for impingement flows. He proposed an anisotropic model with two features, i.e. the nondiagonal terms of the Reynolds stress tensor are estimated from the Boussinesq hypothesis by solving transport equations for  $k$  and

$\epsilon$ , and the anisotropy term,  $g = \overline{u'^2 - v'^2}$ , is calculated by solving an additional equation for this term. However this model did not improve the heat transfer distribution under an impinging jet relative to that predicted with conventional  $k-\epsilon$  models.

A test by Looney and Walsh[1982] of the algebraic stress models of Rodi[1972] and Ljuboja and Rodi[1979] indicated that predicted heat transfer in the impingement region was inferior to that with the  $k-\epsilon$  model. A more complex turbulence model thus does not necessarily improve predictions. The  $k-\epsilon$  model retains a reasonable combination of economy and accuracy even for the complex configuration of impingement flow.

For single and multiple confined turbulent plane jets, the present study predicts heat transfer rates along the impingement surface by solution of the two-dimensional Navier-Stokes, energy and turbulence model equations using an upwind finite difference scheme. The turbulence model used was the high-Re version of the  $k-\epsilon$  model. Of various near-wall models tested, a modified version of the two-layer model of Chieng and Launder[1980] gave the best overall agreement between predictions and experimental data at low values of nozzle-to-surface spacing,  $H/w$ , where prediction is most difficult.

The mathematical formulation, boundary conditions, grid layout, grid independency tests, and numerical scheme are outlined prior to presentation of results for single and multiple jet cases.

## 7.2 MATHEMATICAL FORMULATION OF THE PROBLEM

A general form for the governing equations including the equation of continuity is:

$$\frac{\partial(\rho u \Phi)}{\partial x} + \frac{\partial(\rho v \Phi)}{\partial y} = \frac{\partial}{\partial x} \left( \Gamma_{\Phi} \frac{\partial \Phi}{\partial x} \right) + \frac{\partial}{\partial y} \left( \Gamma_{\Phi} \frac{\partial \Phi}{\partial y} \right) + S_{\Phi} \quad (7.1)$$

where  $\Phi$  represents the variables  $u$ ,  $v$ ,  $h$ ,  $k$  and  $\epsilon$ .  $\Gamma_{\Phi}$  is the transfer coefficient associated with  $\Phi$ , and  $S_{\Phi}$  the corresponding source term. In order to express the governing equation of a particular variable in the above generalized form, the terms other than those in the form of "convection" and "diffusion" terms are collected in the source term,  $S_{\Phi}$ . The terms  $\Gamma_{\Phi}$  and  $S_{\Phi}$  are shown in Table 7.1. As turbulent viscosity,  $\mu_T$ , is determined by flow conditions, it must be modeled in terms of measurable flow quantities. This is done using the two equation  $k$ - $\epsilon$  turbulence model of Jones and Launder[1973].

In the  $k$ - $\epsilon$  model  $\mu_T$  is related to the turbulence terms  $k$  and  $\epsilon$  as

$$\mu_T = C_{\mu} \rho k^2 / \epsilon \quad (7.2)$$

The transport equations for turbulent kinetic energy,  $k$ , and its dissipation rate,  $\epsilon$ , are summarized in Table 7.1.

### 7.2.1 Boundary Conditions

The two flow configurations, Figs. 7.1 and 7.2, are:

(1) a single confined plane turbulent jet impinging normally on a stationary surface and exhausting symmetrically in the direction normal to the plane of the jet, and

(2) a jet in an array of multiple confined impinging slot jets, with exhaust ports in the confinement surface and located symmetrically between adjacent jets.

The boundary conditions are as follows:

Table 7.1 Summary of equations solved

Equation	$\Phi$	$\Gamma_{\Phi}$	$S_{\Phi}$
Continuity	1	0	0
x-momentum	u	$\mu_L + \mu_T$	$-\frac{\partial p}{\partial x} + \frac{\partial}{\partial x} \left[ (\mu_L + \mu_T) \frac{\partial u}{\partial x} \right] + \frac{\partial}{\partial y} \left[ (\mu_L + \mu_T) \frac{\partial v}{\partial x} \right]$
y-momentum	v	$\mu_L + \mu_T$	$-\frac{\partial p}{\partial y} + \frac{\partial}{\partial x} \left[ (\mu_L + \mu_T) \frac{\partial u}{\partial y} \right] + \frac{\partial}{\partial y} \left[ (\mu_L + \mu_T) \frac{\partial v}{\partial y} \right]$
Energy	h	$\frac{\mu_L}{\sigma_L} + \frac{\mu_T}{\sigma_T}$	0
Turbulent Energy	k	$\mu_L + \frac{\mu_L}{\sigma_k}$	$G - \rho \epsilon$
Turbulence Energy Dissipation	$\epsilon$	$\mu_L + \frac{\mu_L}{\sigma_{\epsilon}}$	$C_1 \frac{\rho \epsilon}{k} G - C_2 \frac{\rho \epsilon^2}{k}$

where

$$G = \mu_T \left\{ \left( \frac{\partial u}{\partial y} + \frac{\partial v}{\partial x} \right)^2 + 2 \left[ \left( \frac{\partial u}{\partial x} \right)^2 + \left( \frac{\partial v}{\partial y} \right)^2 \right] \right\}$$

$$C_{\mu}=0.09 ; C_1=1.43 ; C_2=1.92 ; \sigma_k=1.0 ; \sigma_{\epsilon}=1.3 ; \sigma_T=0.9$$



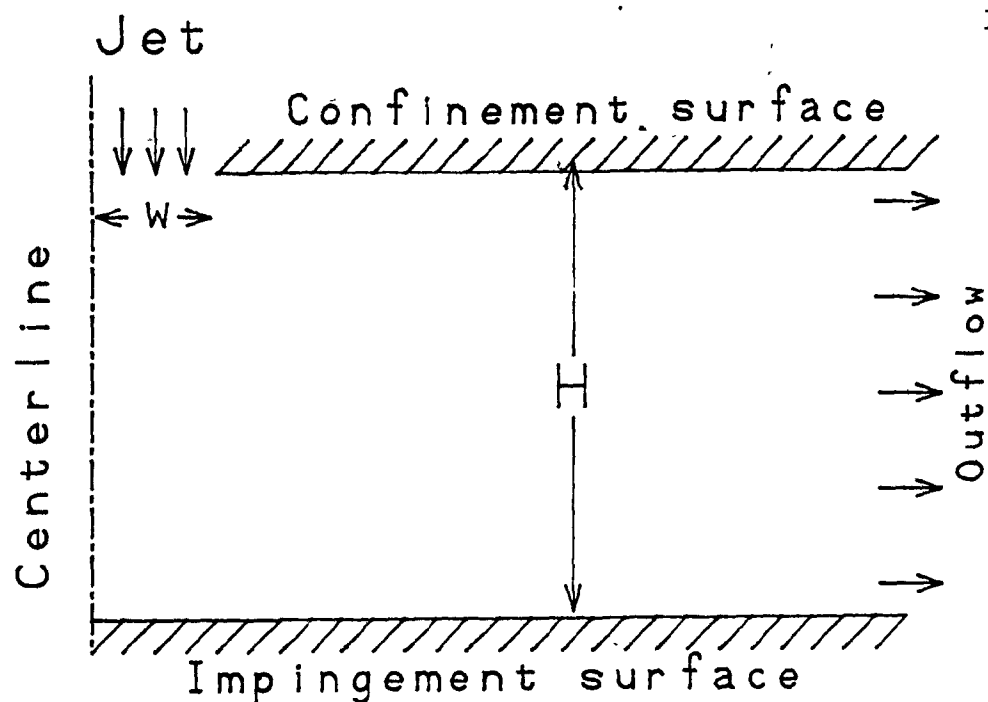


FIGURE 7.1. Flow configuration for a single impinging jet

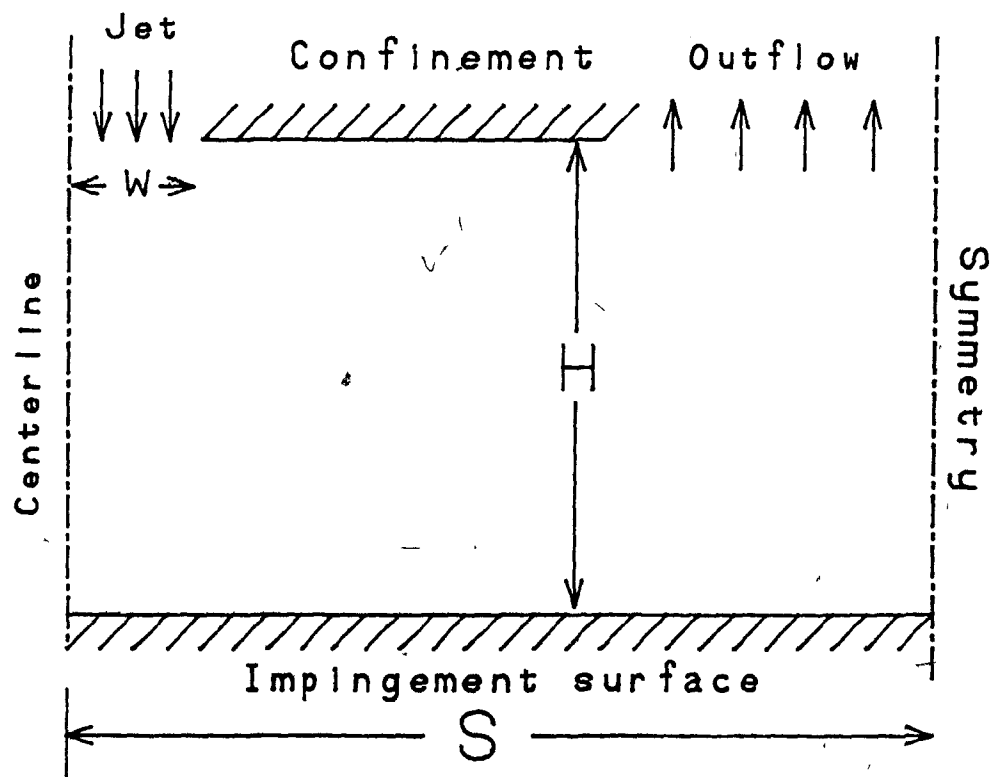


FIGURE 7.2. Flow configuration for multiple impinging jets with symmetrical exhaust ports

Nozzle exit:

Uniform profiles for the jet at the nozzle exit are specified for both velocity,  $u_j$ , and nondimensional temperature,  $h_j=1$ . The boundary conditions for  $v$ ,  $k$ , and  $\epsilon$  are:

$$v_j = 0; \quad k_j = I_j^2 u_j^2; \quad \epsilon_j = C_\mu k_j^{3/2} / (0.03 \frac{W}{2})$$

Symmetry Axes:

$$v = \frac{\partial u}{\partial y} = \frac{\partial k}{\partial y} = \frac{\partial \epsilon}{\partial y} = \frac{\partial h}{\partial y} = 0$$

At the Impingement and Confinement Surfaces:

The high-Re version of the  $k$ - $\epsilon$  model of turbulence implies negligible effect of viscosity on the energy containing motions, and negligible effect of the mean strain field on the dissipative ones. While these assumptions are valid in most of the flow domain, in the immediate vicinity of the impingement and confinement surfaces direct viscous effects are influential due to the no-slip condition. This very thin viscosity-affected flow region near the wall must be handled separately due to the requirements of the turbulence model used. Hence the actual boundary conditions for the variables are specified at the nodes closest to the wall.

Various near-wall models were tested, both those categorized as one-layer (Models 1 and 2) and two-layer (Models 3 and 4). One-layer models assume uniform shear stress and turbulent kinetic energy distributions near the wall. Two-layer models assume that turbulent kinetic energy varies in a parabolic manner within the viscous sublayer, then increases linearly with distance. In two-layer models the turbulent shear stress, zero within the viscous sublayer, undergoes

an abrupt increase at the edge of the sublayer and varies linearly over the remainder of the cell. The model equations are summarized in Table 7.2, with detailed derivations in Appendix 3. When there is throughflow at the impingement surface, the bilogarithmic expression used to predict the shear stress at the wall is:

$$\tau_w = \kappa C \mu^{1/4} \rho v_P k_P^{1/2} / \left( \ln(Ex^+) - \frac{u_s}{4\kappa C \mu^{1/4} k_P^{1/2}} \ln^2(x^+) \right) \quad (7.3)$$

where

$$x^+ = \frac{C^{1/4} \rho x_P k_P^{1/2}}{\mu_L} ; \quad E = 9 ; \quad \kappa = 0.4$$

The following conditions were specified at the confinement and impingement surfaces, respectively:

$$u = 0 \text{ or } u_s ; \quad v = 0 ; \quad h_{con} = 1 ; \quad h_{imp} = 0 ; \quad k = \epsilon = 0$$

Wolfshtein[1967] used a near-wall model in the form of Model 1 in his predictions of impinging jet flow and heat transfer whereas van Heiningen[1982], Huang et al.[1982], Looney and Walsh[1984] and Polat et al.[1985] used Model 2. Amano and Sugiyama[1985] tried various near-wall models, including Models 2 and 3, and a near-wall model they developed in which the generation and dissipation terms for  $\epsilon$  are calculated by integrating appropriate equations in the viscous sublayer and turbulent layer. They found the latter model superior to Model 3 where  $\epsilon$  is calculated at near-wall grid nodes assuming equilibrium between  $k$  and  $\epsilon$ .

#### Outflow:

#### Single impinging jet:

$$u = \frac{\partial v}{\partial y} = \frac{\partial k}{\partial y} = \frac{\partial \epsilon}{\partial y} = \frac{\partial h}{\partial y} = 0$$

To apply these outflow boundary conditions, it had previously been

Table 7.2 Summary of equations of near-wall models

k equation:	<u>Model 1</u>
Generation;	$G_{P,w} = \tau_w v_e \Delta y_{ns}$
k equation:	<u>Model 2</u>
Generation;	$G_{P,w} = 2 \tau_w (u_n - u_s) \Delta x_{We} + \tau_w v_e \Delta y_{ns}$ $+ \mu_T \left( \left( \frac{\Delta u}{\Delta y} \right)_p^2 + 2 \left( \left( \frac{\Delta u}{\Delta x} \right)_p^2 + \left( \frac{\Delta v}{\Delta y} \right)_p^2 \right) \right) \Delta x_{We} \Delta y_{ns}$
k equation:	<u>Common to Models 1 and 2</u>
Dissipation;	$(\rho \epsilon)_{P,w} = \frac{C_\mu \rho^2 k_p^2 v_e}{\tau_w} \Delta y_{ns}$ <p>where <math>\tau_w = \mu_T \frac{\partial v}{\partial x}</math></p>
k equation:	<u>Common to Models 3 and 4</u>
Generation;	$G_{P,w} = \left\{ \frac{\tau_w (v_e - v_v)}{x_e} + \frac{\tau_w (\tau_e - \tau_w)}{\rho \kappa C_\mu^{1/4} k_v^{1/2} x_e} \left( 1 - \frac{x_v}{x_e} \right) + \left( \tau_w \left( 1 - \frac{x_v}{x_e} \right) + \frac{1}{2} (\tau_e - \tau_w) \left( 1 - \frac{x_v}{x_e} \right)^2 \right) \frac{\Delta u}{\Delta y} \right\}_p + 2 \mu_T \left\{ \left( \frac{\Delta u}{\Delta x} \right)_p^2 + \left( \frac{\Delta v}{\Delta y} \right)_p^2 \right\} \Delta x_{We} \Delta y_{ns}$
Dissipation;	$(\rho \epsilon)_{P,w} = \left\{ \frac{2 C_\mu^{1/4} k_v^{3/2}}{11.5 x_v} + \frac{C_\mu^{3/4}}{\kappa x_e} \left( \frac{2}{3} (k_e^{3/2} - k_v^{3/2}) + 2a (k_e^{1/2} - k_v^{1/2}) + b \right) \right\} \rho \Delta x_{We} \Delta y_{ns}$
where	$\tau_w = \mu_T \left( \frac{\partial u}{\partial y} + \frac{\partial v}{\partial x} \right); \quad x_v = \frac{11.5 \nu}{C_\mu^{1/4} k_v^{1/2}}; \quad a = k_p - \frac{k_p - k_E}{x_p - x_E} x_p$
and where	$b = \begin{cases} \text{if } a > 0 & a^{3/2} \ln \left( \frac{(k_e^{1/2} - a^{1/2})(k_v^{1/2} + a^{1/2})}{(k_v^{1/2} - a^{1/2})(k_e^{1/2} + a^{1/2})} \right) \\ \text{if } a = 0 & 0 \\ \text{if } a < 0 & 2(-a)^{3/2} \left[ \tan^{-1} \frac{k_e^{1/2}}{(-a)^{1/2}} - \tan^{-1} \frac{k_v^{1/2}}{(-a)^{1/2}} \right] \end{cases}$
<u>Model 3</u>	$\tau_w = \kappa C_\mu^{1/4} \rho v_p k_p^{1/2} / \ln \left( \frac{E C_\mu^{1/4} \rho x_p k_p^{1/2}}{\mu_L} \right)$
<u>Model 1, 2 and 4</u>	$\tau_w = \kappa C_\mu^{1/4} \rho v_p k_p^{1/2} / \ln \left( \frac{E C_\mu^{1/4} \rho x_p k_p^{1/2}}{\mu_L} \right)$
$\epsilon$ -equation:	<u>Common to all models</u>
Energy equation:	$\epsilon_P = \frac{C_\mu^{3/4} k_p^{3/2}}{\kappa x_p}$
St	$St = \frac{-\dot{q}_w}{(h_p - h_w) \rho v_p} = \frac{\tau_w / \rho v_p^2}{\sigma_T [1 + P(\tau_w / \rho v_p^2)^{1/2}]}; \quad P = 9[(\sigma_L / \sigma_T) - 1](\sigma_L / \sigma_T)^{-1/4}$

considered necessary to place the outflow boundary at a sufficient distance from the jet axis to avoid inflow across part of this boundary. However numerical tests show that with the present algorithm, even with some inflow on the confinement surface side of this boundary, the heat transfer distribution at the impingement surface does not change appreciably provided that continuity over the whole computational domain is preserved. For the sake of computational economy then, with nozzle-to-surface spacings larger than 2.6 the outflow boundary could then be located to allow inflow over part of this boundary.

#### Multiple impinging jets.

At the exhaust ports in the confinement surface

$$v = \frac{\partial k}{\partial x} = \frac{\partial \epsilon}{\partial x} = \frac{\partial h}{\partial x} = 0$$

and  $u = u_{out}$ , a uniform velocity calculated from the overall mass balance. Width of the exhaust port is twice the nozzle width.

#### 7.2.2 Grid Layout

A rectangular coordinate system is used to discretize the flow field. In order to achieve efficiency in terms of computational time as well as accuracy in regions of steep and mild gradients, a combination of uniform and non-uniform grid size appropriate to the flow field is used. In the y-direction, from the jet symmetry line to the nozzle corner a uniform grid spacing is used so that the nozzle wall coincides with a control volume boundary. Downstream of the nozzle, an expanding y-direction grid layout (factor 1.05-1.1) was adopted. In the x-direction, i.e., from confinement to impingement

surface, the grid layout is uniform.

### 7.2.3 Grid Independence of Nusselt Number Profile

The following observations result from extensive tests with the number and distribution of grids, performed to obtain grid independent results.

1 High aspect ratio meshes (as high as 35) in the wall jet region did not create computational difficulties and did not affect the accuracy of predicted Nu distributions.

2 The nondimensional distance,  $x^+$ , from the impingement surface to the first grid line is an important parameter. As a high Reynolds number turbulence model is used, the first grid line must be sufficiently far from the wall to be within the fully turbulent regime, while the intermediate flow is handled by a near-wall model. When the nondimensional distance of the grid next to the wall was between 80 and 200, the shear stress and Nusselt number profiles at the surface were found to be grid independent, as defined by a maximum deviation of 5% at the off-stagnation maximum of the Nusselt profile. (Centerline velocity decay and surface pressure profiles are less dependent on this near-wall grid spacing.

3. Grids located in the jet nozzle parallel to the centerline must be quite dense, at least 5 grid lines in the half jet nozzle width, to achieve grid independent results.

4. At the highest value of jet Reynolds number tested,  $Re_j = 44300$ , decreasing the total number of grid nodes from 1000 (25x40) to 600 (20x30) caused a maximum difference of only 3% in local Nusselt number.

#### 7.2.4 Finite Difference Solution

Of the two common alternatives for solution of finite difference equations, the upwind and hybrid schemes, the former yields better computational economy and stability, faster convergence. A numerical error, "false diffusion", may however occur at locations of the solution domain where the streamlines are not perpendicular to the grid lines. As the error due to false diffusion is then maximum for a  $45^\circ$  angle between streamlines and grid lines, any such error would be maximal in the stagnation region where the flow turns sharply. Both the hybrid and upwind schemes were therefore employed to solve an identical single impinging jet case. As the difference between the two Nusselt number profiles was everywhere less than 2%, negligible error of the false diffusion type was thereby demonstrated. Higher underrelaxation must however be applied with the hybrid scheme, which slows the convergence rate considerably. Patankar[1980] states that false diffusion may not be a problem if sufficiently small grid size is used and if the actual diffusion term is much larger than the false diffusion term. In the stagnation region small grid meshes were used to accommodate the steep velocity gradients. Moreover, turbulent diffusion coefficients are at least one order of magnitude higher than the laminar coefficients. Thus in this case various factors probably contribute to making the false diffusion error negligible. Numerical procedure details are given in Appendix 3.

#### 7.3 EFFECT OF NEAR-WALL MODELLING ON NUSSELT NUMBER

In Fig 7.3 the distributions of local Nu for  $Re_j=30000$  and  $H/w=2.6$ , predicted using the four near-wall models listed in Table 7.2,

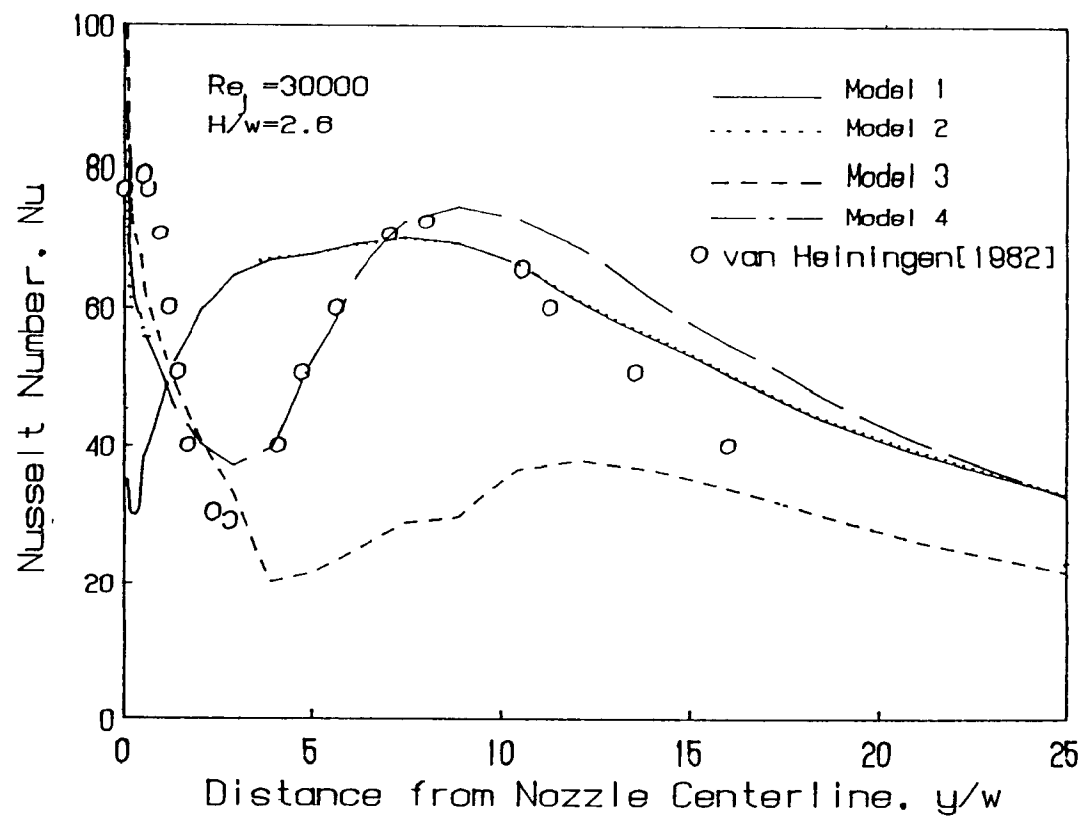


FIGURE 7.3. Effect of near-wall model on predicted local Nusselt number



are displayed together with experimental data of van Heiningen[1982]. In these runs the number of grid nodes was  $15(\text{uniform}) \times 25(1.05)$ , and the nozzle exit turbulence intensity, 1%

Models 1 and 2 differ only as to the calculation of  $G_{P,w}$ . Model 1 makes the Couette flow assumption, Model 2 retains all the velocity gradients in the  $G$  term. As expected, gradients other than  $\partial v / \partial x$  are important only in the stagnation region where the flow turns sharply and accelerates along the impingement surface. The large underprediction of  $Nu$  in the stagnation region indicates the inadequacy of the Couette flow assumption for  $G$  (Model 1). The profiles predicted by Models 1 and 2 become coincident beyond  $\sim 3w$  from the nozzle centerline, but neither model gives predicted heat transfer close to that measured experimentally until beyond the location of the off-stagnation maximum, i.e. until  $y \approx 7w$ .

The  $Nu$  profiles predicted with Models 3 and 4 agree up to  $y \approx 3w$ , then diverge. The profile predicted by Model 4 displays a minimum and approaches the profile predicted by Models 1 and 2 at about  $y/w = 7$ . More important, the profile from Model 4 closely follows the experimentally measured profile, with both the off-stagnation minimum and maximum values of  $Nu$  predicted at about the correct locations and about the correct values of Nusselt number. Beyond the off-stagnation minimum at about  $y/w = 3$ , Model 3 predicts very low values of  $Nu$ , as low as  $1/3$  the experimental value. This model, used by Amano[1980] for flow predictions for a circular impinging jet, derives from a basic concept first suggested by Chieng and Launder[1980]. As comparisons indicate that such mean flow characteristics as centerline velocity decay and normalized pressure profiles along the surface are unaffected

by the choice of near-wall model, Amano's test is not sufficient to establish the validity of this model.

The present study shows that the predicted Nu number and shear stress profiles near the surface are, by contrast, very sensitive to the near-wall model used (Figs. 7.3 and 7.4), and establish that Model 3 is not reliable for heat transfer prediction. Nusselt number calculation involves  $v_p$  and  $\tau_w$  via the Stanton number relationship, Table 7.2. As the development of maximum velocity parallel to the impingement surface is not affected appreciably by the near-wall model used,  $\tau_w$  is clearly responsible for the variation between the Nu profiles with Models 3 and 4. The only difference is that for calculation of  $\tau_w$ , Model 3 uses  $k_v$  Model 4 uses  $k_p$ . Use of  $k_v$  leads to large errors in both  $\tau_w$  and Nu. Clearly  $k_p$  is the correct choice. The similar  $\tau_w$  and therefore Nu profiles predicted by these two models in the stagnation region can be explained by the dominating effect of the unmodelled term  $2\mu_T \left\{ \left( \frac{\partial u}{\partial x} \right)_p^2 + \left( \frac{\partial v}{\partial y} \right)_p^2 \right\}$  in the generation term of the k-equation. The k and  $k_v$  profiles predicted by these two models in this region, Fig. 7.5, are identical.

The differences between the predicted profiles of Nu by Models 2 and 4 derive from modelling the generation and dissipation of k. The assumptions of Model 2 result in overprediction of generation and dissipation rates near the surface, Figs. 7.6 and 7.7, due partly to the  $\tau_w$  definition in these models. In Model 2  $\tau_w$  is proportional to  $(\partial v / \partial x)$ , in Model 4  $\tau_w$  is proportional to  $(\partial v / \partial x + \partial u / \partial y)$ . Correspondingly, in Model 2  $\partial u / \partial y$  appears in the  $G_{p,w}$  expression as an extra term. Another important difference is that in Model 2 turbulence generation occurs throughout the near-wall cell whereas in Model 4, more

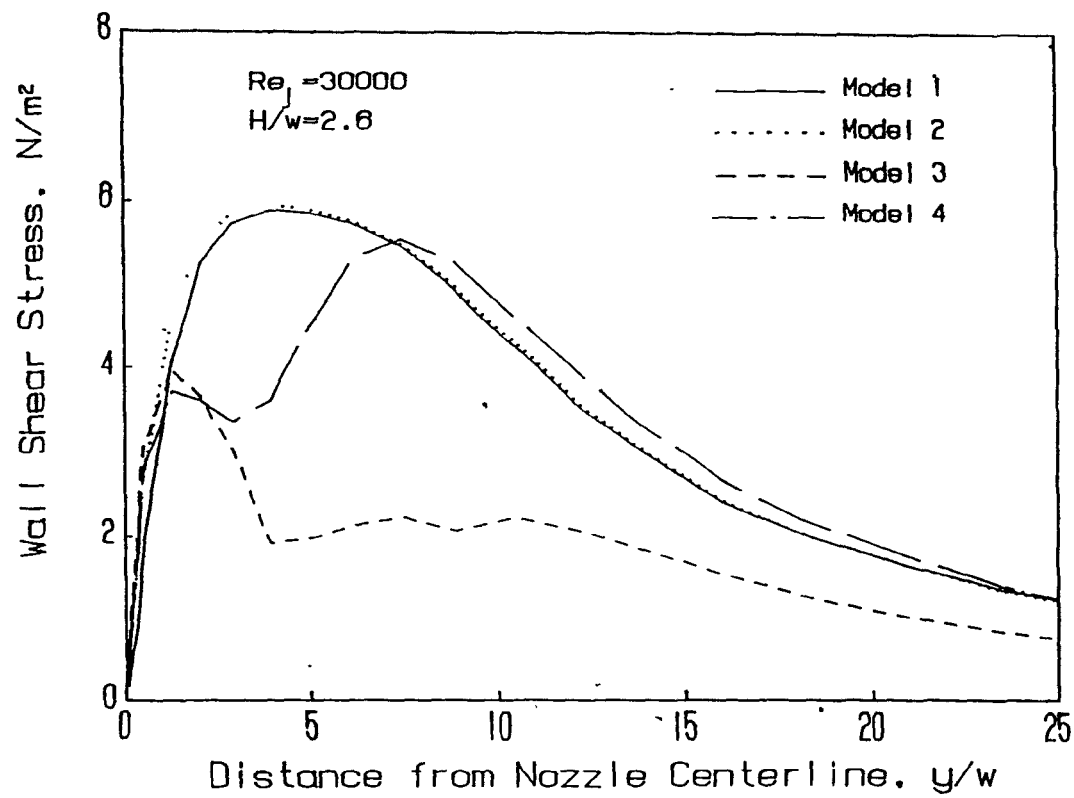


FIGURE 7.4. Effect of near-wall model on predicted wall shear stress

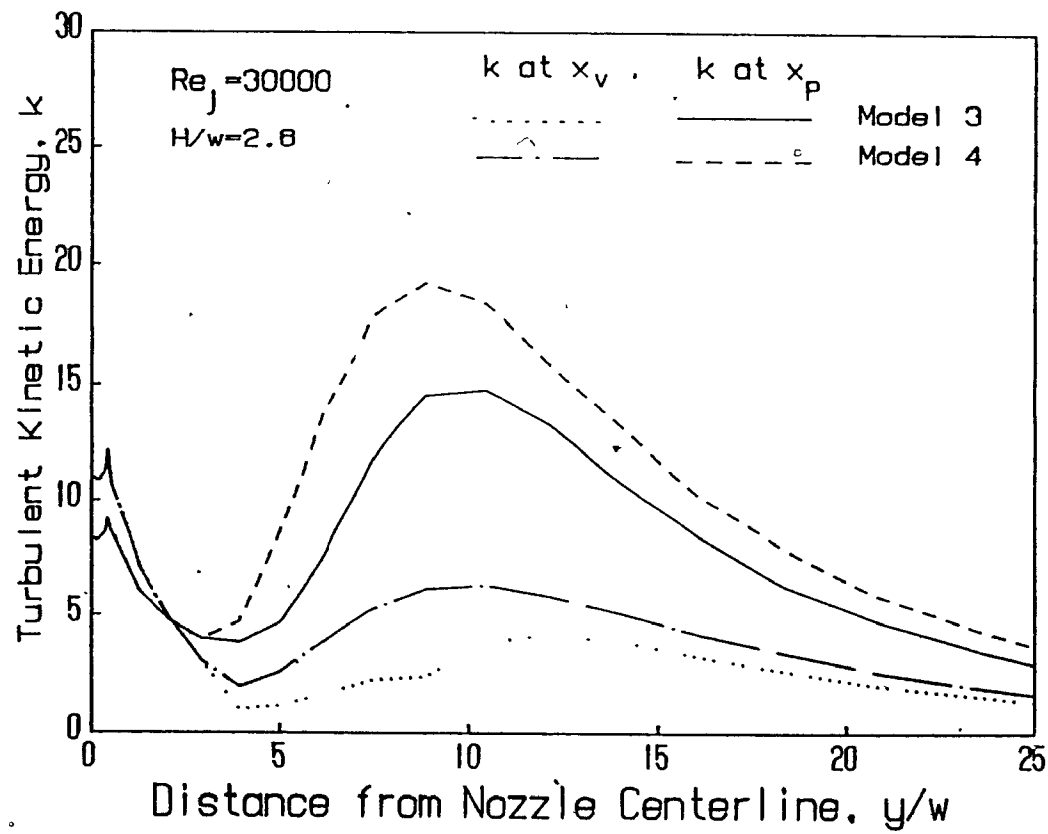


FIGURE 7.5. Effect of near-wall model on predicted turbulent kinetic energy

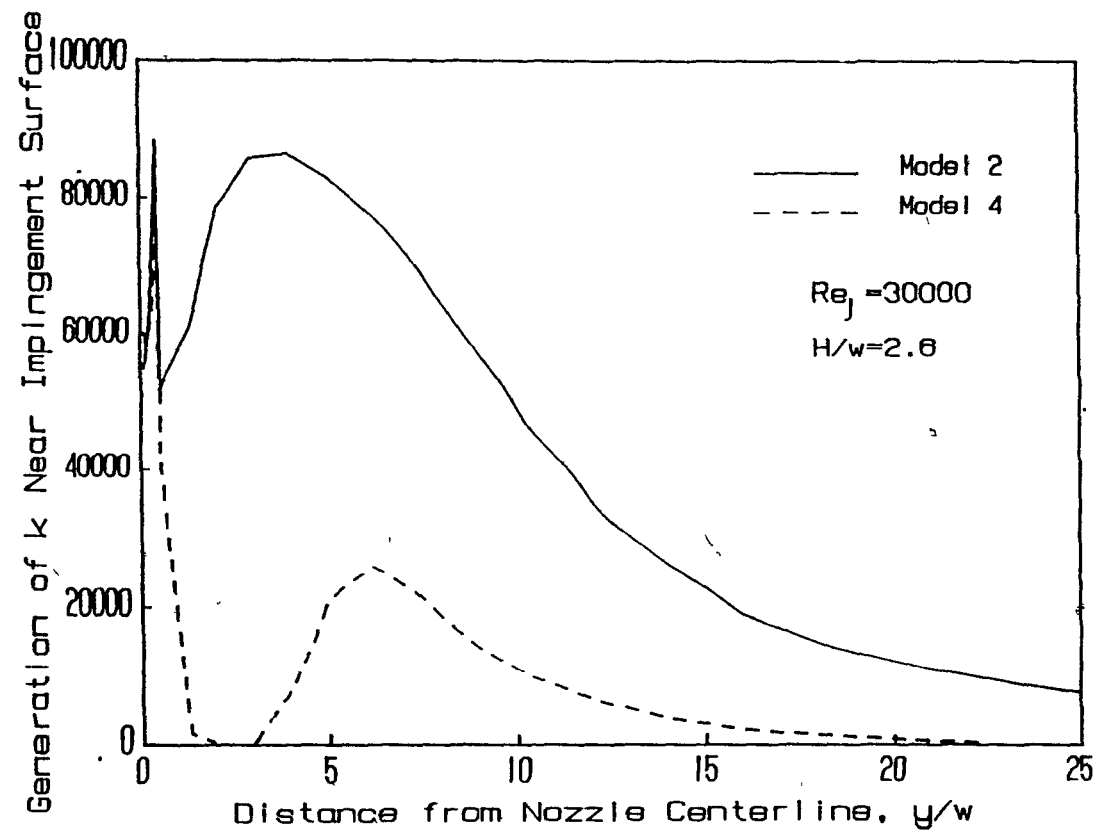


FIGURE 7.6. Effect of near-wall model on predicted generation of turbulent kinetic energy

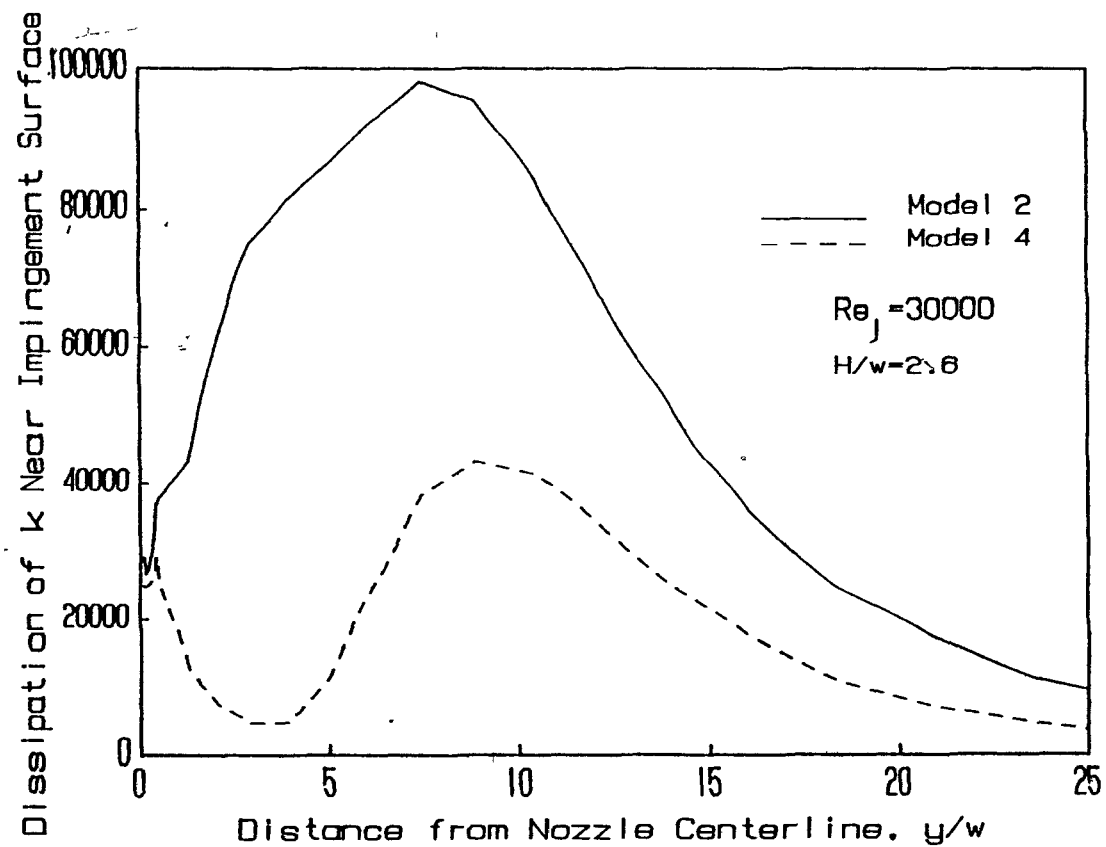


FIGURE 7.7. Effect of near-wall model on predicted dissipation of turbulent kinetic energy

realistically, there is no turbulence generation in the viscous sublayer.

The  $(\rho\epsilon)_{p,w}$  term is calculated in Model 2 using the  $\mu_T$  expression given in Eq. 7.2. This expression with a constant  $C_\mu$  is valid only for high Reynolds number flows. Although it can be modified for a near-wall flow by making  $C_\mu$  a function of the local turbulence Reynolds number, as in the low-Re version of the  $k-\epsilon$  model, this practice is not followed here. Model 2 also assumes  $k_p$  as an average  $k$  in the whole near-wall cell, perhaps overestimating it. Assumption of  $C_\mu$  and  $k_p$  both constant in the near-wall cell is probably the primary reason why the values of predicted  $(\rho\epsilon)_{p,w}$  by Model 2 are much greater than by Model 4. The results of the runs performed using Model 2 as the near-wall model have been reported earlier by Polat, Mujumdar and Douglas[1985]:

Complete isotropy of flow assumed by the turbulence model fails in the stagnation region, i.e.  $y < 3w$ , resulting in large differences between predicted and experimental  $Nu$  values. Moreover, very near the stagnation point the predicted  $Nu$  profiles decay faster due to the choice of separate modelling of near-wall flow. The value defined as stagnation point  $Nu$  number is actually computed at the grid node next to the true stagnation point, hence its value is very sensitive to the location of this node because  $r_w$  and  $v_p$  both approach zero as the true stagnation point is approached.

In summary, the choice of a near-wall model for distributions of shear stress and turbulent kinetic energy is shown to be of extreme importance. The choice of alternate, and apparently reasonable models results in large differences in the predicted distributions of local  $Nu$

and wall shear stress. Of four models tested, that identified as Model 4 in Table 7.2 gives the best overall agreement with experimental results. The predictions obtained are sufficiently good that this model can be accepted for prediction of impingement heat transfer characteristics in the present investigation.

#### 7.4 RESULTS AND DISCUSSION

##### 7.4.1 Single Jet Heat Transfer without Throughflow

Table 7.3 summarizes parameter values for runs performed using Model 4 as the near-wall model for shear stress and kinetic energy distribution.

Table 7.3 Parameter values for single jet simulations without throughflow at the impingement surface

Run no	H/w	$Re_j$	$I_j \times 100$	NX	NY	$y_{max}/w$
1	1.25	21800	7	20(1.05)	40	25
2	2	11000	2.5	12	35	15
3	2	11000	7	12	35	15
4	2	11000	10	12	35	15
5	2.6	10100	1	12	35	30
6	2.5	21800	7	15	30	25
7	2.5	35800	7	20	30	20
8	2.5	44300	7	25	40	20
9	6	10100	1	18	35	36
10	8	20000	7	30	40	46

##### a) Prediction of Pressure and Velocity

Predicted normalized profiles of static pressure at the impingement surface are compared with experimental measurements for close nozzle-to-surface spacings, H/w, on Fig. 7.8a and for an intermediate spacing on Fig. 7.8b. The only measurements for a confined impinging slot jet



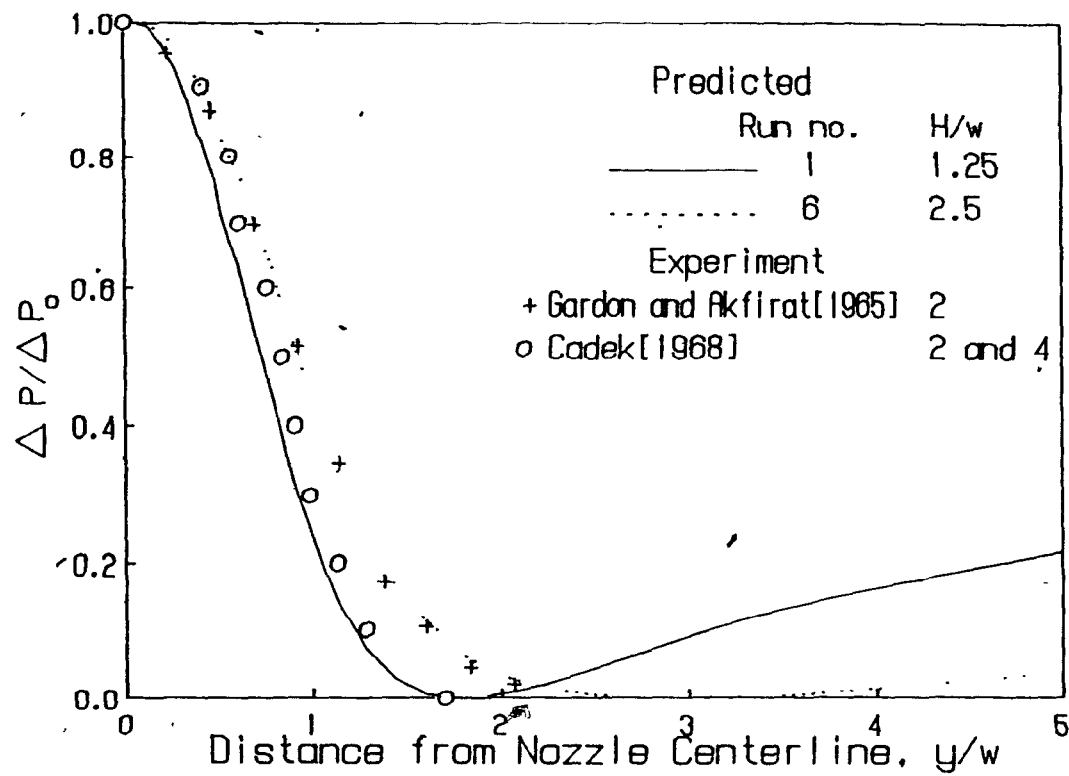


FIGURE 7.8a. Profiles of normalized static pressure at the impingement surface for  $H/w$  of 1.25 and 2.5

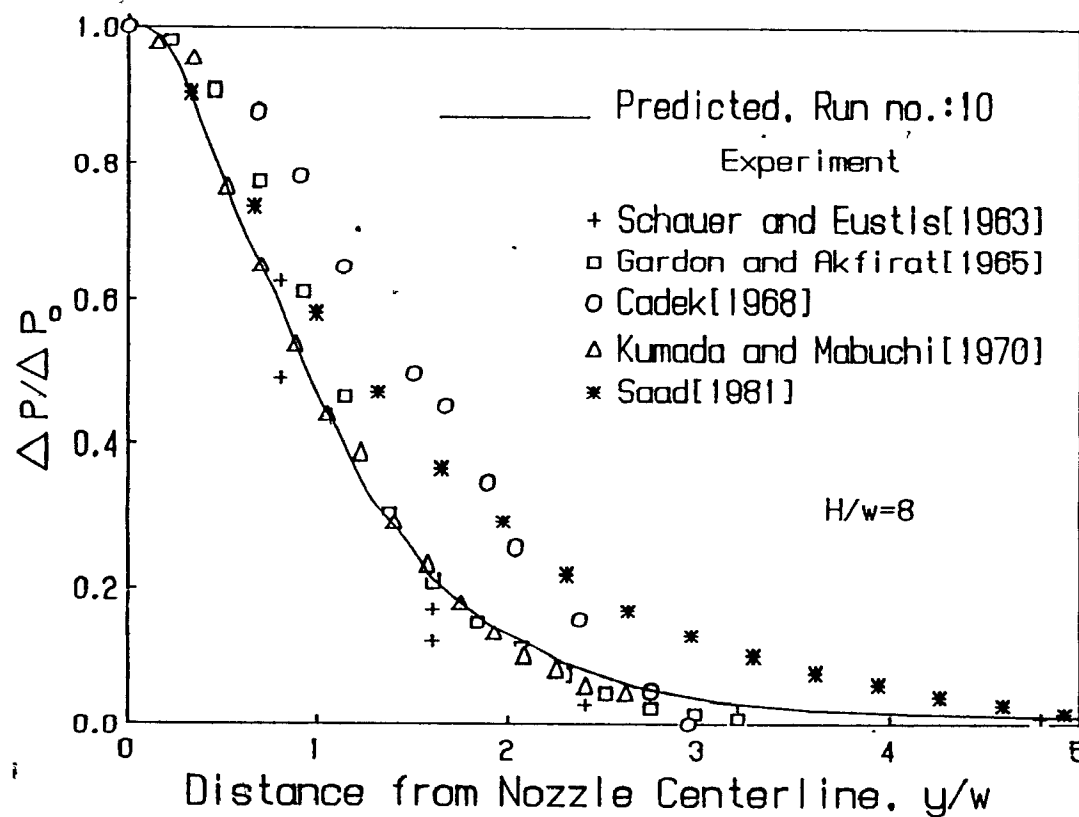


FIGURE 7.8b. Profiles of normalized static pressure at the impingement surface for  $H/w=8$

are those of Saad[1981]. Cadek's[1968] nozzles were only partially confined, and all other studies used unconfined jets. Confined and unconfined impinging jets show quite different static pressure distributions for  $H/w < 8$ . For an unconfined jet, static pressure decreases from the stagnation point maximum to zero at the end of stagnation region. For a confined jet, the end of the stagnation region is marked not by zero pressure, i.e. atmospheric, but by a minimum static pressure which can be negative, as documented by Saad. Thus an important feature of confined jets is recovery of pressure in the wall jet region as static pressure becomes equal to the atmospheric pressure at the outlet of the confinement system. Comparison of static pressure distributions between confined and unconfined jets for small values of  $H/w$  must recognize this basic difference. The reference value in computations of pressure was that at the central grid node of the nozzle. In Fig. 7.8a and 7.8b the reference pressure for  $\Delta P$  and  $\Delta P_0$  for the confined jets was taken to be the minimum pressure, interpreted as marking the end of the stagnation region. The static pressure distribution along the impingement surface was then normalized using  $\Delta P_0$ , stagnation pressure.

Fig. 7.8a displays the excellent agreement in normalized pressure profiles, between that predicted at  $H/w=2.5$  and the experimental profile of Gardon and Akfirat[1965] at  $H/w=2$ . At  $H/w=8$  the agreement between the predicted  $\Delta P/\Delta P_0$  profile and the several experimental profiles at  $H/w \geq 8$ , Fig 7.8b, is within experimental error. The boundary conditions of the experiments of Saad and Cadek are closest to those used in the predictions, i.e. completely or partially confined jets, and the flat nozzle exit velocity profile produced by their

nozzles (ASME, elliptically contoured entry), yet agreement with their pressure profiles is not particularly good. The pressure profiles of Cadek at  $H/w$  of 2 and 4, so close as to be indistinguishable, are lower than the predicted profile at  $H/w=2.5$ , Fig. 7.8a, but the profiles of Saad and Cadek are higher than that predicted at  $H/w=8$ , Fig. 7.8b. The predicted location of zero  $\Delta P$  when  $H/w=8$  shows excellent agreement with the position found by Saad,  $4w-5w$ .

The predicted locus of normalized maximum lateral velocity along the impingement surface for spacings,  $H/w$ , of 2 and 8 is compared with experimental data for an unconfined jet on Fig. 7.9. The kinetic energy of a jet is converted to static pressure at the stagnation point, then back to kinetic energy as the flow accelerates parallel to the impingement surface and static pressure drops correspondingly. When an impingement surface is located at a position corresponding to the potential core of a free jet, as for example with  $H/w=2$ , this process leads to a maximum value of unity for the  $v/u_j$  ratio at the end of the stagnation region, i.e. complete conversion from  $u_j$  to  $P_o$  and back to maximum  $v$ . As an impingement surface at  $H/w=8$  is outside the potential core region, the  $v/u_j=1$  condition is never reached. The predicted and experimental profiles of  $u/u_j$ , Fig. 7.9, agree well up to the peak values, beyond which they differ for reasons which depend on the nozzle-to-surface spacing,  $H/w$ .

For a relatively close nozzle spacing, such as  $H/w=2$  in Fig. 7.9, the pressure gradient with an unconfined jet is always zero but with a confined jet is positive in the pressure recovery region. This difference in pressure gradient causes a faster decay of lateral velocity at the beginning of the wall jet region for a confined than

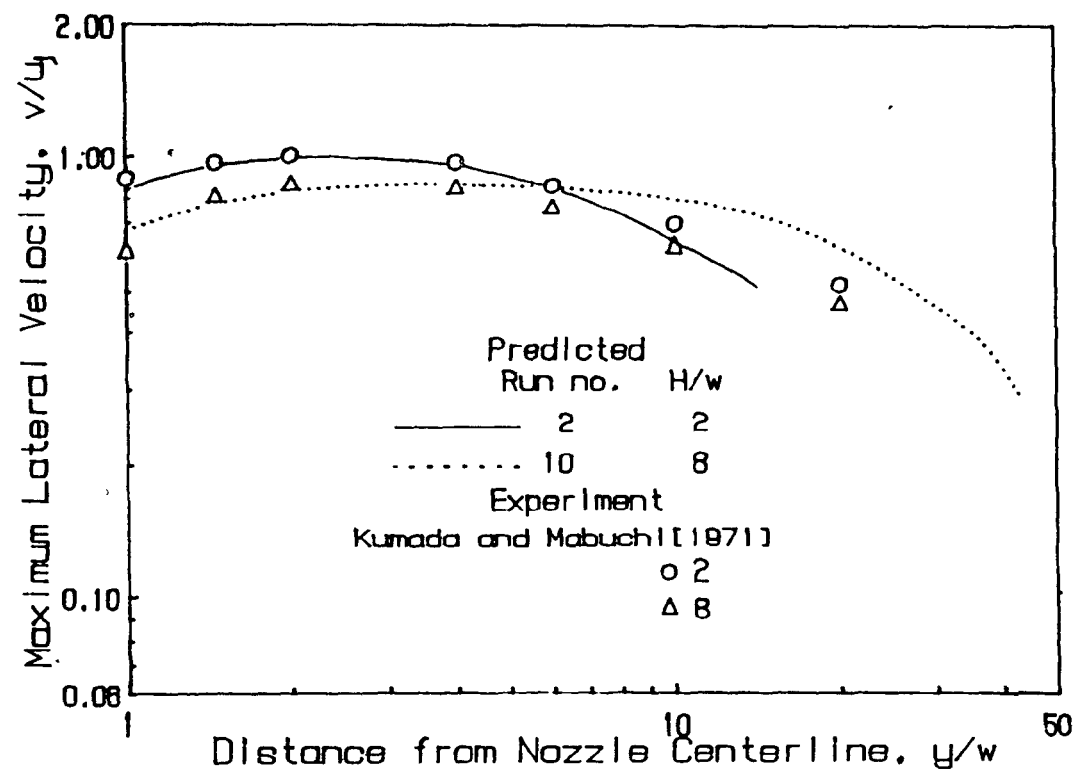


FIGURE 7.9. Effect of nozzle-to-surface spacing on profiles of maximum lateral velocity

for an unconfined jet, which is the trend apparent on Fig. 7.9.

For a nozzle spacing of  $H/w \geq 8$  another mechanism explains the Fig. 7.9 divergence in the opposite direction. Entrainment of ambient air by an unconfined jet, substantial for larger  $H/w$  spacings, consumes jet momentum. This process results in a decay of lateral velocity, after the peak in  $v/u_j$ , which is faster for an unconfined than a confined jet. This effect is correctly predicted in the present study, Fig. 7.9.

In Fig. 7.10 the development of profiles of axial velocity for the case of  $H/w=8$  at locations,  $x$ , of  $2w$ ,  $4w$  and  $6w$  from the nozzle exit is compared with experimental data of Cadec[1968] for a free jet. The nozzle used by Cadec was the ASME standard elliptical contoured entrance nozzle which gives a flat velocity profile, the nozzle exit boundary condition used in the present numerical predictions. Agreement between predicted and experimental results is excellent. The agreement at  $x/w=6$  when  $H/w=8$  shows that the effect of the impingement surface on mean axial velocity is not transmitted a distance more than  $2w$ ,  $0.25H$ , from the impingement surface. This characteristic is displayed again by Fig. 7.11, which shows that for  $H/w=8$ , centerline velocity decay starts at about  $0.25H$  from the impingement surface. Saad[1981] documented the same behaviour for a confined slot jet. In terms of length of the potential core, Fig. 7.11 shows that this region shrinks from about  $6w$  for  $H/w=8$ , to about  $0.5w$  for  $H/w=2.5$ , and disappears for  $H/w=1.25$ . Thus at the  $H/w=1.25$  spacing the presence of the impingement surface is felt by the jet immediately after the nozzle exit while for the higher spacings its effect is not felt until about  $0.25H$  from the surface.

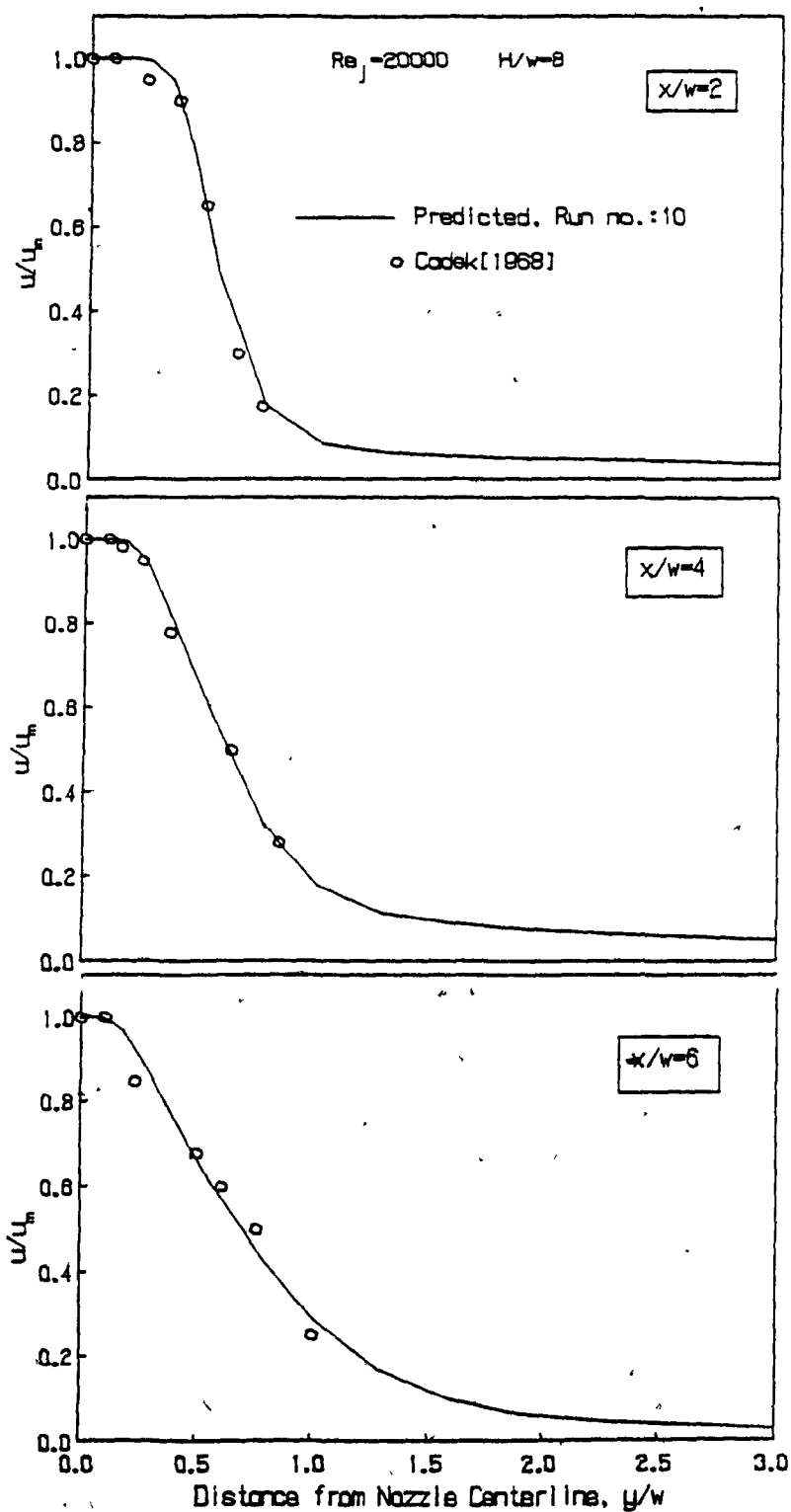


FIGURE 7.10. Effect of distance from nozzle exit on lateral profiles of axial velocity

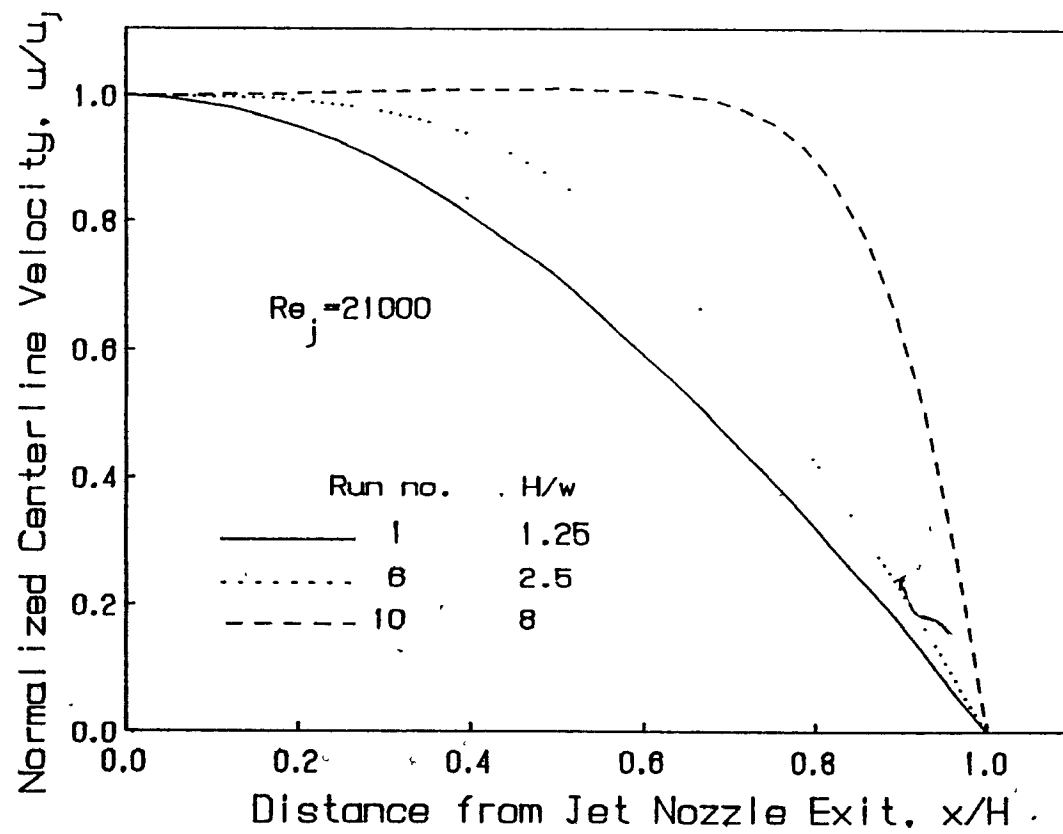


FIGURE 7.11. Effect of nozzle-to-surface spacing on profiles of centerline axial velocity.



b) Prediction of Nusselt Number

In Fig 7.12 the predicted Nu profiles at nozzle spacings,  $H/w$ , of 2 and 2.6 are compared with experimental data at comparable Reynolds numbers. Only van Heiningen[1982] used confined jets. The variation between experimental studies is greatest in the range  $3 < y/w < 10$ , where it is as much as  $\pm 30\%$ . Experimental studies agree on the location and the value of the off-stagnation minimum but not for the secondary maximum, given as  $Nu=40$  at  $y/w=5$  by Kumada et al.[1972], as  $Nu=24$  at  $y/w=8$  by Gardon and Akfirat[1966].

In the stagnation region agreement for the lower Reynolds number range between experimental profiles is good but the predicted profiles are too low over about the first  $2w$  from stagnation, for reasons noted earlier. The value and location of the off-stagnation minimum Nu, on the other hand, is predicted surprisingly well. As for the off-stagnation maximum Nu, its predicted location, about  $7w$  from the nozzle centerline, agrees well with experiments, which locate it at from  $5w$  to  $8w$  from the centerline. Its predicted value is likewise intermediate between the extremes of experimental measurements.

In Figs 7.13 through 7.15, the predicted Nu profiles for  $H/w=2.5$  and for somewhat higher values of  $Re_j$ , 21800-44300, are compared with the present experimental results for the identical conditions, and with earlier experimental results for similar conditions. At these higher values of  $Re_j$  the Nu profiles are predicted quite well from stagnation through the off-stagnation minimum to the secondary maximum,  $0 \leq y/w \leq 7$ , but beyond the secondary maximum the prediction is consistently high. The lower heat transfer rate in the wall jet region for the unconfined cooling jet of Cadek is attributed to the lack of a confinement

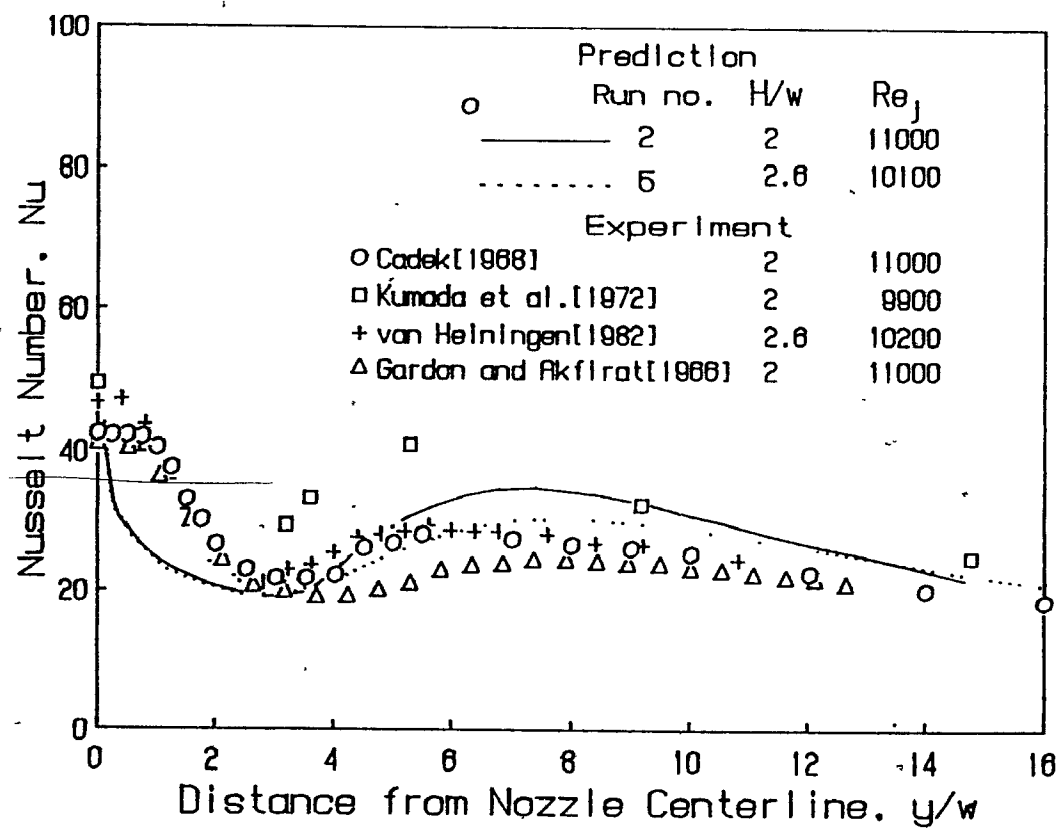


FIGURE 7.12. Profiles of local Nusselt number:  $Re_j=10000$ ,  $H/w$  of 2 and 2.6

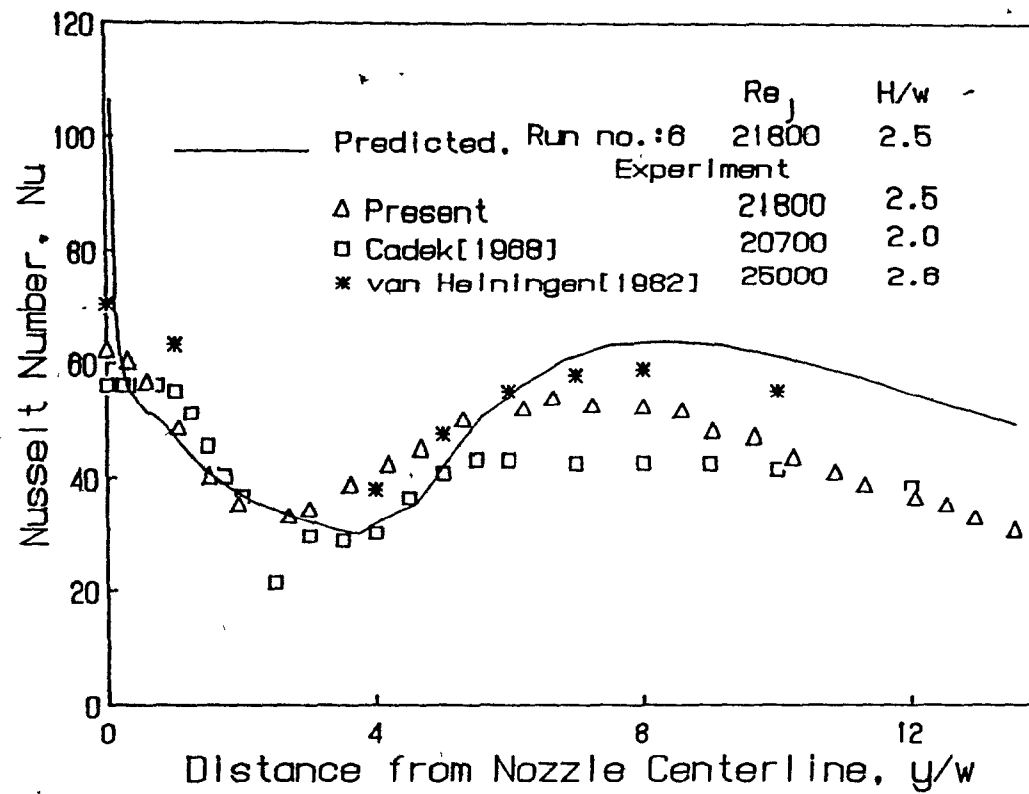


FIGURE 7.13. Profiles of local Nusselt number:  $Re_j=21800$ ,  $H/w=2.5$

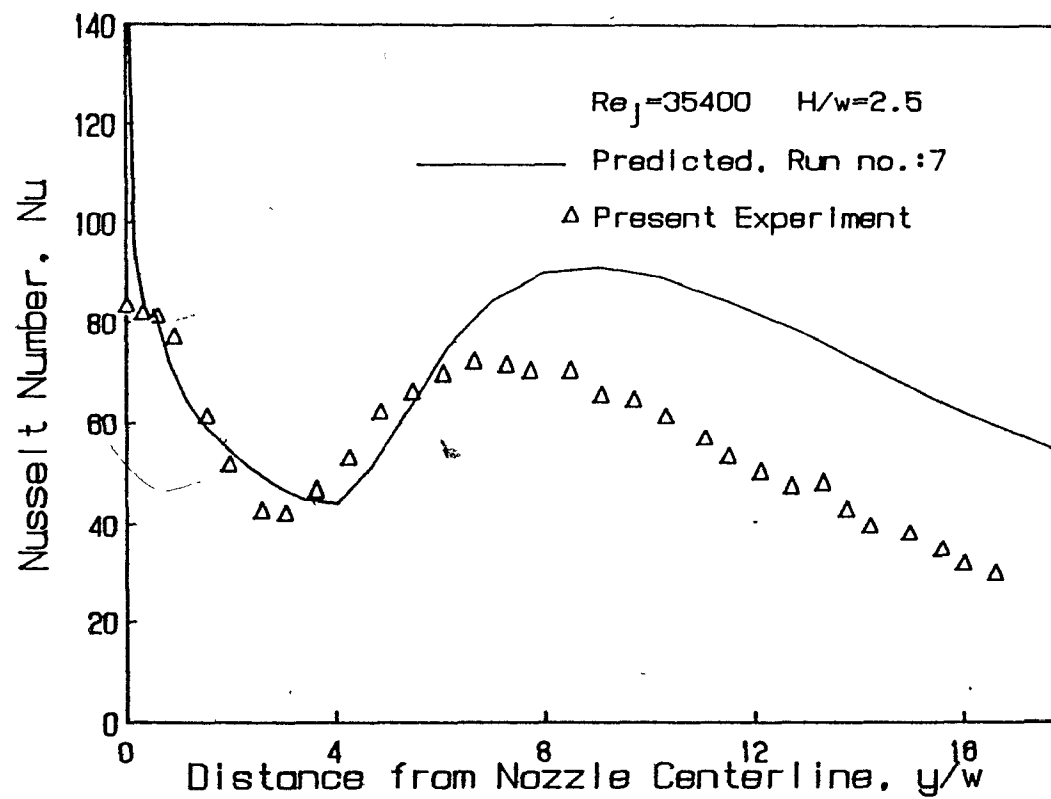


FIGURE 7.14. Profiles of local Nusselt number:  $Re_j=35400$ ,  $H/w=2.5$

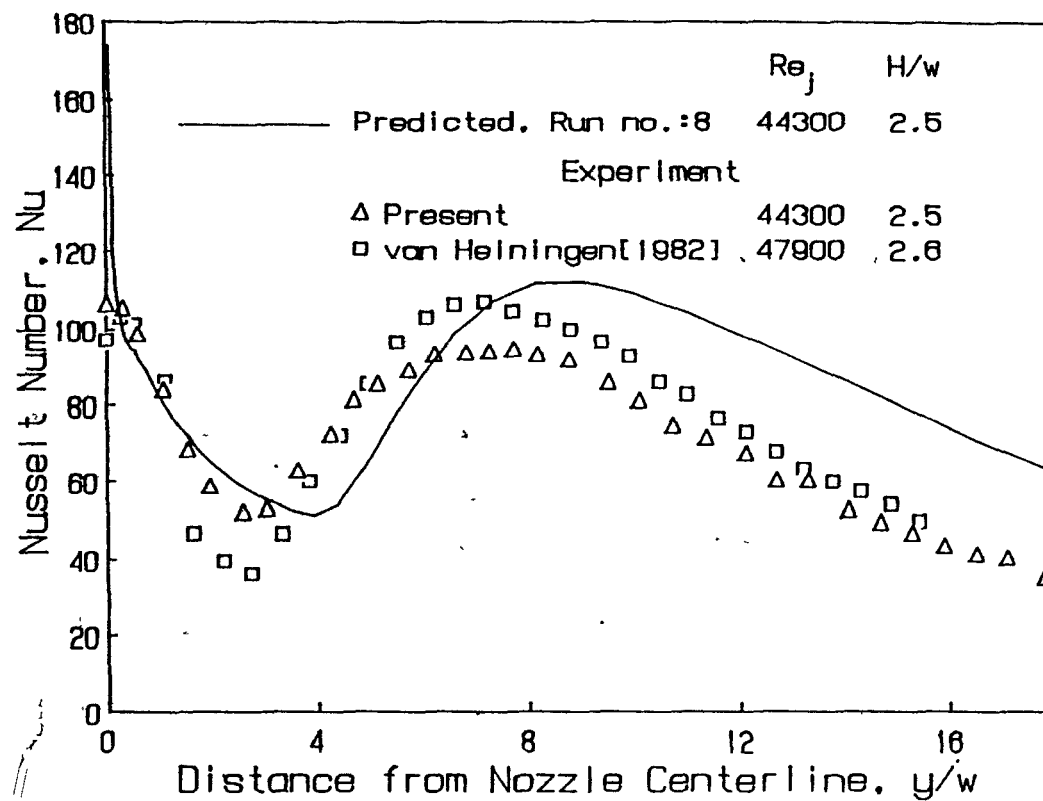


FIGURE 7.15. Profiles of local Nusselt number:  $Re_j=44300$ ,  $H/w=2.5$

surface. The impingement surface is flat for the predictions but cylindrical for the present experimental study and that of van Heiningen. Curvature of the impingement cylinder, expressed as the ratio of its diameter,  $D_c$ , to nozzle width,  $w$ , correspond to  $D_c/w$  values of 24 for the present case, 34 for van Heiningen. A wall jet spreads faster over a convex than a flat surface, an effect which reduces the parallel velocity near the impingement surface. Although heat transfer rates in the wall jet region are therefore expected to be lower over a cylindrical than a flat surface, no data exist which quantify this reduction as a function of  $D_c/w$ .

The reason for an off-stagnation minimum and maximum at  $H/w$  spacings less than 8 was ascribed long ago by Gardon and Akfirat[1966] to boundary layer transition, from laminar at stagnation to turbulent at the end of the impingement region. The phenomenon of transition is beyond the ability of the present turbulence and near-wall models. The prediction of Nusselt number in this region is therefore coincidental to the near-wall modelling of the turbulent kinetic energy generation and dissipation terms. This point is discussed further after examination of the predicted Nu profiles at higher  $H/w$  spacings.

The testing of this model for computer simulation of impingement heat transfer is now extended from the very low range of nozzle-to-surface spacings,  $1.25w$ - $2.6w$ , to spacings in the range  $6w$ - $8w$ . Figs. 7.16 and 7.17 provide comparisons at nozzle spacings of  $6w$  and  $8w$ , respectively, between predicted and experimental Nu profiles. As no claim of accuracy for the Nu predictions in the stagnation region can be made, Nu predictions with the present turbulent model are not examined in the  $y < 3w$  region. As  $Re_j$  is decreased or, as in this series

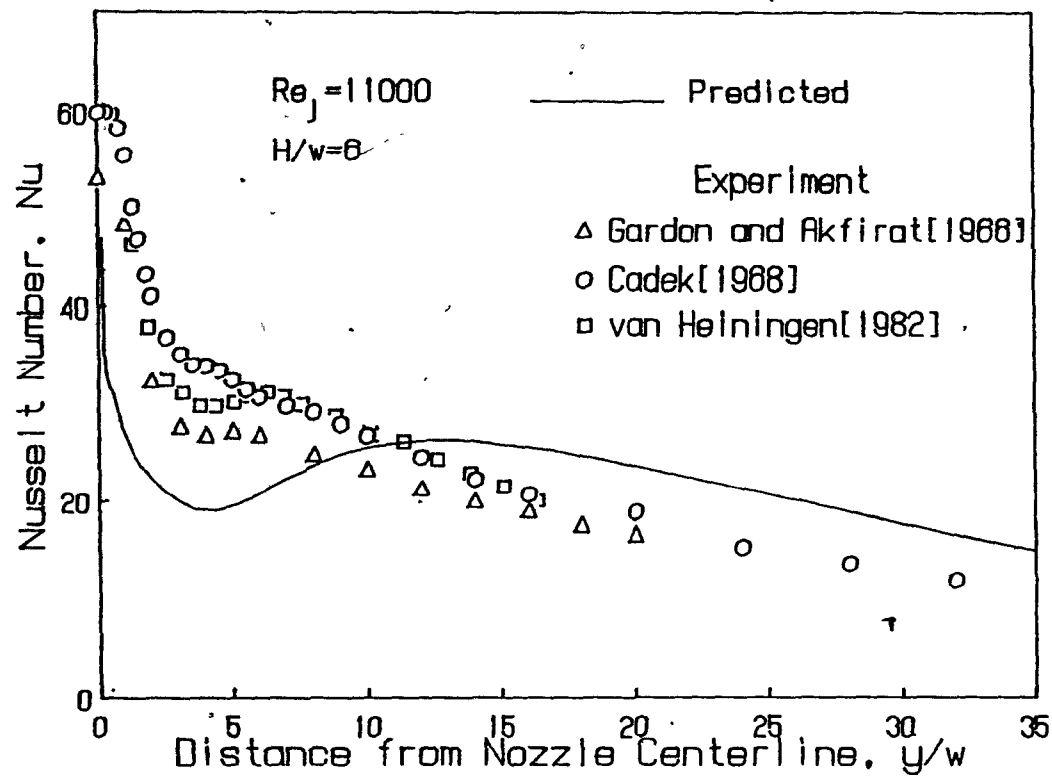


FIGURE 7.16. Profiles of local Nusselt number:  $Re_j = 11000$ ,  $H/w = 6$

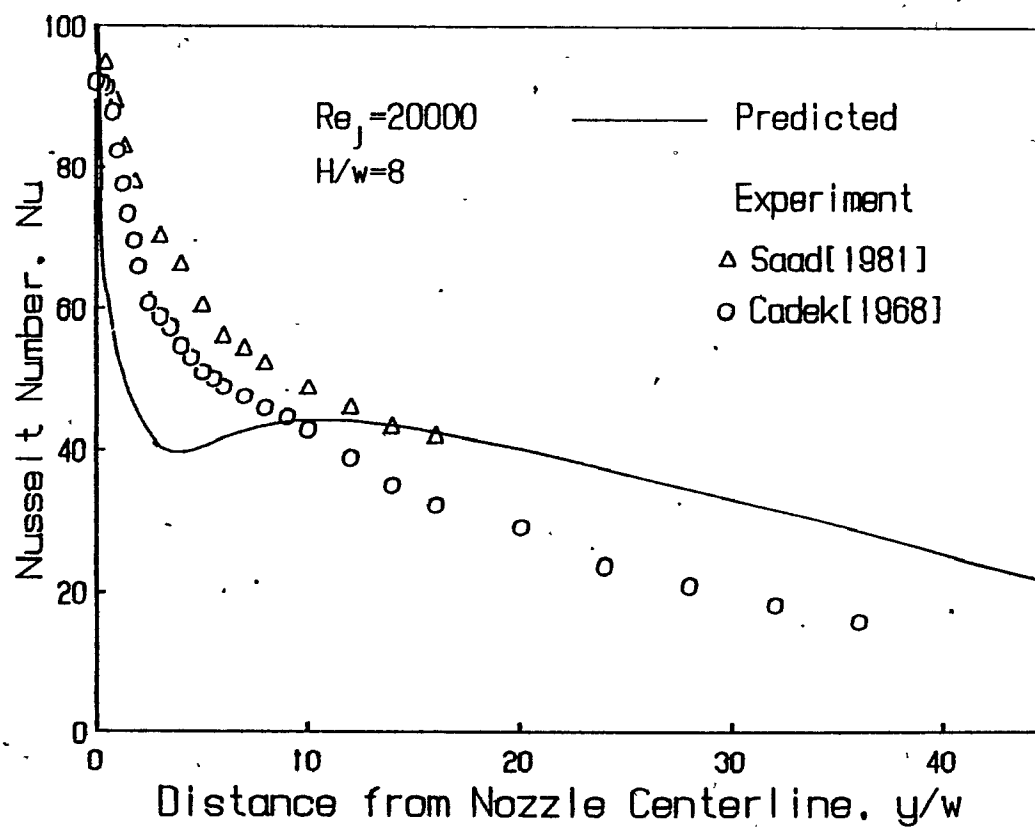


FIGURE 7.17. Profiles of local Nusselt number:  $Re_j = 20000$ ,  $H/w = 8$



of tests,  $H/w$  is increased, the off-stagnation features gradually disappear. The characteristic of the present model of sometimes underpredicting  $Nu$  in the stagnation region is again observed for the  $H/w-Re$  combinations of Figs. 7.16 and 7.17, but by about  $y/w=7$ , the  $Nu$  prediction is again quite good. Ideally the present predictions should be reliable beyond about  $7w$  from stagnation. In the region from about  $7w$  to  $12w$  from stagnation the predictions show  $Nu$  increasing with distance from stagnation but all experimental results decrease. For the wall jet region beyond  $y/w=10$  the results of Cadek and of Gardon and Akfirat fall below the predictions on Figs. 7.16 and 7.17, but as these experimenters used unconfined jets it is not known to what extent their  $Nu$  measurements are changed in the wall jet by entrainment of the ambient air surrounding their equipment. Van Heiningen's results in the wall jet region are likewise lower than the model predictions but his experiments, although with a fully confined jet, were made over a cylindrical impingement surface which acts to reduce  $Nu$  in the wall jet region by an amount which, again, is not known.

There is only one investigator, Saad[1981], who has used both a fully confined jet and a flat impingement surface. It is then highly significant that Saad's experimental measurements, Fig. 7.17, agree with the results predictions of the present study for the region starting at about  $10w$  from stagnation.

#### c) Prediction of Turbulence Characteristics

As prediction of the  $Nu$  distribution at the surface depends greatly on the  $k$  distribution, it is of interest to examine in Figs. 7.18-7.20 the lateral profiles of turbulent kinetic energy at various levels

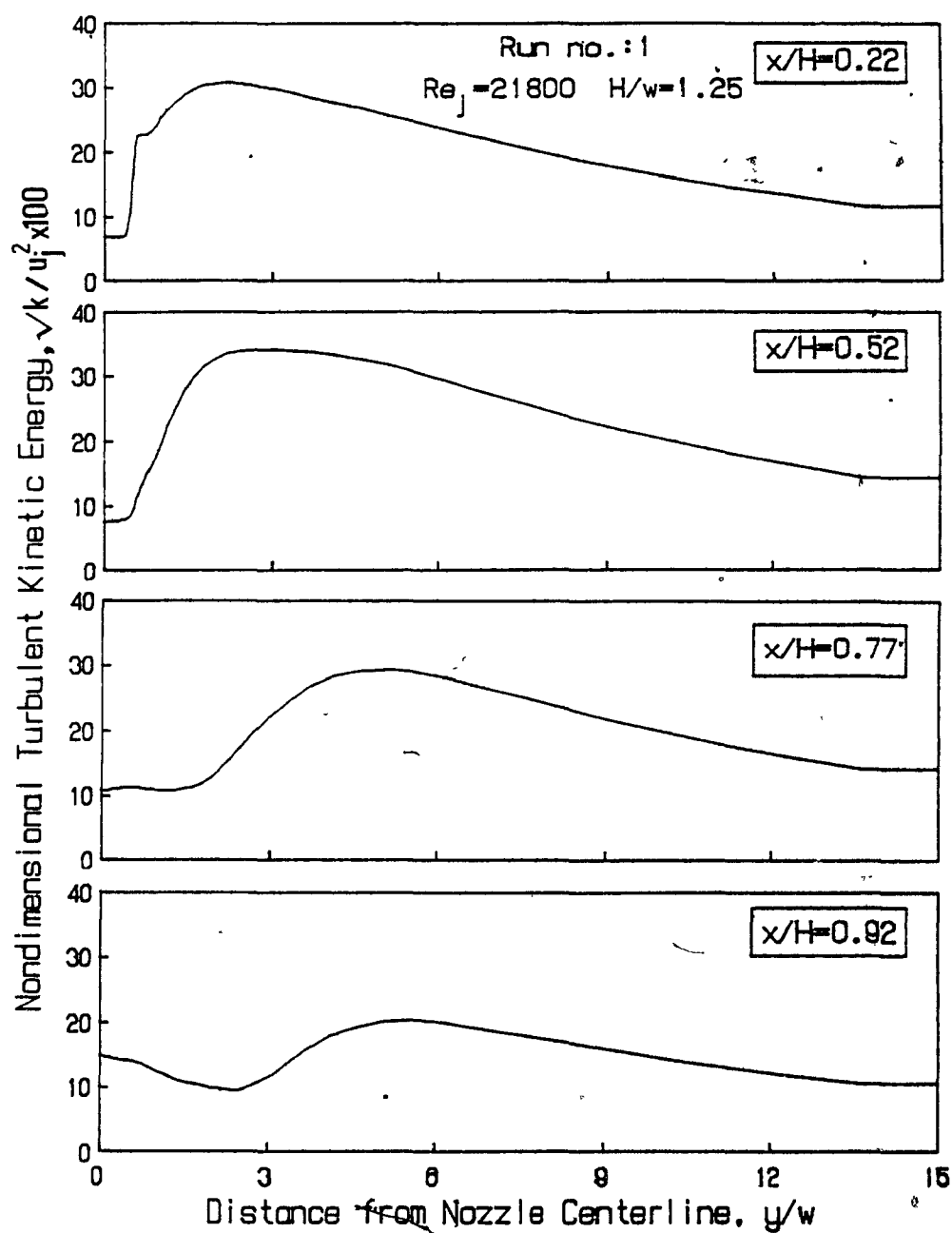


FIGURE 7.18. Effect of distance from nozzle exit on lateral profiles of turbulent kinetic energy:  $H/w = 1.25$

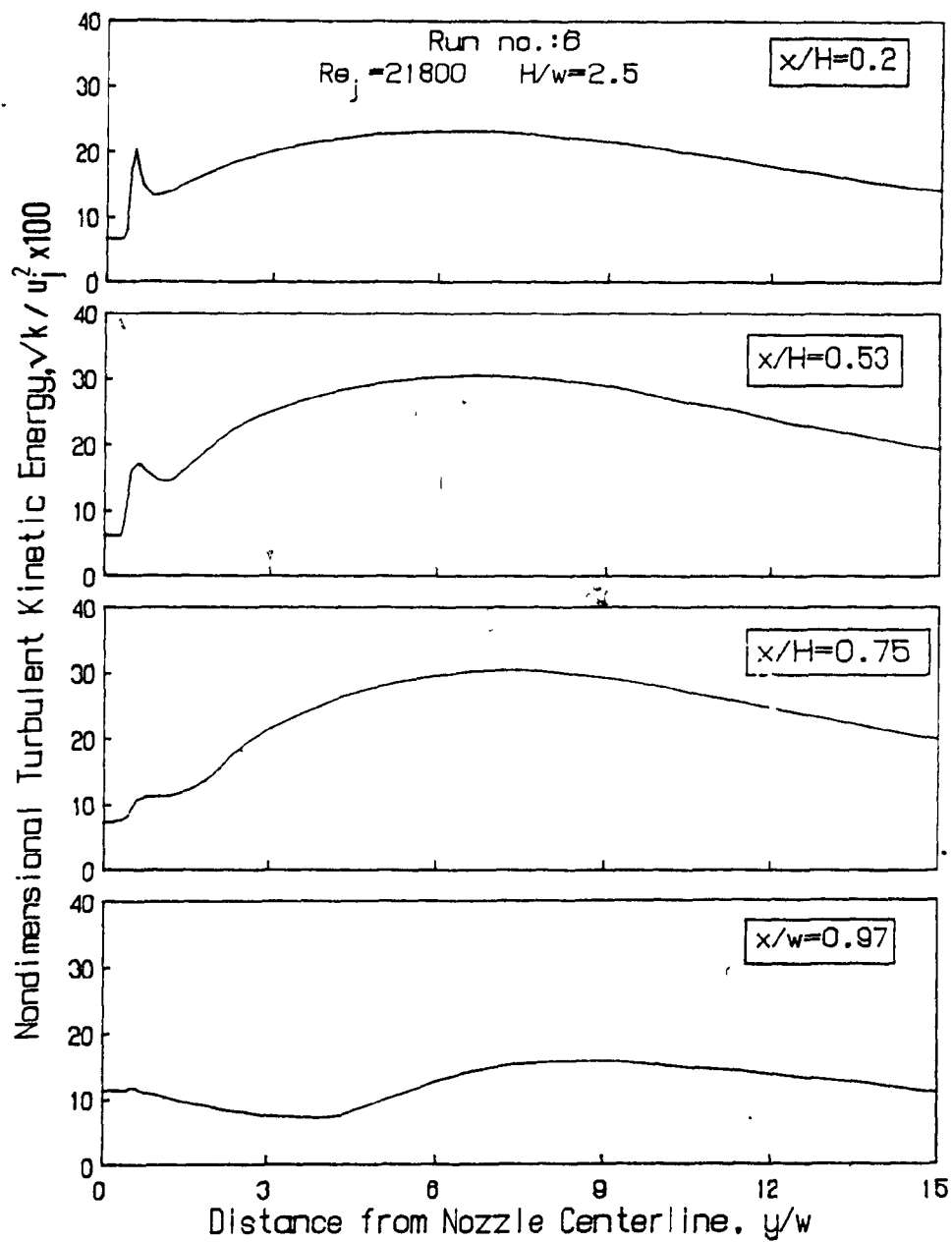


FIGURE 7.19. Effect of distance from nozzle exit on lateral profiles of turbulent kinetic energy:  $H/w = 2.5$

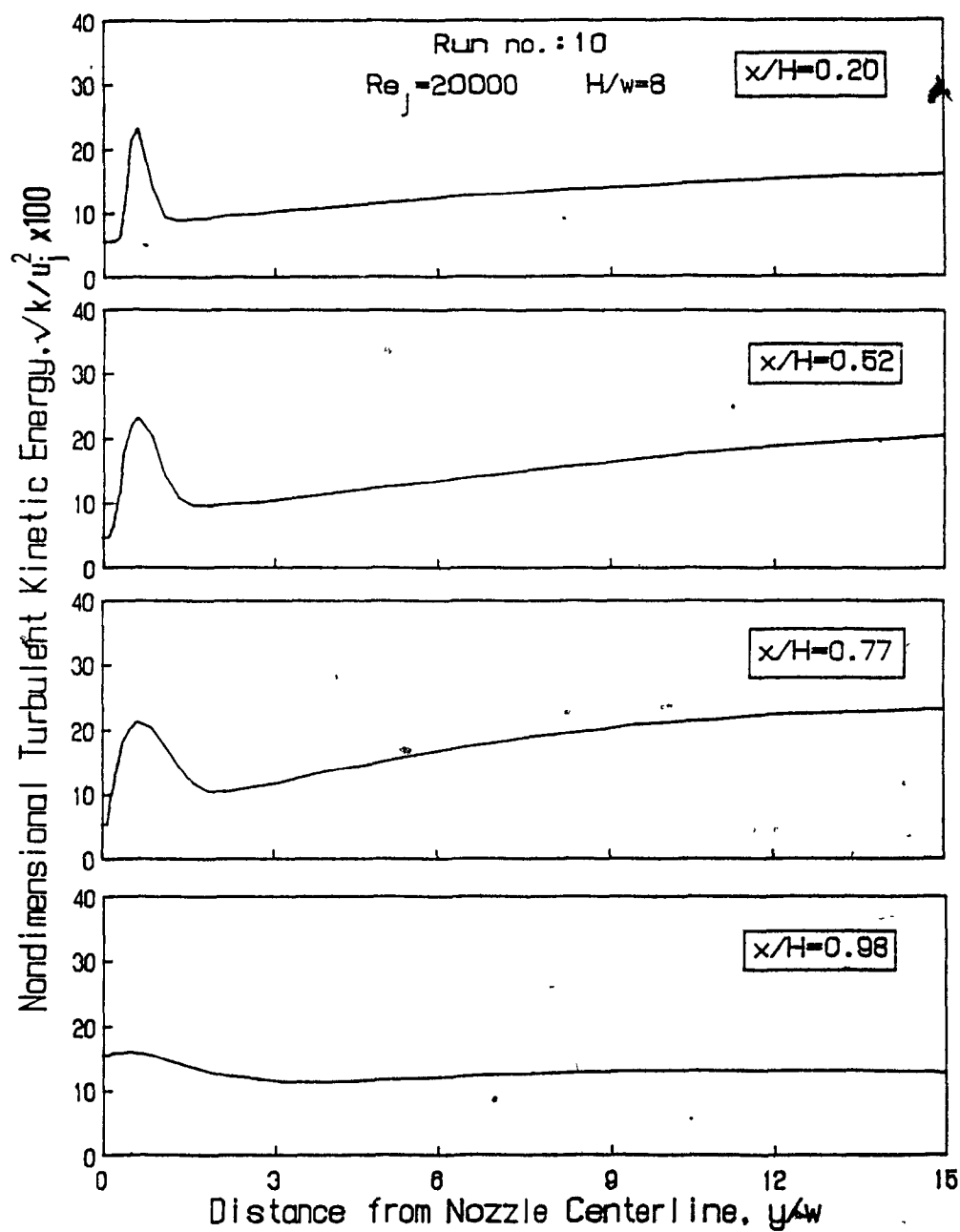


FIGURE 7.20. Effect of distance from nozzle exit on lateral profiles of turbulent kinetic energy:  $H/w = 8$

between the impingement surface and the nozzle exit-confinement surface, for each of three nozzle spacings. For each value of  $H/w$ , the lateral  $k$  profiles are plotted at about the same  $x/H$  location in order to compare turbulent kinetic energy development with increasing nozzle-to-surface spacing. It should be kept in mind that the corresponding values of  $x$  in terms of nozzle width,  $w$ , are quite different for each case.

High velocity gradients under the nozzle edge,  $y/w=0.5$ , generate high turbulent kinetic energy. Because of substantial velocity gradients, the turbulence energy increases in the recirculation region which is enveloped by the streamline emerging from the edge of the nozzle wall. Starting at  $0.5w$  from stagnation, i.e. under nozzle wall, the recirculation region extends out to  $3.5w$  from stagnation for  $H/w=1.25$ , out to  $14w$  for  $H/w=2.5$ , while for  $H/w=8$  the lateral extent of the recirculation region exceeds the  $46w$  width of the confined system. With  $H/w=8$  then, some inflow occurs near the confinement surface at the outflow boundary,  $46w$  from stagnation. The coordinates of the eye of the recirculation region move from  $(x=0.6w, y=1.5w)$  for  $H/w=1.25$ , to  $(x=1.2w, y=2.7w)$  for  $H/w=2.5$ , and to  $(x=4w, y=13w)$  for  $H/w=8$ . Similarly the peak of the high  $k$  region moves away from the stagnation point as  $H/w$  increases. As can be seen in these figures, the closer the spacing between the nozzle and impingement surface, the faster the diffusion of turbulence kinetic energy from under the nozzle wall, where it is generated, into the recirculation region.

Looney and Walsh[1984] reported that the turbulence characteristics of a plane free jet were not predicted well by the standard  $k-\epsilon$  model. They recommended the algebraic stress model of Rodi[1972] for this type.

of flow. In their prediction of impingement heat transfer, however, they observed that the  $k-\epsilon$  model gave better predictions with specification of inlet conditions from free jet predictions at  $0.55H$  from the surface. When the whole flow domain of an impinging jet from nozzle exit to impingement surface is considered, such as in the present study,  $Nu$  predictions with this model are probably less satisfactory at higher than lower spacings due to the inability of the  $k-\epsilon$  model to predict turbulence characteristics accurately in the free jet region.

The extent to which convective transfer rates might be increased by increasing turbulence at the nozzle exit remains an important question in impingement heat transfer. For  $H/w=2$  and  $Re_j=11000$ , Fig. 7.21 compares the predicted effect of jet inlet turbulence intensity on  $Nu$  profiles with the experimental results of Gardon and Akfirat[1965]. For  $H/w<8$  they reported that by increasing the turbulence level artificially at the nozzle exit, the heat transfer was increased, most in the stagnation region, but increased substantially even out to about  $8w$  from the nozzle centerline. Beyond  $8w$  from stagnation,  $Nu$  was unchanged. A similar observation was made by Saad[1981], who varied turbulence intensity at the nozzle exit by varying the width of slot nozzles over the range  $2.5\text{mm}-13.3\text{mm}$ .

The predictions of the present study show a curious nonlinearity, in that over the region of greatest sensitivity,  $4<y/w<9$ ,  $Nu$  is essentially unaffected by an increase in nozzle exit turbulence intensity from 2.5% to 7%, but  $Nu$  increases by 10%-15% for a further increase to 10% turbulence intensity at the nozzle exit. In the stagnation region Gardon and Akfirat's measurements for the same  $H/w$  and  $Re_j$  show a strong and continuous effect of nozzle exit turbulence

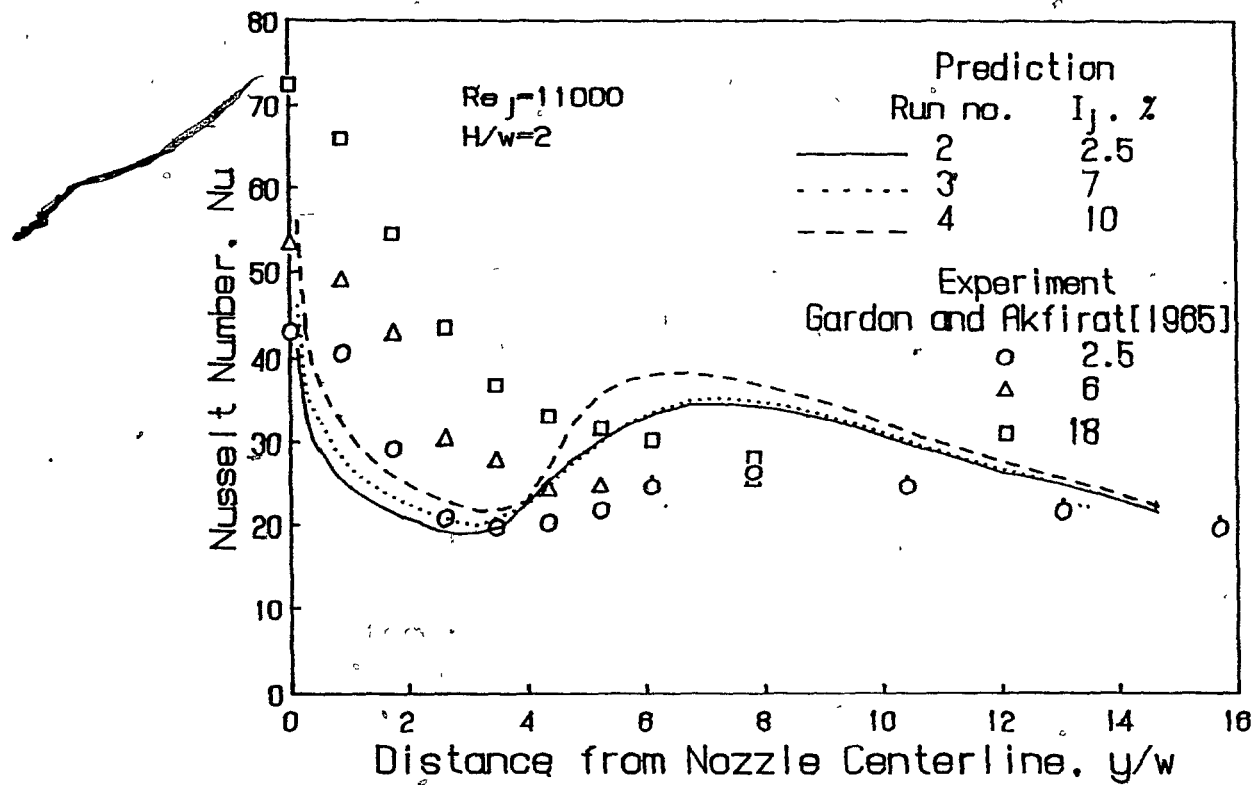


FIGURE 7.21. Effect of nozzle exit turbulence intensity on profiles of local Nusselt number: Re<sub>j</sub> = 11000, H/w = 2

level for their values of 2.5, 6 and 18%. In the present study no predicted profile could be obtained for 18% turbulence because of convergence problems. Gardon and Akfirat observed that at 18% nozzle exit turbulence the increase in stagnation region heat transfer was so large that the secondary peak completely disappeared. Even at 6% turbulence intensity the heat transfer increase in the stagnation region was sufficiently large that only a slight hump remained of the secondary peak. The inability of the  $k-\epsilon$  turbulence model to simulate the actual anisotropy of turbulence in stagnation flows may be the reason why the present model underpredicts the effect of inlet turbulence on heat transfer.

#### 7.4.2. Single Jet Heat Transfer with Throughflow

The range of parameters for simulations to predict effect of throughflow at the impingement surface is listed in Table 7.4.

Table 7.4 Parameter values for single jet simulations with throughflow at the impingement surface,  $H/w=2.5$ ,  $I_j=7\%$ .

Run no	$Re_j$	NX	NY	$u_\infty$ , m/s	$u_\infty/u_j$
6	21800	15	30	0.0	0.0
11	21800	15	30	0.094	0.0044
12	21800	15	30	0.256	0.012
7	35800	20	30	0.0	0.0
13	35800	20	30	0.109	0.0032
8	44300	25	40	0.0	0.0
14	44300	25	40	0.095	0.0023
15	44300	25	40	0.237	0.0058

The nozzle-to-impingement surface spacing,  $H/w=2.5$ , and the values of jet Reynolds number and throughflow rates were selected to duplicate the conditions of experimental runs presented in Chapter 5. The nozzle



exit turbulence intensity used, 7%, is within the range below which the model is insensitive to this parameter, Fig. 7.21. As the simulations were for a constant fluid density the throughflow parameter,  $Mu_s$ , is equal to the velocity ratio  $u_s/u_j$ .

Fig. 7.22 displays Nu profiles predicted for  $Re_j=44300$  with throughflow velocity from 0 to 0.237 m/s ( $0 < Mu_s < 0.58$ ). Relative to the no-throughflow profile, application of uniform throughflow predicts a uniform increase in Nu along the impingement surface, exactly as is measured experimentally, Chapter 5. Comparison with experimental results, Fig. 7.23, is therefore made on the basis developed in Chapter 5, i.e. as enhancement of average Stanton number due to throughflow,  $\Delta \overline{St}$ , relative to the nondimensional measure of throughflow,  $Mu_s$ . Fig. 7.23 shows profiles of enhancement of average heat transfer by throughflow,  $\Delta \overline{St}/Mu_s$ , as a function of the half-width of the heat transfer surface,  $S/w$ , on either side of the nozzle centerline. The second feature documented by the experimental measurements, Chapter 5, is that the ratio  $\Delta \overline{St}/Mu_s=0.175$ , independent of  $Mu_s$ ,  $Re_j$  and  $S/w$ . If the predicted results for  $\Delta \overline{St}/Mu_s$  at  $S/w=8$  are cross-plotted with respect to  $Mu_s$ , they show the enhancement,  $\Delta \overline{St}/Mu_s$ , increasing with  $Mu_s$  rather than independent of throughflow rate. As  $Mu_s \rightarrow 0$ , the predicted  $\Delta \overline{St}/Mu_s$  approaches the experimentally measured value, 0.175. Within the range of  $Mu_s$  measured experimentally in Chapter 5, i.e.  $0 < Mu_s < 0.002$ , the predicted enhancement,  $\Delta \overline{St}/Mu_s$ , agrees within 10% of that measured experimentally, but for  $Mu_s > 0.002$  the model overpredicts the enhancement in average heat transfer by throughflow. This limitation is not of much importance because the range  $Mu_s \leq 0.002$  covers throughflow rates of particular interest for industrial

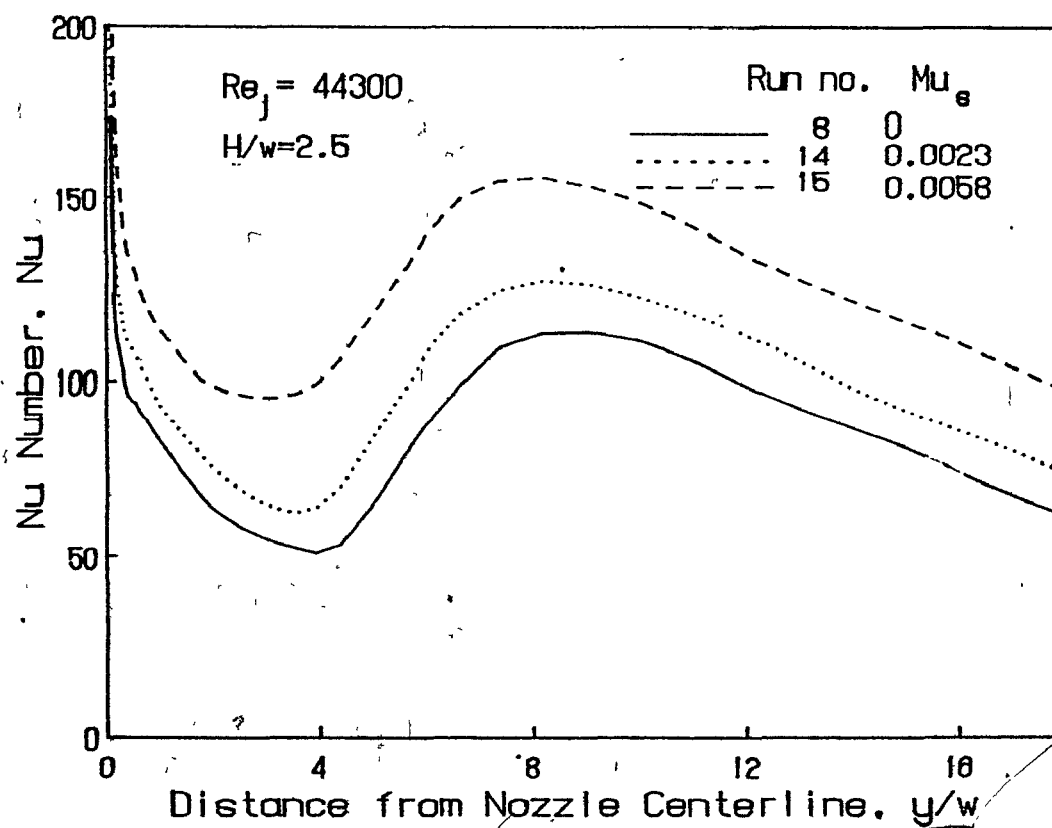


FIGURE 7.22. Effect of throughflow at the impingement surface on profiles of local Nusselt number:  $Re_j = 44300$ ,  $H/w = 2.5$

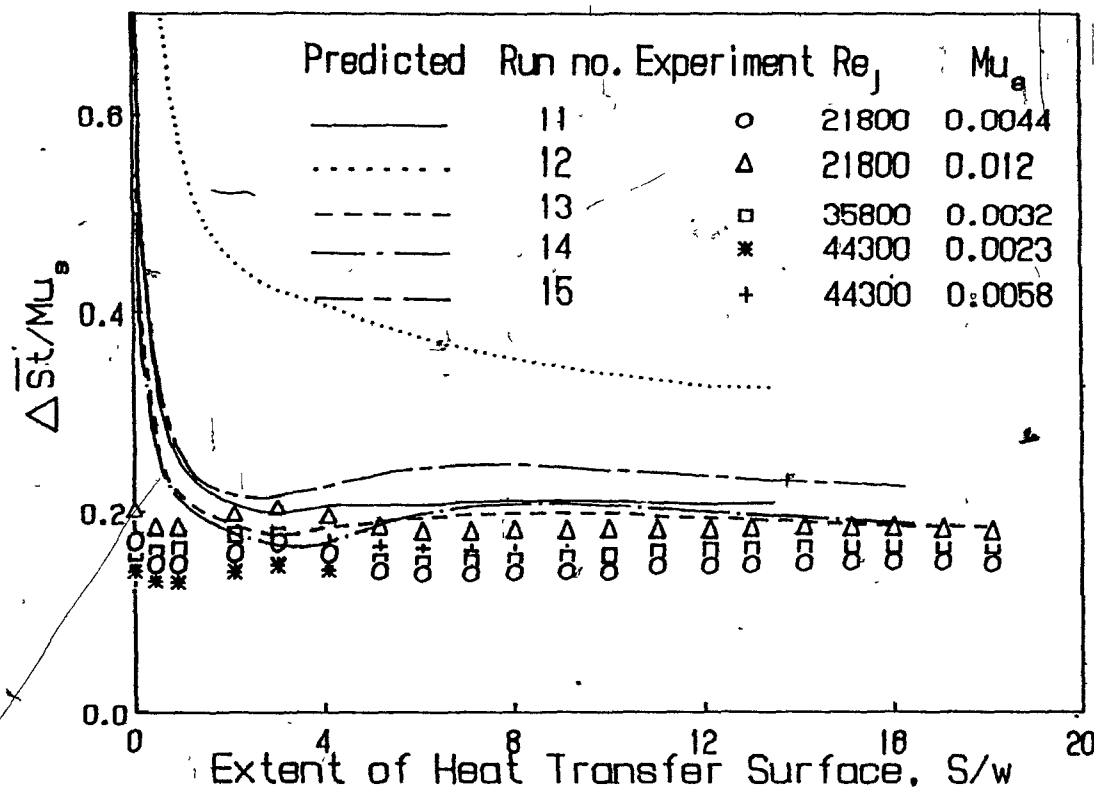


FIGURE 7.23. Profiles of enhancement of average Stanton number

application.

The reason why the predicted values of  $\Delta St/Mu_s$  increase with  $Mu_s$  is probably the fixed values of A and B in the bilogarithmic formula used to calculate wall shear stress in the case of with throughflow. Although the values of A and B in Eq. A3.27 should depend on throughflow velocity (Black and Sarnecki[1958]), as detailed in Appendix 3 these values were instead taken as the respective values for no-throughflow. The data of several studies for boundary layer velocity with throughflow are not sufficiently consistent to permit correlation of A and B in terms of  $u_s$ . One such attempt, presented in Appendix 3 using the data of Favre et al.[1966], was not implemented due to the limited nature of the experimental data. Until additional studies of the effect of throughflow on the boundary layer appear, this problem restricts the maximum throughflow rate for which the model may be used.

As the model gives remarkably good predictions of enhancement in average heat transfer by throughflow, it is of interest to examine the predicted effects of throughflow on axial velocity near the impingement surface, Fig. 7.24, on profiles of lateral velocity, Fig. 7.25, and on turbulent kinetic energy very close to the impingement surface, Fig. 7.26.

From a comparison of predicted lateral profiles of axial velocity at positions  $0.5w$  ( $0.2H$ ) and  $0.1w$  ( $0.04H$ ) from the impingement surface, Fig. 7.24, it is seen that at a nozzle-to-surface spacing,  $H/w$ , of 2.5 almost no effect of throughflow is predicted even as close as  $0.5w$  from the surface. At  $0.1w$  from the impingement surface, throughflow increases axial velocity by an almost uniform amount everywhere, i.e.

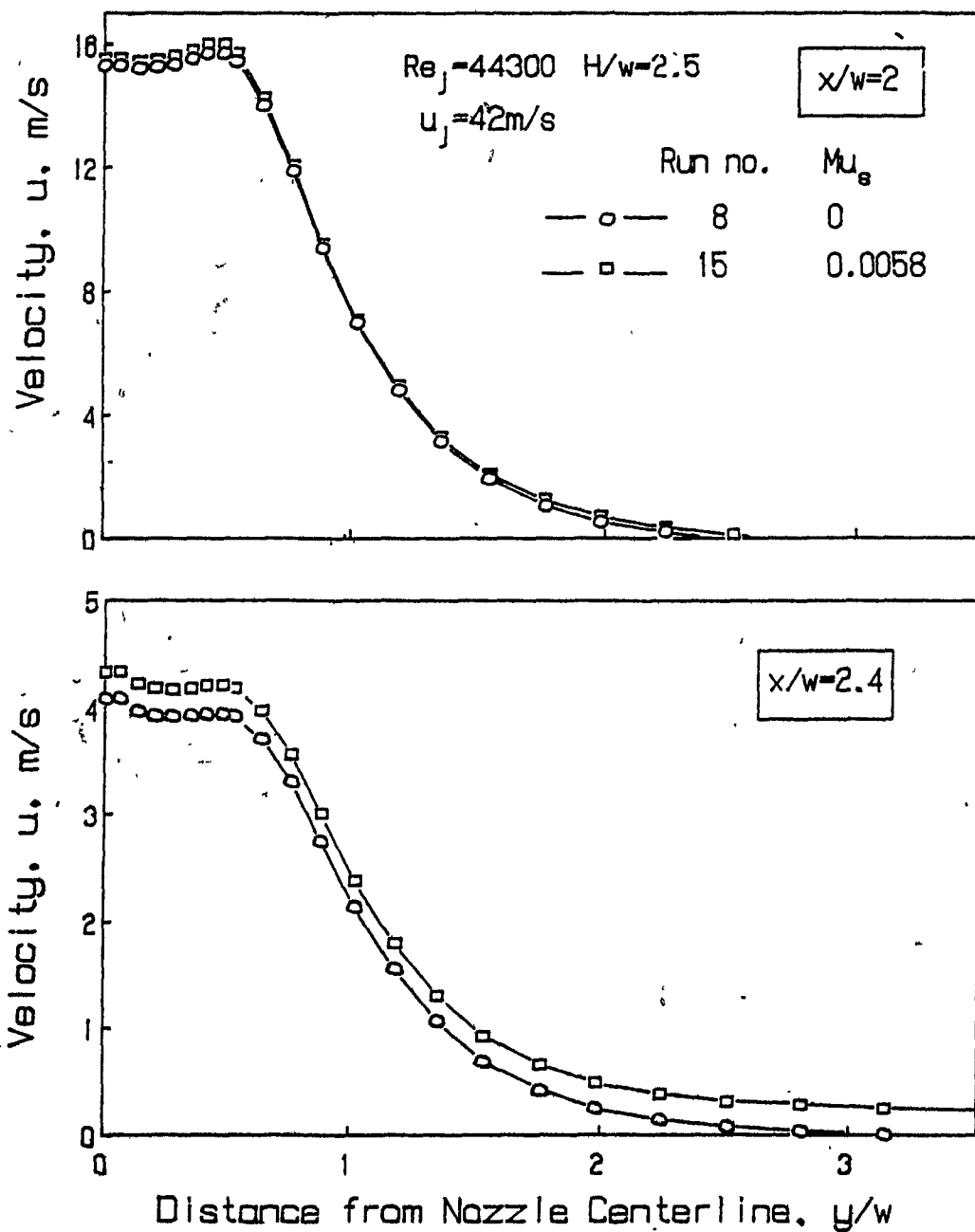


FIGURE 7.24. Effect of throughflow at the impingement surface on lateral profiles of axial velocity at  $0.5w$  and  $0.1$  from the impingement surface:  $Re_j = 44300$ ,  $H/w = 2.5$

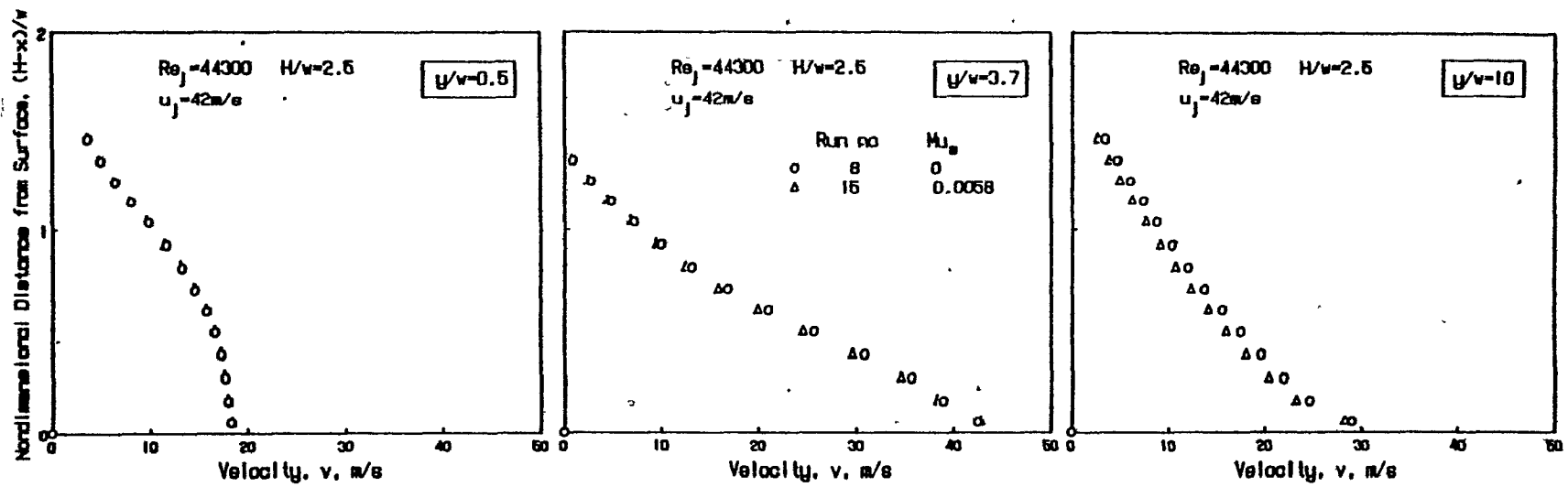


FIGURE 7.25. Effect of throughflow at the impingement surface on profiles of lateral velocity:  $Re_j = 44300$ ,  $H/w = 2.5$

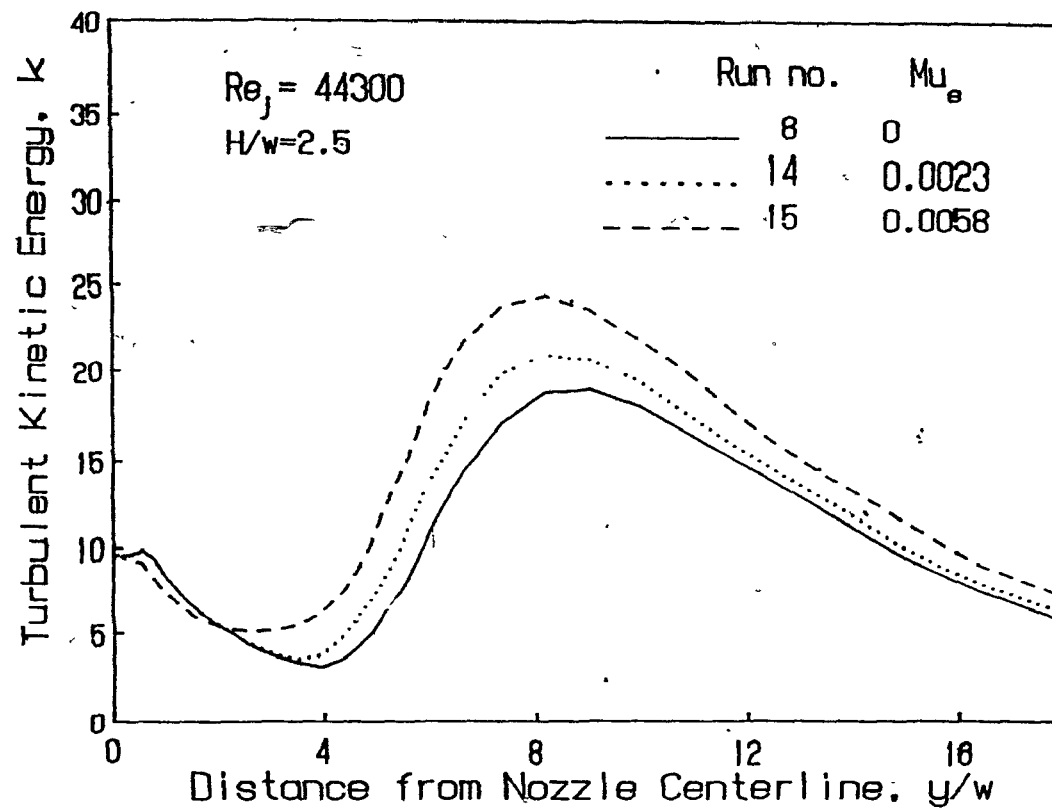


FIGURE 7.26. Effect of throughflow at the impingement surface on profiles of turbulent kinetic energy near impingement surface:  $Re_j = 44300$ ,  $H/w = 2.5$

with a relative increase which becomes very large by even  $3w$  from the nozzle centerline. As this throughflow velocity,  $u_s = 0.237$ , is so small compared with the nozzle exit velocity,  $u_j = 42\text{m/s}$ , a plot of centerline axial velocity, such as Fig. 7.11, with and without throughflow would show no apparent effect of throughflow. For a confined slot and an unconfined round jet, respectively, Saad[1981] and Obot[1981] measured the lateral profiles of the axial velocity at a position  $2w$  ( $0.25H$ ) from the surface when the impingement surface was spaced  $8w$  from the nozzle. Saad's measurements show that at a uniform throughflow velocity of  $0.3\text{m/s}$ , axial velocity increased by a constant amount everywhere, independently of  $Re_j$  ( $11000 < Re_j < 30000$ ). At a jet Reynolds number of 38000 and for a uniform throughflow velocity,  $u_s$ , of  $0.175\text{m/s}$  and  $0.25\text{m/s}$ , Obot observed the same effect. Contrary to the results of these two experimental studies, predictions show no appreciable effect of throughflow on axial velocity at a location  $0.2H$  away from the impingement surface.

The Fig. 7.25 comparison of predicted profiles of lateral mean velocity across the wall jet, with and without throughflow, indicates negligible effect out to  $3.7w$  from stagnation. By  $10w$  from stagnation, this amount of throughflow is predicted to decrease the lateral velocity near the impingement surface slightly, by 5%. For  $Mu_s = 0.0058$  the cumulative amount of air removed by throughflow by  $y/w = 10$  is 12% of the jet inflow. The experimental measurements of Saad[1981] and Obot [1981] indicate that throughflow increases the streamwise velocity near the surface. A similar observation was made by Baines and Keffer[1979] for an unconfined slot jet impinging at a fixed  $u_s/u_j$  value of 0.29%. Thus the predicted effect of throughflow on wall jet velocity profiles



adjacent to the impingement surface is opposite to three experimental observations. Limitations of the turbulence model may be a factor. It is well known that the distance from the impingement surface for the positions of zero shear stress and of maximum wall jet velocity do not coincide. How throughflow affects this relationship is unknown. A turbulent-viscosity model such as used here cannot predict the correct location of the wall jet velocity maximum because it implicitly requires the zero shear stress and velocity maximum to be coincident. Moreover, when a high-Re version turbulence model is used, near-wall properties such as wall shear stress and heat transfer are estimated using wall functions, so detailed features of the near-wall flow cannot be simulated.

Saad[1981] found that throughflow increased axial mean velocity but did not affect axial turbulence velocity, so that axial turbulence intensity decreased with throughflow. For a round jet Obot[1981] found the same effects as Saad for both axial and streamwise turbulence. In Fig. 7.26 the predicted nondimensional turbulent kinetic energy profiles along the grid line next to the impingement surface, i.e. about  $0.1w$  from it, are displayed for the same throughflow rates as those of Fig. 7.25. Thus beyond the impingement region the numerical model is found to predict a decrease in near-wall velocity, Fig. 7.24, accompanied by an increase in turbulent kinetic energy near the surface, Fig. 7.25. Both these trends are opposite to the experimental measurements of Saad and Obot. Thus except at quite high throughflow rates, Fig. 7.23, the model predicts about the correct enhancement in average heat transfer by throughflow but, paradoxically, the mechanisms by which the model does this, Figs. 7.24, 7.25, 7.26, are not

consistent with the experimental evidence.

#### 7.4.3 Multiple Jet Heat Transfer with and without Throughflow

The model was used to predict heat transfer for a multiple confined jet configuration with exhaust ports located symmetrically between the jet nozzles, Fig. 7.2. The width of exhaust ports is twice that of the jet nozzles. For such a multiple jet system composed of repeating units, or flow cells, of dimensions  $S \times H$ , Saad[1981] established that flow cell aspect ratio,  $S/H$ , is a basic parameter which defines conditions of geometric similarity for flow and heat transfer. Due to flow symmetry it is necessary to solve only the domain of a single flow cell,  $S \times H$ . Fig. 7.2 indicates that each such flow cell takes half the flow from a nozzle. The simulation was again performed using Model 4 as the near-wall model, results using Model 2 having been reported previously by Polat, Mujumdar and Douglas[1986]. As the only comparable experimental data are those by Saad[1981] without throughflow, and those of the present study with and without throughflow, two series of simulation runs were made, Table 7.5, one matching the conditions of each of these experimental studies.

Table 7.5 Parameter values for multiple jet simulations

Run no	H/w	$Re_j$	$I_j$	NX	NY	S/H	$u_s$ , m/s	$u_s/u_j$
16	8	21000	1	25	30	1.0	0	0
17	8	21000	1	25	30	0.75	0	0
18	8	21000	1	25	30	0.5	0	0
19	8	21000	1	25	30	0.375	0	0
20	5	8200	5	20	25	0.5	0	0
21	5	8200	5	20	25	0.5	0.043	0.0031
22	5	8200	5	20	25	0.5	0.109	0.0079
23	5	8200	5	20	25	0.5	0.161	0.0117
24	5	8200	5	20	25	0.5	0.268	0.0194

As Saad[1981] measured local Nusselt number profiles for multiple confined slot jets at  $Re=21000$ ,  $H/w=8$ , for flow cell aspect ratio,  $S/H$ , of 1 and 0.75, the model was used to predict  $Nu$  for these conditions. Two lower values of  $S/H$ , 0.5 and 0.375, were added to provide results for very closely spaced nozzles and exhaust ports. In these simulations  $H$  and  $w$  were fixed and the variation in  $S/H$  from 1 to 0.375 was obtained by changing the centerline spacing, nozzle-to-exhaust port,  $S$ . The number of grid nodes was fixed at  $25 \times 30$ , the nozzle exit turbulence intensity at 1%. Saad used elliptically contoured entry nozzles in his multiple jet study, for which he measured nozzle exit turbulence intensities of less than 1%. The present model has been shown, Fig. 7.21, to be insensitive to nozzle exit turbulence intensity over the region 2.5%-7% even for a spacing as small as  $H/w=2$ . Hence the choice of nozzle exit turbulence intensity of 1% is reasonable.

The sharp increase in predicted  $Nu$  within about  $0.25w$  of the centerline of both the exhaust port and the jet nozzle, Fig. 7.27, is the same characteristic apparent very near the nozzle centerline for the single jet profiles displayed in section 7.4.2. The inability of the simulation to predict  $Nu$  satisfactorily within about  $0.25w$  of the jet and exhaust flow centerlines is attributed to the wall-function method used.

Over the central 80% of the nozzle centerline-to-exhaust centerline spacing,  $S$ , Fig. 7.27 shows the agreement is within 30% between  $Nu$  predicted and  $Nu$  measured by Saad for  $S/H$  ratios of 1 and 0.75. { No experimental data exist for  $S/H$  of 0.5 and 0.375. From his measurements over a wide range of  $S/H$  at larger values of  $H/w$ , Saad predicted that average heat transfer rate at any  $H/w$  would pass through a maximum

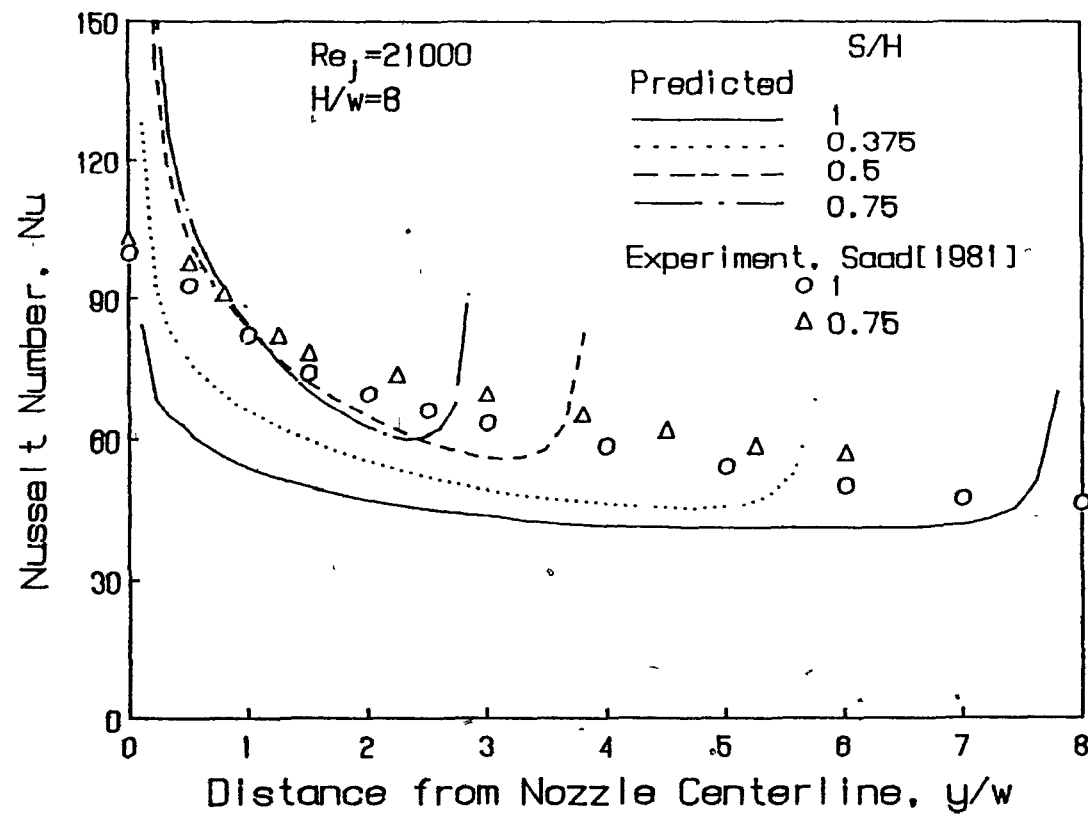


FIGURE 7.27. Effect of jet-to-exhaust spacing,  $S/H$ , on profiles of local Nusselt number in a multiple jet system:  
 $Re_j = 21000$ ,  $H/w = 8$

value for a flow cell aspect ratio around  $S/H=0.5$ . The runs for  $S/H$  of 0.5 and 0.375 were performed to determine predicted trends in this range. The Fig. 7.27 results indicate that heat transfer rate increases as  $S/H$  is decreased from 1 to 0.75 to 0.5. For  $S/H=0.375$ , i.e.  $S/w=3$ , the simulation predicts a lower  $Nu$  over the central region  $1 < y/w < 2.5$  for which the simulation is not distorted by the near-centerline problem discussed above. Thus the simulation model is consistent with the experimentally based prediction of Saad that  $\bar{Nu}$  passes through a maximum for a spacing about  $S/H=0.5$ .

The effect of throughflow on multiple jet impingement heat transfer was predicted in a second set of runs at  $S/H=0.5$ ,  $H/w=5$  and with the other conditions corresponding to the experimental measurements of the present study, Chapter 6. In these runs the number of grid nodes was  $20 \times 25$ , the inlet turbulence intensity was 5%. For the case without throughflow Fig. 7.28 displays both the predicted and experimental  $Nu$  number profiles. For a flow cell this narrow, the two critical regions with anisotropic characteristics, i.e. the impingement and exit flows, are immediately adjacent. Prediction of such a flow configuration with a turbulence model which assumes isotropy is expected to be less satisfactory. Yet agreement between experimental and predicted  $Nu$  profiles is surprisingly good, within 15% over the central 80% of the impingement surface,  $0.25 < y/w < 2.25$ , i.e. excluding the two near-centerline regions for which the model is not reliable.

A detailed comparison of near-wall models was not performed for the multiple jet configuration as was done for the single jets (Section 7.3). However, relative to the results of Polat et al.[1986] with Model 2, use of Model 4 improves the agreement between predicted and

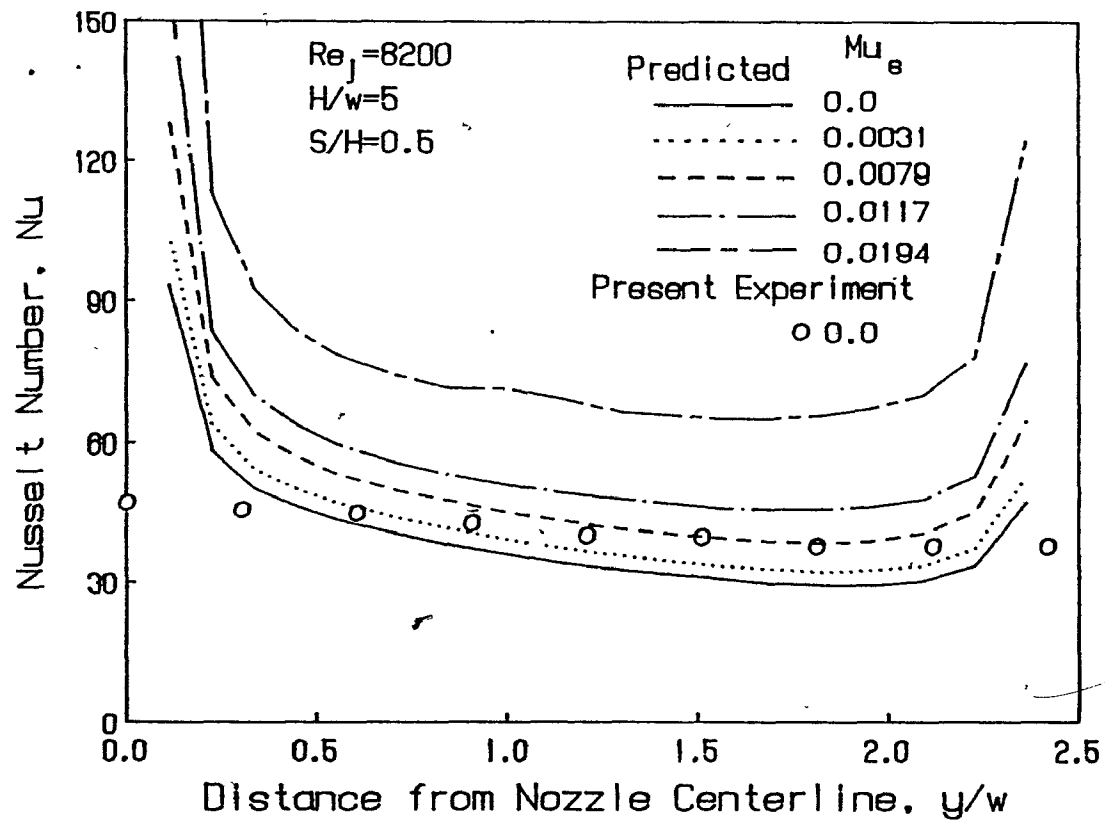


FIGURE 7.28. Effect of throughflow at the impingement surface on profiles of local Nusselt number in a multiple jet system:  $Re_j = 8200$ ,  $H/w = 2.5$ ,  $S/H = 0.5$

experimental Nu profiles significantly, by as much as 20%.

The predicted effect of throughflow, Fig. 7.28, like that measured experimentally, is for local enhancement of heat transfer by an almost uniform amount across the impingement surface, excluding the 10% of the surface adjacent to the two centerlines where, for reasons noted earlier, the simulation is not valid. For the average heat transfer comparison of Fig. 7.29, the predicted values of  $\bar{Nu}$  were calculated by excluding the region of invalid predictions within  $0.25w$  of the nozzle and exhaust port centerlines. The agreement between predicted and experimentally measured average heat transfer due to throughflow is good for  $Mu_s < 0.01$ . At higher  $Mu_s$  values the predicted  $\bar{Nu}$  becomes much too high for the same reasons noted in the single jet case, i.e. constants of the Eq. A3.27 of Appendix 3 are not adjusted for throughflow velocity because of a lack of reliable studies on the effect of throughflow on the near-wall flow. Hence for this multiple jet system this near-wall model can be used only for values of the throughflow parameter,  $Mu_s$ , smaller than 0.01. For a single jet, Section 7.4.2, the model gives good predictions of the heat transfer enhancement by throughflow up to a much smaller throughflow rate about  $Mu_s = 0.002$ . It is pertinent to note that, because the simulations for the single jet were performed at much higher jet Reynolds numbers, 22000-44000, this limiting value of  $Mu_s$  for a single jet corresponds to a throughflow velocity,  $u_s$ , about the same as that for the multiple jets at  $Re_j = 8200$  and  $Mu_s = 0.01$ , i.e.  $u_s \approx 0.1 \text{ m/s}$  in both cases.

In summary, the tests performed establish that for multiple confined slot jets the present model predicts Nusselt number to within 15% of that measured experimentally, and shows trends close to those

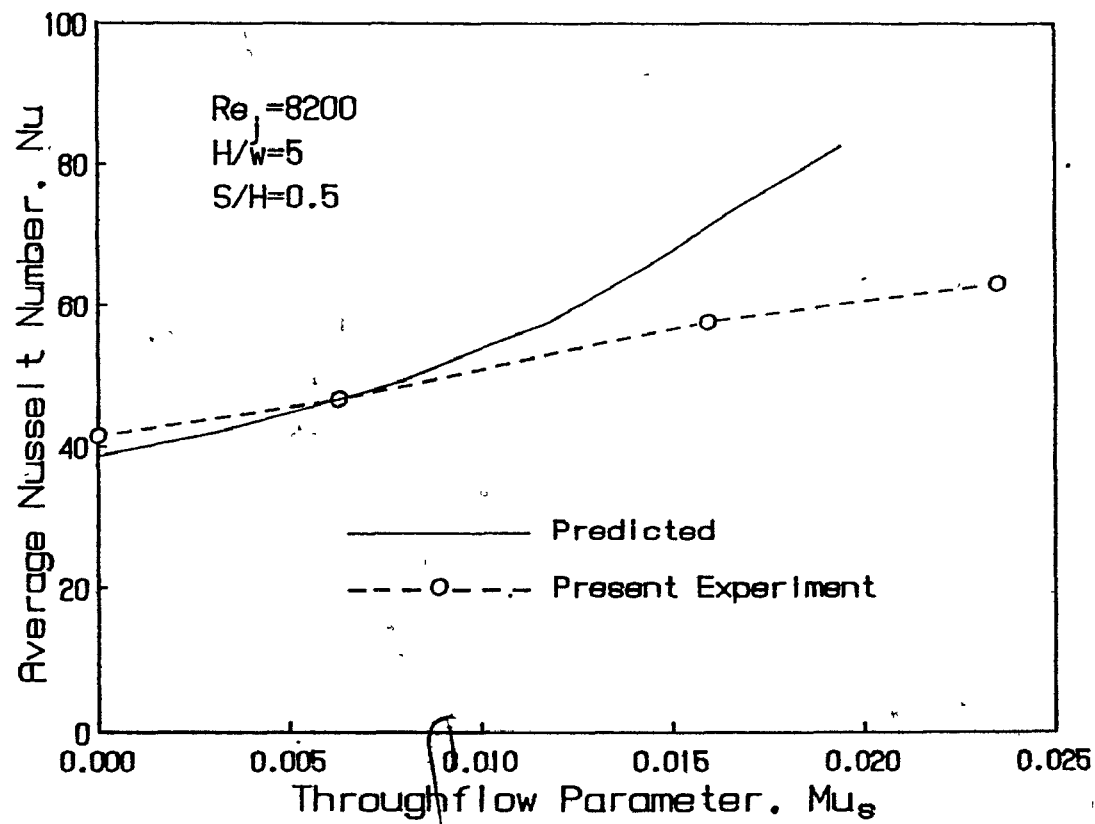


FIGURE 7.29. Effect of throughflow on average Nusselt number in a multiple jet system:  $Re_j=8200$ ,  $H/w=2.5$ ,  $S/H=0.5$



observed experimentally for the effect of internozzle spacing,  $S/H$ , and for the effect of the throughflow up to quite high values of  $u_s$ .

### 7.5 SUMMARY

Tests were made of several schemes for the numerical prediction of impingement heat transfer, all involving solution of the two dimensional Navier-Stokes, energy and turbulence model equations using an upwind finite difference scheme. The turbulence model used was the high-Re version of the  $k-\epsilon$  model. Various near-wall models were tested. Two configuration of confined plane jets were used, a single jet and a multiple jet array with spent flow exhausted symmetrically between the jet nozzles. The ability of the computer simulations to predict the effect of throughflow at the impingement surface was tested for both configurations.

The effect of choice of near-wall model on mean flow properties such as pressure distribution, mean axial velocity and maximum lateral velocity along the impingement surface was found to be negligible. For shear stress and Nu distribution, however, the predictions are sensitive to this choice. Among the near-wall models tested a modified Chieng-Launder model gave the best agreement of predicted Nu distribution with experiments, including the location and Nu value of the off-stagnation features which occur for small nozzle-to-surface spacings. It must be realized, however, that at the current state of development no numerical simulation technique involving any combination of a high-Re turbulence model and a near-wall model is capable of simulating the phenomena that create these features, i.e. the growing laminar boundary layer from the stagnation point to the off-stagnation

minimum, and the boundary layer transition from laminar to turbulent from that point to the location of the secondary maximum in Nu. Therefore obtaining good agreement between predicted and experimental Nu profiles for these off-stagnation features at low H/w values is coincidental to the modelling of shear stress and turbulent kinetic energy near the wall.

Calculation of near-wall generation of turbulent kinetic energy according to the earlier used Couette flow assumption is completely invalid for predicting heat transfer in the stagnation region. This assumption, Model 1, produces an unrealistic minimum for heat transfer around the stagnation point. Near-wall models that do not make this assumption produce results which are independent of the near-wall model used due to the dominating effect of unmodelled term  $2\mu_T \left[ \left( \frac{\partial u}{\partial x} \right)^2 + \left( \frac{\partial v}{\partial y} \right)^2 \right]$  in this region. Moreover, prediction of heat transfer in the stagnation region, where the turbulence is known to be highly anisotropic, by a model which assumes isotropy may not be sound. Predictions of Nu in this region, however, in general agree acceptably with experiments, except within about 0.25w of the nozzle and exhaust centerlines due to reasons which have been identified.

Extensive testing of the ability to predict profiles of local Nu at close nozzle-to-surface spacings,  $2 \leq H/w \leq 2.6$ , established the acceptability of the numerical technique which incorporates the high-Re version of the k- $\epsilon$  model with a modified Chieng and Launder near-wall model. Testing of predictions at wider spacings,  $6 \leq H/w \leq 8$ , showed that the model continues to predict off-stagnation minima and maxima for combinations of H/w and Re for which such features no longer occur. Beyond the location of the secondary maximum these predictions of Nu

are either about correct or somewhat overpredict  $Nu$ , as there is considerable disagreement between the experimental data. The testing by Looney and Walsh[1984] of various algebraic stress models as well as the standard  $k-\epsilon$  model for a plane turbulent free jet showed that the  $k-\epsilon$  model is inferior for that case. At larger nozzle-to-surface spacings the inability of the present numerical technique to reproduce the experimental trends is therefore attributed to the deficiencies of the  $k-\epsilon$  model for the free jet region.

When turbulence intensity at the nozzle exit is increased for small nozzle-to-surface spacings, the model fails to predict the enhancement of impingement heat transfer experimentally observed out to about  $8w$  from stagnation. This deficiency may be related to the inability of the technique to predict boundary layer phenomena involved in that enhancement.

The prediction of enhancement of heat transfer by throughflow at the impingement surface according to this model is accurate to within 10% for small rates of throughflow,  $Mu_s < 0.002$ , for the single jet. For higher throughflow rates the model substantially overpredicts the enhancement. The source of the error for high throughflow rates is probably that, due to lack of studies on the effect of throughflow on the near-wall flow, the parameters of the bilogarithmic formula used for wall shear stress cannot be related to throughflow rate.

For the case of a confined multiple jet configuration with exhaust ports located symmetrically between the jets, the predicted  $Nu$  profile is as much as 30% lower than experimental measurements. When the nozzle centerline-to-exhaust centerline spacing,  $S$ , was varied, the model results indicate that average Nusselt number passes through a

maximum near the same value of the flow cell aspect ratio,  $S/H=0.5$ , as was indicated by the experimental measurements of Saad[1981]. The predicted effect on heat transfer of throughflow at the impingement surface agrees quite well with experimental measurements for values of the throughflow parameter up to  $Mu_s=0.01$ . The limiting value of  $Mu_s$  for good agreement between predicted and experimental results for the effect of throughflow is quite different for single and multiple jets but, interestingly, the throughflow velocities corresponding to these limiting values of  $Mu_s$  are about the same,  $u_s \approx 0.1 \text{ m/s}$ .

In conclusion, the mean flow characteristics of a turbulent impinging jet can be predicted accurately with the present numerical technique. Prediction of impingement heat transfer varies with nozzle-to-impingement surface spacing, reasonably good at close spacings but poor at larger spacings. The enhancement of convective heat transfer due to throughflow at the impingement surface can be predicted with reasonable accuracy up to substantial throughflow rates of  $0.1 \text{ m/s}$  but overpredicts the enhancement at higher throughflow. The model does not predict the heat transfer enhancement with increasing nozzle exit turbulence which has been experimentally measured. Therefore the present technique, which incorporates a high-Re version of the  $k-\epsilon$  model, with a modified Chieng-Launder near-wall model, lacks the generality which is sought for numerical prediction methods. Use of a more complex turbulence model may be justified in view of the complex turbulence structure of a confined impinging jet system. However such models, not adequately tested, are still in the development stage. Prediction of heat transfer under impinging jets remains a stringent test for the performance of any such turbulence model.

## CHAPTER 8

## CONCLUSIONS

## 8.1. CONTRIBUTIONS TO KNOWLEDGE

1. A sensor for transient heat flux at a surface with throughflow

A permeable, high sensitivity, fast responding thin-film heat flux sensor was developed which has made it possible to measure rapidly changing heat flux at a surface with or without throughflow at the heat transfer surface. This sensor and the associated measurement system was shown to produce accurate results for a specific case, one where the rapidly changing heat flux is due to jets impinging on a heat transfer surface with throughflow and which is moving at high speed. At the highest surface velocity tested, the sensor measures Nusselt number to an rms accuracy of 5% for a heat flux which cycles from its lowest to highest value in as little as 3.1ms. This new type of heat flux sensor is not restricted to this particular case but is of general applicability for the measurement of rapidly changing heat flux at a permeable surface at which there may be throughflow.

2. Multiple slot jets: condition of maximum heat transfer

Multiple jet heat transfer is a function of two geometric parameters, nozzle-to-surface spacing,  $H/w$ , and nozzle-to-exhaust port spacing,  $S/H$ . The correlation of Saad[1981] indicated that the geometric condition for maximum average heat transfer would be  $H/w=5$ ,  $S/H=0.5$ . The present study, the first to provide an experimental measurement for this geometry, documents  $Nu$  over a wide range of jet Reynolds number,  $8200 < Re_j < 25800$ , for this condition of maximum heat transfer rate.

### 3. Effect of impingement surface motion: single slot jets

The disagreement concerning the effect of impingement surface motion on convective heat transfer from impinging slot jets has been resolved. Subba Raju and Schlunder[1977] reported that convective heat transfer rates for single slot jets increased by a factor of 1.5 to 2 with increasing speed of an impingement surface. Fechner[1971] and Haslar and Krizek[1984] reported some increase in convective mass transfer rates with increasing speed of an impingement surface under multiple slot jets. Baines and Keffer[1979] found no effect of surface motion on average wall shear stress under a single slot jet. Van Heiningen[1982] found that Nusselt number decreases with increasing speed of the heat transfer surface moving under a single confined slot jet. The present study, carried out in such a way as to avoid factors which contribute uncertainty to some of the earlier studies, has confirmed and extended van Heiningen's finding that convective transport coefficients for a slot jet decrease significantly as impingement surface motion increases. The decrease of  $\bar{Nu}$  was found to be a unique function of the nondimensional surface motion parameter,  $Mv_s$ , independent of jet Reynolds number,  $Re_j$ , and width of the heat transfer surface over a wide range tested. For a rapidly moving impingement surface ( $Mv_s = 0.34$ ), average heat transfer is about 1/4 lower than for a stationary impingement surface.

### 4. Effect of impingement surface motion: multiple slot jets

The first documentation is provided of the effect of impingement surface speed on Nusselt number for the industrially important case of confined multiple impinging slot jets. As for single jets,  $\bar{Nu}$  dec-

reases as a unique function of  $Mv_s$ , independent of  $Re_j$ . For a multiple slot jet system of closely spaced jets at the geometric condition of maximum average heat transfer,  $H/w=5$  and  $S/H=0.5$ ,  $\bar{Nu}$  is somewhat less sensitive to  $Mv_s$  than for a single jet. The sensitivity of  $\bar{Nu}$  to impingement surface speed is however not negligible for the range of surface motion parameter,  $Mv_s$ , used in industry. For example, for the conditions of one important industrial application, the Yankee dryer for drying paper, an impingement surface moving at the velocity found in a modern high speed paper machine would reduce convective heat transfer coefficients of a multiple/impinging slot jet system by a substantial amount, .17%.

#### 5. Effect of throughflow: single and multiple slot jets

The effect of throughflow on impingement heat transfer at a stationary surface is shown to be linearly additive, independent of Reynolds number, for both systems tested, a single confined slot jet at  $H/w=2.5$  and a confined multiple jet system of closely spaced jets at  $S/H=0.5$ ,  $H/w=5$ . For both the single and multiple jets the direct proportionality between enhancement of average heat transfer by throughflow, expressed as  $\Delta \bar{St}$ , and the nondimensional throughflow parameter,  $Mu_s$ , is found to have effectively the same value, 0.17.

#### 6. Effect of throughflow at a moving impingement surface: single jets

The effect of throughflow on convective heat transfer for jet systems impinging on moving surfaces has previously not been open to experimental study for lack of a heat flux sensor applicable to this difficult combination of conditions. With the unique heat flux sensor

developed in the present study, such measurements are reported here for the first time. For a jet at  $H/w=2.5$  the measurement of profiles of local heat transfer with very high spatial resolution served to identify flow and heat transfer effects in the boundary layer that are associated with throughflow, with surface velocity and with the combination of these conditions. The single jet results establish that, over the substantial limits tested, the enhancement of average heat transfer with throughflow at a moving impingement surface, expressed as the ratio  $\Delta\overline{ST}/Mu_s$ , is a constant, 0.17, independent of  $Mv_s$ ,  $Re_j$  and extent of the heat transfer area. Close agreement of the enhancement ratio,  $\Delta\overline{ST}/Mu_s$ , with the results at low  $Mu_s$  obtained by Saad[1981] for a stationary impingement surface at  $H/w=8$  indicates that this correlation for throughflow effect should apply also for  $H/w$  spacings over the range 2.5 to 8, which covers the extent of major industrial interest.

#### 7. Effect of throughflow at a moving impingement surface: multiple jets

The effect of throughflow on impingement heat transfer at a moving surface is shown to be linearly additive for the confined multiple jet system of closely spaced jets,  $S/H=0.5$ ,  $H/w=5$ , as was established for a single jet at  $H/w=2.5$  with heat transfer widths up to  $S/H=6.4$ . The fact that  $\Delta\overline{ST}$  relates to  $Mu_s$  with effectively the same proportionality constant for multiple jets and for a single jet, independently of jet Reynolds number or extent of heat transfer surface, indicates a conclusion of considerable scope. Specifically, the evidence obtained is that the throughflow enhancement ratio,  $\Delta\overline{ST}/Mu_s=0.17$ , appears applicable over a much broader range of parameters than tested in the present



investigation.

#### 8. Comprehensive correlation for heat transfer: single slot jets

Local and average heat transfer under a confined slot jet impinging on a stationary or moving surface, with or without throughflow, was determined for a jet spacing of  $H/w=2.5$  and over the ranges of  $16000 < Re_j < 58000$ ,  $0 < Mu_s < 0.02$  and  $0 < Mv_s < 0.35$ . A correlation of analytical form for average heat transfer was determined for heat transfer surfaces of half-width,  $S$ , in the range represented by  $1.2 < S/H < 6.4$  (i.e.  $3 < S/w < 16$ ). The corresponding range of nozzle open area is 16.7% down to 3.1%. Although in practice heat transfer surfaces smaller than this would probably be avoided as uneconomical, average heat transfer over smaller surfaces may be determined from the graphical relations provided. The analytic single jet correlation incorporating surface motion and throughflow which was obtained in this study, the first such correlation to be published, may be used also for a confined multiple jet system when individual jets are spaced sufficiently apart that their interaction does not significantly affect heat transfer.

#### 9. Comprehensive correlation for heat transfer: multiple slot jets

For a multiple jet system with  $H/w=5$  and  $S/H=0.5$ , the geometric condition for maximum heat transfer, the first comprehensive analytical correlation, Eq. 6.5, has been obtained with which average convective heat transfer rate may be predicted in the presence of surface motion and throughflow for the wide range of parameters  $8200 < Re_j < 25800$ ,  $0 < Mu_s < 0.0235$  and  $0 < Mv_s < 0.38$ .

#### 10. Modelling of an industrial application

With the present findings on the effects of surface motion and throughflow on impingement heat transfer, the assumptions of the two models, Crotogino and Allenger[1979] and Randall[1984], for a paper dryer incorporating combined impingement and throughflow were reexamined. In the absence of reliable data, both models neglected the effect of surface motion, now shown to decrease impingement heat transfer by 17% at  $Mv_s = 0.3$ , a value comparable to that of a Yankee dryer. Again in the absence of reliable data, Crotogino and Allenger assumed that impingement heat transfer decreases linearly with increasing  $Q_s$ , the fraction of jet flow removed as throughflow, while Randall[1984] assumed no effect of throughflow on impingement heat transfer. The present results indicate that in the  $Re_j$  range tested both models substantially underestimate convective heat transfer rate, the first model by 65%-88%, the second model by 53%-76%. Thus the results of the present investigation have a substantial positive impact on the economics of a potentially major new industrial process.

#### 11. Numerical prediction of impingement heat transfer: near-wall models

The effect of near-wall models on predictions for a confined impinging slot jet was tested for the first time when the choice of turbulence model is the high- $Re$  version of the  $k-\epsilon$  model. Shear stress and  $Nu$  distribution were shown to be highly sensitive to the choice of near-wall model, while mean flow properties such as pressure distribution, mean axial velocity decay and maximum velocity development along the impingement surface are independent of the model. It has been demonstrated that among several near-wall models a Chieng-Launder type

model, modified as proposed here, i.e. using  $k_p$  instead of  $k_v$  in the equation to predict wall shear stress, gives much improved agreement between predicted Nu distribution and experiments, including the location and Nu value of the off-stagnation features which occur for small nozzle-to-surface spacings.

#### 12. Numerical prediction of impingement heat transfer: Couette flow

Calculation of near-wall generation of turbulent kinetic energy by assuming Couette flow has been shown to be completely invalid for predicting heat transfer in the stagnation region.

#### 13. Numerical prediction of impingement heat transfer: multiple jets

After application of the new version of near-wall model with the equations for the high-Re version of the  $k-\epsilon$  turbulence model for the prediction of heat transfer under confined single slot jets, the model was applied for the first time to the prediction of heat transfer for the industrially important case of multiple impinging turbulent jets. For a confined multiple slot jet system of closely spaced jets with  $H/w=5$ ,  $S/H=0.5$ , the geometric condition for maximum heat transfer, predicted heat transfer was found to agree within 30% with that experimentally measured over the central 80% of the impingement surface between adjacent jets and exhaust flows.

#### 14. Numerical prediction of impingement heat transfer: turbulence effect

It is shown that in spite of its positive features, this most recent form of numerical model for impingement heat transfer shares an undesirable feature of all such models proposed to date, in that it

does not predict the enhancement of impingement heat transfer with increasing nozzle turbulence intensity which, at small nozzle-to-surface spacings, has been observed experimentally out to about  $8w$  from stagnation. The source of this deficiency is identified as the inability of this model to predict the boundary layer phenomena that create this enhancement, which thus points the direction required for resolution of this long standing problem.

#### 15. Numerical prediction of impingement heat transfer: throughflow effect

The first prediction of the enhancement of impingement heat transfer by throughflow has been obtained. For both single and multiple jets, this numerical model is shown to predict enhancement by throughflow at the impingement surface with an accuracy within 10% up to throughflow rates,  $u_s = 0.1m/s$ , beyond which it is believed that the model substantially overpredicts the enhancement. The source of the error for high throughflow rates is identified as the use of constants in the bilogarithmic formula for wall shear stress which, in the absence of quantitative studies of the effect of throughflow on the near-wall flow, could not be related to throughflow rate.

### 8.2 RECOMMENDATIONS FOR FUTURE STUDIES

1. The permeable sensor developed and validated for measurement of impingement heat transfer in this study can be used in flow configurations other than impinging jets where measurement of rapidly changing heat transfer under throughflow conditions is of interest. The possibility of using this sensor under blowing conditions may also be investigated.

2. The heat flux measurements with the SIMTEST III apparatus should be extended to other combinations of  $H/w$  and  $S/H$  for multiple slot jets and other values of  $H/w$  for a single confined slot jet.
3. The possibility of measuring heat flux for multiple round jets in the SIMTEST III apparatus should be considered.
4. The effect of alternate shapes of slot nozzles on impingement heat transfer at small nozzle-to-surface spacings should be investigated. In this context the enhancement of heat transfer with nozzle exit turbulence should be considered. Such heat transfer measurements must be accompanied with detailed turbulence measurements at the nozzle exit as well as in entire flow domain.
5. Measurements of velocity and temperature profiles near a permeable impingement surface with and without throughflow conditions should be conducted in order to understand the mechanism of heat transfer enhancement with throughflow.
6. Continuing efforts towards developing a reliable general numerical technique for the heat transfer characteristics of impinging jets are required. A low-Re turbulence model that does not require use of wall functions would remove the ambiguity as to whether the wall functions or the turbulence model itself is the cause of the discrepancies between prediction and experiment. Recommendations 4 and 5 would provide a strong basis for comparison.

## REFERENCES

- Abdul-Wahab, H., A.S. Mujumdar and W.J.M. Douglas[1975], Flow measurements in a bounded turbulent impinging slot jet with suction, Technical Report, McGill University.
- Abramovitch, G.N.[1963], The theory of turbulent jets, Trans. by Scripta Technica, MIT Press.
- Agarwal, R.K. and W.W. Bower[1982], Navier-Stokes computations of turbulent compressible two-dimensional impinging jet flowfields, AIAA J., 20, No. 5, pp. 577-584.
- Ahmad, I.[1987], Simulation of turbulent flow and heat transfer under an impinging round jet discharging into a crossflow, M.Eng. thesis, Chem. Eng. Dept., McGill University.
- Amano, R.S.[1980], Numerical study of a turbulent jet impinging on a flat plate and flowing into an axisymmetric cavity, Ph.D. Thesis, University of California, Davis.
- Amano, R.S.[1983], Turbulence effect on the impinging jet on a flat plate, Bull. of JSME, 26, No. 221, pp. 1891-1899.
- Amano, R.S. and H. Brandt[1984], Numerical study of turbulent axisymmetric jets impinging on a flat plate and flowing into an axisymmetric cavity, J. Fluids Eng., 106, pp. 410-417.
- Amano, R.S. and S. Sugiyama[1985], An investigation on turbulent heat transfer of an axisymmetric jet impinging on a flat plate, Bull. of JSME, 28, No. 235, pp. 74-79.
- Baines, D.J.[1970], A comparative theoretical evaluation of five commonly used types of unsteady heat flux sensor, Report HSA 27, Australian Defence Scientific Service, Weapons Research Establishment, January.
- Baines, W.D. and J.F. Keffer[1976], Shear stress and heat transfer at a stagnation point, Int. J. Heat Mass Transfer, 19, pp. 21-26.
- Baines, W.D. and J.F. Keffer[1979], Shear stress measurements for an impinging air jet, Transactions of the Technical Section, Canadian Pulp and Paper Association, June, pp. 39-44.
- Bentley, J.P. and J. Riley[1983], A microcomputer based computer program for orifice plate sizing using ISO 5167, Int. Conf. on the use of Micros in Fluid Engrs., London, June 7-8, Paper 2.
- Black, T.J. and A.J. Sarnecki[1958], Turbulent boundary layer with suction or injection, Aeronautical Research Council Reports and Memoranda, R.&M. No:3387.
- Burgess, B.W., S.M. Chapman and W. Seto[1972a], The Papiridryer Process, Part I, The basic concepts and laboratory results, Pulp and

Paper Mag. Can., 73, 11, pp. 314-322.

Burgess, B.W., W. Seto, E. Koller and I.T. Pye[1972b], The Papridryer Process, Part II, Mill Trials, Pulp and Paper Mag. Can., 73, No. 11, pp. 323-331.

Cadek, F.F.[1968], A fundamental investigation of jet impingement, heat transfer, Ph.D. thesis, University of Cincinnati.

Carman, P.J.[1956], Flow of Gases Through Porous Media, Butterworths Publications, London

Cartwright, W.G. and P.J. Russell[1967], Characteristics of a turbulent slot jet impinging on a plane surface, Proc. Instn. Mech. Engrs., 182, Pt. 3H, pp. 309-319.

Chapman, A.J.[1967], Heat Transfer, 2nd Ed., The Macmillan Co., New York, p. 149.

Chieng, C.C. and B.E. Launder[1980], On the Calculation of Turbulent Heat Transport Downstream from an Abrupt Pipe Expansion, Numerical Heat Transfer, 3, pp. 189-207.

Crotogino, R.H. and V. Allenger[1979], Mathematical model of the Papridryer Process, Transaction of the Technical Section, Canadian Pulp and Paper Association, 5, 4, pp. 84-91.

Dosdogru, G.A.[1969], Über die Ausführung von Schlitzdüsen im Unterschallbereich, Mitteilungen Heft 2, Forschungsgesellschaft Druckmaschinen e.V.

Favre, A., R. Dumas, E. Verollet and M. Coantic[1966], Couche limite turbulente sur paroi poreuse avec aspiration, Journal de Mecanique, 5, No. 1, pp. 3-28.

Fechner, G.[1971], Wärmeübergang bei senkrecht auftreffendem Strahl an der Platte und am-Rotor, Dissertation, T. U. München.

Folayan, C.O.[1977], Impingement cooling, Ph.D. thesis, Imperial College, London.

Gardon, R. and J.C. Akfirat[1965], The role of turbulence in determining the heat transfer characteristics of impinging jets, Int. J. Heat Mass Transfer, 8, pp. 1261-1272.

Gardon, R. and J.C. Akfirat[1966], Heat transfer characteristics of impinging two-dimensional air jets, J. Heat Transfer, 88, No. 1, pp. 101-108.

Gauntner, J.W., J.N.B. Livingood and P. Hrycak[1970], Survey of literature on flow characteristics of a single turbulent jet impinging on a flat plate, NASA TN D-5652.

Guo, C.Y.[1982], Numerical modeling of normal turbulent plane jet

impingement on a solid wall, Ph.D. thesis, University of Illinois, Urbana.

Guo, C.Y. and W.H.C. Maxwell[1984], Numerical modeling of normal turbulent plane jet impingement on a solid wall, J. Eng. Mech., 110, No. 10, pp. 1498-1509.

Gutmark, E., M. Wolfshtein and I. Wygnanski[1978], The plane turbulent impinging jet, J. Fluid Mech. 88, part 4, pp. 737-756.

Haslar, F. and F. Krizek[1984], Mass transfer of impact flow from slit nozzles on rotating drying cylinder, Presented at the 8th Int. Congress of Chemical Eng., Chemical Equipment Design and Automation, Praha, Czechoslovakia, Sept. 3-7.

Hinze, J.O.[1959], Turbulence, an Introduction to Jets Measurements and Theory, McGraw-Hill Inc.

Huang, B.[1988], Heat transfer under impinging oblique slot jets, Dept. of Chem. Eng., McGill University.

Huang, G.P., A.S. Mujumdar and W.J.M. Douglas[1984], Numerical prediction of fluid flow heat transfer under a turbulent impinging slot jet with surface motion and crossflow, ASME Paper, #84-WA/HT-33.

Ioffe, A.V. and A.F. Ioffe[1958], Measurement of thermal conductivity of semiconductors in the vicinity of room temperature, Soviet Physics-Technical Physics, 3, No. 11, pp. 2163-2168.

Jayatilleke, C.L.[1969], The Influence of Prandtl Number and Surface Roughness on the Resistance of the Laminar Sub-layer to Momentum and Heat Transfer, Prog. in Heat and Mass Transfer, 1, pp. 193-329.

Jones, W.P. and B.E. Launder[1973], The Calculation of Low-Reynolds-Number Phenomena with a Two-Equation Model of Turbulence, Int. J. Heat Mass Transfer., 16, pp. 1119-1130.

Korger, M. and F. Krizek[1966], Mass transfer coefficient in impingement flow from slotted nozzles, Int. J. Heat Mass Transfer, 9, pp. 337-344.

Kumada, M and I. Mabuchi[1970], Studies on the Heat Transfer of Impinging Jets, Bull. of JSME, 13, No. 55, pp. 77-85.

Kumada, M, I. Mabuchi and Y. Kawashima[1972], Mass transfer on a cylinder in the potential core region of a two-dimensional jet, Trans. Japan Soc. Mech. Engrs., 38, pp. 315.

Ljuboja, M. and W. Rodi[1979], Calculation of turbulent wall jets with an algebraic stress model, Proc. Symp. on Turbulent Boundary Layers: Forced, Incompressible, Non-reacting, pp. 131-138.

Looney, M.K. and J.J. Walsh[1984], Mean flow and turbulent characteristics of free and impinging jet flows, J. Fluid Mech., 147,



pp.397-429.

Martin, H.[1977], Heat and mass transfer between impinging gas jets and solid surfaces, Advances in Heat Transfer, Volume 13, Academic Press, pp. 1-60.

Martin, H. and E.U. Schlunder[1973], Optimierung von Schlitzdüsentrocknern auf Grund neuer Versuchsergebnisse über den Wärme-und Stoffübergang in solchen Apparaten, Chemie-Ing.-Techn., 45, Jahrg. 1973/Nr. 5.

Metzger, D.E.[1962], Spot cooling and heating of surfaces with high velocity impinging air jets, Technical Report No. 52, Mech. Eng. Dept., Stanford University.

Mickley, H., R.C. Ross, A.L. Squyers and W.E. Stewart[1954], Heat, mass and momentum transfer for flow over a flat plate with blowing and suction, NACA TN-3208.

Miyazaki, H. and E. Silberman[1972], Flow and heat transfer on a flat plate normal to a two-dimensional laminar jet issuing from a nozzle of finite height, Int. J. Heat Mass Transfer, 15, pp. 2097-2107.

Moffat, R.J. and W.M. Kays[1968], The turbulent boundary layer on a porous plate: Experimental heat transfer with uniform blowing and suction, Int. J. Heat Mass Transfer, 11, pp. 1547-1566.

Mujumdar, A.S. and W.J.M. Douglas[1972], Impingement heat transfer - Literature review, Paper presented at TAPPI Conf., New Orleans.

Obot, N.T.[1981], Flow and heat transfer for round turbulent jets impinging on permeable and impermeable surfaces, Ph.D. thesis, Chem. Eng. Dept., McGill University.

Obot, N.T.[1982], Effect of suction on impingement heat transfer, Heat Transfer 1982, Proceedings of the 7th Int. Heat Transfer Conference, U. Grigull, E. Hahne, K. Stephan, Ed., pp.389-394.

Obot, N.T., A.S. Mujumdar and W.J.M. Douglas[1979], Design correlations for heat and mass transfer under various turbulent impinging jet configurations, Developments in Drying, Hemisphere Publications, pp. 388-402.

O'Neill[1966], M.J., Measurement of specific heat functions by differential scanning calorimetry, Analytical Chemistry, 38, pp.1331.

Patankar, S.V.[1980], Numerical Heat Transfer and Fluid Flow, Hemisphere Publications., New York, p. 70.

Polat, S., A.S. Mujumdar and W.J.M. Douglas[1985], Heat transfer distribution under a turbulent impinging jet - A numerical study, Drying Technology, 3, No. 1, pp. 15-38.

Polat, S., A.S. Mujumdar and W.J.M. Douglas[1986], Numerical prediction of multiple impinging turbulent slot jets, Proc. of 5th

Int. Drying Conf., August 13-15, Cambridge, Hemisphere Publications.

Polat, S., B. Huang, A.S. Mujumdar and W.J.M. Douglas[1988], Numerical Flow and Heat Transfer under Impinging Jets- A Review, Annual Review of Numerical Fluid Mechanics and Heat Transfer, Volume 2, pp. 157-197.

Pope, S.B. and J.H. Whitelaw[1976], The Calculation of Near-Wake Flows, J. Fluid Mech., 73, pp. 9-32.

Pun, W.M. and D.B. Spalding[1977], A General Computer Program for Two-Dimensional Elliptic Flows, Report no. HTS/76/2, Imperial College of Sci. and Tech., Mech. Engg. Dept., London, U.K.

Randall, K.R.[1984], Using high velocity impingement air to improve through drying performance on semi-permeable webs, Drying'84, A.S. Mujumdar, Ed., Hemisphere Publications, pp.254-263.

Rodi, W.[1972], Ph.D. thesis, University of London

Romanenko, P.N. and M.I. Davidzon[1970], Heat transfer in the zone of accelerated flow during the normal impingement of a system of two-dimensional jets onto a flat surface, Int. Chem. Eng., 10, No. 2, pp. 223-228.

Rose, P.H.[1958], Development of the calorimeter heat transfer gage for use in shock tubes, AVCO Research Report 17, February.

Russell, P.J. and A.P. Hatton[1972], Turbulent flow characteristics of an impinging jet, Proc. Instn. Mech. Engrs., 186, pp. 635-644.

Saad, N.R.[1981], Flow and heat transfer for multiple turbulent impinging slot jets, Ph.D. thesis, Chem. Eng. Dept., McGill University.

Schauer, J.J. and R.H. Eustis[1963], The flow development and heat transfer characteristics of plane turbulent impinging jets, Technical Report No. 3, Mech. Eng. Dept., Stanford University.

Scheuter, K.R. and G.A. Dosdogru[1970], Die Messung der örtlichen Wärmeübergangszahl mittels eines geheizten Bandes, Schweizer Archiv für angewandte Wissenschaft und Technik, 36, 10, pp. 3-19.

Schlichting, H.[1979], Boundary Layer Theory, 7th Edition, McGraw-Hill Book Co., New York.

Schlunder, E.U., P. Krotzsch and W. Hennecke[1970], Gesetzmäßigkeiten der Wärme- und Stoffübertragung bei der Prallströmung aus Rund- und Schlitzdüsen, Chemie-Ing.-Techn., 42, 6, pp. 333-338.

Schuh, H. and R. Pettersson[1966], Heat transfer by arrays of two-dimensional jets directed normal to surfaces including the effects of a superposed wall-parallel flow, Proceedings of 3rd Int. Heat Transfer Conference, August 7-12, Chicago, II, pp.280-291.

Spalding, D.B.[1960], A standard formulation of the steady convective mass transfer problem, Int. J. Heat Mass Transfer, 1, pp.192-207.

Spalding, D.B.[1967], Heat Transfer from Turbulent Separated Flows, J. Fluid Mech., 27, p.97.

Subba Raju, K. and E.U. Schlunder[1977], Heat transfer between an impinging jet and a continuously moving flat surface, Wärme- und Stoffübertragung, 10, pp. 131-136.

Toutoungi, N[1983], A study of thermal conductivity and diffusivity of polymers, M. Eng. thesis, Chem. Eng. Dept., McGill University.

van der Meer, T.[1987], Heat transfer from impinging flame jets, Ph.D. thesis, Delf University, Holland.

van Heiningen, A.R.P.[1982], Heat transfer under an impinging slot jet, Ph.D. thesis, Chem. Eng. Dept., McGill University.

van Heiningen, A.R.P., A.S. Mujumdar and W.J.M. Douglas[1976], On the use of hot and cold-film sensors for skin friction and heat transfer measurements in impingement flows, Letters in Heat and Mass Transfer, 3, pp. 523-528.

van Heiningen, A.R.P., A.S. Mujumdar and W.J.M. Douglas[1985], A high sensitivity, fast response heat flux sensor, Int. J. Heat Mass Transfer, 28, No.9, pp. 1657-1667.

Wolfshtein, M.[1967], Convective process in turbulent impinging jets, Ph.D. thesis, Imperial College, London.

Yoshida, F., D. Ramaswami and O.A. Hougen[1962], Temperatures and partial pressures at the surfaces of catalyst particles, A.I.Ch.E. Journal, 8, No.1, pp. 5-11.

## APPENDIX 1

## DETERMINATION OF THERMAL PROPERTIES OF THE POROUS GLASS CYLINDER

Three principal thermal properties, thermal conductivity, specific heat and thermal diffusivity, of the 3M porous glass material (Grade 50) are needed in order to determine the transient surface heat flux. The following procedures were followed.

## Thermal Conductivity

Two independent techniques were used:

A. Transient method of Ioffe and Ioffe[1958]

Equipment based on this method was built, as shown in Fig. A1.1.

It consists of:

1. Lower copper cylindrical block
2. Upper copper block
3. Inner stainless steel cover for the upper copper block
4. Test sample
5. High thermal conductivity material
6. Copper-constantan thermocouples to measure the temperature of upper block and the temperature difference between upper and lower blocks.
7. Teflon screw to clamp the sample between blocks
8. Teflon insulator between the lower block and the stainless steel covers
9. Outside stainless steel cover

In order monitor the temperature continuously, the thermocouples were connected to a three-pen chart recorder (Yokogawa Electric Co,

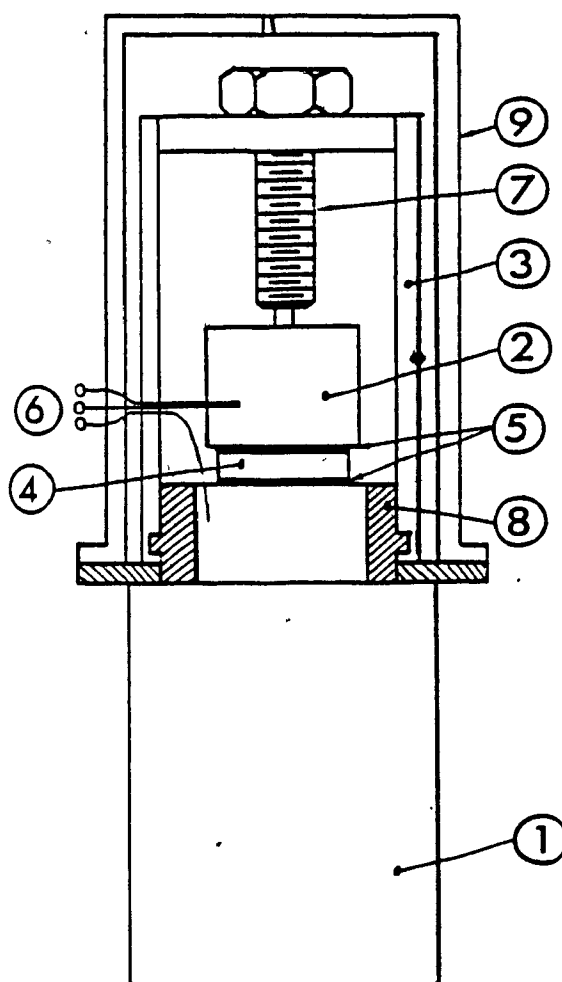


FIGURE A1.1. Test assembly for thermal conductivity measurements using transient method of Ioffe and Ioffe[1958]

Model 3066) with adjustable chart speed. A chart speed of 10 cm/s gave satisfactory outputs. Room temperature reference for the upper block thermocouple permitted to adjust the recorder pen sensitivity at 25 microvolts. The adjustment for the pen to record the temperature difference between the blocks was 50 microvolts. The following experimental procedure was used

1. Measure the dimensions of the sample
2. Apply the highly conductive paste (Omegatherm 201) on the two surfaces of the sample in order to minimize contact resistance
3. Replace the sample centrally between the blocks
4. Clamp half of the inner cover and tighten the teflon screw on the upper block
5. Clamp the other half of the inner cover to isolate the sample and the upper copper block from surroundings
6. Replace the outside cover
7. Wait until temperature difference between blocks is zero and upper block temperature is steady.
8. Immerse and retain the lower block in a continuously stirred ice bath until temperature difference between the two blocks begins to fall. This indicates the end of the experiment.

A typical output is shown in Fig. A1.2. When temperature difference between the blocks reaches a maximum (AB on  $(T_u - T_l)$  curve),  $\frac{\Delta T_u}{t} / (T_u - T_l)$  remains almost constant. The slope of the  $T_u$  curve at the corresponding interval (CD) is found and the effective thermal conductivity is calculated from the following relation:

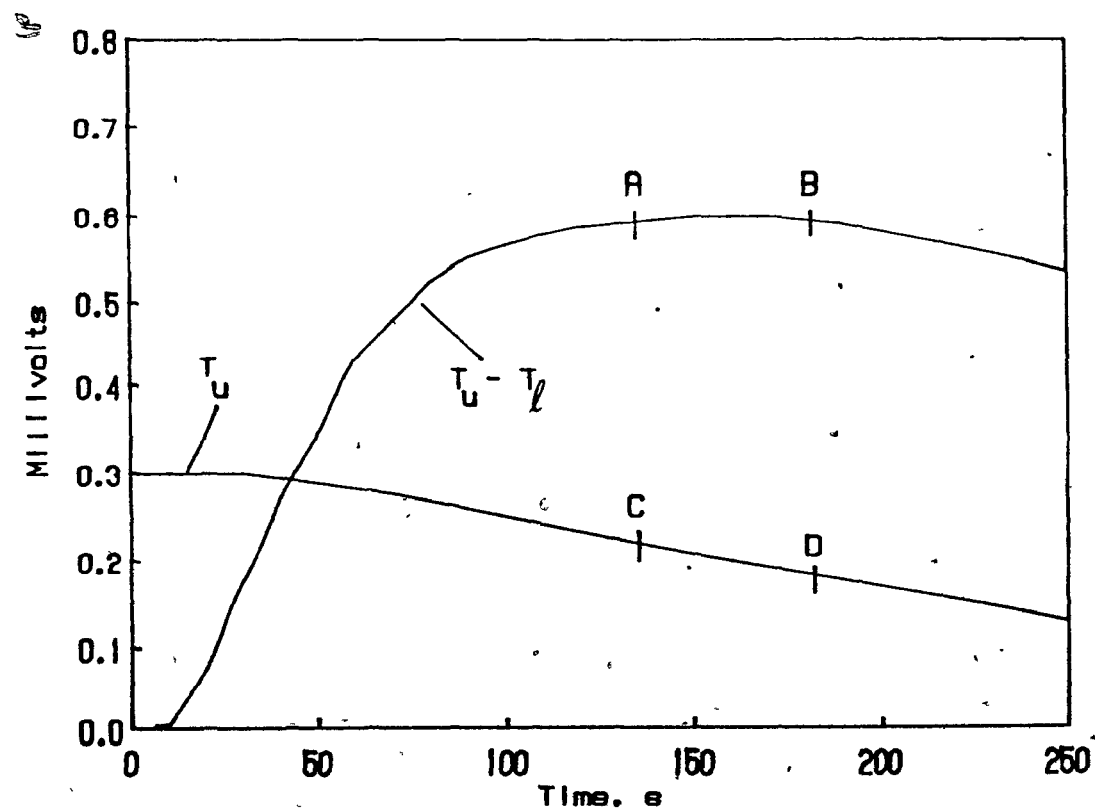


FIGURE A1.2. Typical output of thermal conductivity experiment

$$k_{eff} = \frac{C_u \frac{\Delta T_u}{\Delta t}}{(T_u - T_l)} (L_s/S)$$

where

$C_u$  = heat capacity of upper copper block (194.41 J/°C)

$k_{eff}$  = effective thermal conductivity (W/m -°C)

$L_s$  = thickness of the sample (m)

$S$  = surface area of the sample (m<sup>2</sup>)

$T_u$  = temperature of the upper block (°C)

$T_l$  = temperature of the lower block (°C)

$\Delta T_u$  = change in upper block temperature in time interval  $\Delta t$  (°C)

In order to ensure that the equipment worked properly, the thermal conductivities of pyrex and teflon samples were determined using the above procedure except, instead of the paste, about 1 mm thick circular lead foils were used on both sides of the samples. Between the foil and the copper block and the sample and the foil, a thin layer of glycerine was applied to provide good contact. Thermal conductivities of pyrex and teflon samples were determined to be 1.14 and 0.227 W/m-K respectively, within 6% of the the reported literature values. The reproducibility of the experiments was within 5%.

The porous glass samples used in thermal conductivity experiments were cut from the same porous glass cylinder used as the heat transfer surface. The diameter of the samples was fixed at 50mm but their thickness was varied to check that contact resistance that may exist between the block and the sample does not effect the results.

With this unsteady state method the thermal conductivity of the porous glass was found to be 0.377W/m°C at an average temperature of -12°C. Reproducibility of the experiments was within 9% with the porous samples. This average thermal conductivity value was not used



in the calculations because the temperature at which the thermal conductivity could be obtained was much lower than the average temperature of the impingement surface attained during experiments.

B. Steady-state apparatus of Toutoungi [1983]

This apparatus, available from the Chemical Engineering Polymer Laboratory of McGill University, is shown in Fig. A1.3. It consists of

1. Heater
2. Test samples
3. Guard plates
4. Thermocouples

To make sure that the guard plates were at a uniform temperature throughout the experiment, this cell was placed in an oven at the selected temperature.

The following procedure was followed:

1. Measure the dimensions of the samples. The two samples should be identical to ensure equal heat flux into the samples from the heater.
2. Apply the highly conductive paste (Omegatherm 201) on the two surfaces of the samples in order to minimize contact resistance.
3. Replace the samples centrally between the heater and the guard plates.
4. Close the oven door and set the temperature of the oven.
5. Monitor the thermocouples on each side of the samples.
6. Allow some time (usually ~10-15 minutes) to reach steady-state.

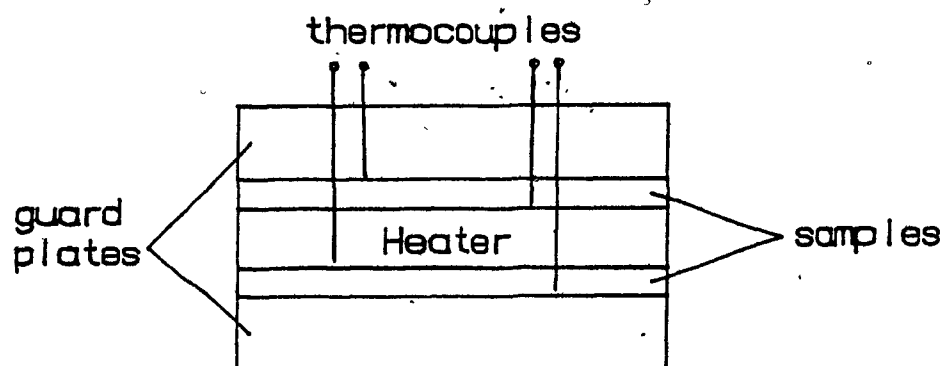


FIGURE A1.3. Schematic of the apparatus of Toutoungi[1983]

7. Turn on the D.C. power supply of the heater to apply a high intensity current to the heater nichrome wire.
8. Again allow 10-15 minutes to reach steady-state.

Power supplied to the nichrome wire is calculated using

$$q = \frac{U \times I}{4.18 \times 2A}$$

where  $U$  is the voltage,  $I$  the current and  $A$  the heat transfer area, i.e. the sample surface area. The thermal conductivity of the samples are calculated from the steady state temperature variation using  $q$

$$k = q \frac{L_s}{\Delta T}$$

where  $\Delta T$  is the temperature difference between the two surfaces of each sample.

Since the temperature dependency of the thermal conductivity in the range from 40°C to 50°C was within the experimental reproducibility, 10%, an average value of 0.414 W/m°C as measured with this method was used in the calculations.

#### Specific Heat

Specific heat of the porous glass was measured by Differential Scanning Calorimetry (DSC). This standard procedure is available in the literature (O'Neill[1966]) and need not be repeated here. Standard reference material used in the measurements was synthetic sapphire ( $Al_2O_3$ ). The following equation was obtained from the linear regression analysis of the data.

$$C_p = 875.51 - 6.48 T_s + 7.23 \times 10^{-2} T_s^2$$

where  $T_s$  and  $C_p$  are in °C and J/kg°C respectively.

### Density

In order to evaluate thermal diffusivity of the porous glass material its density must be known. The density was found to be  $1440\text{kg/m}^3$  with a reproducibility of  $\pm 5\%$  by weight and volume measurements of the porous glass samples.

# APPENDIX 2

## ERROR ANALYSIS

Total rms error is expressed as:

$$\delta f = \left( \sum_{i=1}^n \left\{ \left( \frac{\partial f}{\partial x_i} \delta x_i \right) \right\}^2 \right)^{1/2} \quad (A2.1)$$

Error analysis for Nu:

$$Nu = \frac{hw}{k_j}$$

where  $h = \frac{q_s}{T_j - T_s}$ , and where  $q_s = \frac{k_{eff} (T_s - T_1)}{\Delta x}$

Hence,

$$Nu = \frac{T_s - T_1}{T_j - T_s} \cdot \frac{w}{\Delta x} \cdot \frac{k_{eff}}{k_j}$$

$$\frac{\partial Nu}{\partial T_j} = - \frac{Nu}{T_j - T_s}; \quad \frac{\partial Nu}{\partial T_s} = \frac{Nu}{\Delta x} \cdot \frac{k_{eff}}{q_s} + \frac{Nu}{T_j - T_s};$$

$$\frac{\partial Nu}{\partial \Delta x} = - \frac{Nu}{\Delta x}; \quad \frac{\partial Nu}{\partial k_j} = - \frac{Nu}{k_j}; \quad \frac{\partial Nu}{\partial k_{eff}} = \frac{Nu}{k_{eff}}$$

rms error in Nu due to uncertainties in  $T_j$ ,  $T_s$ ,  $w$ ,  $k_j$  and  $k_{eff}$  is calculated for two  $Re_j$ , one low and one high. These calculations showed that the rms error in Nu is about 5% independently of  $Re_j$  and Nu. Table 1 summarizes the results of rms error calculation at the stagnation point of Nu profile for  $Re_j = 20400$ .

Table A2.1 Error analysis for Nu

	$x_1$	$\partial \text{Nu} / \partial x_1$	$\delta x_1$	$[(\partial \text{Nu} / \partial x_1) \delta x_1]^2$
$T_j, ^\circ\text{C}$	86.15	-2	0.15	0.099
$T_s, ^\circ\text{C}$	59.99	35	0.0005	0.0003
$w, \text{m}$	0.02	2749	0.00025	0.472
$k_j, \text{Wm}^{-2}\text{C}^{-1}$	0.027	2037	0.00054	1.210
$k_{eff}, \text{Wm}^{-2}\text{C}^{-1}$	0.414	133	0.0207	7.560
Nu	55			Sum : 9.35
% rms error:	5.4			(Sum) <sup>1/2</sup> : 3.06

Error analysis for  $\text{Re}_j$ :

$$\text{Re}_j = \frac{\rho_j u_j w}{\mu_j}$$

where  $\rho_j u_j w L = \dot{m}_{or}$ . Therefore:

$$\text{Re}_j = \frac{\dot{m}_{or}}{\mu_j L}$$

and

$$\frac{\partial \text{Re}_j}{\partial \dot{m}_{or}} = \frac{\text{Re}_j}{\dot{m}_{or}}; \quad \frac{\partial \text{Re}_j}{\partial L} = - \frac{\text{Re}_j}{L}$$

$\dot{m}_{or}$  is calculated by the following equation:

$$\dot{m}_{or} = \frac{C}{\sqrt{(1-\beta^4)}} A_2 \sqrt{(2g_c \Delta P \rho_1)}$$

where  $\Delta P = \rho_1 h g / g_c$ . Then;

$$\frac{\partial \dot{m}_{or}}{\partial C} = \frac{\dot{m}_{or}}{C}; \quad \frac{\partial \dot{m}_{or}}{\partial A_2} = \frac{\dot{m}_{or}}{A_2}; \quad \frac{\partial \dot{m}_{or}}{\partial h} = \frac{\dot{m}_{or}}{2h}$$

Table 2 gives the summary of the error analysis for  $\dot{m}_{or}$  and  $\text{Re}_j$  at  $\text{Re}_j = 20400$ .

Table A2.2, Error analysis for  $Re_j$ 

	$x_i$	$\partial(\dot{m}_{or})/\partial x_i$	$\delta x_i$	$[(\partial(\dot{m}_{or})/\partial x_i)\delta x_i]^2$
C	0.61	0.154	0.01	0.0000026
$A_2$ , $m^2$	0.00811	11.59	0.00047	0.000022
h, m	0.016	2.94	0.0005	0.0000022
$\dot{m}_{or}$ , kg/s: 0.094				Sum: 0.0000268
% rms error: 5.5				(Sum) <sup>1/2</sup> : 0.0052

	$x_i$	$\partial(Re)/\partial x_i$	$\delta x_i$	$[(\partial(Re)/\partial x_i)\delta x_i]^2$
$\dot{m}_{or}$ , kg/s	0.094	217021	0.0052	1273536
L, m	0.203	100492	0.003	90889
$Re_j$ : 20400				Sum: 1364424
% rms error: 5.7				Sum <sup>1/2</sup> : 1168

Error analysis for St:

$$St = \frac{Nu}{Re_j Pr}$$

and

$$\frac{\partial(St)}{\partial(Nu)} = \frac{St}{Nu}; \quad \frac{\partial(St)}{\partial(Re_j)} = -\frac{St}{Re_j}$$

Table 3 summarizes the results of the rms error calculation for Stanton number for the case considered for Nu and  $Re_j$  error analysis.

Table A2.3 Error analysis for St

	$x_i$	$\partial(St)/\partial x_i$	$\delta x_i$	$[(\partial(St)/\partial x_i)\delta x_i]^2$
Nu	60	0.00007	3.06	0.00000005
$Re_j$	20400	$-2. \times 10^{-7}$	1168	0.00000005
St: 0.00420				Sum: 0.0000001
% rms error: 7.5				(Sum) <sup>1/2</sup> : 0.00032

### APPENDIX 3

#### COMPUTATIONAL ASPECTS

#### A3.1 MATHEMATICAL FORMULATION

The following set of equations incorporating the Boussinesq turbulent viscosity concept describe the mean flow and temperature fields in statistically stationary turbulent flows of an incompressible slot jet impinging on a flat surface.

Continuity equation.

$$\frac{\partial}{\partial x} (\rho u) + \frac{\partial}{\partial y} (\rho v) = 0 \quad (A3.1)$$

Navier-Stokes equations

x-momentum:

$$\frac{\partial(\rho uu)}{\partial x} + \frac{\partial(\rho vu)}{\partial y} = \frac{\partial}{\partial x} (\mu_{\text{eff}} \frac{\partial u}{\partial x}) + \frac{\partial}{\partial y} (\mu_{\text{eff}} \frac{\partial u}{\partial y}) - \frac{\partial p}{\partial x} + S_u^* \quad (A3.2)$$

where

$$S_u^* = \frac{\partial}{\partial x} (\mu_{\text{eff}} \frac{\partial u}{\partial x}) + \frac{\partial}{\partial y} (\mu_{\text{eff}} \frac{\partial v}{\partial x})$$

y-momentum:

$$\frac{\partial(\rho uv)}{\partial x} + \frac{\partial(\rho vv)}{\partial y} = \frac{\partial}{\partial x} (\mu_{\text{eff}} \frac{\partial v}{\partial x}) + \frac{\partial}{\partial y} (\mu_{\text{eff}} \frac{\partial v}{\partial y}) - \frac{\partial p}{\partial y} + S_v^* \quad (A3.3)$$

where

$$S_v^* = \frac{\partial}{\partial x} (\mu_{\text{eff}} \frac{\partial u}{\partial y}) + \frac{\partial}{\partial y} (\mu_{\text{eff}} \frac{\partial v}{\partial y})$$

and where

$$\mu_{\text{eff}} = \mu_L + \mu_T \quad (A3.4)$$

In the  $k$ - $\epsilon$  model  $\mu_T$  is related to the turbulence quantities  $k$  and  $\epsilon$  in the following manner:

$$\mu_T = C_\mu \rho k^2 / \epsilon \quad (A3.5)$$

where the turbulent kinetic energy,  $k$ , and the turbulent kinetic energy dissipation rate,  $\epsilon$ , are calculated by solving the following differential equations.



Turbulent kinetic energy equation:

$$\frac{\partial(\rho uk)}{\partial x} + \frac{\partial(\rho vk)}{\partial y} = \frac{\partial}{\partial x} \left( \mu_L + \frac{\mu_T}{\sigma_k} \right) \frac{\partial k}{\partial x} + \frac{\partial}{\partial y} \left( \mu_L + \frac{\mu_T}{\sigma_k} \right) \frac{\partial k}{\partial y} + G - \rho \epsilon \quad (A3.6)$$

Turbulent energy dissipation rate equation:

$$\begin{aligned} \frac{\partial(\rho u \epsilon)}{\partial x} + \frac{\partial(\rho v \epsilon)}{\partial y} = & \frac{\partial}{\partial x} \left( \mu_L + \frac{\mu_T}{\sigma_\epsilon} \right) \frac{\partial \epsilon}{\partial x} + \frac{\partial}{\partial y} \left( \mu_L + \frac{\mu_T}{\sigma_\epsilon} \right) \frac{\partial \epsilon}{\partial y} \\ & + C_1 \frac{\epsilon}{k} G - C_2 \rho \frac{\epsilon^2}{k} \end{aligned} \quad (A3.7)$$

where

$$G = \mu_T \left\{ \left( \frac{\partial u}{\partial y} + \frac{\partial v}{\partial x} \right)^2 + 2 \left[ \left( \frac{\partial u}{\partial x} \right)^2 + \left( \frac{\partial v}{\partial y} \right)^2 \right] \right\} \quad (A3.8)$$

The asymptotic high-Re values of the coefficients in above equations are listed in Table A3.1.

Energy equation:

$$\frac{\partial(\rho uh)}{\partial x} + \frac{\partial(\rho vh)}{\partial y} = \frac{\partial}{\partial x} \left( \frac{\mu_L}{\sigma_L} + \frac{\mu_T}{\sigma_T} \right) \frac{\partial h}{\partial x} + \frac{\partial}{\partial y} \left( \frac{\mu_L}{\sigma_L} + \frac{\mu_T}{\sigma_T} \right) \frac{\partial h}{\partial y} \quad (A3.9)$$

where

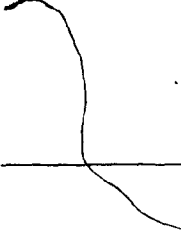
$$h = \frac{T - T_s}{T_j - T_s} \quad (A3.10)$$

A constant turbulent Prandtl number,  $\sigma_T$ , of 0.9 was used in the computations (Pun and Spalding[1977]).

### A3.2 NEAR-WALL MODELS

Turbulent flow near a solid boundary has different characteristics than flow away from solid boundaries. Because of the no-slip condition at the solid surface, the gradients of the dependent variables vary rapidly with distance from the wall. Local isotropy, which is the basic assumption of high-Re modeling, is no longer valid and molecular transport coefficients, which are negligible compared to turbulent ones, away from a solid surface, dominate the flow as the solid boundary is

Table A3.1. High-Reynolds-number values of empirical constants  
in turbulent kinetic energy and energy dissipation  
equations (Jones and Launder [1973])



$C_\mu$	$C_1$	$C_2$	$\sigma_k$	$\sigma_\epsilon$
0.09	1.44	1.92	1.0	1.3

approached

Two methods to handle the near-wall flows have been suggested. These are

1. the low-Re modelling method and,
2. the wall-function method.

The first method requires use of a very fine grid configuration near solid walls which increases the cost of the computation appreciably. Convergence problems may also arise due to the increased number of grids (which are usually highly irregular) required (Chieng and Launder[1980]). More significantly, these types of models have not been tested as extensively as the high-Re models.

The second method is usually preferred because of its computational advantages. It also allows introduction of empirical information easily for special types of flows. One disadvantage of this application is that when the predictions do not agree with the experimental results,

it is hard to judge whether the turbulence model or the near-wall model is responsible for the discrepancies.

In this study, two types of near-wall models were used in the computations. They will be referred to as "one-layer models" (Model 1 and Model 2) and "two-layer models" (Model 3 and Model 4).

### A3.2.1 One-Layer Models

Consider the grid point W on a surface and the adjacent grid point P as shown in Fig. A3.1. We assume that the point P lies in the fully turbulent region of the flow. For the purpose of estimating the frictional force applied at the wall, we need a relationship between the velocity  $v$  and the wall shear stress  $\tau_w$ . When there is no flow through the impingement surface this relationship is assumed to be the universal logarithmic law of the wall which is derived from the Couette flow assumptions

$$v^+ = \frac{1}{\kappa} \ln(E x^+) \quad (\text{A3.11})$$

where  $\kappa = 0.4$  and  $E = 9.0$  for smooth walls, and

$$v^+ = v / (\tau_w / \rho)^{1/2} \quad \text{and} \quad x^+ = x (\tau_w \rho)^{1/2} / \mu_L. \quad (\text{A3.12})$$

The effect of turbulence quantities is introduced to this relationship by assuming the thin fluid layer close to the wall to be in local equilibrium. Then the following relationship exists between  $\tau_w$  and  $k_P$ :

$$k_P = |\tau_w| / (\rho C_\mu^{1/2}) \quad (\text{A3.13})$$

Incorporating Eq. A3.13 into Eq. A3.11 and rearranging the following equation for  $\tau_w$  is obtained:

$$\tau_w = \frac{\kappa \rho v_P C_\mu^{1/4} k_P^{1/2}}{\ln \left( \frac{E \rho x_P C_\mu^{1/4} k_P^{1/2}}{\mu_L} \right)} \quad (\text{A3.14})$$

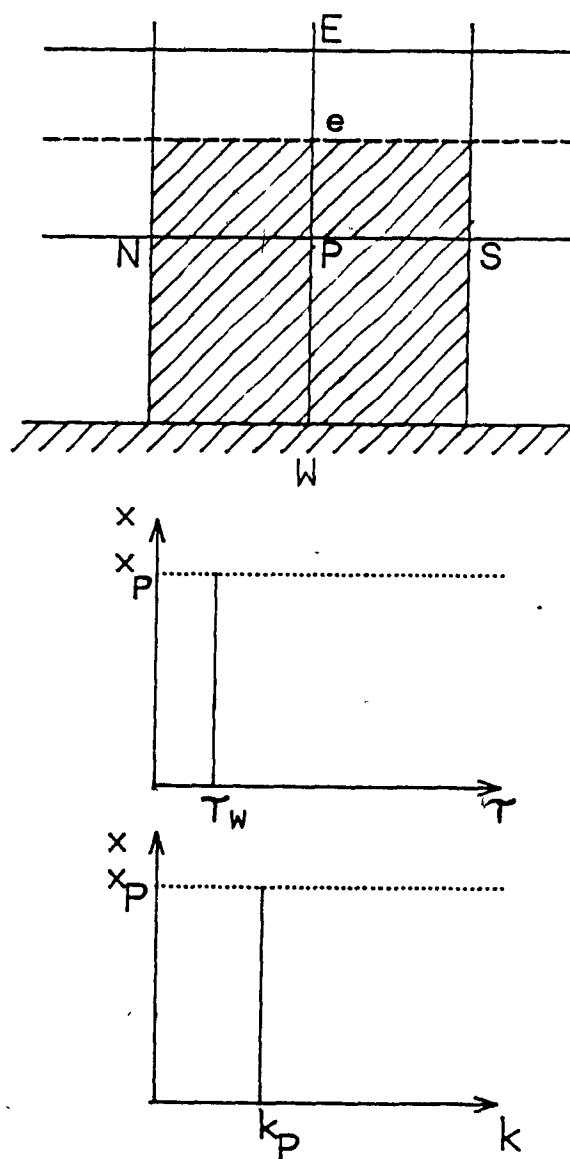


FIGURE A3.1. Control volume and near-wall distributions of  $\tau_w$  and  $k$  for Models 1 and 2

In Model 1 and Model 2 the turbulent kinetic energy generation term in the grid cell next to the wall is obtained using

$$\text{Model 1: } G_{P,W} = \iint_V \tau_w \frac{dv}{dx} dx dy = \tau_w v_e \Delta y_{ns} \quad (\text{A3.15a})$$

$$\begin{aligned} \text{Model 2: } G_{P,W} = & \iint_V \left\{ 2 \tau_w \left( \frac{\partial u}{\partial y} \right) + \tau_w \frac{\partial v}{\partial x} + \mu_T \left( \frac{\partial u}{\partial y} \right)^2 \right. \\ & + 2 \mu_T \left[ \left( \frac{\partial u}{\partial x} \right)^2 + \left( \frac{\partial v}{\partial y} \right)^2 \right] \} dx dy - 2 \tau_w (u_n - u_s) \Delta x_{We} + \tau_w v_e \Delta y_{ns} \quad (\text{A3.15b}) \\ & + \mu_T \left[ \left( \frac{\Delta u}{\Delta y} \right)_P^2 + 2 \left[ \left( \frac{\Delta u}{\Delta x} \right)_P^2 + \left( \frac{\Delta v}{\Delta y} \right)_P^2 \right] \right] \Delta x_{We} \Delta y_{ns}. \end{aligned}$$

where

$$\tau_w = \mu_T \frac{dv}{dx}$$

Dissipation of turbulent kinetic energy term in Eq. A3.6,  $\rho \epsilon$ , is approximated using Eq. A3.5 for  $\epsilon$ , i.e.

$$\epsilon = \frac{C \mu \rho k_P^2}{\mu_T} \quad (\text{A3.16})$$

Then by assuming  $\mu_T = \tau_w / (\partial v / \partial x)$ , and integrating in the near-wall control volume, we obtain

$$(\rho \epsilon)_{P,W} = \frac{C \mu \rho^2 k_P^2 v_e}{\tau_w} \Delta y_{ns} \quad (\text{A3.17})$$

The energy dissipation term at P is calculated from the following relation (Spalding[1967]):

$$\epsilon_P = \frac{C^{3/4} k_P^{3/2}}{\mu} / \kappa x_P \quad (\text{A3.18})$$

We also need a relationship to relate the wall heat flux,  $\dot{q}_w$  to the dimensionless temperature at the grid node P. This relationship is given by Jayatilleke[1969]:

$$St_w = \frac{-\dot{q}_w}{(h_P - h_w) \rho |v_P|} = \frac{\tau_w / (\rho v_P^2)}{\sigma_T \{1 + P \sqrt{\tau_w / (\rho v_P^2)}\}} \quad (\text{A3.19})$$

where

$$P = 9 \left( (\sigma_L / \sigma_T) - 1 \right) (\sigma_L / \sigma_T)^{-1/4}$$

### A3.2.2 Two-Layer Models

Again a scalar node P whose associated volume is bounded on the west side by a wall is considered as shown in Fig. A3.2. The near wall flow is considered viscous in the laminar sublayer and fully turbulent beyond this point. The thickness of the laminar sublayer is calculated assuming the value of the dimensionless distance from the wall,  $x^+$ , is constant and equal to 11.5 at the edge of this layer

$$x_v = \frac{11.5 \mu_L}{C^{1/4} \rho k_v^{1/2}} \quad (A3.20)$$

The generation and the destruction terms of the  $k_p$  equation are calculated in the following way (Chieng and Launder[1980]). The shear stress at the wall,  $\tau_w$ , which is constant and equal to the wall shear stress in the laminar sublayer, is assumed to increase suddenly at the edge of this layer due to the turbulence contribution. Beyond this point a linear variation of  $\tau_w$  with distance from the wall is considered. The precise form of this linear variation is obtained by connecting the turbulent shear stress at the outer edge of the cell,  $\tau_e$  with the wall shear stress,  $\tau_w$ . The wall shear stress is calculated using Eq. A3.14 by Model 4. In Model 3  $\tau_w$  is again calculated using the same equation by replacing  $k_p$  with  $k_v$ .

Since there is no turbulence generation in the viscous sublayer

$G_{P,w}$  is evaluated as :

$$G_{P,w} = \left( \frac{1}{x_e} \int_{x_v}^{x_e} \left( \tau_w + (\tau_e - \tau_w) \frac{x}{x_e} \right) \left( \frac{\partial v}{\partial x} + \frac{\partial u}{\partial y} \right) dx \right) \Delta x_w \Delta y_{ns} \quad (A3.21)$$

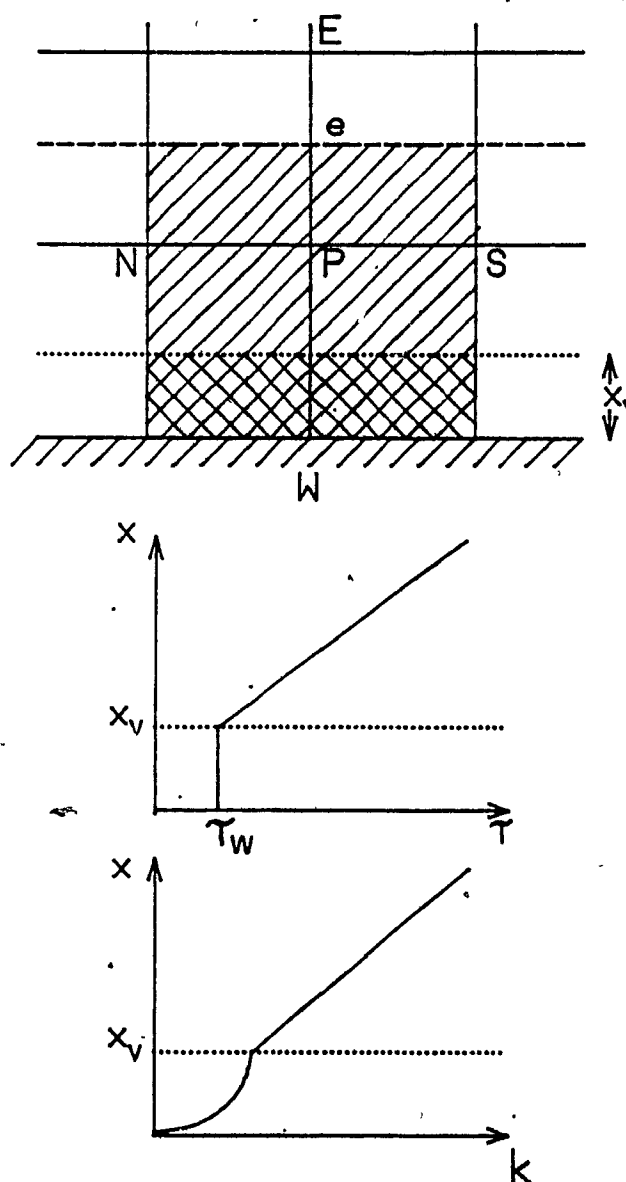


FIGURE A3.2. Control volume and near-wall distributions of  $\tau_w$  and  $k$  for Models 3 and 4

$$+ \iint_V 2 \mu_T \left[ \left( \frac{\partial u}{\partial x} \right)^2 + \left( \frac{\partial v}{\partial y} \right)^2 \right] dx dy$$

Using Eq. A3.14 to calculate  $\partial v / \partial x$ ,  $G_{P,w}$  can be obtained from Eq. A3.21 as:

$$G_{P,w} = \left[ \frac{\tau_w (v_e - v_v)}{x_e} + \frac{\tau_w (\tau_e - \tau_w)}{\rho \kappa C_\mu^{1/4} k_v^{1/2} x_e} \left( 1 - \frac{x_v}{x_e} \right) + \left\{ \tau_w \left( 1 - \frac{x_v}{x_e} \right) + \frac{1}{2} (\tau_e - \tau_w) \left( 1 - \frac{x_v}{x_e} \right)^2 \right\} \frac{\Delta u}{\Delta y} \right]_P + 2 \mu_T \left\{ \left( \frac{\Delta u}{\Delta x} \right)_P^2 + \left( \frac{\Delta v}{\Delta y} \right)_P^2 \right\} \Delta x_w \Delta y_{ns} \quad (A3.22)$$

where

$$\tau_w = \mu_T \left( \frac{\partial u}{\partial y} + \frac{\partial v}{\partial x} \right)$$

Here the turbulence kinetic energy at the edge of the viscous sublayer,  $k_v$ , is used as the approximate average  $k$  in the cell.

The dissipation rate of turbulence energy in the viscous sublayer is given by  $\epsilon = 2\nu(\partial k^{1/2}/\partial x)^2$ , Pope and Whitelaw[1976]. By assuming a parabolic distribution of  $k$  in the laminar sublayer,  $k = k_v(x/x_v)^2$ , the following expression is obtained for the dissipation rate inside the viscous sublayer:

$$\epsilon = \frac{2 \nu k_v}{x_v^2} \quad (A3.23)$$

In the turbulent region, by assuming linear variation of  $k$  with the distance from the wall beyond the edge of the viscous sublayer, Eq. A3.18 is integrated between  $x_v$  and  $x_e$  to obtain the mean value of  $\epsilon$  over the cell. Including the contribution of dissipation in the laminar sublayer the following expression is found for  $\bar{\epsilon}$

$$\bar{\epsilon} = \frac{2 C_\mu^{1/4} k_v^{3/2}}{x_v 11.5} + \frac{1}{\kappa C_\mu^{3/4} x_e} \left[ \frac{2}{3} (k_e^{3/2} - k_v^{3/2}) + 2a(k_e^{1/2} - k_v^{1/2}) + b \right] \quad (A3.24)$$

where



$$a = k_p - \frac{k_p - k_E}{x_p - x_E} x_p$$

and

$$b = \begin{cases} a^{3/2} \ln \left[ \frac{(k_e^{1/2} - a^{1/2})(k_v^{1/2} + a^{1/2})}{(k_v^{1/2} - a^{1/2})(k_e^{1/2} + a^{1/2})} \right] & \text{for } a > 0 \\ 0 & \text{for } a = 0 \\ (-a)^{3/2} \left[ \tan^{-1} \frac{k_e^{1/2}}{(-a)^{1/2}} - \tan^{-1} \frac{k_v^{1/2}}{(-a)^{1/2}} \right] & \text{for } a < 0 \end{cases}$$

Note that  $\epsilon_p$  is calculated using Eq. A3.18 while the dimensionless temperature at P,  $h_p$ , is related to the heat flux at the wall,  $\dot{q}_w$  via Eq. A3.19 as in the case of the "one-layer" models.

With the help of the wall function formulae the wall shear stress, the heat flux from the wall,  $\dot{q}_w$ , and the turbulent energy dissipation rate at the grid node P can be calculated and introduced into the finite difference equations as boundary conditions via the source terms. The details of this procedure are given in Section A3.6.

### A3.2.3 Near-Wall Models for Throughflow at the Surface

To account for throughflow at the impingement surface, the expression for the wall shear stress, Eq. A3.14, has to be modified to account for the effect of mass transfer at this boundary. This is accomplished in the following way.

Assuming that  $u_s \partial v / \partial x$  is much greater than  $v \partial v / \partial y$  in the neighborhood of the wall we write the boundary layer equation in the following form:

$$u_s \frac{\partial v}{\partial x} = \frac{1}{\rho} \frac{\partial \tau}{\partial x} \quad (\text{A3.25})$$

According to Prandtl's mixing length hypothesis

$$\tau = \rho \kappa^2 x^2 \left( \frac{\partial v}{\partial x} \right)^2 \quad (\text{A3.26})$$

Substituting Eq. A3.26 into Eq. A3.25 and solving for  $v$ , the following bilogarithmic expression is obtained:

$$v^+ = A + B \ln x^+ + \frac{1}{4\kappa^2} \frac{u_s}{v_\tau} \ln^2 x^+ \quad (\text{A3.27})$$

where  $A$  and  $B$  are constants and  $v_\tau = (\tau_w / \rho)^{1/2}$ .

Eq. A3.27 reduces to the no throughflow expression for  $v^+$  when  $u_s$  is set equal to zero. Theoretically,  $A$  and  $B$  should be functions of the throughflow velocity,  $u_s$ . In an attempt to find  $A$  and  $B$  in terms of  $u_s$ , the data of Favre et al. [1966] were used. Fig. A3.3 displays  $A$  and  $B$  plotted against the dimensionless throughflow velocity,  $u_s/v_\tau$ . It is seen that  $B$  does not vary appreciably with throughflow whereas  $A$  displays a maximum. The average value of  $B$  was found to be 2.5 which is equal to inverse of the von Karman constant,  $\kappa=0.4$ . As a first approximation  $A$  was chosen in such way that the constant 'E' in the log law of the wall retained its original value of 0.9 for smooth, non-transpiring walls.

### A3.3 GENERAL FORM OF DIFFERENTIAL EQUATIONS

The governing equations including the equation of continuity can be expressed in the following general form:

$$\underbrace{\frac{\partial(\rho u \Phi)}{\partial x} + \frac{\partial(\rho v \Phi)}{\partial y}}_{\text{CONVECTION}} = \underbrace{\frac{\partial}{\partial x} \left( \Gamma_\Phi \frac{\partial \Phi}{\partial x} \right) + \frac{\partial}{\partial y} \left( \Gamma_\Phi \frac{\partial \Phi}{\partial y} \right)}_{\text{DIFFUSION}} + \underbrace{S_\Phi}_{\text{SOURCE}} \quad (\text{A3.28})$$

where  $\Phi$  stands for the variables  $u$ ,  $v$ ,  $k$ ,  $\epsilon$  and  $h$ . For continuity equation  $\Phi = 1$ .  $\Gamma_\Phi$  is the exchange coefficient associated with  $\Phi$  and  $S_\Phi$  is the corresponding source term. In order to express the governing

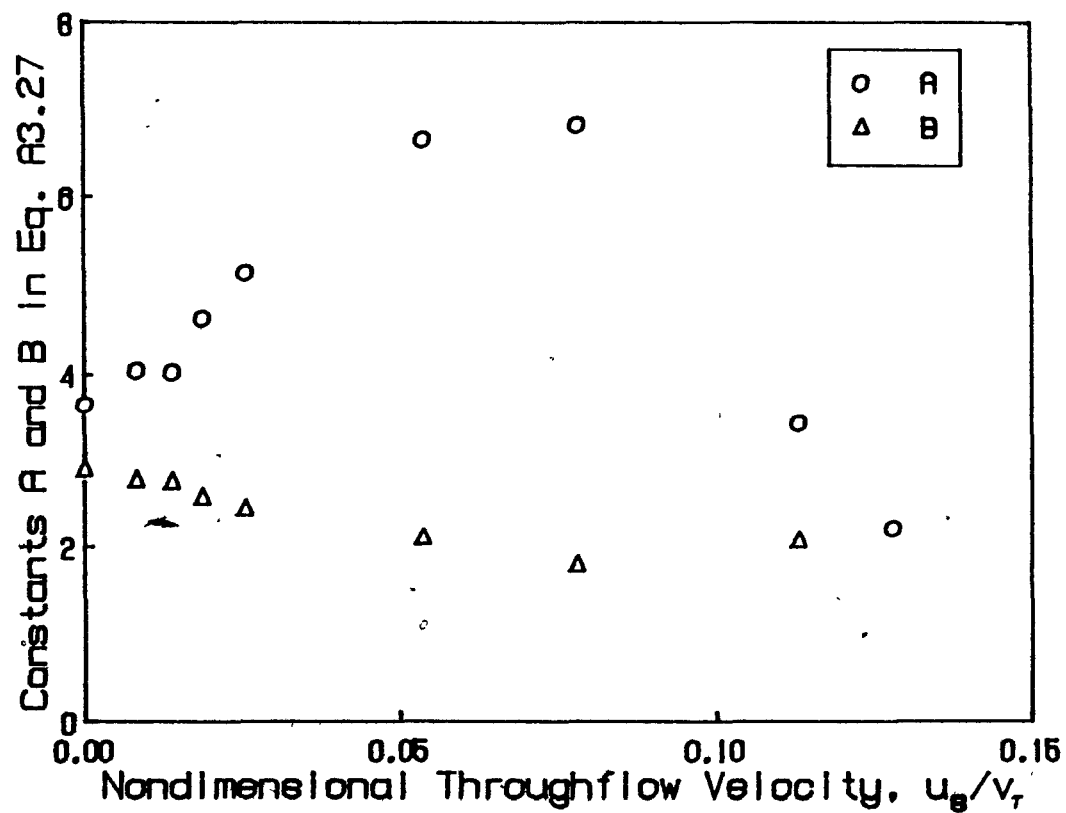


FIGURE A3.3. Constants A and B of Eq. A3.27 as a function of throughflow

Table A3.2. Summary of equations solved

Equation	$\Phi$	$\Gamma_\phi$	$S_\phi$
Continuity	1	0	0
x-momentum	u	$\mu_L + \mu_T$	$-\frac{\partial p}{\partial x} + \frac{\partial}{\partial x} \left[ (\mu_L + \mu_T) \frac{\partial u}{\partial x} \right]$ $+ \frac{\partial}{\partial y} \left[ (\mu_L + \mu_T) \frac{\partial v}{\partial x} \right]$
y-momentum	v	$\mu_L + \mu_T$	$-\frac{\partial p}{\partial y} + \frac{\partial}{\partial x} \left[ (\mu_L + \mu_T) \frac{\partial u}{\partial y} \right]$ $+ \frac{\partial}{\partial y} \left[ (\mu_L + \mu_T) \frac{\partial v}{\partial y} \right]$
Energy	h	$\frac{\mu_L}{\sigma_L} + \frac{\mu_T}{\sigma_T}$	0
Turbulent			
Energy	k	$\mu_L + \frac{\mu_T}{\sigma_k}$	$\rho G - \epsilon$
Turbulent			
Energy	$\epsilon$	$\mu_L + \frac{\mu_T}{\sigma_\epsilon}$	$C_1 \frac{\rho \epsilon}{k} G - C_2 \frac{\rho \epsilon^2}{k}$
Dissipation			

equation of a particular variable in the above generalized form, terms other than those in the form of "convection" and "diffusion" terms, are collected in the source term,  $S_\phi$ .  $\Gamma_\phi$  and  $S_\phi$  terms are shown in Table A3.2.

#### A3.4 GENERAL FORM OF FINITE-DIFFERENCE EQUATIONS

By integrating the general differential equation given in Eq. A3.28 over the control volume shown in Fig. A3.4 one obtains the following general finite difference equation at node P (Pun and Spalding[1976]).

$$\left( \sum_i A_i - S'_P \right) \phi_P = \sum_i A_i \phi_i + S_P \quad (A3.29)$$

where  $\sum_i$  means summation over the four neighboring nodes N, E, W, S.  $\sum_i A_i$  expresses the combined effect of convection and diffusion. As an example, consider the west face of the control volume shown in Fig. A3.4. The finite difference expression for the diffusion flux at this face is the following:

$$a_w J_{\phi,w}^d = -a_w \Gamma_{\phi,w} (\phi_P - \phi_W) / \delta_w \quad (A3.30)$$

where  $a_w$  is the area of the west face and  $\delta_w$  is the distance separating nodes W and P. The finite difference equation for the convective flux is

$$a_w J_{\phi,w}^c = (\rho u a)_w \phi_w \quad (A3.31)$$

where

$$\left. \begin{array}{ll} \phi_w = \phi_W & \text{for } (\rho u a)_w \geq 0 \\ \phi_w = \phi_P & \text{for } (\rho u a)_w < 0 \end{array} \right\} \begin{array}{l} \text{in "upwind difference"} \\ \text{scheme} \end{array} \quad (A3.32)$$

Hence, the total flux expression at the west face using the "upwind scheme" is

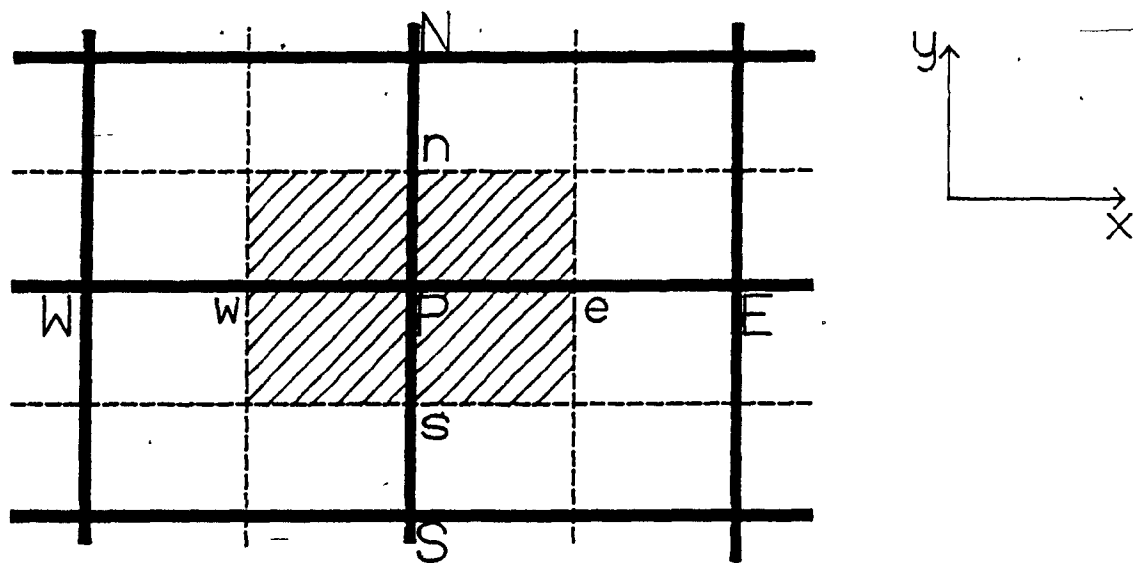


FIGURE A3.4. Control volume for scalar variables

$$C_w \geq 0 : A_w = a_w J_{\phi,w} - (D_w + C_w) \phi_w - D_w \phi_P ; \quad (A3.33)$$

$$C_w < 0 : A_w = a_w J_{\phi,w} - D_w \phi_w - (D_w - C_w) \phi_P \quad (A3.34)$$

where

$$C_w = (\rho u a)_w \text{ and } D_w = \Gamma_{\phi,w} a_w / \delta_w . \quad (A3.35)$$

Similar  $A_E$ ,  $A_S$ ,  $A_N$  equations for the east, south and north surfaces can be written following the same procedure.

For each node in the flow domain there is one equation of the form of Eq. A3.29 for each  $\phi$ . These equations are coupled together through  $A_i$ 's and through  $S_P$  or  $S_P'$ . The next task is to discretize the source terms and then to solve these equations iteratively until convergence is obtained.

### A3.5 TREATMENT OF THE SOURCE TERMS

Each of the source terms,  $S_\phi$ , is integrated over the control volume shown in Fig. A3.4 to obtain the corresponding finite difference forms. The following linearization procedure is adopted in the code.

$$\int S_{\phi,P} dx dy = S_P' \phi_P + S_P \quad (A3.36)$$

The source terms for  $u$ ,  $v$ ,  $k$  and  $\epsilon$  are derived as follows:

#### Source Term for u-velocity

$$\iint_V S_{u,e} dx dy = \iint_V \left( - \frac{\partial \tau}{\partial x} + S_{u,e}^* \right) dx dy \quad (A3.37)$$

$$= S_P u_e + S_P'$$

By referring to the control volume for  $u$  as shown in Fig. A3.5a,

$$S_P = \left\{ p \left[ \frac{1}{\Delta x_{EP}} + \left( \mu_{eff} \frac{\Delta u}{\Delta x} \right) \right] \Big|_P^E + \left( \mu_{eff} \frac{\Delta v}{\Delta x} \right) \Big|_{ES}^{EN} \frac{1}{\Delta y_{ns}} \right\} \Delta x_{EP} \Delta y_{ns}$$

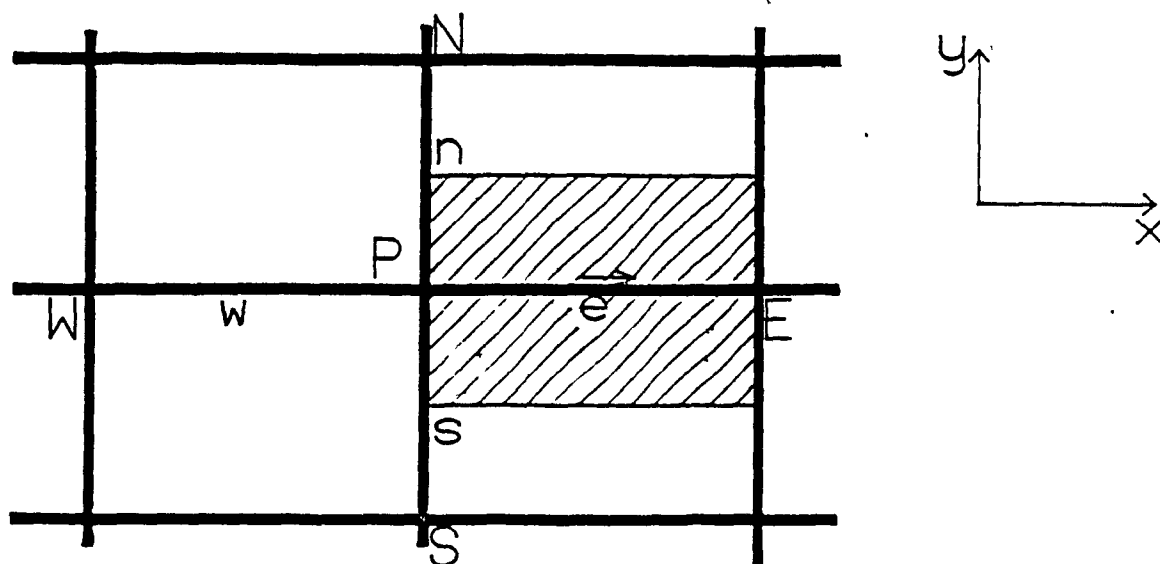


FIGURE A3.5a. Control volume for velocity in x-direction

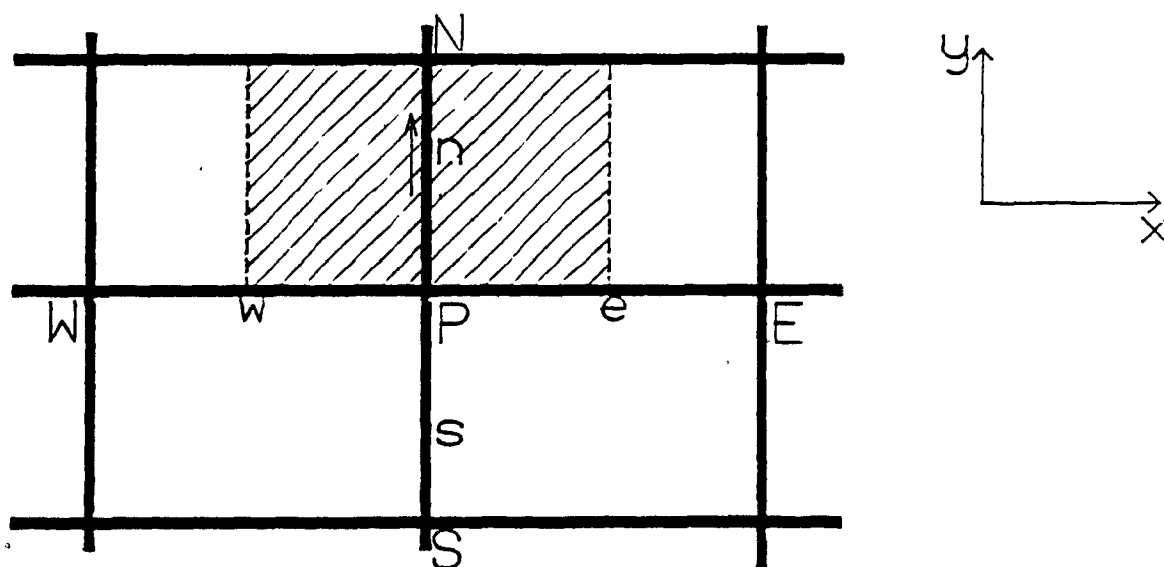


FIGURE A3.5b. Control volume for velocity in y-direction



(A3.38)

and  $S'_P = 0.$

Source Term for v-velocity

$$\begin{aligned} \iint_V S_{v,n} dx dy &= \iint_V \left( -\frac{\partial p}{\partial y} + S_{v,n}^* \right) dx dy \\ &= S_P v_n + S'_P \end{aligned} \quad (A3.39)$$

By referring to the control volume of v as shown in Fig. A3.5b,

$$S'_P = \left\{ p \left[ \frac{1}{\Delta y_{NP}} + \left( \mu_{eff} \frac{\Delta u}{\Delta y} \right) \right]_{WN}^{EN} \frac{1}{\Delta x_{we}} + \left( \mu_{eff} \frac{\Delta v}{\Delta y} \right) \left[ \frac{1}{\Delta y_{NP}} \right]_P^N \right\} \Delta x_{we} \Delta y_{NP} \quad (A3.40)$$

and  $S'_P = 0$

Source Term for the Turbulent Kinetic Energy

$$\begin{aligned} \iint_V S_k dx dy &= \iint_V (G - \rho \epsilon) dx dy \\ &= S'_P k_P + S_P \end{aligned} \quad (A3.41)$$

By referring to the control volume shown in Fig. A3.4

$$S'_P = - (C_2 \rho_P \epsilon_P + 0.5 G_P) \frac{\Delta x_{we} \Delta y_{sn}}{k_P^*}$$

and

$$S_P = 1.5 G_P + (C_2 - 1) \rho_P \epsilon_P \Delta x_{we} \Delta y_{sn}.$$

Note that  $k_P^*$  is the value of  $k_P$  obtained from the previous iteration.

### Source Term for the Turbulence Energy Dissipation Rate

$$\begin{aligned} \iint_V S_\epsilon \, dx \, dy &= \iint_V \left( C_1 \frac{\epsilon}{k} G - C_2 \rho \frac{\epsilon^2}{k} \right) dx \, dy \\ &= S'_P \epsilon_P + S_P \end{aligned} \quad (A3.42)$$

where

$$S'_P = -\rho_P (2C_2 - 1) \frac{\epsilon_P^*}{k_P} \Delta x_{we} \Delta y_{sn}$$

and where

$$S_P = \left( C_1 G_P + (C_2 - 1) \rho_P \epsilon_P \right) \frac{\epsilon_P^*}{k_P} \Delta x_{we} \Delta y_{sn}.$$

Note that  $\epsilon_P^*$  is the value of  $\epsilon_P$  obtained from the previous iteration

### A3.6 NUMERICAL TREATMENT OF NEAR-WALL BOUNDARIES

#### Velocity Component Parallel to Wall

Fig. A3.6 illustrates the boundary condition for velocity  $v$

As described previously in Section A3.3, the wall shear stress is calculated using Eq. A3.14 or Eq. A3.27 for each scalar grid node on the line next to the wall. These equations are valid only if the flow is fully turbulent, i.e.  $x^+ > 11.5$ . However, during an iteration  $x^+$  may drop below 11.5, in which case the following laminar relationships are employed for the no-throughflow and throughflow cases respectively.

$$\tau_w = -\mu_L \frac{v_P}{x_P} \quad (A3.43)$$

$$\tau_w = - \frac{u_s \rho_P v_P}{(1 - \exp(-u_s \rho_P \Delta x_{ew} / \mu_L))} \quad (A3.44)$$

Since Eqs. A3.14, A3.27, A3.43 and A3.44 determine how the shear stress due to the presence of the wall is related to the velocity  $v_P$  one

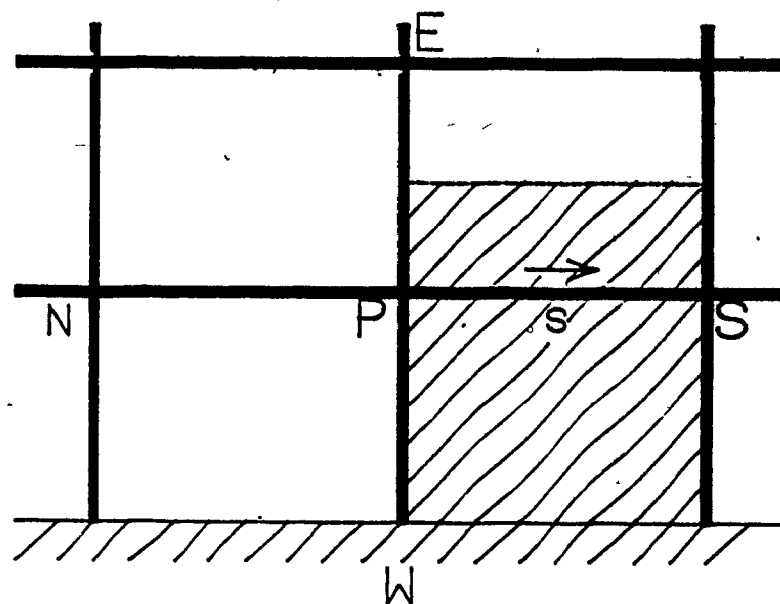


FIGURE A3.6. Near-wall control volume for velocity component parallel to wall

may set the finite difference coefficient of the wall grid node,  $A_w$ , in Eq. A3.29 equal to 0 and add the wall shear stress to the source term in the following way.

$$S_P = S_P + \tau_w \Big|_n \Delta y_{NP} \quad (A3.45)$$

where  $\tau_w \Big|_n$  is obtained by averaging  $\tau_w$  terms at the scalar grid nodes P and N.

### Turbulent Kinetic Energy

Fig. A3.7 illustrates the near-wall control volume cell for  $k$  and  $\epsilon$ .

The source terms of the finite difference equation for  $k_P$  at the grid nodes next to the wall are modified to include the wall effects.

All models:

$$S_P = G_{P,w} \quad (A3.46)$$

Models 1 and 2:

$$S'_P = - \frac{(\rho \epsilon)_{P,w}}{k_P}$$

Models 3 and 4:

(A3.47)

$$S'_P = - \frac{\rho \bar{\epsilon}}{k_P} (\text{volume})$$

### Turbulent Kinetic Energy Dissipation Rate

The turbulent kinetic energy dissipation rate at point P of Fig. A3.7 is given by Eq. A3.18. It should be noted that  $\epsilon_P$  is the boundary condition for  $\epsilon$  not  $\epsilon_w$ . In the code  $\epsilon_P$  is defined as follows:

$$S_P = 10^{10} \epsilon_P \quad (A3.48)$$

$$S'_P = - 10^{10}$$

### Energy

With throughflow at the impingement surface, if during an iteration

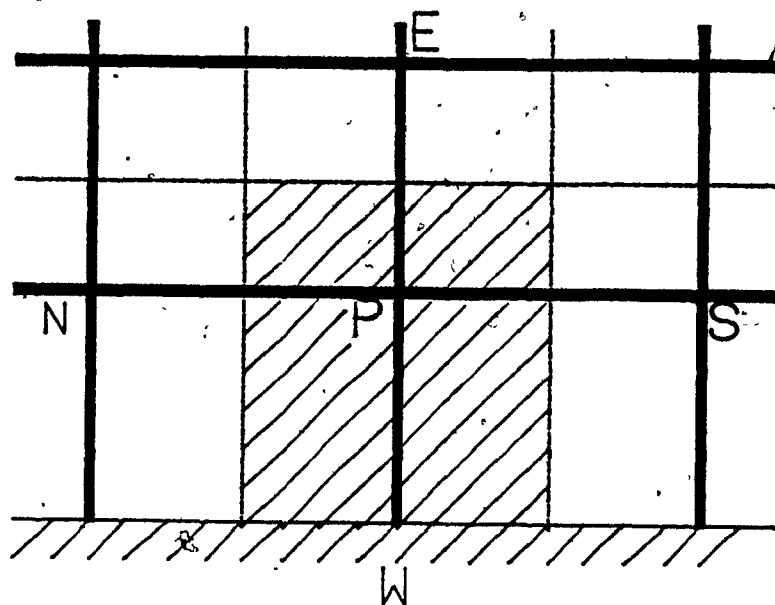


FIGURE A3.7. Near-wall control volume for scalar variables

$x^+$  drops below 11.5,  $\dot{q}_w$  is calculated using

$$St_w = \frac{-\dot{q}_w}{\rho v_p (h_p - h_w)} = \frac{u_s / v_p}{\exp\left(-\frac{Re_x u_s \sigma_h}{v_p}\right) - 1} \quad (A3.49)$$

For no-throughflow Eq. A3.19 applies.

The following modifications to the source terms are made to implement the calculated heat flux at the wall to the main flow by setting  $A_w=0$ ;

$$\begin{aligned} S_p &= S_p + St_w \rho v_p \Delta y_{ns} h_w \\ S'_p &= S'_p - St_w \rho v_p \Delta y_{ns} \end{aligned} \quad (A3.50)$$

### A3.7 SOLUTION OF THE FINITE DIFFERENCE EQUATIONS

#### A3.7.1 Line-by-Line Procedure

Equations of a particular variable  $\Phi$  for nodes on a line are solved simultaneously using TDMA (Tri-Diagonal Matrix Algorithm). While  $\Phi$  values along a line are being updated,  $\Phi$  values on both sides of the line are kept unchanged. Therefore, the general finite difference equation can be rewritten in the following form for a point on a particular line in S-N direction (see Fig. A3.8):

$$\Phi_P = a_P \Phi_N + b_P \Phi_S + c_P \quad (A3.51)$$

where

$$a_P = \frac{A_N}{\sum_i A_i - S'_P}, \quad b_P = \frac{A_S}{\sum_i A_i - S'_P} \quad (A3.52)$$

and  $c_P$  includes the terms related to  $\Phi_E$ ,  $\Phi_W$  and  $S_P$  terms which are assumed to be known at this moment. For convenience in presenting TDMA, it is necessary to use somewhat different nomenclature. Suppose the grid points in Fig. A3.8 were numbered 1, 2, 3, ..... N with points 1 and N denoting the boundary points. The Eq. A3.51 then takes the following

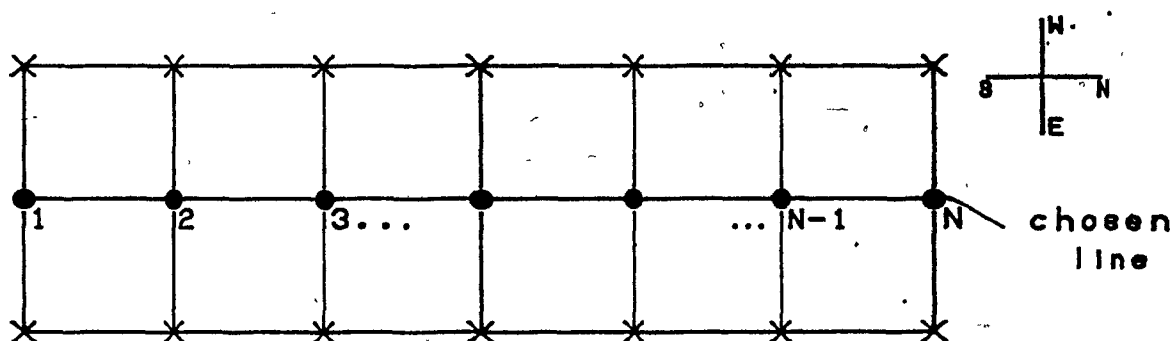


FIGURE A3.8. Line-by-line procedure

form:

$$\phi_i = a_i \phi_{i+1} + b_i \phi_{i-1} + c_i \quad (\text{A3.53})$$

for  $i = 1, 2, 3, \dots, N$ .

An expression in the following form is used in the backward-substitution process

$$\phi_i = P_i \phi_{i+1} + Q_i \quad (\text{A3.54})$$

Substitution of the same expression for the  $(i-1)^{\text{th}}$  node into Eq. A3.53 leads to

$$\phi_i = a_i \phi_{i+1} + b_i (P_{i-1} \phi_i + Q_{i-1}) + c_i \quad (\text{A3.55})$$

which can be arranged to look like Eq. A3.54. Hence the following expressions for  $P_i$  and  $Q_i$  can be obtained

$$P_i = \frac{a_i}{1 - b_i P_{i-1}} \quad (\text{A3.56})$$

$$Q_i = \frac{b_i Q_{i-1} + c_i}{1 - b_i P_{i-1}} \quad (\text{A3.57})$$

These are recurrence relations since they give  $P_i$  and  $Q_i$  in terms of  $P_{i-1}$  and  $Q_{i-1}$ . At node  $i=1$ ,  $\phi_1$  is defined by a boundary condition, therefore at  $i=2$ ,  $P_2$  and  $Q_2$  are given by

$$P_2 = \frac{b_2}{a_2} \quad \text{and} \quad Q_2 = \frac{c_2 \phi_1 + d_2}{a_2} \quad (\text{A3.58})$$

Now, by forward-substitution,  $P$  and  $Q$  terms for all grid nodes on the line can be obtained using recurrence relations. At node  $N$ , which is the end of the  $P_i$ ,  $Q_i$  sequence  $Q_N = \phi_N$ . Now the back substitution process can be started via Eq. A3.54 to obtain  $\phi_{N-1}$ ,  $\phi_{N-2}$ ,  $\dots$ ,  $\phi_2$ .

The flow, turbulence and energy quantities are updated by the TDMA process on each line in a predefined order which will be described next. The old values are replaced immediately by the updated quantities; so, the latest information is rapidly transferred to the



coupling equations. This computational arrangement is often called the NEAT (Nearly-Exact Adjustment of Terms) algorithm. The line-by-line procedure is repeated in the west-to-east direction until the prescribed number of sweeps are completed or until pre-set convergence criteria are met.

#### A3.7.2 Order of Updating the Variables

The order of updating the variables is done in such a way that it actually promotes faster convergence. By referring to Fig. A3.9 a forward step in the code can be described in the following manner.

1. At start  $u_1$ 's and  $p_2$ 's are "known".
2. Calculate  $u_3$ 's from guessed values of  $v_2$ 's and  $p_4$ 's
3. Solve the momentum equations for  $v_2$ 's.
4. Update  $k_2$ 's and  $\epsilon_2$ 's.
5. Update  $h_2$ 's.
6. Update  $\mu_T$  using  $k_2$ 's and  $\epsilon_2$ 's
7. Correct  $u$ 's,  $v$ 's and  $p$ 's for continuity errors.
8. Go back to step (1) for the next line.

Since incompressible, constant property flow is considered,  $h$ 's are updated only in the last 50 iterations of the total number of sweeps for each run.

The 7th step of the above sequence requires special attention. Therefore the next section is devoted to the process of making adjustments for "cell-wise continuity".

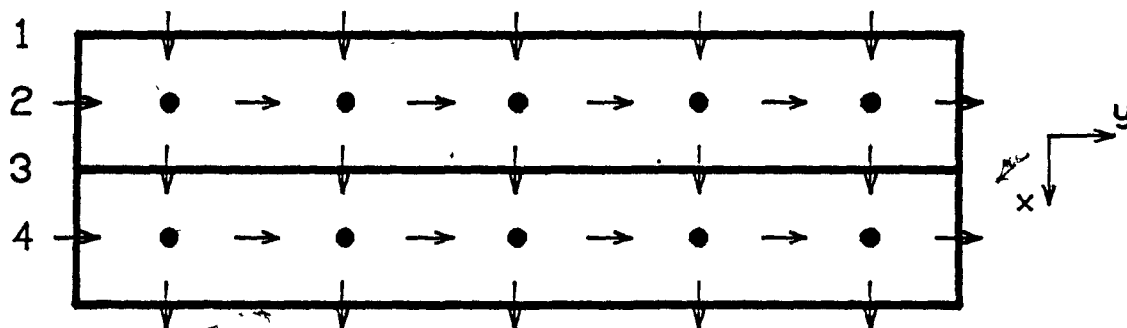


FIGURE A3.9. Order of updating the variables

## A3.8 CELL-WISE CONTINUITY

A3.8.1 Finite Difference Formulation of Momentum Equations

Control volumes for the x- and y-momentum equations are shown in Fig. A3.5. In relation to the normal control volume shown in Fig. A3.4 the control volumes for "u" and "v" velocities are staggered in x- and y- directions respectively. Since pressures are stored at the main grid nodes, the differences  $(p_P - p_E)$  and  $(p_P - p_S)$  can be used to calculate the pressure forces acting on the control volumes for velocities u and v correspondingly. This is one of the main advantages of the staggered grid.

The discretization equations for u and v velocities can be written in the following form.

$$(\sum A_{nb} - S'_e) u_e - \sum A_{nb} u_{nb} + (p_P - p_E)a_e + S_e \quad (A3.59)$$

$$(\sum A_{nb} - S'_n) v_n - \sum A_{nb} v_{nb} + (p_P - p_N)a_n + S_n \quad (A3.60)$$

where  $A_{nb}$ 's represent the combined convection-diffusion effect from neighboring nodes. Here the calculation of diffusion and convection terms at the control volume faces require appropriate interpolations. These equations are very similar to Eq. A3.29 except that the pressure gradient terms are not included in  $S'$  and  $S$ .

The momentum equations can be solved correctly only when the pressure field is known. Unless the correct pressure values are used in the computation, the resulting velocity field will not satisfy continuity. Therefore the computed u's, v's and p's using guessed values need to be corrected to satisfy continuity in each control volume cell.

Suppose  $u^*$ 's and  $v^*$ 's were obtained using a guessed pressure field,  $p^*$ , solving the following discretization equations.

$$(\sum A_{nb} - S'_e) u_e^* = \sum A_{nb} u_{nb}^* + (p_P^* - p_E^*) a_e + S_e \quad (A3.61)$$

$$(\sum A_{nb} - S'_n) v_n^* = \sum A_{nb} v_{nb}^* + (p_P^* - p_N^*) a_n + S_n \quad (A3.62)$$

Let the correct pressure  $p$  be obtained from

$$p = p^* + p' \quad (A3.63)$$

where  $p'$  is called the "pressure correction term". In a similar manner, velocity corrections  $u'$  and  $v'$  can be added to the velocity components

$$u = u^* + u' \quad v = v^* + v' \quad (A3.64)$$

If we subtract Eqs. A3.61 and A3.62 from Eqs. A3.59 and A3.60, by substituting Eq. A3.64 the following equation is obtained

$$(\sum A_{nb} - S'_e) u_e' = \sum A_{nb} u_{nb}' + (p_P' - p_E') a_e \quad (A3.65)$$

$$(\sum A_{nb} - S'_n) v_n' = \sum A_{nb} v_{nb}' + (p_P' - p_N') a_n \quad (A3.66)$$

At this point the underlined terms on the right hand side of these equations are dropped. The reasons for doing so are explained by Patankar[1980] and will not be repeated here. We may simply note that the final converged results are not affected by this omission. The result is

$$(\sum A_{nb} - S'_e) u_e' = (p_P' - p_E') a_e \quad (A3.67)$$

$$(\sum A_{nb} - S'_n) v_n' = (p_P' - p_N') a_n \quad (A3.68)$$

$$\text{or} \quad u_e' = d_e (p_P' - p_E') \quad \text{and} \quad v_n' = d_n (p_P' - p_N') \quad (A3.69)$$

$$\text{where} \quad d_e = \frac{a_e}{(\sum A_{nb} - S'_e)} \quad \text{and} \quad d_n = \frac{a_n}{(\sum A_{nb} - S'_n)} \quad (A3.70)$$

These are the velocity correction formulas.

### A3.8.2 Pressure Correction Equation

The pressure correction equation is derived by integrating the continuity equation (Eq. A3.10) over the control volume shown in Fig. A3.4 giving

$$[(\rho u)_e - (\rho u)_w] \Delta y + [(\rho v)_n - (\rho v)_s] \Delta x = 0. \quad (A3.71)$$

By combining Eqs. A3.64 and A3.69 the following velocity expressions are obtained:

$$u_e = u_e^* + d_e (p'_P - p'_E) \quad \text{and} \quad v_n = v_n^* + d_n (p'_P - p'_N). \quad (A3.72)$$

The correction formulas for  $u_w$  and  $v_s$  can be written similarly as:

$$u_w = u_w^* + d_w (p'_W - p'_P) \quad \text{and} \quad v_s = v_s^* + d_s (p'_S - p'_P). \quad (A3.73)$$

By replacing Eqs. A3.72 and A3.73 in Eq. A3.71, and rearranging the following discretization equation for  $p'$  is obtained:

$$A_P p'_P = A_E p'_E + A_W p'_W + A_N p'_N + A_S p'_S + S_P \quad (A3.74)$$

where

$$A_E = \rho_e d_e \Delta y, \quad A_W = \rho_w d_w \Delta y, \quad A_N = \rho_n d_n \Delta x, \quad A_S = \rho_s d_s \Delta x,$$

$$A_P = A_E + A_W + A_N + A_S$$

and where

$$S_P = [(\rho u^*)_w - (\rho u^*)_e] \Delta y + [(\rho v^*)_s - (\rho v^*)_n] \Delta x.$$

It may be realized that the source term  $S_P$  is actually the negative of the discretized continuity equation (Eq. A3.71) in terms of the starred velocities; when the value of the term  $S_P$  is equal to zero continuity is satisfied in the cell. This term is often referred to as the "error mass source".

### A3.8.3 Residual Sources and Convergence Criteria

Residual source for a variable at the grid point  $P$ ,  $RS_P$ , is defined

as

$$RS_P = \phi_P \left( \sum_{i=N,E,W,S} a_i' - S_P' \right) - \sum_{i=N,E,W,S} a_i \phi_i - S_P$$

Just before values of a variable on a line are updated, the absolute value of the algebraic sum of the residual sources on the line for the variable can be calculated with the finite difference coefficients available. These residual sources represent the error sources that need to be reduced and eliminated by the subsequent updating processes. All residual sources are suitably normalised with the jet inlet quantities. The largest  $RS_P$  value is compared to a very small value ( $10^{-3}$  is used in the present case), and if it is less than this value, the iteration process is terminated.

#### A3.8.4 Under Relaxation

Due to the highly coupled and nonlinear character of the finite difference equations, large change in coefficient values from iteration to iteration may lead to divergence. To cope with this problem under-relaxation of the dependent variables is essential. Thus,

$$\phi = \phi^* + \alpha (\phi - \phi^*)$$

where  $\alpha$  is the under-relaxation factor which is a real number between 0 and 1. Depending on the boundary conditions, the number of grid lines and their configurations, different combinations of under-relaxation factors were employed in this study. For example, when the two-layer model was employed as the boundary condition at the wall, during the initial 200 iterations, under-relaxation factors of 0.2, 0.2, 0.3, 0.3 were employed for  $u$ ,  $v$ ,  $k$  and  $\epsilon$  respectively. For the later iterations the under-relaxation factors of 0.5, 0.5, 0.7 and 0.7 were found appropriate to speed convergence.

When difficulties are encountered in obtaining converged results, experimenting with different combinations of under-relaxation factors usually helped. As a rule of thumb, a higher under-relaxation factor was applied to the fastest diverging variable. As the convergence got better, under-relaxation factors were increased.